Universitat Politècnica de València
Departamento de Máquinas y Motores Térmicos

Development of measurement and visualization techniques for characterization of mixing and combustion processes with surrogate fuels

Doctoral Thesis
Presented by:
D. Carlos Micó Reche
Directed by:
Prof. José Vicente Pastor Soriano

Valencia, September 2015

DOCTORAL THESIS

DEVELOPMENT OF MEASUREMENT AND VISUALIZATION TECHNIQUES FOR CHARACTERIZATION OF MIXING AND COMBUSTION PROCESSES WITH SURROGATE FUELS

Presented by:	D. Carlos Micó Reche
Directed by:	Prof. José Vicente Pastor Soriano

Evaluation Board:

President:	Prof. Raúl Payri Marín
Secretary:	Dr. Ezio Mancaruso
Examiner:	Dr. José Enrique Juliá Bolívar

External examiners:

Dr. Ezio Mancaruso
Dr. Michele Bardi
Dr. Blanca Giménez Olavarría

Valencia, September 2015

Resumen

El desarrollo y optimización de nuevos modos de combustión constituye actualmente un campo importante de investigación, para reducir la emisión de contaminantes en motores de combustión interna alternativos. Su desarrollo requiere del uso de gran variedad de herramientas experimentales y teóricas, que permitan conocer y comprender sus fundamentos. En este contexto se enmarca el objetivo principal de esta Tesis: la mejora y el desarrollo de técnicas de visualización y medida, para alcanzar el nivel de detalle y la precisión requeridos para estudios actuales y futuros de esta índole. El trabajo se ha basado en la caracterización de la combustión diésel por difusión para poder centrar el estudio en la parte metodológica, gracias al amplio conocimiento disponible sobre este modo de combustión.

El trabajo se ha dividido en dos apartados principales. El primero de ellos se centra en la caracterización de los procesos de evaporación y formación de la mezcla aire-combustible. Para ello, se he desarrollado y puesto en práctica una técnica basada en la absorción de luz por parte de las moléculas de combustible (UV-VIS LAS), que permite medir la concentración local de combustible evaporado en el seno de un chorro diésel. Esta ha sido optimizada para ser aplicada en condiciones de operación semejantes a las de un motor de encendido por compresión con combustibles cuyas propiedades ópticas no son óptimas, pero que son de gran interés para investigación dada su simplicidad. Además, se ha desarrollado una metodología para la medida del coeficiente de absorción de los combustibles, bajo las mismas condiciones de operación (presión y temperatura) que las que se dan en la cámara de combustión de un motor de encendido por compresión. Los resultados obtenidos se han analizado con detalle, para poder definir los límites y la fiabilidad de la metodología propuesta.

El segundo apartado corresponde a la caracterización del proceso de combustión y la formación de hollín. Para ello, se ha desarrollado un montaje óptico complejo que ha permitido aplicar de forma simultánea las tres técnicas más utilizadas en la literatura para la medida del hollín en una llama diésel: Método de Extinción Láser, Pirometría 2-Colores e Incandescencia Inducida por Láser. Los resultados obtenidos mediante las tres técnicas han sido comparados detalladamente, no sólo para identificar las principales ventajas e inconvenientes de cada técnica, sino también la fiabilidad de las mismas para distintas condiciones de operación.

Resum

El desenvolupament y optimització de nous modes de combustió constitueixen actualment un camp important d'investigació, para reduir la emissió de contaminants en motors de combustió internat alternatius. El seu desenvolupament requereix del us de gran varietat de ferramentes experimentals i teòriques, que permeten conèixer i comprendre els seus fonaments. En este context s'emmarca l'objectiu principal d'esta Tesi: la millora i el desenvolupament de tècniques de visualització i mesura, per a conseguir el nivell de detall i la precisió requerits per a estudis actuals i futurs d'esta índole. El treball s'ha basat en la caracterització de la combustió dièsel per difusió per a poder centrar l'estudi en la part metodològica, gràcies a l'ampli coneixement disponible sobre este mode de combustió.

El treball s'ha dividit en dos apartats principals. El primer d'ells es centra en la caracterització dels processos d'evaporació i formació de la mescla aire-combustible. Per això, s'ha desenvolupat i posat en pràctica una tècnica basada en la absorció de llum per part de les molècules de combustible (UV-VIS LAS), que permet mesurar la concentració local de combustible evaporat en el si d'un esprai dièsel. Esta ha sigut optimitzada per a ser aplicada en condicions d'operació semblants a les d'un motor d'encesa per compressió i combustibles amb propietats òptiques que no son les òptimes, però els quals són de gran interés en investigació donada la seua simplicitat. A més, s'ha desenvolupat una metodologia per a la mesura del coeficient d'absorció dels combustibles, a les mateixes condicions d'operació (pressió i temperatura) que les que es donen en la cambra de combustió d'un motor d'encesa per compressió. Els resultats obtinguts s'han analitzat amb detall, per a poder definir els límits i la fiabilitat de la metodologia proposada.

El segon apartat correspon a la caracterització del procés de combustió i la formació de sutja. Per a això, s'ha desenvolupat un muntatge òptic complex que permés aplicar de forma simultània les tres tècniques més utilitzades en la literatura per a la mesura de la sutja en una flama dièsel: Mètode d'Extinció Làser, Pirometria 2-Colors i Incandescència Induïda per Làser. Els resultats obtinguts per mitjà de les tres tècniques han sigut comparats detalladament, no sols per a identificar els principals avantatges i inconvenients de cada tècnica, sinó també la fiabilitat d'aquestes per a distintes condicions d'operació.

Abstract

The development and optimization of new combustion modes is nowadays an important research field, to reduce the pollutant emissions of the reciprocating internal combustion engines. Their development requires the use of a wide variety of experimental and theoretical tools, which make it possible to know and understand their fundamentals. In this context the main objective of this Thesis is framed: the development and optimization of measuring and visualization techniques, to reach the level of accuracy and detail required for current and future studies of that kind. The work has been based on the characterization of the diesel diffusion combustion to be able to focus the study on the methodological part, thanks to the extensive knowledge available on this combustion mode.

The work has been divided in two main blocks. The first one is focused on the characterization of evaporation and air-fuel mixture formation processes. For this purpose, a new technique has been developed and applied, based on the light absorption by the fuel molecules (UV-VIS LAS), which allows measuring the vapour fuel local concentration within a diesel spray. It has been optimized to be applied under operating conditions similar to those found in a compression ignition engine with fuels whose optical properties are not optimal, but which are interesting for research due to its simplicity. Moreover, a new methodology has been developed for measuring the absorption coefficient of the fuels, under similar operating conditions (i.e. pressure and temperature) than those found within the combustion chamber of a compression ignition engine. Results have been analysed in detail, to be able to define the limitations and reliability of the methodology proposed.

The second block corresponds to the characterization of the combustion process and the soot formation. For this purpose, a complex optical set-up has been developed which made it possible to simultaneously apply the three most used techniques that can be found in literature for soot measuring within a diesel flame: Laser Extinction Method, 2-Colour Pyrometry and Laser-Induced Incandescence. Results obtained by means of the three techniques have been compared in detail, not only to identify the main advantages and drawbacks of each technique, but also their reliability under different operating conditions.

a la memoria de mi padre
a mi madre y a mi hermana
a Carmen

Acknowledgements

I would like to acknowledge that part of this work has been funded by the Spanish Ministry of Science and Technology through the grant BES-2012-059721, linked to the project “Clean and high efficiency combustion using dual-fuel in compression ignition engines” (TRA2011-26359).

I would like also to acknowledge that part of this work has been developed in the frame of project B03_T02 Modelling of Emission Formation and Exhaust Gas Aftertreatment, Multicomponent Diesel Combustion Modelling and Validation with financial support of the “COMET K2-Competence Centres for Excellent Technologies Programme” of the Austrian Federal Ministry for Transport, Innovation and Technology (BMVIT), the Austrian Federal Ministry of Economy, Family and Youth (BMWFJ), the Austrian Research Promotion Agency (FFG), the Province of Styria and the Styrian Business Promotion Agency (SFG). I would furthermore like to thank our supporting industrial and scientific project partners, namely Kompetenzzentrum-Das Virtuelle Fahrzeug Forschungsgesellschaft mbH (ViF), AVL List GmbH, OMV Refining and Marketing GmbH, CMT Motores Térmicos - Universitat Politècnica de València (CMT-UPVLC), Institute for Internal Combustion Engines and Thermodynamics (IVT)-Graz University of Technology and to the Graz University of Technology.

Besides, I would like to acknowledge that some equipment used in this work has been partially supported by FEDER project funds (FEDER-ICTS-2012-06), framed in the operational program of unique scientific and technical infrastructure of the Ministry of Science and Innovation of Spain.

I can not forget to thank to the CMT - Motores Térmicos, and more specifically to Prof. Francisco Payri and Prof. José María Desantes, for accepting me into their research group and giving me this opportunity. Moreover, I would like to include also Prof. Jesús Benajes, director of the combustion group. These gratitude must be also extended to all members of the institute, who have assisted in a major or minor way to the conclusion of this thesis and whose contribution perhaps is never recognised as it deserves. From Juan Yustas (Figo) to all women from the administration department (Teresa, Amparo, Haby, Julia, Elvira, Carmina and Elena), thank you very much.

Obviously I would like to mention the contribution of my director, Prof. José Vicente Pastor, for all the help he has given me. He has been not only a scientific but also a “spiritual” guide, in the good and bad moments. He helped me to give some meaning to all my work and, without that, this document would have never been written. Besides him, there are other professors in the department who I might be always grateful to. Thus, I would like to highlight Dr. José María García-Oliver as he has been also a scientific “guru” to me and a big part of this thesis has been completed thanks to him. I would like to include also Dr. Antonio García, because he taught and gave me advise at some difficult moments.

I consider that I must include in these acknowledgements the technical staff of the department, because without them get the job done is almost impossible. Starting with the coordinator, Dr. Vicente Bermúdez, and going through each and every member of the staff. I would like to highlight the help provided by Daniel Lérida, who taught me all the secrets of the laboratory; Gabriel Alcantarilla, who always helped me when I asked; and José Enrique del Rey, whom I will be always grateful to for everything he has done for me and whose jokes I think I will miss with time. I can not forget mentioning José Gálvez "el troner" and his last time parts. Finally, I would like also to highlight the contribution of Vicente Calabuig, who assisted me like a good friend does during hard working periods in the laboratory.

It is sure that everybody who reaches this point sooner or later discovers that there is not only important the people who is directly involved in your work but also everyone who surrounds you and who helps you moving forward day by day. Colleges (and friends) like Vicent, Eduardo, Johannes or Javier who are one of the best things that I take from this stage of my life. Obviously, I can not leave without any mention Daniela, Manuel, Adrián or Walter with whom it has been a pleasure to share all this time and experience. Finally, I would like to mention also all my former officemates as Francisco, Jean-Guillaume, Gustavo o Mattia, who have been able to tolerate me and taught me a lot of things during these years.

I am sure that I am not mentioning everybody who deserves it, but I have shared these last years with so many people that it is difficult for me to not forget anybody. Please, do not hesitate to inform me and I will include you next time.

Table of Contents

Index of Figures

Index of Tables

Nomenclature

Latin

$\dot{\mathrm{m}}_f$	Mass flow rate
$\dot{\mathrm{M}}_f$	Spray momentum flux
u_0	Fuel effective exit velocity
A_{ef}	Effective nozzle output area
C_d	Discharge coefficient of a nozzle hole
A/F	Air-fuel ratio
P	Pressure
T	Temperature
DEC	n-Decane
50DEC	50% n-Decane/50% n-Hexadecane
30DEC	30% n-Decane/70% n-Hexadecane
HEX	n-Hexadecane
K_s	Conicity factor of the nozzle
1D	One-dimensional
HEP	n-Heptane
HAF	High-absorptive multi-component fuel
ϕ_{CO}	Schlieren cutoff diameter
ϕ_{LS}	Schlieren light-source diameter
LL	Liquid Length
S	Spray penetration
$\overline{LL}$	Steady-stage averaged liquid length
$Y_{f,evap}$	Mass fraction at LL
ρ_{vf}	Vapour fuel partial density
L	Optical path

Q_{ext}	Droplet extinction coefficient
R	Ratio of the drop optical thickness at two wavelengths
Y_f	Fuel mass fraction
X_f	Fuel mole fraction
HEPB#	HEP and HAF blend number #
I	Attenuated light intensity
I_0	Original light intensity
Abs	Absorption
Att	Attenuation
ϕ_{eq}	Equivalent diameter
DOD	n-Dodecane
T_{inj}	Fuel injection temperature
$\varDelta P$	In-cylinder pressure difference between combustion and motored cycle.
k_{soot}	Dimensionless soot extinction coefficient of soot
Y_{soot}	Soot volume fraction
I_{soot}	Intensity of soot thermal radiation
I_{LII}	Laser-Induced Incandescence signal intensity
S_{LII}	Accumulated Laser-Induced Incandescence signal along optical path

Greek

ρ	Density
θ	Beam-steering angle
α	Spray cone angle
μ	Mean value
σ	Standard deviation
λ	Wavelength
ε	Absorption coefficient
ξ	Efficiency of extinction by liquid droplets
Ω	Detection solid angle

Subscripts

c	Relative to in-cylinder conditions
int	Relative to intake conditions
inj	Relative to injection
f	Relative to fuel
LL	Relative to liquid length measurements

S	Relative to spray penetration measurements
ang	Relative to spray cone angle measurements
Abs	Relative to light absorption
Att	Relative to light attenuation
cl	Relative to the axis of the spray
COL	Relative to collimated-light based measurements
$DIFF$	Relative to diffuse-light based measurements
$soot$	Relative to soot
LEM	Relative to Laser Extinction Method
$2C$	Relative to 2-Colour Pyrometry
LII	Relative to Laser-induced incandescence
st	Relative to Stoichiometric conditions

Initials and acronyms

ICE	Internal Combustion Engine
CI	Compression Ignition
BSFC	Brake Specific Fuel Consumption
CFD	Computational Fluid Dynamics
RoHR	Rate of Heat Release
SoI	Start of Injection
SoC	Start of Combustion
EoI	End of Injection
DI	Direct Injection
MIE	Mie Scattering
BL	Backlit illumination
PDA	Phase Doppler Anemometry
PDS	Planar Droplet Sizing
BI	Ballistic Imaging
SLIPI	Structured Laser Illumination Planar Imaging
PRS	Planar Rayleigh Scattering
PLIF	Planar Laser Induced Fluorescence
PLIEF	Planar Laser Induced Exciplex Fluorescence
LAS	Light Absorption and Scattering
UV	Ultraviolet
CCD	Charge-coupled device

ICCD	Intensified Charge-coupled device
CN	Cetane Number
DCN	Derived Cetane Number
aSoE	after Start of Energizing
LOL	Lift-off Length
LII	Laser-Induced Incandescence
2C	2-Colour Pyrometry
LEM	Laser Extinction Method
EVC	Exhaust vent close
TDC	Top dead centre
CAD	Crank angle degree
PIV	Particle Image Velocimetry
fps	Frames per second
LRT	Log-Likelyhood ratio test
PDF	Probability density function
CDF	Cumulative density function
CoV	Coefficient of Variation
MW	Molecular weight
LoS	Line-of-Sight
FWHM	Full-Width Half-Maximum
STP	Standard Temperature and Pressure
OP	Onion-peeling method
A3P	Three-point Abel inversion
TR	Tikhonov regularization
ID	Ignition delay

Chapter 1

Introduction

Contents

1.1 Introduction

The aim of this chapter is to give an approach to the global framework for the research performed in this thesis. A brief introduction to the history of compression ignition (CI) engines is presented, followed by a discussion of their current relevance on different aspects such as environment or economy and the challenges that society has to face in the near future in this regard. Finally, the main objectives and the methodology followed in this work to address them are outlined, as well as the contents of every chapter of this document.

1.2 Context and Motivations of the Study

1.2.1 The Compression Ignition Engine

In 1892, the French-German engineer Rudolph Diesel patented the design of an engine based on the fuel ignition by the heat of air compressed in the combustion chamber. In 1893 Diesel created the first working model of his engine, obtaining a remarkable 26% fuel efficiency, more than double the current standard set at that time by the steam engines. The suppression of pumping losses and the use of higher compression ratios in comparison to the spark ignited engine, offered a significant improvement in terms efficiency. Since then, the diesel engine has evolved becoming more sophisticated and the field of application has widened considerably.

The first diesel engines were large, due to the materials needed to be used to withstand the high compression cycles of fuel ignition. They were used primarily at high-power applications like electricity power plants, locomotives, ships or even trucks, where the size was not a problem and fuel efficiency was important. Later on, some advances at the combustion chamber geometry together with the refinement on injection systems allowed reducing the size of the engine. It was in 1936 when Daimler-Benz mounted the first diesel engine at a production passenger car. Since then, the diesel engine continued evolving and spreading all over the world.

In 1973 and 1978 two oil crises hit the occidental world. At that moment, the economy of most countries was firmly dependent on oil imports and thus energy saving policies became important. In Europe, governments promoted the implantation of diesel engines (thanks to its higher efficiency) on passenger cars and light-duty vehicles, by adapting their tax policy in favour of this technology. It encouraged the manufacturers to invest on research and development. In 1978 Mercedes-Benz released the first diesel turbocharged driven passenger car, which made it possible to obtain higher specific power whilst reducing the engine size. In 1988, Fiat released the first direct injection engine on the Croma 2.0 TDI. Both technologies made the difference in terms of emissions, performance and power. They redefined the diesel engine and opened new fields for research and development.

Nowadays, diesel engines are dominant in the heavy-duty sector due to their lower specific fuel consumption and higher specific torque performance, compared to gasoline engines. For light-duty vehicles, the market share grew rapidly in the early 90's. Currently in Europe, there is a significant variation among the Member States of the European Union. Belgium, France and Spain

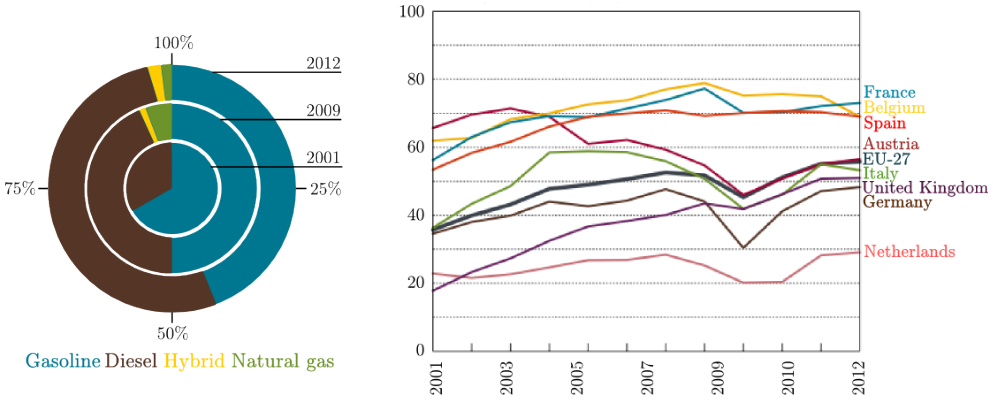

Figure 1.1. *Evolution of market share in Europe per motorization technology in the past decade. Source [1].*

have diesel take-up rates of around 70% [1], while in the Netherlands the rate is much lower. However, despite the differences in absolute market share and increasing rates, most of the countries of the EU-27 show a growing interest in light-duty diesel vehicles. In 2012, 55% [1] of newly registered cars were powered by diesel engines (figure 1.1). In terms of light-duty commercial vehicles, the market share of the diesel motorization during 2012 in the EU-27 achieved 97% [1].

1.2.2 The Current Challenges: Energy framework and exhaust emissions

In the last decades, society is facing two of the most important challenges related to the use of the internal combustion engines (ICE): The foreseen shortage of fossil fuels and the effects of engine exhaust emissions on the environment. Since the discovery and introduction of the first petrol fuels as energy sources, at the end of 19th century, society's development has been really attached to them. Since then, the worldwide oil consumption kept increasing and spreading to a lot of different aspects of our daily lives. In a global economy with an expected increase of energy consumption of 56% between 2010 and 2040, the fossil fuels (which comprise coal, liquid and gas fuels) play a major role representing almost 80% of world consumed energy [2].

The liquid fuels (both petroleum derived liquids and to a minor extent other liquid fuels including GTL, BTL, etc.) are the major energy source with a 34% share of the world energy pool in 2010 (figure 1.2). However,

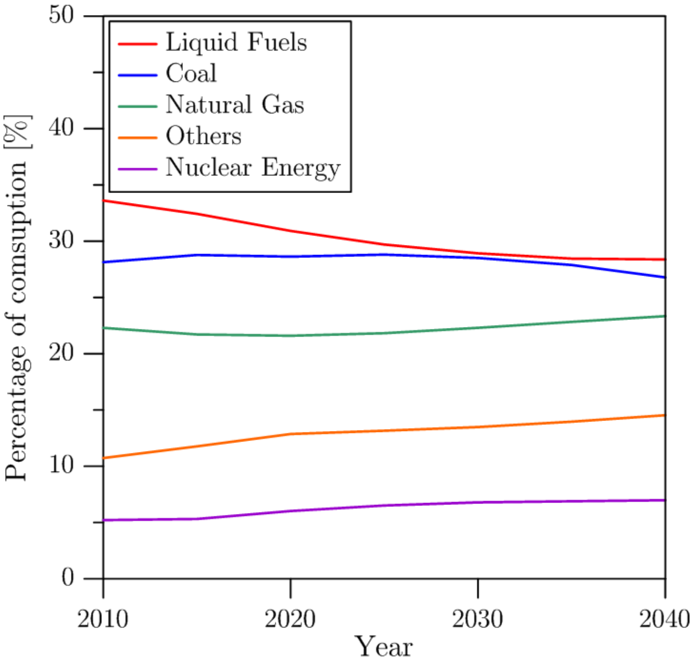

Figure 1.2. *Worldwide energy usage estimations by fuel type. Source [2].*

a reduction of this share to 28% in 2040 is expected, due to high oil prices and the appearance of other energy alternatives. Even though, liquid fuels will remain as the major energy source as it is expected that markets will move to a more efficient usage instead of changing to other energy sources. Most of the consumption of liquid fuels can be attributed to the industrial and transportation sectors. Even in the second one, these fuels still provide the major part of the energy consumed and this situation is expected not to change drastically up to 2040. Moreover, despite the rising fuel prices, the use of liquid fuels in transportation would increase by an average of 1.1 percent per year. This would account for the 63% of the total increase in liquid fuel use expected between 2010 and 2040.

The 1 st of January 2013, the proved world oil reserves were estimated at 1.638 billion barrels (120 billion barrels higher than the estimate for 2012) [3]. The "proved reserves" concept is often used to "evaluate" the potential of the petroleum fuel reserves but it takes in consideration only estimated quantities of crude oil from known resources and therefore it is not a good statistic of the future potential of this energy source. Even if the proved world oil reserves increase in the future, different experts in the field suggest that oil production

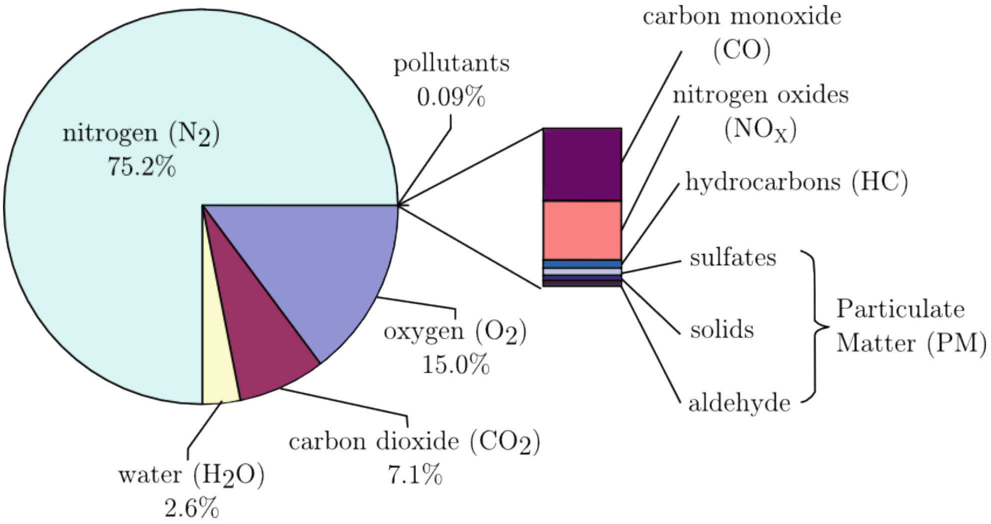

Figure 1.3. *Exhaust gas components during real diesel combustion in percent by weight [8].*

will reach a maximum point known as “Peak Oil”, after which it is expected to enter into a terminal decline [4]. Some optimistic estimations forecast that the global decline will begin after 2020 while some other suggest that the process already started after 2007 [5].

This massive usage of ICE powered by petroleum derived fuels also raises concerns about their effect over air quality and the environment. The ideal combustion of a hydrocarbon molecule generates Carbon Dioxide (CO_2), water (H_2O) and Nitrogen (N_2). However, actual diesel combustion also generates pollutants (figure 1.3) such as Carbon Monoxide (CO), Particulate Matter (PM), unburned hydrocarbons (UHC) and Nitrogen Oxides ($NO_x = NO + NO_2$), which have been identified as potentially harmful for human health and/or environment. Although the direct effect on humans is difficult to quantify, different reports from medical scientific community have shown the existence of a relation between traffic-related air pollution and mortality [6, 7]. Since 1940’s there have been systematic efforts in California to reduce the effect of the road transportation emission on the air quality. In Europe, the alarm was raised in 1960’s due to the direct harmful of CO to human health. The PM is also responsible for respiratory diseases as asthma or bronchitis. During 1970’s and 1980’s different rural regions were affected by the acid rain and photooxidants, whose formation has been directly related to NO_x and UHC.

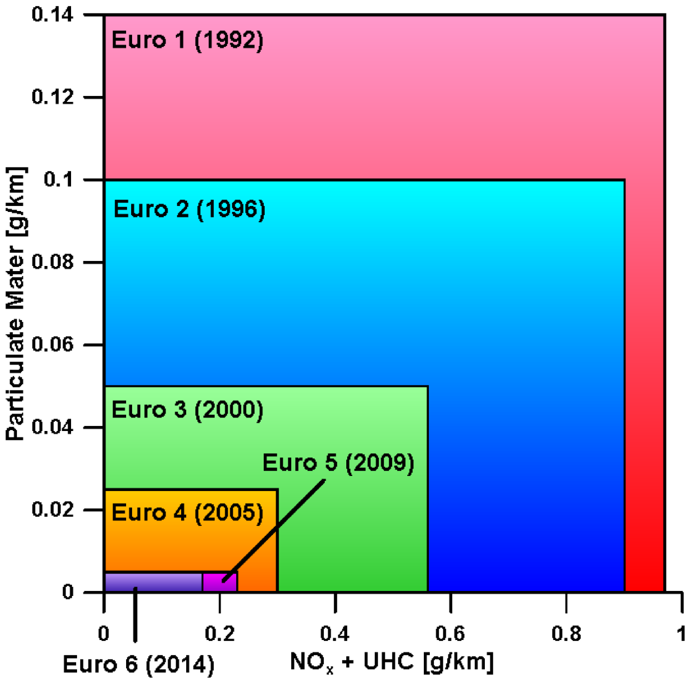

Figure 1.4. *Evolution of European emission standards in terms of HC+NOx and PM emissions for diesel cars. Source [9]..*

By the beginning of 1990's there was a clear raise awareness regarding the existence of some exhaust emissions that were not harmful for humans, but were affecting the environment. As a consequence, the different environmental agencies around the world initiated legislation programs. It started in 1961 in the United States and it was followed by Japan in 1966 and Europe in 1970. Since then, the legislation has been updated periodically with more and more restrictive limitations. In figure 1.4, the evolution of the European emission standards is represented by the limitations established in terms of PM and NO_x emissions for light-duty vehicles.

For CO_2 and other "greenhouse gases" emissions, regulations inforced only recently, although fuel consumption (which is directly linked to CO_2 emissions) was already considered in earlier regulations such as Corporate Average Fuel Economy (CAFE) standards established for passenger cars and light-duty trucks since 1975. The first carbon dioxide emission targets for new passenger cars were set in 1998/99 through voluntary agreements between the European Commission and the automotive industry. While significant CO_2 emission reductions were achieved in the initial years, since around 2004 the manufacturers could no longer meet their voluntary targets. In response, the Commission developed a mandatory CO_2 emission reduction program, and CO_2 emission targets for new passenger cars to be sold in 2015 were adopted in April 2009.

To face these severe limits, major technological improvements have been brought to the diesel engines during the past decades. Although they increased the cost of the engines, they made it possible to progressively improve its performance and achieve better efficiency while continuously reducing pollutant formation. In this regard, it is important to highlight the introduction of the high-pressure injection systems that allowed in-cylinder direct injections and the use of different strategies combining injection pressures and injection rates [8, 10] or the number of injection per cycle [11, 12]. The direct injection combined with the introduction of the turbocharger, which increased the specific power of the diesel engines while reducing fuel consumption and the pollutant emissions. The exhaust gas recirculation is also a quite spread measure, used nowadays in the majority of diesel vehicle engines.

The optimization of a diesel engine normally entails a conflict between fuel consumption and emission reduction. Individual measures are seldom able to reduce all pollutants in the same proportion and additional strategies are usually necessary to achieve the global objective. Thus, the tuning of the engine requires a compromise between the cost and complexity of the different measures applied and the results obtained. In table 1.1, the effect of the currently common methods [8] to reduce emissions over the different species mentioned before is summarized. It is possible to see that no measure individually affects all the elements positively and normally a combination of several measures is required to compensate a detrimental effect. One of the main conflicts regarding ICE optimization is the simultaneous reduction of NO_x and PM, known as "PM/NO_x trade-off". Nowadays, fulfilling the standard limits require the use of heavy after-treatment systems in both passenger cars and heavy duty engines. However, aftertreatment equipment increases the costs of the powertrain and even could affect the efficiency of the engine [8]. For this reason, many research efforts are dedicated to improve and develop new combustion concepts by reducing pollutant formation and fuel consumption inside the combustion chamber of the ICE.

During last years researchers are focussed on the development of new engine combustion strategies to promote premixed (reduce PM formation) and low-temperature combustion (avoid NO_x). In the Toyota UNIBUS (Uniform Bulky Combustion System) a double-injection strategy is used [13] with some

Measure	**NO_x**	**HC/CO**	**Soot**	**BSFC**	**Noise**
Retarded Start of Injection	+	−	−	−	+
Exhaust gas recirculation	+	−	−	−	+
Cooled EGR	+	−	+	+	0
Supercharging	−	+	+	+	0
Intercooling	+	−	+	+	0
Pilot Injection	0	+	−	0	+
Added post-injection	+	0	+	−	0
Injection pressure increase	0	+	+	+	0
Lower compression ratio	+	−	+	0	−

Table 1.1. *Different measures for the optimization of the diesel combustion and their effect on different parameters. Symbols: + reduce; − increase; 0 no effect. Source [8].*

fuel injected very early in the cycle to get better mixing with air. Nissan's MK (Modulated Kinetics) design utilizes high levels of EGR in conjunction with high swirl [14] and late injection to promote fuel/air mixing by increasing the ignition delay. Reduction of NO_x could also be achieved by PREDIC (Premixed Lean Diesel Combustion) at low to part loads and its evolution, MULDIC (Multiple Stage Diesel Combustion), with multiple fuel injectors and injections, at higher loads [15]. In homogeneous-charge compression-ignition (HCCI) fuel and air are fully premixed and compressed till the charge auto-ignites. However, there is no in-cycle control of combustion phasing with HCCI unlike with the spark timing in SI engines or the injection timing in regular CI engines. Hence, HCCI combustion is very difficult to control and is also limited to low loads.

Strategies based on changing and controlling the reactivity of the fuel have shown promising results. More specifically, it has been previously reported in literature that the use of blends made of fuels with different reactivity characteristics (i.e. gasoline and diesel) offers several benefits [16]. In their neat forms, each fuel (diesel and gasoline) has specific advantages and shortcomings for HCCI operation. Gasoline has a high volatility and thus, evaporation is rapid and premixed charge can be obtained using port fuel injection. However, the autoignition qualities of gasoline are poor and it becomes difficult to achieve combustion at low-load conditions [17]. Diesel fuel has superior auto-ignition quality. However, this can lead to higher difficulties to control combustion phasing as engine load increases. In this sense, recent results [18–22] suggest that different fuel blends will be required at different operating conditions.

It can be concluded that the development of new modes of combustion offers a promising roadmap to reduce pollutant formation. Besides, the use of similar engine architectures and similar fuels than the ones used nowadays would make it possible to reduce development costs. However, more research is still necessary before these technologies are released.

1.3 Objectives of the Study

The development and optimization of new combustion modes, which promote low temperature reactions and lean mixtures, has shown promising results regarding the reduction of pollutant formation. More particularly, concepts like the dual-fuel strategy have shown important advantages. They are based on the use of new fuels (or blends of the existing ones), which combine the most suitable properties to improve engine performance and reduce pollutant formation in a wide range of operating conditions.

Computer Fluid Dynamic (CFD) codes are powerful research tools that can be used for the development of these new combustion modes. However, the present state of the art of CFD for engine simulation is widely based on the use of hydrocarbon mixtures, with the corresponding thermophysical properties but a simplified treatment of the evaporation process. Thus, despite evaporation can be resolved in 3D with current engine CFD codes, only average values of the local composition and amount of vapour are estimated. This is sufficient for global characteristic predictions (i.e. in-cylinder pressure and rate of heat release). However, proper simulation of the pollutant formation processes and estimates of emissions values require locally resolved composition and maps of temperature evolution to be known. But the estimation of these latter magnitudes depends on the detailed description of the local combustion process involving local fuel composition. Therefore, the development of theoretical sub-models to be implemented in CFD codes require to address the multi-component evaporation and combustion simulations.

The validation and tuning[1] of these new codes are mandatory to guarantee accuracy and reliability [23]. In this regard, the optical diagnostic techniques have shown big potential during last decades. A large variety of this type of experimental tools can be found in literature for the study of all sort of phenomena involved in the combustion process of an ICE. The non-intrusive nature of these techniques makes them suitable for their application in both simplified environments (e.g. isolated flames in spray vessels [24]) or real engines with minimum modifications [25]. However, a continuous improvement of these techniques is necessary to fulfil future objectives and requirements.

Within this framework, the study performed in this thesis pursues *the development and improvement of experimental methodologies for the study of the different stages of the injection-combustion process of fuel sprays, with sufficient detail and accuracy to assist development and validation of current and future multi-component evaporation and combustion models.* In order to complete this main task, the following partial objectives were identified:

- *To (further) develop a novel optical diagnostic technique and adapt it to the measurement of the vapour concentration of different volatility fuels injected into the high-pressure and high-temperature ambient of the combustion chamber of a CI engine.*
- *To deepen into the performance and limitations of the main optical diagnostics tools utilized for the characterization of the fuel evaporation and combustion processes, aiming to determine the level of reliability of each tool.*

The techniques considered as the keystones of this work are expected to be used to improve knowledge of novel combustion modes. However, in order to minimize risks and uncertainties associated to the lack of knowledge of such combustion modes, it was decided to use diesel diffusion combustion conditions as the baseline case for the development of this methodological work. Thus, a large amount of previous experimental information, computational tools and well established knowledge could be used to facilitate analysis and to explore the limits of applicability of the new experimental techniques under development. Besides, fuel type and composition were chosen to allow appropriate measurement to be made with well known techniques, whilst they could be used for modelling tasks for the CFD codes and, at the same time, facilitate evidencing both applicability limits and measurement limitations of the techniques which are analysed in depth in this document.

---

[1] It is referred to the selection of proper values for some constants of the model to fit experimental observations

1.4 Approach and Content of the Study

As described in the following chapters, the diesel-like combustion process is really complex. In order to simplify the study, it was decided to carry it out in an optically-accessible engine, which made it possible to isolate the fuel spray from different sources of interference that can be found in commercial engines (e.g. interaction with walls). Most of the experimental work was performed with two single-component fuels and three blends in order to fulfil the requirements of the new CFD codes that are being developed nowadays. Additionally, controlled blends of other more complex fuels have been used in specific parts of the work either to validate results or to check the limits of validity of the experimental methodology developed. All these simplifications made it possible to analyse with higher accuracy the uncertainties related to the different tools employed.

An scheme of the structure of the study and the document is presented in figure 1.5. A detailed description of the state of knowledge in relation to the combustion process in direct injection diesel engines is presented in *Chapter 2*. The aim is to give a global vision of the different processes that are involved in the final combustion of the fuel and the pollutants formation. This chapter defines most part of the terminology used in the document and it helps understanding the physics behind the optical techniques utilized in the different stages of the study. In *Chapter 3* the research tools used in the present thesis are presented. It includes a complete description of the boundary conditions for the experiments (e.g. test rig operating conditions or fuel properties), as well as the theoretical 1D-Model used at certain parts of the study.

The study was divided in two groups of experiments. *Chapter 4* describes the first set, which has been focused on analysing the evaporation and mixing processes. The fuels are injected in a steady-state high-pressure and high-temperature ambient, but with nitrogen instead of oxygen in order to avoid the possibility of combustion reactions. One of the main topics that has been included in this chapter is *the development of a novel optical technique to measure the air-fuel mixture formation (local vapour fuel concentration) under diesel experimental conditions (UV-VIS LAS)*, which is one of the most relevant contributions of this PhD thesis.

A second set of experiments was performed to characterize combustion and soot formation at different thermodynamic conditions. The results obtained have been presented in *Chapter 5*. These experiments were performed in the same test rig, but replacing nitrogen by air at 21% oxygen. In this case, a

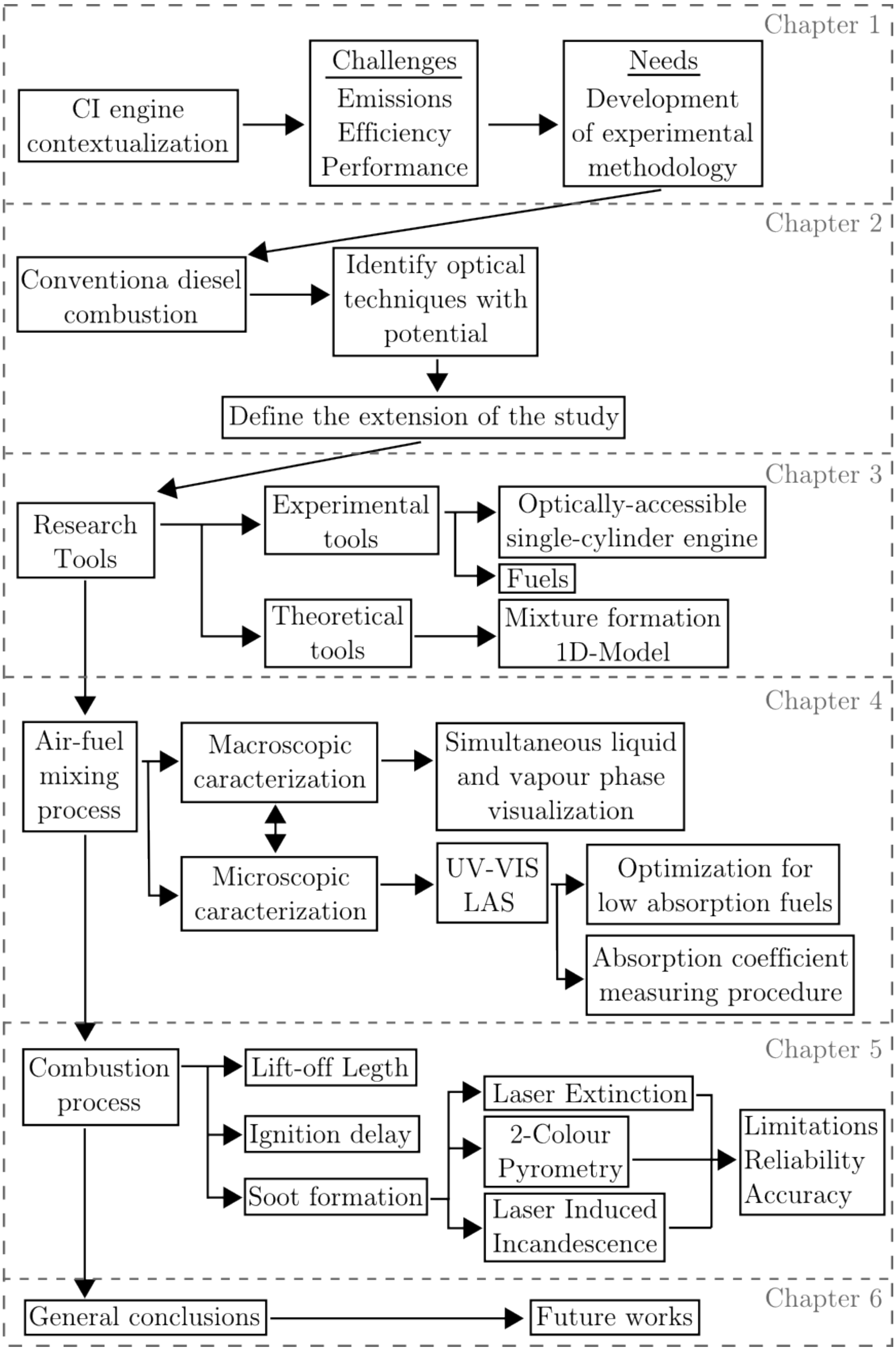

Figure 1.5. *Scheme of the structure of the study.*

large set of optical diagnostic tools was employed. In particular, three different techniques to characterize soot formation were simultaneously applied. Thus, the results presented in this chapter include a deep discussion on the accuracy and performance (benefits and drawbacks) of each technique. The aim is that the analysis could be used in future as a guideline to select the most suitable technique when future experiments are designed.

Finally, *Chapter 6* summarizes the main results presented in previous chapters. All the conclusions included in the document, regarding the experimental tools (i.e. optical diagnostic techniques), have been summarized highlighting the most relevant contributions of the study and outlining some ideas on some topics which could not be properly addressed here but which show a clear potential for future works and, in the author opinion, are worthy to be considered. Some ideas about future possible works to continue and improve the present study are proposed.

Bibliography

[1] "European Vehicle Market Statistics". *The International Council on Clean Transportation*, 2013.

[2] "Internal Energy Outlook 2013". *U.S. Department of Energy*, 2013.

[3] "Worldwide look at Reserves and production". *Oil & Gas Journal*, Vol. 110.12, pp. 28–31, 2012.

[4] "Peak Oil News and Message Boards". *Information available at http://www.peakoil.com.*

[5] Miller R.G. and Sorrell S.R. "The future of oil supply". *Philosophical Transactions of the Royal Society A: Mathematical, Physical and Engineering Sciences*, Vol. 372, 2014.

[6] Stieb D.M., Judek S. and Burnett R.T. "Meta-analysis of time-series studies of air pollution and mortality: Effects of gases and particles and the influence of cause of death, age, and season". *Journal of the Air and Waste Management Association*, Vol. 52 n^o 4, pp. 470–484, 2002.

[7] Jerrett M., Finkelstein M.M., Brook J.R., Arain M.A., Kanaroglou P., Stieb D.M., Gilbert N.L., Verma D., Finkelstein N., Chapman K.R. and Sears M.R. "A cohort study of traffic-related air pollution and mortality in Toronto, Ontario, Canada". *Environmental Health Perspectives*, Vol. 117 n^o 5, pp. 772–777, 2009.

[8] Mollenhauer K. and Tschoeke H. *HandBook of Diesel Engines.* Springer Heidelberg Dordrecht London New York, 2010.

[9] "DieselNet: Diesel emissions online". *Information available at http://www.dieselnet.com.*

[10] Molina S.A. *Estudio de la influencia de los parámetros de inyección y la recirculación de gases de escape sobre el proceso de combustión, las prestaciones y las emisiones de un motor diesel de 1.8 litros de cilindrada.* Doctoral Thesis, Universitat Politècnica de València, Departamento de Máquinas y Motores Térmicos, 2003.

[11] García A. *Estudio de los efectos de la post-inyección sobre el proceso de combustión y la formación de hollín en motores diesel.* Doctoral Thesis, Universitat Politècnica de València, Departamento de Máquinas y Motores Térmicos, 2009.

[12] Chartier C. *Spray Process in Optical Diesel Engine - Air-Entrainment and Emissions.* Doctoral Thesis, Lund Univesity, Faculty of Engineering, Department of Energy Sciences, 2012.

[13] Yanagihara H., Sato Y. and Minuta J. "A simultaneous reduction in NOx and soot in diesel engines under a new combustion system (Uniform Bulky Combustion System - UNIBUS)". *17th International Vienna Motor Symposium*, pp. 303–314, 1996.

[14] Kimura S., Aoki O., Ogawa H., Muranaka S. and Enomoto Y. "New combustion concept for ultra-clean and high-efficiency small di diesel engines". *SAE Technical Papers*, 1999.

[15] Akagawa H., Miyamoto T., Harada A., Sasaki S., Shimazaki N., Hashizume T. and Tsujimura K. "Approaches to solve problems of the premixed lean diesel combustion". *SAE Technical Papers*, 1999.

[16] Reitz R.D., Kokjohn S.L., Hanson R.M. and Splitter D.A. "High efficiency, ultra-low emission combustion in a heavy-duty engine via fuel reactivity control". *Global Powertrain Congress 2009*, Vol. 54, pp. 349–381, 2009.

[17] Weall A. and Collings N. “Gasoline fuelled partially premixed compression ignition in a light duty multi cylinder engine: A study of low load and low speed operation”. *SAE Technical Papers*, 2009.

[18] Bessonette P.W., Schleyer C.H., Duffy K.P., Hardy W.L. and Liechty M.P. “Effects of fuel property changes on heavy-duty HCCI combustion”. *SAE Technical Papers*, 2007.

[19] Inagaki K., Fuyuto T., Nishikawa K., Nakakita K. and Sakata I. “Dual-fuel PCI combustion controlled by in-cylinder stratification of ignitability”. *SAE Technical Papers*, 2006.

[20] Belarte E. *Estudio del procesio de combustión premezclada concontrol por la reactividad del combustible en un motor de encendido por compresión.* Doctoral Thesis, Universitat Politècnica de València, Departamento de Máquinas y Motores Térmicos, 2015.

[21] Molina S., García A., Pastor J.M., Belarte E. and Balloul I. “Operating range extension of RCCI combustion concept from low to full load in a heavy-duty engine”. *Applied Energy*, Vol. 143 n^o 0, pp. 211 – 227, 2015.

[22] Benajes J., Molina S., García A. and Monsalve-Serrano J. “Effects of direct injection timing and blending ratio on RCCI combustion with different low reactivity fuels”. *Energy Conversion and Management*, Vol. 99, pp. 193 – 209, 2015.

[23] Müller S., Dutzler G.K., Priesching P., Pastor J.V. and Micó C. “Multi-component modeling of diesel fuel for injection and combustion simulation”. *SAE Technical Papers*, 2013.

[24] “Engine Combustion Network”. *Information available at http://www.sandia.gov/ecn/.*

[25] Gessenhardt C., Zimmermann F., Schulz C., Reichle R., Pruss C. and Osten W. “Endoscopic imaging LIF diagnostics in IC engines”. *Proceedings of the European Combustion Meetings*, 2009.

Chapter 2

The Combustion Process in a Direct Injection Diesel Engine

Contents

2.1 Introduction

The objective of the current chapter is to provide a description of the phenomena that take place inside the combustion chamber of a CI engine and lead to the transformation of the fuel energy into a pressure increase. Besides, this thread has been used to present the wide variety of optical techniques that can be found in literature, for the study of the different stages of the diesel combustion process. Therefore the basics of the studied processes and the criteria for the selection of the experimental tools used along the work can be found in this chapter.

Dec [1] presents the diesel combustion as "*a complex, turbulent, three-dimensional, multiphase process that occurs in a high-temperature and high-pressure environment*". In a diesel engine, a liquid fuel is injected at very high pressure in a high-density and high-temperature environment. The liquid phase atomizes and penetrates up to a point where enough energy is entrained to heat up and evaporate the fuel. If oxygen is available, the vapour region auto-ignites and the flame tip spreads and continue to develop downstream. The event takes place in a millisecond order of magnitude but involves complex interaction between numerous physical and chemical processes.

The aim of this chapter is to provide a good basis for the understanding of the work presented in this document. With regard to offer a complete description of the combustion process in a diesel engine, a similar structure as the one followed by García-Oliver [2], Nerva [3], Zapata [4] or García [5] has been chosen. Thus, firstly a traditional description of the different stages of the diesel combustion process is presented based on the analysis of a fuel injection rate diagram and the corresponding heat release rate. Finally, a conceptual model of the diesel diffusion flame is presented. The nature of the ideas and concepts handled in the major part of the chapter are rather descriptive and qualitative, but accurate enough to offer a complete description of the complex processes that are being considered. The narration follows the point of view of the liquid fuel that after being injected, gets mixed with air and evaporates until it reaches autoignition and the diffusion flame gets established.

At each stage, different physical and chemical phenomena take place and transform the fuel and the surrounding atmosphere into new chemical species. From the point of view of the experimental methodology, it makes necessary to draw on a big variety of optical diagnostic techniques to completely characterize the whole process. In this regard, a brief review of the optical techniques employed for the study of each phase of the conventional diesel diffusion combustion is included. The aim is not to provide a detailed database of all existent optical techniques, but to highlight the most common ones that are being used nowadays.

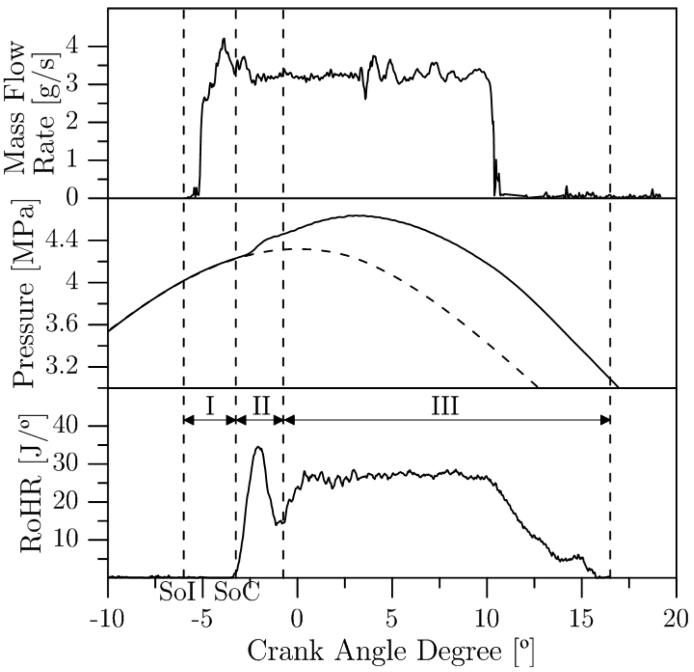

Figure 2.1. *Fuel mass flow rate of injection (up), in-cylinder pressure (centre) and rate of heat release (down) for a CI engine. Combustion Phases: I = Auto-ignition delay;*
II = Premixed Combustion; III = Diffusive Combustion.

2.2 Phases of the combustion process

The most classic way to start the review of the diesel combustion process is the analysis of the rate of heat release (RoHR). The RoHR is obtained from the analysis of the in-cylinder pressure trace, based on the application of the first law of thermodynamics to the volume enclosed in the cylinder [6, 7]. It represents the intensity of the chemical energy released by the fuel per unit time. Due to the interrelation between the injected fuel and the combustion in a CI engine, it is interesting to compare the RoHR with the rate of fuel mass injected into the cylinder. In figure 2.1, the time evolution of both magnitudes and the in-cylinder pressure of a real case is presented and compared. The mass flow rate curve makes it possible to define when the introduction of fuel into the combustion chamber starts and finishes. When it is compared with the RoHR, it is possible to see that there is a delay between the start of injection and the first traces of heat released which indicates the beginning of the chemical reactions. In this curve, a local maximum can be found at the first part, followed by a relative minimum. Its value depends on the engine and the operating conditions. However, it is usual that both local minimum and maximum are close. All these characteristic points allow defining three main stages of the combustion process, which are commonly identified in literature [2, 7, 8]:

- *Ignition Delay*: This phase comprises the interval between the start of injection (SoI), when the first liquid droplet is injected into the cylinder; and the start of combustion (SoC), when the spontaneous ignition of the air-fuel mixture takes place. In the diagram presented in 2.1, these two events are represented with the beginning of the mass flow rate and the point when the RoHR starts growing significantly. During this lapse, the fuel is already being injected but apparently no significant heat release activity is detected (further discussion is presented in section 2.4). During this stage, the fuel undergoes through a succession of purely physical processes. The spray is injected into a high dense atmosphere and starts breaking up into small droplets which increase the air/fuel interphase. At the same time, the spray momentum forces the entrainment of the surrounding air into the spray core. Both processes (atomization and air entrainment), which are described in detail in section 2.3, are key phenomena for heating and evaporating the injected fuel. At the same time, while the physical processes take place, the chemical part related to the autoignition process begins only once the vapour fuel appears. For conventional diesel-like fuels, the autoignition processes can be divided in two stages. The first one is characterized by low exothermic reactions occurring at low temperature (below 750 K), which are difficult to detect at the RoHR. This stage is followed by a more exothermic process, and its appearance points out the beginning of the premixed combustion phase. Besides the chemical phenomena that take place during the ignition delay stage, the physical processes continue as more fuel keeps evaporating and mixing with the surrounding air while the injection event extends. Therefore, these phenomena keep playing an important role in the heating of the air-fuel mixture.

- *Premixed Combustion*: In this phase combustion propagates quickly to all the vaporized fuel that mixed with air during the lag before ignition. A high-temperature stage begins and the fuel burning rate grows, and so it does the heat release rate. This stage is usually identified by a characteristic peak on the RoHR trace. Afterwards, the RoHR drops to a relative minimum, which points out the end of the premixed combustion phase. During this stage some final species (CO_2 and H_2O) are formed as well as other intermediate ones, that are considered as soot precursors. They lead to the appearance of incandescence soot on the front side of the flame, which gives its typical yellow and orange tone. At the end of the premixed combustion phase the diffusion flame front gets established. This remarks the transitory nature of this stage as it links the non-reactive spray with the diffusion flame.

- *Diffusion Combustion*: During this stage the flame front consolidates. The RoHR is assumed to be controlled mainly by the rate at which fuel mixes with air [7]. While the injection event takes place, the rate of mixture formation is mainly controlled by the momentum that the spray introduces into the combustion chamber. If the injection is long enough, the flame reaches its natural length and thus stationary conditions. This state lasts until the end of the injection. From the instant when the introduction of liquid fuel and momentum stops, the mixture formation is dominated by the remaining turbulence due to both the air movement and the residual motion of the spray. The remaining mixture burns slowly as it is reflected in the final part of the RoHR (figure 2.1). The combustion looses intensity until the flame extinguishes.

This definition of the diesel combustion process provides a global overview of how it develops along each engine cycle. However, to offer a detailed view of some of the phenomena occurring in this process, it is useful to analyse the evolution of a diesel spray injected into a high-temperature and high-pressure atmosphere. In this regard, a sequence of images is presented in figure 2.2. They correspond to an injection of n-Dodecane into a constant-pressure test facility, capable of mimicking the in-cylinder thermodynamic conditions of a diesel engine [10]. Images have been taken with a high-speed camera, applying the Schlieren visualization technique. With this technique, the combustion chamber is illuminated by a broadband collimated light beam. When the light rays do not cross any density gradient (uniform temperature, pressure and composition), they keep their original direction and are registered at the detector as homogeneously illuminated areas. These areas correspond, for example,with the surrounding gases in the combustion chamber that do not interact with the spray. However, when the light rays cross a density gradient (e.g. fuel spray or hot gases from the combustion) they get deviated and part of them do not reach the detector, generating grey areas in the image. Therefore, this technique allows identifying the spray and burnt gases inside the combustion chamber.

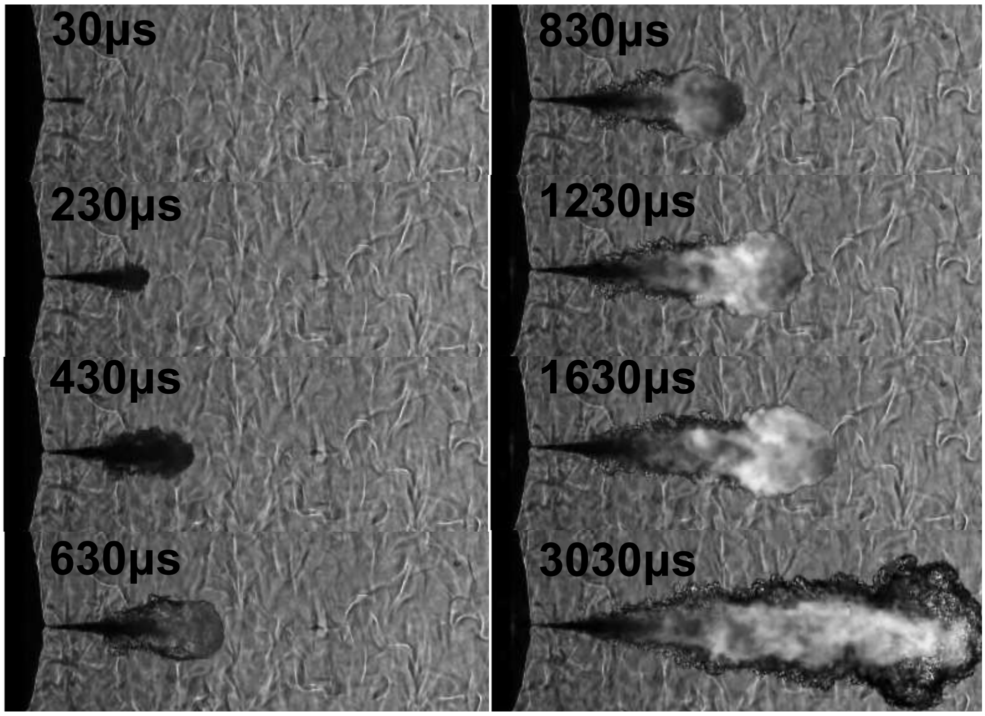

Figure 2.2. *Schlieren images of a n-Dodecane spray. Oxygen concentration 21%, ambient temperature 900 K, ambient density 22.8 kg/m*^{3}*, injection pressure 50 MPa, ECN spray-A single-hole injector. Source: ECN [9].*

From a quick view of the images presented, one can identify most of the stages described in the previous paragraphs. Once the injection starts, the spray penetrates into the combustion chamber thanks to its momentum. Meanwhile, the fuel is mixing with the surrounding air while evaporating and increasing its temperature (30 μs and 230 μs). At the same time, the first low-temperature reactions start. However, the energy released is not high enough to have detectable effect on the spray evolution. At certain point, when the required thermodynamic and chemical conditions are achieved, the high-temperature reactions start (430 μs). At this point, the increase of temperature caused by the high amount of energy released creates large density gradients at the tip of the spray, which are detectable by the Schlieren technique. Moreover, it is possible to see that this region broadens as a consequence of the combustion process. From this point, a flame front can be identified thanks to the luminosity of the hot soot formed inside the flame. The momentum of the spray allows the flame front to keep advancing while the air entrainment continues (from 630 μs to 3030 μs). Finally, if the injection event is long enough (as it is in this case), the flame reaches a maximum length (3030 μs) where the flame front gets stabilized. Since the beginning of the combustion process, the flame is easily identified in these images by the luminosity of soot. Furthermore, it can be seen that the flame is surrounded by dark clouds which correspond to the products that leave the flame at high temperature. This description, apart from providing a more clear view of the different stages which the diesel combustion moves through, represents a clear example of the usefulness of the optical diagnostic tools for analysing and characterizing any in-cylinder combustion process.

2.3 Fuel injection and formation of air-fuel mixture

The air-fuel mixture formation and the latter combustion in a CI engine are closely linked and in some stages of the process both phenomena take place simultaneously. Therefore, it is usually difficult to find a clear frontier between them. When the engine is running, the fuel is injected into a highly dense ambient. During the first stages liquid gets atomized, heated and evaporated thanks to a sequence of events where a exchange of physical properties is taking place with the surrounding atmosphere. Until the oxygen triggers the first chemical reactions, the process can be considered the same as if it would take place in an inert atmosphere.

Based on this premise, and due to the interest of analysing separately the physical and chemical basic aspects, different type of experiments and studies can be found in literature under non-reactive ambient conditions. If the temporal sequence of phenomena is followed, it should be mentioned in a first instance the characterization of the internal-flow of the injector. It has been widely studied by Payri, Gimeno and Salvador [11–14], who describe the effect of friction forces inside the nozzle and the appearance of cavitation. One step further on the development of the mixture formation is the atomization of the liquid fuel once it is injected into the combustion chamber. For this purpose, an additional simplification of the experimental conditions can be introduced in the study. If the fuel is injected into high dense low-temperature inert ambient, fuel evaporation is avoided and makes it possible to study the atomization and coalescence of fuel droplets with more detail. The works of Arrègle [15], Correas [16], Ruiz [17] and López [18] provide in-depth discussion about the physical aspects leading to liquid jet atomization and their modelling. When the fuel is injected into a high-density and high-temperature inert ambient, it evaporates and completes the formation of the mixture with the surrounding gases. In this regard, García-Oliver [2] presents a complete description of the physical framework that dominates the final stages of mixture formation. Nevertheless, as it has been said previously, the mixture formation continues after ignition takes place. For this reason, during last years several studies have been performed under reacting conditions [19, 20] to determine the effect of the combustion over the mixing process.

A review of the main aspects that allow explaining the behaviour of the diesel spray under engine conditions has been included in the following paragraphs. The reader can be addressed to any of the references already cited, to find a more detailed discussion regarding the physical phenomena involved.

2.3.1 Internal Flow

In a direct injection (DI) system, the fuel has to be injected at high pressure in order to get a proper mixture formation. Therefore, it has to be pressurized several tens of megapascals before it is introduced into the combustion chamber. Current injection systems reach 200 MPa, which generate a pressure drop between both sides of the orifices that is transformed into flow velocity according to Bernoulli's Law [7]. The understanding of the phenomena involved is essential for engine design as it strongly influences two main characteristics of the injection system: mass flow rate ($\dot{\mathrm{m}}_f$) and the spray momentum flux ($\dot{\mathrm{M}}_f$). However, the study of the internal flow inside diesel injector orifices is really complicated due to:

- Minimal dimensions of the discharge holes, with characteristic lengths of 1 mm and diameters around 100 μm.
- High flow velocity due to the high pressure drop, up to several hundreds of meters per second.
- The transient nature of the injection process, which lasts at most several milliseconds and it is influenced by the dynamics of the needle during opening and closing.
- The flow can be both single-phase (liquid) or dual-phase (liquid and vapour, due to cavitation phenomenon).

Nevertheless, in [13] a protocol to measure both $\dot{\mathrm{m}}_f$ and $\dot{\mathrm{M}}_f$ can be found. Their combination makes it possible to calculate the fuel exit velocity (u_0)

and the effective output area (A_{ef}) of the nozzle, which play a major role on the characteristic mixing length and mixing time (as it will be described in the following sections). Besides that, u_0 and A_{ef} allows defining one of the most used parameters to evaluate the efficiency of the fuel discharge through the nozzle hole: the discharge coefficient (C_d) [13, 14].

One of the main research fields regarding the internal flow in diesel injector holes is the cavitation effect. The strong pressure gradients along the orifice accelerates the fuel to high velocities decreasing the local pressure until it reaches, in certain points, values below fuel vapour pressure. This phenomenon usually takes place at the entrance of the orifice, where kernels of fuel vapour are formed and dragged by the fuel stream towards the nozzle exit, strongly affecting the shape and characteristics of the fuel flow [12, 21–25]. The phenomenon of cavitation has been characterized in different ways. Several studies of this process can be found, based on the evolution of the mass flow rate and the momentum flux of the spray and CFD simulations [21, 23, 26, 27]. Nevertheless, despite the difficulties mentioned in the previous paragraphs, it had been possible to characterized the cavitation effect by means of optical techniques. The most extended approach is the visualization of the fuel flow in transparent scale models [24, 28, 29] (figure 2.3) or even real size ones [30, 31]. The scattering of light generated by the appearance of bubbles within the liquid fuel makes it possible to detect cavitation regions and even its propagation to the output of the orifice.

From the point of view of practical applications, cavitation is favoured by high pressure drop in the orifices (i.e. high injection pressure and low in-cylinder pressure) and small diameters, but also by important changes in the flux direction. In this regard, the cylindrical holes are more prone to cavitation while more convergent geometries (i.e. conical holes, with smoother input edges) can minimize or even avoid it. In the same way, nozzles that are designed to inject in the radial direction of the piston bowl are more susceptible to produce cavitation compared to axially drilled single-hole nozzles. There is no clear agreement on the beneficial or disadvantageous nature of cavitation. Several studies suggest that it improves the mixing process in different ways. However, cavitation produces harmful effects as the mass flow collapses, limiting the discharge capacity of the orifice. During the last years, the trends point out to a variation from cylindrical holes to more convergent ones. Nevertheless, the effects over mixture formation, together with some other apparent benefits (i.e. the cleaning of deposits inside the orifice by the implosion of bubbles), leave an open future in this regard.

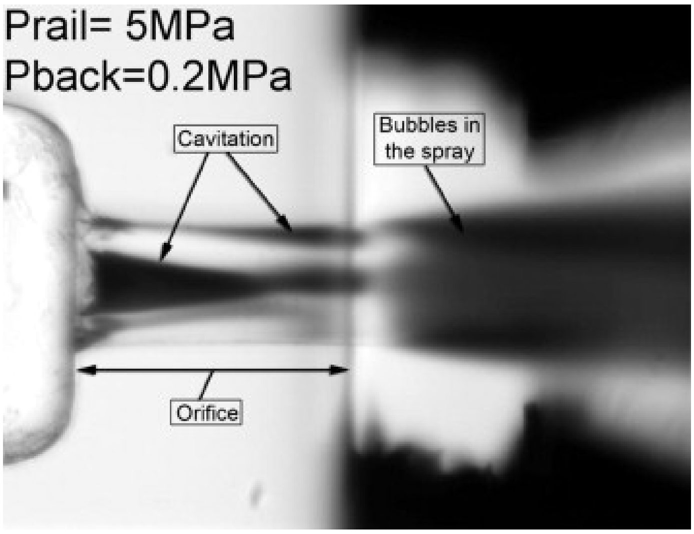

Figure 2.3. *Average image of cavitation for commercial diesel at 5 MPa injection pressure and 0.2 MPa chamber pressure. The orifice has 500 μm diameter and 1 mm length. Source: Payri et al. [28].*

2.3.2 Atomization

The first phenomenon that takes place after fuel discharge is the atomization of the fuel vein, which shreds into a cloud of droplets of multiple sizes. Its high velocity, relative to surrounding dense air, causes droplets to shear off the liquid core. Thereby the contact surface between the air and the fuel increases, favouring the physical processes (heat, mass and momentum diffusion) that will dominate the air-fuel mixture formation. An scheme of this process is shown in figure 2.4.

The atomization phenomenon has been widely studied in the field of diesel jets, to improve the insight into the mechanisms that control the break up and the coalescence of the droplets (aerodynamic interaction, cavitation, turbulence, etc.). Different optical techniques, like *backlight illumination* (BL) or *Mie Scattering* (MIE) [33–35], made it possible to analyse the geometry of the spray (macroscopic description) even at its first millimetres. More detailed characterizations of the droplet distribution and/or velocity have been performed by point-measure techniques as *Phase Doppler Anemometry* (PDA) [29, 36]. However, its application is limited to less dense regions, further from the nozzle orifice. For 2D-resolved measurements, more complex tools like *Planar Droplet Sizing* (PDS) [37, 38], *Ballistic Imaging* (BI)

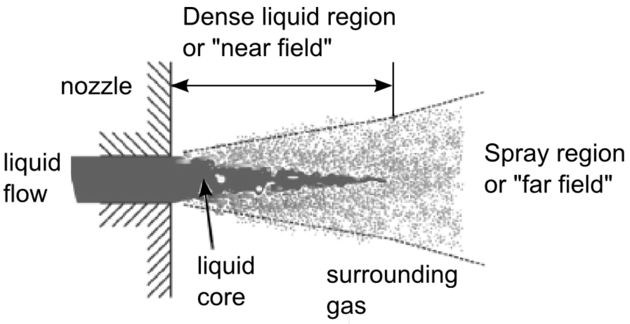

Figure 2.4. *Diagram of "near field" spray region. Source: Linne [32].*

[39–41], *Structured Laser Illumination Planar Imaging* (SLIPI) [42] or *X-Ray tomography* [43, 44] have been employed to visualize fuel and even measure concentration and droplet size distribution in the near field region. These techniques have been also put to the test for measuring droplet size distributions at the most dense parts of the spray [45].

PDS uses the ratio of a Planar Laser Induced Fluorescence (PLIF) image to a planar Mie scattering image to obtain the Sauter Mean Diameter (SMD). However, the multiple scattering has been identified as a major error source. In this regard, SLIPI was developed to overcome this drawback. It utilizes three signals obtained from a intensity-modulated light source, with 120^o phase offset between them. When these signals are properly combined the contribution from singly scattered light adds, while multiple scattering is strongly suppressed. A major simplification of SLIPI has been recently demonstrated [46], where only two images are required. A comparisson between PDS and SLIPI is shown in figure 2.5

While PDS and PLIF are planar-based techniques, ballistic imaging and X-ray tomography are based on line-of-sight measurements. Both techniques can be considered as a sophisticated versions of backlight illumination. An extensive review on both techniques can be found in [32]. BI is based on filtering photons that have been scattered multiple times. When a femtosecond laser pulse crosses a spray, the photons that earliest arrive to the detector are the unscattered ones (i.e. ballistic photons). However, in the dense regions of the spray these are too few so the ones that have been scattered only a few times (typically arrive a few picoseconds later) are also considered. With a proper exposure time and filtering, the photons that have suffered multiple scattering are rejected. A comparison between BL and BI is shown in figure

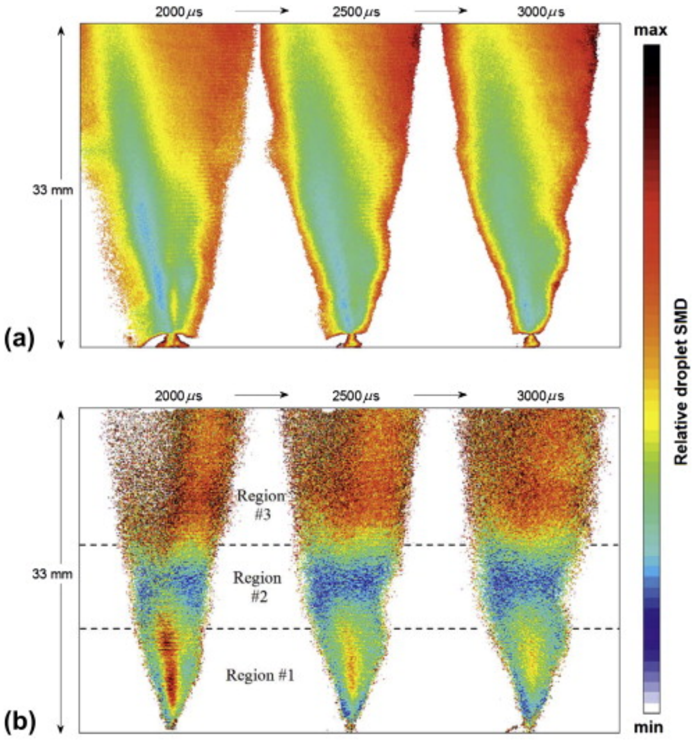

Figure 2.5. *Relative droplet SMD calculated from PDS (a) and SLIPI (b). Note that the spray was illuminated from the right side. Source: Berrocal et al. [42].*

2.6. In contrast, X-Ray tomography is based on the attenuation of X-rays, mainly caused by absorption rather than scattering.

In liquid jets under turbulent regime (e.g. the diesel jets), the atomization is complete after a certain axial distance from the outlet orifice (figure 2.4). This distance depends a lot on the scenario (fuel, ambient conditions, flow speed, fuel density, nozzle geometry, etc.), which makes it possible to distinguish different atomization regimes [47, 48]. Downstream this distance, the liquid core disappears and only fuel droplets remain, surrounded by the entrained gas. This dimensional parameter is known as “liquid length” or “break-up length”. In the present work the second term has be used whilst the term “liquid length” will be used for the maximum length that liquid fuel reaches until it gets completely evaporated.

Figure 2.7 shows an example of the visualization of a diesel spray in the near-nozzle region. It represents the initial development of the spray under non-evaporative conditions. In the sequence it is possible to see how

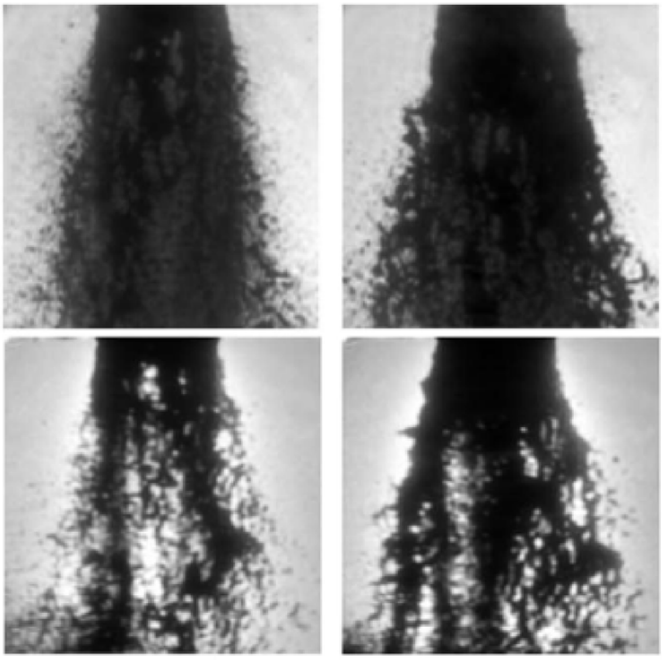

Figure 2.6. *A comparison between backlight illumination (up) and ballistic imaging (down). Images correspond to rocket sprays, which were recorded with the same laser source but rejecting multiply scattered photons. Sources: Schmidt et al. [41].*

the liquid core evolves, growing during the first stages until it reaches a maximum (around 2 mm at 70 μs after SoI). From this point, the liquid core starts decreasing rapidly until the break-up length is almost null. In the work presented by Arrègle [15], it is stated that the atomization regime at regular diesel-like conditions is the same as for fuel jets under non-evaporative and non-reacting atmospheres: *Complete atomization.* In this regime the break-up length is independent of the fuel speed and droplet size, and is of the same order of magnitude as the diameter of the nozzle hole. This guarantees that the mechanisms controlling the liquid atomization are the same for all the operating conditions.

There is no clear agreement on the final value of the break-up length. However, it is usually accepted that the relation between densities of the jet and the surrounding gas is the controlling parameter that determines its value. The mayor part of the studies coincide that this distance is reached at a few orifice diameters from the nozzle exit (figure 2.7), according to Smallwood and Gülder's review [49]. The main implication of this analysis

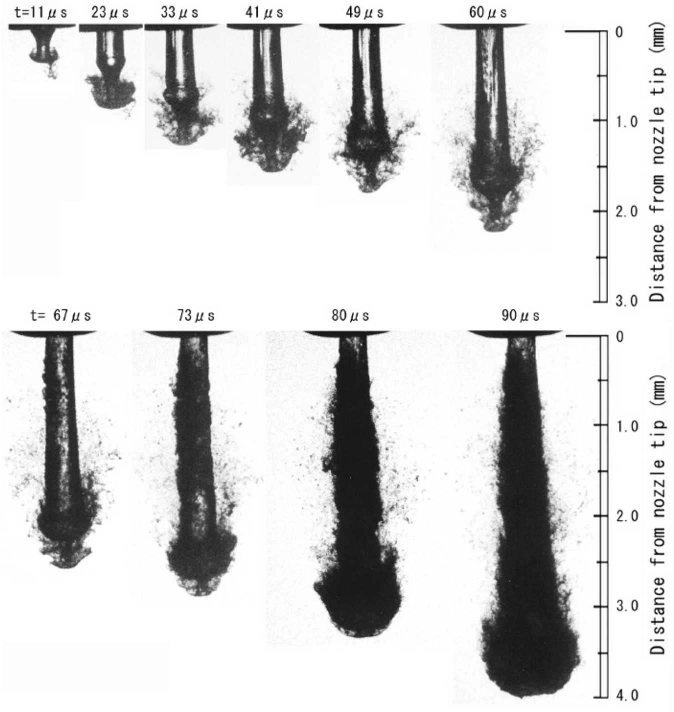

Figure 2.7. *Temporal sequence of a spray at the near-nozzle region, taken by means of backlight illumination. Source [34].*

is that the jet could be considered as a mixture of gas and liquid completely atomized almost since it leaves the nozzle. Regarding droplet size, it is worth mentioning that several authors refer to an important spatial and temporal variability. Such observation can be explained, partially, by the complexity of performing measurements in such dense media [32, 36, 40]. However, the main contribution is usually attributed to the coalescence of droplets downstream. This effect is specially significant in the dense regions near the axis.

In accordance to the above mentioned, it can be concluded that the atomization occurs so fast and the size of the droplets is so small that the dynamic equilibrium between them and the surrounding gas is achieved immediately. Thereby, the mixture will achieve both thermal and velocity equilibrium between phases and it can be characterized locally by a unique value of velocity, composition and thermodynamic conditions. This statement simplifies the behaviour of the diesel spray and resembles it to a gas jet, so the influence of the atomization process upon combustion is limited. This assumption has been widely used and establishes the basis for numerous works about isothermal and evaporative diesel sprays that will be considered in the current work.

2.3.3 Evaporation and air-fuel mixing

Once detached from the intact core of the spray, fuel droplets get completely surrounded by hotter gases. Heat transfer increases the temperature of the droplet and its vapour pressure, which increases the amount of evaporated fuel. This evaporation process diminishes continuously the size of the droplet until it is completely evaporated.

Several optical diagnostic techniques can be found in literature for the study of the liquid phase and the evaporation process. Most of them are based on the scattering of light caused by the liquid droplets that, in the case of DI diesel jets, can be described by the *Mie theory of light scattering by spherical particles* [50, 51]. When a light ray hits a fuel droplet, it is scattered in all directions. On the one hand, the light scattered can be registered, obtaining an image of the liquid phase of the spray (figure 2.8 -top-). This is the basis of the *Mie scattering technique* (MIE). On the other hand, the *backlight illumination technique* (BL) is based on measuring the attenuation suffered by light when it traverses the spray liquid region. The intensity of light that propagates in the direction of the original light source gets reduced as it is scattered in all directions by fuel droplets. Consequently, the liquid region is visualized as a darker area (figure 2.8 -bottom-).

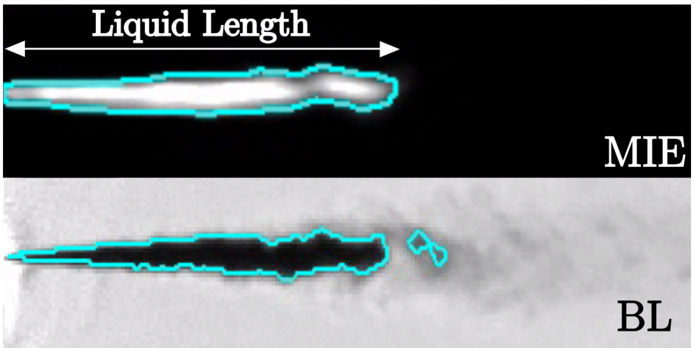

Figure 2.8. *Comparison between MIE (top) and BL (bottom). The coloured line represents the contour of the liquid spray. Source: ECN [9].*

Both techniques have been commonly utilized for the investigation of the injection process and the evolution of the liquid phase. MIE [52–62] requires high intensity light sources and/or high-sensitivity detectors. In contrast, BL [2, 35, 52, 63, 64] does not require so intense light sources, but it is necessary to have two aligned optical accesses as the light source and the detector must be confronted. Therefore, this technique is usually employed in spray vessels while MIE is more commonly used in optical engines.

Numerous experimental studies state that when fuel is injected into a high-temperature ambient, the liquid phase reaches its maximum penetration soon after the start of the injection process. This limit, which is known as *maximum liquid length* or just *liquid length*, is fixed by both fuel properties and thermodynamic conditions of the surrounding gas. From that point, droplets are completely evaporated and only vapour-phase fuel can be found. This maximum liquid length is influenced by the different boundary conditions as the nozzle orifice diameter [55, 63], temperature and chamber density [54, 55, 62–65] and fuel characteristics [54, 55, 62, 63, 66]. However, the injection pressure seems to have no influence [55, 62, 64, 65]. Through their observations, Espey and Dec [54] concluded that the main heat source that promotes fuel evaporation is the hot gas entrained by the spray and not the energy released during the combustion process. They observed that, in most of the cases, the maximum liquid length was reached prior to the start of combustion. These dependences led Siebers [55] to conclude that the evaporation process under diesel-like conditions is mostly controlled by the air-fuel mixing rate. The fuel droplets evaporate as the surrounding air provides the necessary enthalpy and the local transfer rates of mass, momentum and energy between the two phases are fast in comparison with the turbulent mixture[1]. This reinforces the hypothesis that at any point of the spray, under evaporative conditions, there is a thermal equilibrium between the species present.

The air-fuel mixing process has been studied from different approaches [45]: macroscopic spray properties and microscopic fuel distribution. The first one considers the interaction between the spray and the surrounding air in a generalized way. The spray volume is directly related to the air entrainment and its quantification enables to address the mixing process quality. In consequence, *spray penetration* and *the spray cone angle* are parameters of interest and have been largely considered in literature. The most extended optical technique for this type of studies is the *Schlieren visualization* [3, 4, 59, 62, 67]. The spray is illuminated with a collimated light beam[2] and it is registered after crossing the whole combustion chamber. The density gradients inside the spray (caused by the mixing process) deviate the

---

[1] Despite the general rule is that evaporation is controlled by mixing, it is possible that under certain conditions diffusion phenomena control the process.

[2] All the light rays that form the beam propagate in the same direction

light rays so that they do not arrive to the detector. The result is a dark region in the image, which corresponds to the spray and makes it possible to obtain the geometric parameters previously mentioned (figure 2.9). The application of this technique is usually limited to spray vessels and single sprays, as it requires two aligned optical accesses. However, several solutions can be found in literature [59, 68] which make it possible to use it with multi-hole nozzles.

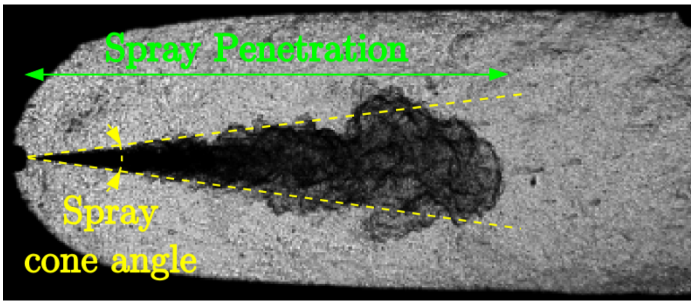

Figure 2.9. *Schlieren visualization of a n-Decane spray under evaporative conditions.*

In comparison with the macroscopic characterization of the spray, the measurement of the fuel distribution offers a more detailed view of the mixing process. Nevertheless, the complexity of the experimental tools increase substantially. For example, *the Raman Spectroscopy* is based on the analysis of the inelastic[3] scattering of a laser beam, caused by the fuel molecules. The frequency of the light scattered is characteristic of each specie, and makes it possible to determine the local air-fuel ratio and temperature at the same time [69–72]. However, the signal is very weak which limits measurement to small areas and requires careful signal-to-noise considerations.

In contrast, *Planar Rayleigh Scattering* (PRS) and *Planar Laser Induced Fluorescence* (PLIF) present more intense signals, which makes it possible to obtain spatially resolved measurements. On the one hand, PRS is based on measuring the elastic scattering caused by particles that are small in comparison with the light wavelength (e.g. fuel molecules) [72–76]. The amount of light scattered is proportional to the particle density, but it is not sensitive to different species. The Rayleigh scattering signal is some orders of magnitude lower than MIE, so PRS can be only applied in complete absence of liquid. In figure 2.10 an example of PRS is shown. It is possible to see that, despite avoiding the liquid fuel region, some saturated points can be observed

---

[3] The concept of elastic or inelastic scattering is referred to the type of interaction between light and particles. In the first case, the photon is deviated without varying its wavelength. In the case of inelastic scattering, the wavelength of the photon is also varied

which could affect the measurement. On the other hand, PLIF technique is based on the fluorescence emitted by the fuel molecules, when they are excited with a laser pulse at a certain wavelength. A tracer molecule is usually required, as not all hydrocarbons are fluorescent when excited with visible or ultraviolet light [77]. In this sense, the accuracy of the technique is limited by how close are the main evaporation characteristics (e.g. vapour pressure) of the tracer and the fuel. Quantitative LIF require calibration as well as numerous corrections [77, 78]. The use of exciplex tracers enables characterizing both vapour and liquid phase concentration simultaneously (PLIEF) [77–80]. In this particular case of Exciplex LIF, some difficulties are usually found due to cross-talk between monomer (vapour) and exciplex (liquid) fluorescence caused by emission spectra overlap. Moreover, quantitative measurements under high temperature become difficult due to a strong dependence of fluorescence on this parameter [77] or quenching with other molecules.

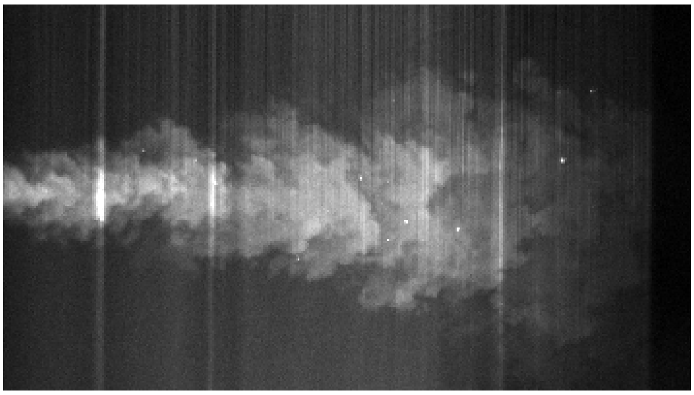

Figure 2.10. *Rayleigh scattering from n-Dodecane, at ECN thermodynamic conditions [9]. The first part of the spray is avoided according to limitations of the technique. Source: Pickett [76].*

PRS and PLIF are the most widely used techniques for characterizing the air/fuel mixture process. Nevertheless, the *Light Absorption and Scattering* technique (LAS) can be considered as a promising alternative. LAS is based on combining the interaction of fuel molecules (absorption and scattering)with light in the liquid and vapour phases, at different wavelengths. The first applications of LAS were based on combining infrared and visible wavelengths (IR-VIS LAS) [81–83]. However, infrared extinction usually presents strong temperature dependence, which introduces uncertainties when local temperature distribution is unknown. Moreover, infrared signal can be interfered by the presence of water vapour (absorption) or heat radiation from hot surfaces. Most applications are based on point measurements. A similar combination of ultraviolet and visible light (UV-VIS LAS) has been more commonly used during the last years [84–88]. It is not influenced by water vapour or heat radiation, temperature dependence is weaker than for other techniques and it makes it possible to obtain spatially resolved measurements. Besides, as both wavelengths are more similar between them than for IR-VIS LAS, different simplifications can be applied without affecting the measurement accuracy. In comparison with PRS and PLIF, UV-VIS LAS allows measuring the fuel concentration in the liquid and vapour region simultaneously, without using any tracer. Contrarily, the first two techniques offer results at a given plane of the spray (e.q. the symmetry plane), while LAS is based on line-of-sight measurements and a deconvolution (inversion) algorithm is necessary. An example of UV-VIS LAS application is shown in figure 2.11. The optical thickness of the spray (vapour and liquid) is shown for the visible (left) and ultraviolet (right) wavelengths.

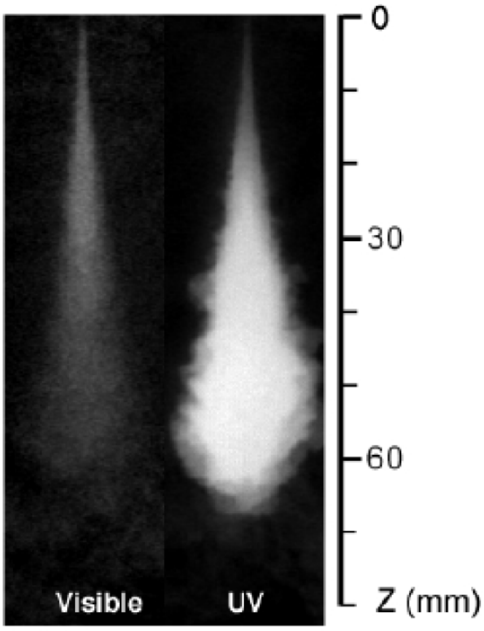

Figure 2.11. *Images of the optical thickness of a spray in the visible (left) and ultraviolet (right) wavelengths. Source: Gao et al. [87].*

2.4 Autoignition of a diesel spray

If the fuel injection would have taken place into a non-reactive atmosphere, the evolution of the spray would be completely described with the different phenomena mentioned in the previous sections. However, the main objective of an internal combustion engine is burning the fuel to produce work. The oxygen present in a reactive atmosphere results in a highly unstable mixture, which reacts and eventually ignites after certain time since the start of the injection process. Autoignition takes place where local conditions of air-fuel mixture and temperature are appropriate to trigger the first chemical reactions. As a consequence, intermediate species are generated while some energy is released. This promotes the propagation of the reaction and consolidates the spray combustion reaction. But these exothermic reactions also influence the local thermodynamic conditions of the spray, affecting the evaporation and mixing that takes place simultaneously with the reactions. Thus, the physical and chemical aspects of the diesel combustion are intertwined.

2.4.1 Stages of the Process

The autoignition process is one of the classic problems of the combustion science. A wide variety of experimental approaches have been employed to get insight into this field and, as a consequence, different criteria to define the start of combustion can be found in literature. In this regard, different authors base their studies on the analysis of pressure or heat released (as the one followed in figure 2.1) or on the detection of characteristic chemical species.

Studies based on the use of optical diagnostic techniques are a clear example of how criteria could change while experimental techniques evolve. The first studies where mainly based on measuring broadband radiation from the flame, which was always delayed in comparison with the variations detected in the pressure signal [6]. As equipment sensitivity has been continuously improving, it has been possible to detect certain low-intensity radiation even prior to the pressure-defined start of combustion. As an example, the study presented by Edward et al. [89] discusses the difference in criteria followed to determine the start of combustion depending on whether high-speed camera images or a photodiode signal (more sensitive) were considered. Moreover, they describe how the photodiode is able to detect some signal even before a change in the chamber pressure is detected. Most recent studies have been based on the analysis of the evolution of the spray/flame geometry. Pastor et al. [19] and Desantes et al. [20] were able to detect first reactions before the first natural luminosity of the flame was observed (by means of Schlieren visualization), as they caused an increase of the volume of the spray due to the energy released. Therefore, considering all the foregoing, it can be stated that the definition of the start of combustion depends on the technique employed and its sensitivity.

Numerous studies have been carried out to characterize the diesel autoignition process [20, 89–93]. All of them describe the spray ignition as a two-stage process. They suggest that a phase of low-intensity and low-temperature reactions exist prior to the start of the premixed-burn heat release as defined in section 2.2. The long hydrocarbon chains that are injected in hot air break down due to different reactions of pyrolysis and oxidation. Some intermediate products obtained during these reactions are excited radical species, which emit light at characteristic wavelengths when they spontaneously change to equilibrium states (chemiluminescence). The most important chemiluminescent radicals that should be considered in a diesel combustion process are the methylidyne- (CH^*), hydroxil- (OH^*), carbon- (C_2) and formaldehyde- (CH_2O^*) [94].

Different studies can be found in literature in which the authors resort to complex optical diagnostic tools to visualize the species previously mentioned. For example, the use of PLIF makes it possible to detect the whole radical population and not only the excited state[4], while providing high sensitivity, high spatial resolution and species specificity [95]. It has been applied to visualize CH_2O [96–98], OH [90, 98–100] and even CH (in atmospheric flames). However, the implementation of PLIF is rather laborious and requires both special care and complex hardware. Moreover, the ability of this technique to follow transient processes is usually limited by the repetition rate of the laser (normally few hertz), although more recent works can be found where this has been improved [101, 102]. For these reasons, a more commonly used technique is the line-of-sight visualization of radiation emitted by the excited radicals. A simple photodiode [89, 92] or more complex spectroscopes [91, 103–106] can be used to register this luminosity. The absorption spectra is also characteristic of each radical specie, and its measurement has been addressed to describe different combustion modes [**?**, 107]. However, photodiodes and spectroscopes rather limit spatial resolution and the use of UV-Sensitive ICCD cameras is preferred [2, 3, 93]. This kind of detectors have been traditionally characterized by high spatial resolution and sensitivity, but low repetition rates (in the same order as lasers). However, nowadays different technological solutions can be found to improve the repetition rate without sacrificing sensitivity or spatial

---

[4] As it was described in section 2.3, the florescence is achieved by exciting the radical with a short energetic laser pulse

resolution. In figure 2.12, a comparison between OH* chemiluminescence and OH PLIF visualization is shown [99]. The chemiluminescence images are shown in grayscale, while the contour line indicates the border of the OH PLIF image. The edge of the bowl rim is represented by the white arc, while the dotted line represents the edges of the laser sheet. The white circle indicates the location of the injector.

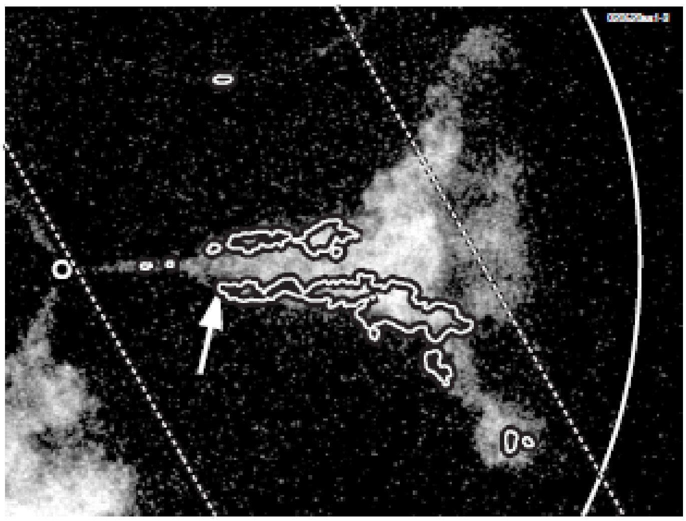

Figure 2.12. *An example of simultaneous OH PLIF and OH chemiluminescence visualization. The chemiluminescence signal is shown in grayscale, while the contour line indicates the border of the OH PLIF signal. The dotted line represents the edges of the laser sheet. Source: Musculus [99].*

The spatial location of the mentioned radicals and prominence of its radiation is expected to evolve in time as the combustion progresses along its different phases. Dec and Espey [91] studied in detail the phasing between the in-cylinder pressure and the radiation development. They observed a weak emission prior to the main heat release. Some isolated spots were first detected, which progressed uniformly in the rich leading portion of the jet. A further spectroscopic analysis revealed that such chemiluminescence corresponded to CH_2O^* but also, and above all to CH^*. This makes it possible to consider this radical as an autoignition marker. When the first heat-release rises (see figure 2.1) was reached, the main radiation was coming from the vapour-fuel region. Besides, it was demonstrated that at this stage the main chemiluminescence source was the OH^* radical. Finally, for all the conditions evaluated, the light intensity increased suddenly several orders of magnitude as the first hot soot particles appeared.

In order to get more insight into the description of the autoignition process, Higgins et al. [92] performed similar measurements under quiescent conditions (constant-volume combustion chamber). They confirmed that the autoignition process can be splitted in three consecutive phases, which are detailed in the following paragraphs. Figure 2.13 will serve as the support of the following description. It is the result of tests conducted with a ternary blend of single-component fuels (representative of diesel fuel) injected at a pressure of 140 MPa through a single-hole nozzle in conditions of ambient temperature and density of 1000 K and 14.8 kg/m^3. In (a), the first two plots represent the same variable (ΔP) with different scales. The last two plots represent the apparent heat release (AHRR), obtained from a first-law analysis of ΔP, and the natural luminosity measured with a photodiode. All four plots are represented as a function of time after the start of injection (named in this figure as TASI). In (b), the corresponding image sequence of the autoignition process is shown, obtained with an intensified CCD camera. According to this information, the three defined stages are:

- *Physical induction stage*: this phase extends from the start of injection (0 ms TASI) until the very first heat release, which is coincident with the emission of the low-intensity chemiluminescence (0.2 ms after TASI). During this period, the mixture formation is dominated by physical processes as described in previous sections. Fuel is heating and evaporating (consuming energy) so the heat release rate goes negative. The temperature of the mixture increases up to a level where heat released becomes higher than heat absorbed. From this point, reactions become unstable and start propagating to the surroundings.

- *First-stage ignition period*: this phase begins with the first detectable chemical activity in terms of chemiluminescence and/or pressure. It progresses until significant heat release is achieved due to the beginning of the premixed burn. It should be noted the uncertainty on the definition of this period. On one hand, it has been stated previously that the first limit depends on the resolution of the hardware and the experimental technique used. On the other hand, the end of the phase depends on when the AHRR is considered as “significant”. In figure 2.13 (a), this period corresponds to the low amount of heat released between 0.2 and 0.4 ms TASI. This period is usually referred in literature as “low-temperature autoignition” or “cool-flame”. As observed in the first images of the figure 2.13 (b), the first-stage ignition reactions usually grow in the region between the liquid length and the tip of the spray, which is in agreement with the description presented by Dec et al. [91].

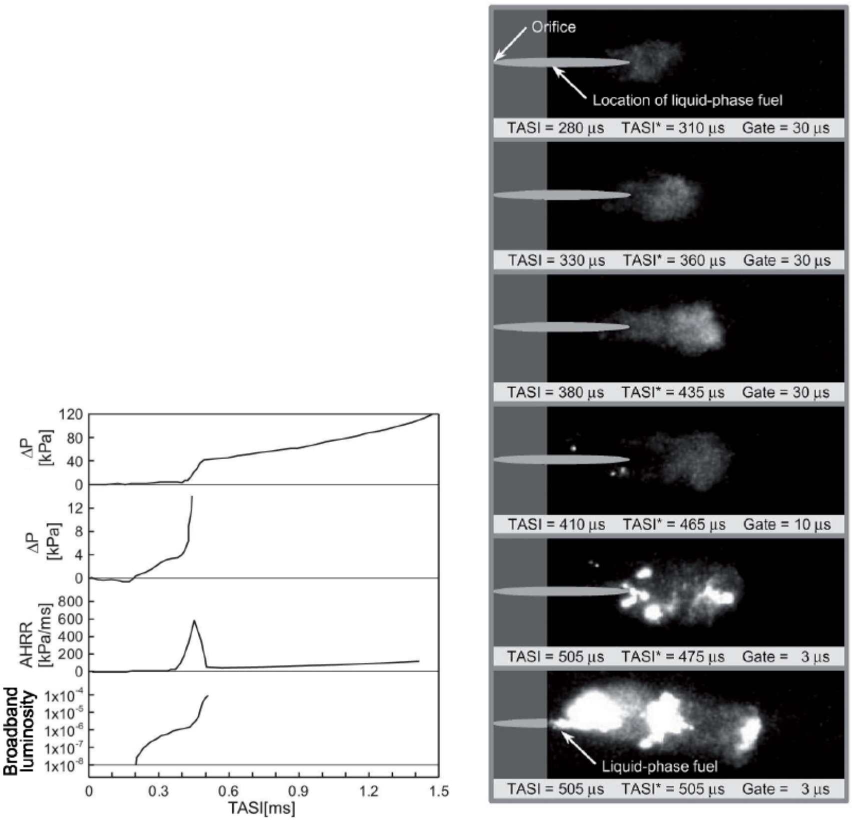

(a) (b)

Figure 2.13. *(a) Evolution of pressure increase (ΔP), apparent heat release rate (AHRR) and relative luminosity during the self-ignition of a diesel spray in a constant volume chamber. (b) Corresponding broadband images (no filtered) of the spray autoignition sequence. TASI stands for time after start of injection. TASI* accounts for TASI after time-correction due to cycle-to-cycle dispersion. Gate is the energizing time of the intensifier. Air conditions: 1000 K, 14.8 kg/m^3, 21% O$_2$. Source: Higgins et al. [92].*

However, depending on ambient conditions and the sensitivity of the hardware employed, it has been observed that radiation can also appear around the liquid spray (before the maximum liquid length) during the first instants, and then propagates to the front part of the spray.

- *Second-stage ignition/premixed burn period*: this phase corresponds to the sudden increase of the heat release rate. It starts once the energy transferred to the mixture by both hot air entrainment and

> cool-flame reactions meet the threshold condition required to enter in the phase of high-temperature ignition. Higgins et al. [92] comment that this transition is caused by the trigger of hydrogen peroxide dissociation, which turns out to dominate the chemistry and produce significant heat release. This phase is delimited by each ridge of the AHRR peak, between 0.4 and 0.5 ms TASI. At this stage, reaction propagates to the regions of vaporized mixture accumulated during the ignition delay and which did not start ignition themselves. At this stage, incandescent soot appears due to the local temperature increase. Soot requires rich mixtures but also temperatures above 1300 K. The corresponding thermal radiation extends rapidly, and dominates the broadband luminosity produced by the flame.

This description corresponds to a generic autoignition process for a certain fuel and engine conditions. However, it is important to note that the most specific details of the process, e.g. spatial distribution of species and characteristic times, depend on these factors. More specifically, ambient conditions play a major role over the development of the different stages. For independent variation of either air temperature or density, similar effects are observed. The increase of any of this variables usually produces a reduction of all the characteristic times, keeping the same phases but occurring in a shorter period of time. Both variables influence the physical and chemical phenomena involved in the autoignition. On one hand, temperature does not modify too much the spatial evolution of the spray, but it is a factor that clearly increases the rate of any chemical reaction. On the other hand, air density modifies the air entrainment rate and thus the fuel evaporation and spatial evolution. Dec et al. [91] state that the effect of these variables is more noticeable over the start and duration of second stage of ignition (premixed phase) than over the first stage of low-temperature reactions. In the same way, it could be expected that injection pressure has influence over the autoignition development as it is a factor that clearly affects the spatial evolution of the spray. However, there are few studies which have reported a clear influence of this parameter over the autoignition process. Heywood [6] suggests that injection pressure reduces ignition delay, but its effect is small. Along the same lines, Molina [8] obtains a statistical dependence of ignition delay with injection pressure to the power of -0.2. In this regard, it has been previously reported that injection pressure does not change the spray structure (e.g. maximum liquid length is not modified) [3], but the evaporation and mixing processes will be accelerated due to an increase of the air entrainment rate. If the reduction of the characteristic mixing time were important in comparison with the characteristic chemical kinetics, the effect would be noticeable. However, based on experimental results, it can be stated that the influence of the injection pressure will always be lower than the other two considered variables.

Considering the importance of the chemical processes, fuel characteristics are also essential with regard to the autoignition process. The ignitability of a fuel, represented by the global indicator octane number (ON) and/or the cetane number (CN)), depends typically and fundamentally on their chemical structure. The capacity of a hydrocarbon molecule to ignite resides on its facility to first break one of its bonds, whose strength varies respect to numerous parameters. For example, carbon-oxygen (C-O) and double carbon-hydrogen (C=H) bonds are energetically expensive to cut so that fuel molecules rather break through a single C-H bond first. The strength of these bonds also varies with their position in the molecule, and with the kind of radicals connected to the other branches of the same carbon atom. For instance, a C-H bond of a primary carbon (CH_3) is stronger than that of a secondary carbon (CH_2). In the particular case of linear alkanes, it can be concluded that an increase of the number of carbon atoms will increase their ignitability.

To sum up, a generic autoignition process in a CI engine starts when there is a mixture of evaporated fuel and air, under certain thermodynamic conditions which are favourable to the development of chemical reactions. These reactions develop in parallel to the evaporation and air-fuel mixing processes. A first physical induction stage can be identified, when the mixture is formed while it achieves reacting conditions. This phase is followed by two stages characterized by the chemical reactions that take place. The first one occurs at low temperature, with low heat release and low chemiluminescence radiation. The second stage starts when high-temperature reactions appear, which are characterized by a rapid increase of heat released and coincides with what is usually known as premixed combustion. At this stage, soot starts forming. The characteristic times and spatial evolution of these three stages depend on variables like ambient temperature or density, injection pressure and fuel properties.

2.5 Diffusion combustion phase

Once the chemical reaction has gone through all the stages previously defined, the combustion process achieves a state which is known as *diffusion combustion phase*. It extends until all the fuel injected is consumed. The previous description of the different stages of autoignition remarks the transitory nature of that phase. When it finishes, the combustion process has reached conditions which are favourable to the establishment of a self-sustained reaction. A diffusion flame front appears and stabilizes, which will keep its basic structure while fuel injection continues.

The diffusion phase is considered as the main combustion stage, and is so named according to the traditional classification of the combustion reactions [108]. The diffusion combustion is considered as the process in which fuel and oxygen are not previously mixed and, therefore, mixing and combustion take place simultaneously. During this stage reaction stabilizes and the flame front gets consolidated and is sustained thanks to the convective and diffusive contribution of fuel and oxygen. During injection, the dominating process is convection thanks to the momentum introduced by the spray. When injection finishes, the diffusion process becomes more relevant and dominates the remaining reaction. In fact, some authors like Heywood [6] or Lyn [109] consider the stage after the end of injection as a final independent phase, known as *late diffusion combustion phase*.

Plee and Ahmad [110] present an interesting discussion about the phenomena that control combustion under diesel-like conditions. They consider both the mixing process and the chemical kinetics by calculating characteristic times of ignition, mixing and combustion. Comparing the values obtained for diesel engines with direct injection systems and high compression ratios, they conclude that the air-fuel mixing rate controls the diffusion combustion process. The characteristic mixing times during this stage ($\backsim$2 ms) are several orders of magnitude higher than the characteristic reaction times ($\backsim$ 1μs). Considering this, it can be deduced that the diffusion combustion cannot be analysed independently from the air-fuel mixing process. An example of this close relation is represented by the work of López [18], who compares the air-fuel mixing rate under non-reactive conditions and the combustion rate in an engine, with a good agreement between them.

OH PLIF and OH* chemiluminescence have been widely used for the study of the transition between the premixed and the diffusion combustion. OH radical appear at several levels of the kinetic mechanisms for hydrocarbon oxidation but, under diesel-like conditions, it recombines and disappears at a high rate. Therefore, OH radicals are good markers to identify where and when high-temperature reactions are taking place. Dec and Coy [90] observed that, during the transition between premixed and diffusion combustion, OH first established as a thin layer surrounding the flame head vortex and then extended back towards the injector to a point where it stabilizes. Similar results were reported by Pickett et al. [111], Musculus et al. [99] and Bruneaux [96]. This phenomenon is known as *flame lift-off*, and means that the diesel diffusion flame is separated from the nozzle as reactions start at a certain distance downstream from the injector.

Siebers and Higgins [112], Musculus [99] and García-Oliver [2] have reported that the *lift-off length* (LOL) is mainly influenced by:

- *Fuel velocity at the orifice outlet*: A variation of the fuel velocity at the orifice outlet shifts the position where the convective flux (caused by the momentum of the fuel) equalises the turbulent combustion propagation velocity. An increase of the fuel velocity would increase the lift-off length.
- *Air temperature*: Temperature has a strong effect over the combustion velocity and thermal diffusivity. An increase of the ambient temperature would accelerate reactions, and thus the equilibrium previously mentioned will be achieved closer to the injector.
- *Air density*: The dependence between this parameter and the lift-off length is caused by the variations in thermal diffusivity, combustion velocity and spray angle. An increase of the air density would produce a reduction of the lift-off length.
- *Oxygen concentration*: The dependence of the lift-off length of a diesel spray with this parameter is related with the stoichiometric mixture fraction and the combustion velocity. When oxygen concentration is increased, the lift-off length is reduced.
- *Nozzle orifice diameter*: The explanation of this dependence is not so clear and Siebers and Higgins [112] hypothesize that maybe is related with the heating and evaporation processes that have to be completed before reactions take place. It has been reported that an increase of the orifice diameter increases the lift-off length.

From all the variables cited above, the most influencing is the air temperature. In contrast, the effect of the orifice diameter is an order of magnitude smaller. Different statistical correlations can be found [2, 3, 99, 112] which correlate the lift-off length with the value of the different boundary conditions.

2.5.1 The structure of the diesel flame and soot formation

Several conceptual models can be found in literature [1, 96, 97, 113], that seek to provide a clear and neat explanation of the structure of a reactive DI diesel jet. Currently, the most widespread and accepted vision is probably the conceptual model proposed by Dec [1] and later extended by Flynn et al. [114]. Figure 2.14 shows an schematic representation of this approach, derived from laser-sheet imaging for a typical instant during the first part of the diffusion combustion phase (i.e. prior to the end of injection). The series of experiments used to produce the conceptual model were primarily obtained at a typical range of operating conditions normally seen in a diesel engine.

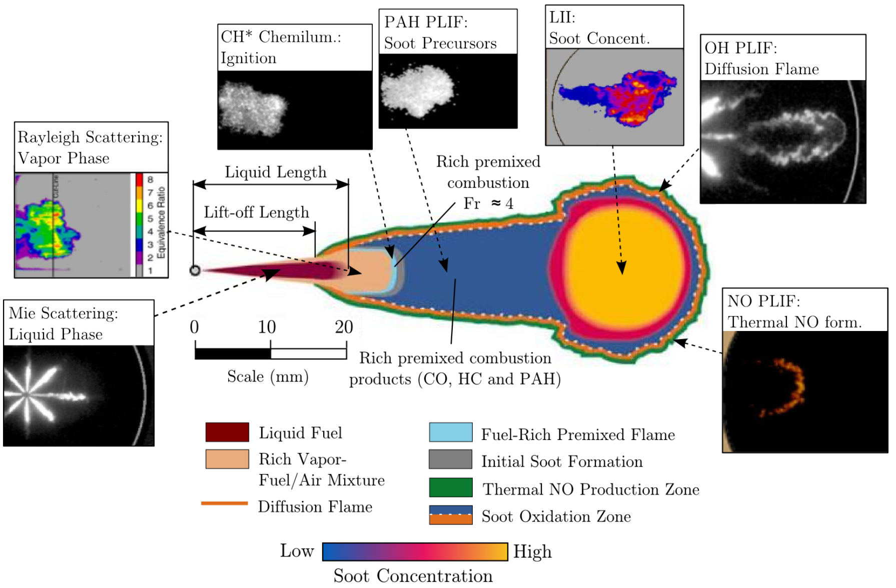

Figure 2.14. *Structure of the DI reactive diesel jet in queasy steady state (diffusion combustion) according to the conceptual model proposed by Dec. Source: Dec [1].*

As it has been described in previous sections, hot air is entrained into the jet as fuel travels into the cylinder, forming a cone-shaped spray. The fuel is heated and completely evaporated defining the characteristic liquid length (as it is depicted in figure 2.14). A fuel-rich premixed combustion region (cyan) appears downstream the liquid fuel penetration and extends to a fixed distance from nozzle (lift-off length). For the conditions considered by Dec, the equivalence ratio at this fuel-rich region is in the range of 2-4 [114]. In this region, most of the previously entrained oxygen is consumed resulting in a local temperature increase and the formation of carbon monoxide (CO) and partially oxidized hydrocarbons. It is worth mentioning the formation of polyciclic aromatic hydrocarbons, as they are considered soot precursors. According to Flynn et al. [114], during this combustion stage, around 10 - 15% of the chemical energy of the fuel is released. After reacting, they continue moving downstream, entrain other combustion products and diffuse towards the surrounding diffusion flame front. The amount of oxygen which progresses into the jet is limited as the surrounding diffusion flame and the premixed combustion area impede the penetration of the oxygen into this region. The amount of oxygen present in the premixed combustion and progressing within the jet is strongly related to the LOL of the flame as it determines the amount of air entrained before the premixed reaction zone is achieved. Therefore, this characteristic length has been identified as critical for soot formation in compression ignition engines [115, 116]. A review about this topic can be found at [2, 3, 117].

When the premixed combustion region is crossed, the energy released rises the temperature of the jet up to around 1600 K. Moving downstream and outwards radially, the mixture fraction decreases as products are mixed with fuel. The stoichiometric mixture radial location separates from the axis as the distance to the nozzle increases, giving the flame its characteristic conical shape. The resulting internal volume is occupied by intermediate combustion products (blue) surrounded by a stoichiometric surface, known as the diffusion flame front (orange). Based on the visualization of OH PLIF, Dec states that this surface is a thin layer (120 μm) [90]. Dec includes a head vortex on the leading portion of the flame (yellow), which is created during the transient development before flame reaches its natural length. He suggests that soot particles start forming near the rich premixed region, and formation and growth continues as they move down to the head vortex. In this region, soot particles accumulate and have enough time to grow to a very large size. Eventually, soot particles reach the diffusion flame at the periphery of the jet where they are oxidized by the OH radicals, releasing the chemical energy remaining (around 85%) from the original fuel. Bartok and Sarofim [118] say that OH is most likely to dominate soot oxidation under fuel-rich and stoichiometric conditions, while under lean conditions soot is oxidized by both OH and O_2. Haynes and Wagner [119] state that about 10 - 20% of all OH collisions with soot are effective at gasifying a carbon atom, since at this region temperature rises up to 2700 K. Dec and Canaan [120] visualized the induced fluorescence of the NO specie and reported that, at the outer part of the stoichiometric surface, the nitrogen oxides are formed thanks to the high local temperature and oxygen concentration.

The evolution of the soot particles within the flame is represented by figure 2.15, which has been extracted from a detailed review presented by Tree and Svensson [117]. The authors state that this evolution involves five commonly identified processes: pyrolysis, nucleation, coalescence, surface growth and agglomeration. The sequence is completed by the oxidation,

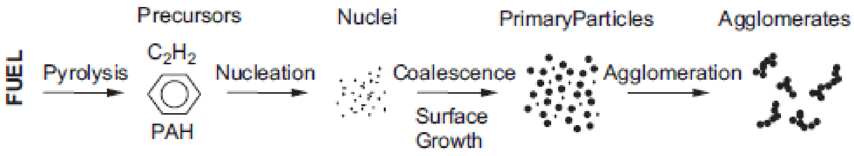

Figure 2.15. *Diagram of the steps in the soot formation process from gas phase to solid agglomerate particles. Source: Tree and Svensson [117].*

that converts hydrocarbons to CO, CO_2 and H_2O at any point in the process. Pyrolysis is the process by which organic compounds, such as fuels, alter their molecular structure in presence of high temperature without significant oxidation. It results in the production of some species that are precursors of soot. The next step is the nucleation, which is the formation of soot particles from gas-phase reactants, referred as nuclei. The authors describe the nucleation process as starting with the formation of a first aromatic ring by the combination of two propynyl radicals (C_3H_3). Then, more alkyl groups are added which turn it into a polyaromatic hydrocarbon (PAH) structure. At some point, the PAH is large enough (1.5 to 2 nm) to form the nuclei. This process occurs in the radical-rich region and requires temperatures between 1300 and 1600 K. The next step is the surface growth, despite there is no clear distinction between the end of nucleation and the beginning of this stage. In fact, they can be considered as concurrent. The majority of the soot mass is added during this stage, by the addition of gas-phase hydrocarbons to the surface of the soot particles. This process continues while particles leave the premixed reaction zone and move away into cooler and less reactive regions. The final step is the coalescence and agglomeration processes, by which particles combine. The exhaust soot from diesel engines consists of primary particles which are spherical in shape and agglomerate to form long chain-like structures.

Dec's model was published in 1997 and, since then, it inspired numerous studies. The constant evolution of either experimental methodologies or test facilities (e.g. constant pressure vessels) made it possible to carry on numerous works which have contributed directly or indirectly to the improvement of this model. Several of them have kept the same qualitative approach followed by Dec, providing major conceptual contributions. Kosaka et al. [97] observed that, once the quasi-steady diffusion combustion period is achieved, the mechanisms become quite different (figure 2.16). Soot precursors keep forming within the central fuel-rich part of the jet, while they are surrounded by a thick leaner region of OH radicals flowing towards the centre of the flame and consumed before reaching spray axis. The soot precursors at the spray axis form soot and achieve the spray head, where they grow and are pushed aside to the spray periphery by the motion of the head vortex. Finally, the soot particles are convected to the upstream part and re-entrained through the lean regions, where are rapidly oxidized. These observations agree with results presented later by Bruneaux [96]. The author simultaneously combined OH PLIF with PLIF at 355 nm so it was possible to locate OH in relation to formaldehyde (low temperature ignition tracers), PAH (soot precursor) and soot. It allowed defining an internal core formed almost by PAH, but surrounded by a thick layer of hydroxyl radicals which concentrate at the periphery suggesting the existence of this fuel-lean region. More recently, Jing et al. [113] (figure 2.17) utilized the visualization of natural luminosity and chemiluminescence of the flame to propose the existence of a CH_2O/PAH and CH^* layers (green band) between the fuel-lean (red) and soot (grey) regions.

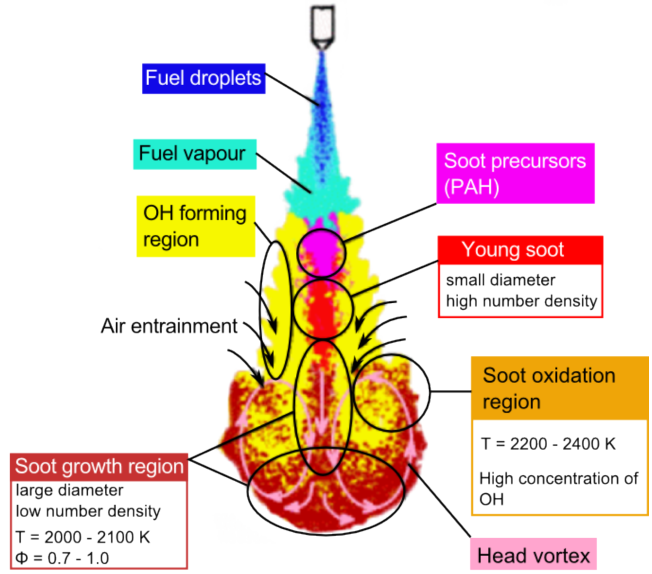

Figure 2.16. *Conceptual model of soot formation and oxidation processes in a Diesel spray flame. Source: Kosaka et al. [97].*

While studies presented in the previous paragraphs describe the diesel combustion processes in a qualitative way, other several studies have investigated and attempted to provide a more quantitative description of the process. In this regard, measuring the amount of soot formed within the flame has been one of the key topics. Three main optical techniques can be

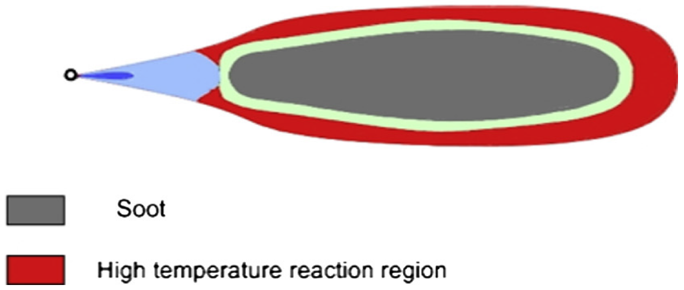

Figure 2.17. *Conventional high-load quasi-steady diesel flame diagram, based on chemiluminescence and natural luminosity visualization. Source: Jing et al. [113].*

found in literature for its characterization: Laser-Induced Incandescence (LII), 2-Colour Pyrometry (2C) and Laser Extinction Method (LEM).

LII is based on registering the high intensity radiation emitted by soot particles, which have been previously heated by a laser pulse. The magnitude of the signal can be correlated with the soot volume fraction in the detection region. This technique has been used extensively for qualitatively [56, 98, 115, 121] and even quantitative measurements [122–124]. The main advantage is that it makes it possible to quantify the soot distribution with full spatial resolution. However, quantitative measurements require a firm understanding of the factors that influence the LII signal [125]. An alternative has appeared during the last years, where LII signal is calibrated with LEM measurements to obtain the soot volume fraction distribution [126–131]. A variation of this technique (TiRe-LII) has been developed to measure particle size distributions considering the relation between the decay of the LII signal with the size of the particle [132–135]. One of the main drawbacks of conventional LII is its limited temporal resolution, due to the reduced pulsing rate of the lasers and the detectors that are usually employed. Nevertheless, during the last years several works have been published, which describe the use of high-frequency pulsed lasers and detectors [136].

The 2-Colour Pyrometry is based on the detection at two different wavelengths of the thermal radiation emitted by incandescent soot particles. The technique makes it possible to obtain not only the soot distribution but also the corresponding temperature. Signal can be detected by regular CCD and CMOS sensors, which enable to use modern high-speed cameras to achieve high temporal resolution. This technique has been widely used by the diesel engine research community [137–145]. However, the analysis of the results does not always consider the intrinsic limitations of the technique [142, 143]. A variation of this technique can be found in literature, where the whole emission spectra of soot is measured at different positions of the flame [146, 147]. However, in this case the spatial resolution is small.

It has been reported that 2C [142] and LII [125] can be strongly affected by the interaction between emitted radiation and other soot particles within the flame (absorption and scattering). However, LEM is based on this type of interactions. A light beam crosses the soot cloud and suffers attenuation due to its interaction with the particles. This attenuation can be related to the optical thickness of the soot cloud and, eventually, to the soot volume fraction. This technique has been widely used in single diffusion flames [116, 148, 149] and, with the proper considerations [149], reliable results can be obtained. Most LEM applications are based on point measurements along the flame, using a small laser beam. It allows high temporal resolution but it is spatially limited by the beam size. However, nowadays applications start to appear where a larger light source is combined with high-speed cameras, offering both good spatial and temporal resolution [150].

2.6 Summary and conclusions

The foregoing sections have analysed in detail the main phenomena that take place during the different stages of the diesel combustion process and the most relevant optical techniques utilized for their study. A conceptual description has been given to establish a link between the jet-flame structure and the different phases defined, which is summarized in figure 2.18.

The figure is divided in four sections. From top to bottom, the first one shows a typical injection mass flow rate and heat release rate traces, which have been extracted form figure 2.1. Following, the different stages described in this chapter are listed, in relation with the evolution of the previous curves. Each stage is accompanied by the keywords that best describe it. In the third part of the figure, a schematic representation of the evolution of the jet-flame through the different stages is shown. This representation is based on the one presented by Musculus et al. [151], which summarizes the conceptual model presented by Dec and Flynn [1, 114]. A couple of coloured bars are also represented related to the stages and the structure of the flame, which make reference to the radiation emitted at each stage of the combustion process. Finally, the main optical techniques that have been used to derive the conceptual model and deepen into the different phenomena dominating every stage are indicated.

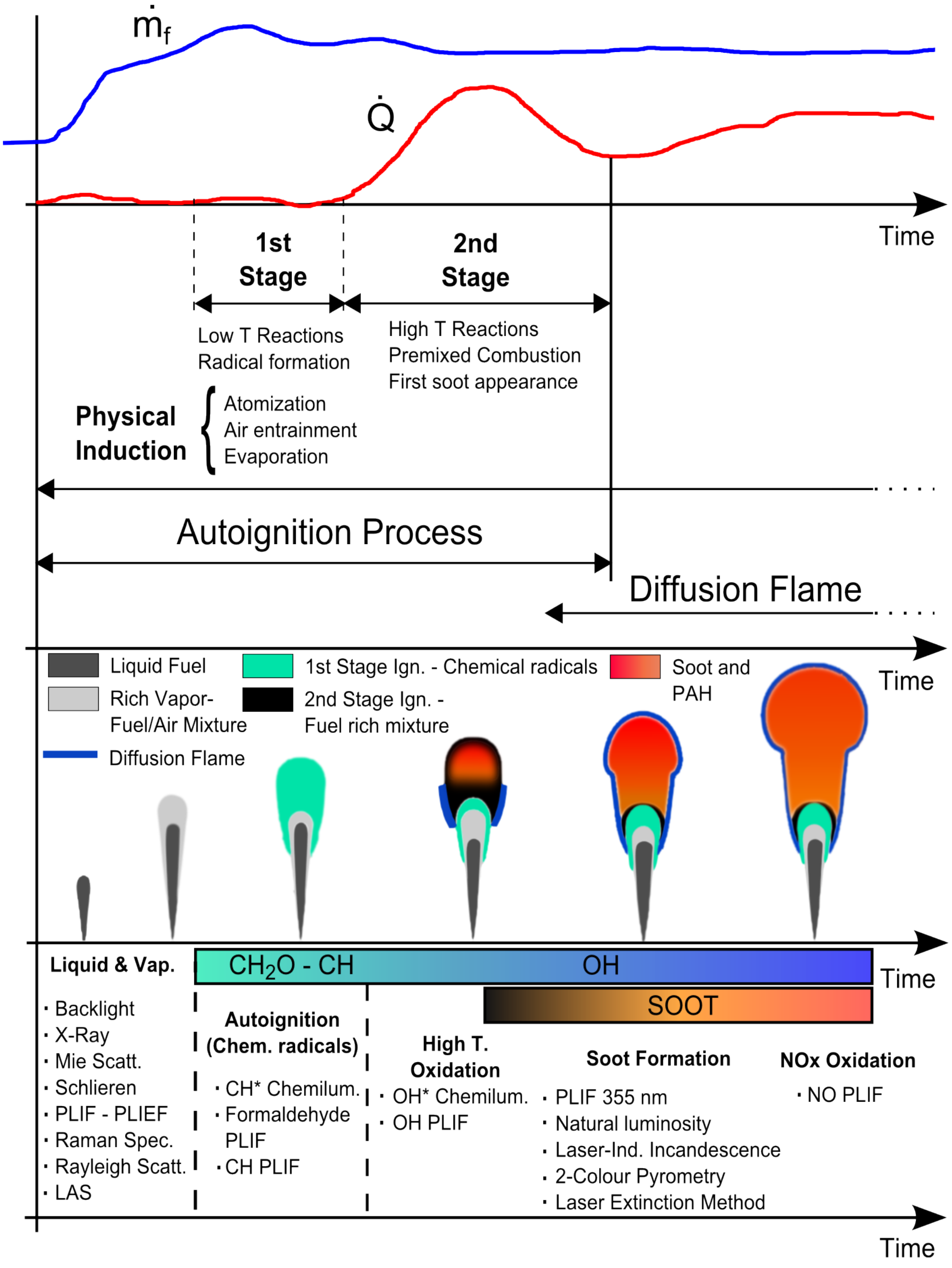

Figure 2.18. *Summarized description of the sequence of events that take place during de development of the combustion of a DI diesel jet. The spray schemes have been obtained from Musculus et al. [151].*

The narration begins when the liquid spray starts being injected into the combustion chamber. The spray immediately starts to break up into small droplets due to its interaction with the high-density atmosphere, which drastically increases the air-fuel interphase. Besides, the momentum introduced by the spray forces the air to entrain into the spray core. Both phenomena promote the mixture formation and the heat up of the liquid droplets, which start evaporating. Therefore, as spray penetrates, the liquid phase starts to disappear while the vapour phase consolidates, specially in the outer regions of the spray front.

With the vapour appearance, the first stage of the autoignition process begins. It takes place at low temperatures in comparison with the ones reached at the following stages. The fuel starts oxidizing at a very low rate and produces the first chemical radicals. It is usually difficult to detect these first reactions on the heat release curve, but it produces a slight pressure variation in the combustion chamber. Moreover, a weak chemiluminescence is emitted, mostly due to CH* radical and excited formaldehyde. Simultaneously with these chemical reactions, the air-fuel mixing continues (and so it will be during the whole injection process) which also keeps increasing the temperature of the mixture. After a certain time, the radicals formed and the low heat released makes it possible to move on to the high-temperature autoignition stage, also known as premixed combustion phase. This stage is characterized by three basic phenomena. Firstly, the chemical kinetic enters into a high-temperature stage, so the fuel consumption rate rises rapidly with the corresponding increase of the heat release rate. At this point, both final species ($\mathrm{C}O_2$ and $\mathrm{H_2O}$) and soot precursors are formed. This causes a characteristic phenomenon of this stage, which is the appearance of incandescent soot at the front part of the flame. From now on, the light emission will be dominated by the thermal radiation of soot. Finally, at the end of this stage, a flame front gets established, which will characterize the rest of the combustion process. This highlights the transient nature of the second stage of the autoignition process, which can be considered as a link between the non-reactive spray and the diffusion flame.

After the autoignition, the process enters into the diffusion combustion stage. The flame front consolidates and the flame enters into a quasi-stationary state. The flame structure has been described in detail in figures 2.14, 2.16 and 2.17. It consists of a non-reactive part near the nozzle, delimited by a rich premixed reaction region established during the previous stage. Downstream this location, a zone appears formed mainly by partial combustion products and soot precursors. This mixture travels downstream while incipient soot particles gets formed and grow until they reach the diffusion flame where oxygen and OH radicals oxidise it. During this phase, radiation from the flame is dominated by incandescent soot as its thermal emission is very intense. Nevertheless, the chemiluminescence emitted by the OH radical is also important and makes it possible to define the flame front which surrounds the inner soot. Moreover, this radiation is dominant in the area near the nozzle, which defines the lift-off length. This structure is maintained until injection finishes, when the introduction of momentum and consequently the mixing process finishes. From now on, the combustion rate decays and oxidation is dominated by the residual turbulence in the combustion chamber.

2.6.1 Approach of this work

Throughout the chapter, the relevance of the optical diagnostic techniques for the study of the diesel combustion process has been highlighted. They allow to get deeper insight into these phenomena, not only qualitatively but also quantitatively. This justifies the relevance of the current work, as it will be focused on the development of a variety of optical diagnostic tools.

The air-fuel mixture formation has been chosen as one of the main topics in the current work. In this regard, different techniques have been listed (Rayleigh, PLIF, PLIEF and Raman) which present different advantages and drawbacks but are quite accepted nowadays. The LAS technique, however, is not so common but it presents certain advantages that rise the interest on it. Moreover, the author considers that the development on new experimental tools gives to the work the scientific relevance it should require. The second part of the work will be focused on the characterization of soot formation. Regarding this topic, several studies have been listed which try to characterize the soot formation process quantitatively. Moreover, it has been possible to identify three main optical techniques (LII, 2C and LEM) that are nowadays used for this purpose. However, there is still no clear criteria about which one is the most reliable or its range of application. For this reason, a direct comparison between these techniques has been proposed under diesel-like conditions, to provide more insight into this discussion.

Bibliography

[1] Dec J.E. "A Conceptual Model of DI Diesel Combustion Based on Laser-Sheet Imaging". *SAE Technical Papers*, 1997.

[2] García-Oliver J. M. *Aportaciones al estudio del proceso de combustión turbulenta de chorros en motores diesel de inyección directa.* Doctoral Thesis, Universitat Politècnica de València, Departamento de Máquinas y Motores Térmicos, 2004.

[3] Nerva J-G. *An assessment of fuel physical and chemical properties in the combustion of a Diesel spray.* Doctoral Thesis, Universitat Politècnica de València, Departamento de Máquinas y Motores Térmicos, 2013.

[4] Zapata L.D. *Caracterización de los Procesos de Inyecciónn-Combustiónn Diesel Mediante Visualización y Procesado Digital de Imágenes.* Doctoral Thesis, Universitat Politècnica de València, Departamento de Máquinas y Motores Térmicos, 2010.

[5] García A. *Estudio de los efectos de la post-inyección sobre el proceso de combustión y la formación de hollín en motores diesel.* Doctoral Thesis, Universitat Politècnica de València, Departamento de Máquinas y Motores Térmicos, 2009.

[6] Heywood J. B. *Internal Combustion Engine Fundamentals.* McGraw-Hill, Inc., 1988.

[7] Payri F. and Desantes J. M. *Motores de Combustión Interna Alternativos.* Reverté, 2011.

[8] Molina S.A. *Estudio de la influencia de los parámetros de inyección y la recirculación de gases de escape sobre el proceso de combustión, las prestaciones y las emisiones de un motor diesel de 1.8 litros de cilindrada.* Doctoral Thesis, Universitat Politècnica de València, Departamento de Máquinas y Motores Térmicos, 2003.

[9] "Engine Combustion Network". *Information available at http://www.sandia.gov/ecn/.*

[10] Benajes J., Payri R., Bardi M. and Martí-Aldaraví P. "Experimental characterization of diesel ignition and lift-off length using a single-hole ECN injector". *Applied Thermal Engineering*, Vol. 58, pp. 554 – 563, 2013.

[11] Payri R., García J.M., Salvador F.J. and Gimeno J. "Using spray momentum flux measurements to understand the influence of diesel nozzle geometry on spray characteristics". *Fuel*, Vol. 84 n^o 5, pp. 551–561, 2005.

[12] Payri F., Bermúdez V., Payri R. and Salvador F.J. "The influence of cavitation on the internal flow and the spray characteristics in diesel injection nozzles". *Fuel*, Vol. 83 n^o 4-5, pp. 419–431, 2004.

[13] Gimeno J. *Desarrollo y Aplicación De La Medida Del Flujo De Cantidad de Movimiento De Un Chorro Diesel.* Doctoral Thesis, Universidad Politècnica de València, Departamento de Máquinas y Motores Térmicos, 2008.

[14] Salvador F.J. *Estudio Teórico Experimental De La Influencia De La Geometría De Toberas De Inyección Diesel Sobre Las Características Del Flujo Interno y Del Chorro.* Doctoral Thesis, Universitat Politècnica de València, Departamento de Máquinas y Motores Térmicos, 2003.

[15] Arrègle J. *Análisis De La Estructura y Dinámica Interna De Chorros Diesel.* Doctoral Thesis, Universitat Politècnica de València, Departamento de Máquinas y Motores Térmicos, 1997.

[16] Correas D. *Estudio Teórico-Experimental Del Chorro Libre Diesel Isotermo.* Doctoral Thesis, Universitat Politècnica de València, Departamento de Máquinas y Motores Térmicos, 1998.

[17] Ruiz S. *Estudio Teórico-Experimental De Los Procesos De Atomización y De Mezcla En Los Chorros Diesel D.I.* Doctoral Thesis, Universitat Politècnica de València, Departamento de Máquinas y Motores Térmicos, 2003.

[18] López J.J. *Estudio teórico-experimental del chorro libre Diesel no evaporativo y de su interacción con el movimiento del aire.* Doctoral Thesis, Universitat Politècnica de València, Departamento de Máquinas y Motores Térmicos, 2003.

[19] Pastor J.V., Payri R., Garcia-Oliver J.M. and Briceño F.J. "Schlieren Methodology for the Analysis of Transient Diesel Flame Evolution". *SAE International Journal of Engines*, Vol. 6 n^o 3, pp. 1661–1676, 2013.

[20] Desantes J.M., Pastor J.V., García-Oliver J.M. and Briceño F.J. "An experimental analysis on the evolution of the transient tip penetration in reacting Diesel sprays". *Combustion and Flame*, Vol. 161 n^o 8, pp. 2137–2150, 2014.

[21] Desantes J.M., Payri R., Pastor J.M. and Gimeno J. "Experimental characterization of internal nozzle flow and diesel spray behavior. Part I: Nonevaporative conditions". *Atomization and Sprays*, Vol. 15 n^o 5, pp. 489–516, 2005.

[22] Desantes J.M., Pastor J.V., Payri R. and Pastor J.M. "Experimental characterization of internal nozzle flow and diesel spray behavior. Part II: Evaporative conditions". *Atomization and Sprays*, Vol. 15 n^o 5, pp. 517–543, 2005.

[23] Payri R., Molina S., Salvador F.J. and Gimeno J. "A study of the relation between nozzle geometry, internal flow and sprays characteristics in diesel fuel injection systems". *KSME International Journal*, Vol. 18 n^o 7, pp. 1222–1235, 2004.

[24] Sou A., Hosokawa S. and Tomiyama A. "Effects of cavitation in a nozzle on liquid jet atomization". *International Journal of Heat and Mass Transfer*, Vol. 50 n^o 17-18, pp. 3575–3582, 2007.

[25] Hiroyasu H. "Spray breakup mechanism from the hole-type nozzle and its applications". *Automization and Sprays: Journal of the International Institutions for Liquid Atomization and Spray Systems*, Vol. 10 n^o 3-5, pp. 511–527, 2000.

[26] Macian V., Payri R., Margot X. and Salvador F.J. "A CFD analysis of the influence of diesel nozzle geometry on the inception of cavitation". *Atomization and Sprays*, Vol. 13 n^o 5-6, pp. 579–604, 2003.

[27] Payri F., Payri R., Salvador F.J. and Martínez-López J. "A contribution to the understanding of cavitation effects in Diesel injector nozzles through a combined experimental and computational investigation". *Computers and Fluids*, Vol. 58, pp. 88–101, 2012.

[28] Payri R., Salvador F.J., Gimeno J. and Venegas O. "Study of cavitation phenomenon using different fuels in a transparent nozzle by hydraulic characterization and visualization". *Experimental Thermal and Fluid Science*, Vol. 44, pp. 235–244, 2013.

[29] Suh H.K. and Lee C.S. "Effect of cavitation in nozzle orifice on the diesel fuel atomization characteristics". *International Journal of Heat and Fluid Flow*, Vol. 29 n^o 4, pp. 1001 – 1009, 2008.

[30] Li H. and Collicott S.H. "Visualization of cavitation in high-pressure diesel fuel injector orifices". *Atomization and Sprays*, Vol. 16 n^o 8, pp. 875–886, 2006.

[31] Badock C., Wirth R., Fath A. and Leipertz A. "Investigation of cavitation in real size diesel injection nozzles". *International Journal of Heat and Fluid Flow*, Vol. 20 n^o 5, pp. 538–544, 1999.

[32] Linne M. “Imaging in the optically dense regions of a spray: A review of developing techniques”. *Progress in Energy and Combustion Science*, Vol. 39 n^o 5, pp. 403 – 440, 2013.

[33] Desantes J.M., Payri R., Salvador F.J and De La Morena J. “Influence of cavitation phenomenon on primary break-up and spray behaviour at stationary conditions”. *Fuel*, Vol. 89, pp. 3033–3041, 2010.

[34] Hattori H., Narumiya K., Tsue M. and Kadota T. “Analysis of Initial Breakup Mechanism of Diesel Spray Injected into High-Pressure Ambience”. *SAE Technical Papers*, 2004.

[35] Manin J., Bardi M., Pickett L.M., Dahms R.N. and Oefelein J.C. “Microscopic investigation of the atomization and mixing processes of diesel sprays injected into high pressure and temperature environments”. *Fuel*, Vol. 134, pp. 531 – 543, 2014.

[36] Araneo L., Soare V., Payri R. and Shakal J. “Setting up a PDPA system for measurements in a Diesel spray”. *Journal of Physics: Conference Series*, Vol. 45 n^o 1, pp. 85–93, 2006.

[37] Le Gal P., Farrugia N. and Greenhalgh D.A. “Laser Sheet Dropsizing of dense sprays”. *Optics and Laser Technology*, Vol. 31 n^o 1, pp. 75–83, 1999.

[38] Jermy M.C. and Greenhalgh D.A. “Planar dropsizing by elastic and fluorescence scattering in sprays too dense for phase Doppler measurement”. *Applied Physics B: Lasers and Optics*, Vol. 71 n^o 5, pp. 703–710, 2000.

[39] Linne M., Paciaroni M., Hall T. and Parker T. “Ballistic imaging of the near field in a diesel spray”. *Experiments in Fluids*, Vol. 40 n^o 6, pp. 836–846, 2006.

[40] Linne M., Paciaroni M., Berrocal E. and Sedarsky D. “Ballistic imaging of liquid breakup processes in dense sprays”. *Proceedings of the Combustion Institute*, Vol. 32 n^o 2, pp. 2147 – 2161, 2009.

[41] Schmidt J.B., Schaefer Z.D., Meyer T.R., Roy S., Danczyk S.A. and Gord J.R. “Ultrafast time-gated ballistic-photon imaging and shadowgraphy in optically dense rocket sprays”. *Applied Optics*, Vol. 48 n^o 4, pp. B137–B144, 2009.

[42] Berrocal E., Kristensson E., Hottenbach P., Aldén M. and Grönefeld G. “Quantitative imaging of a non-combusting diesel spray using structured laser illumination planar imaging”. *Applied Physics B: Lasers and Optics*, Vol. 109 n^o 4, pp. 683–694, 2012.

[43] Yue Y., Powell C.F., Poola R., Wang J. and Schaller J.K. “Quantitative measurements of diesel fuel spray characteristics in the near-nozzle region using X-ray absorption”. *Atomization and Sprays*, Vol. 11 n^o 4, pp. 471–490, 2001.

[44] Powell C.F., Yue Y., Poola R. and Wang J. “Time-resolved measurements of supersonic fuel sprays using synchrotron X-rays”. *Journal of Synchrotron Radiation*, Vol. 7 n^o 6, pp. 356–360, 2000.

[45] Fansler T.D. and Parrish S.E. “Spray measurement technology: A review”. *Measurement Science and Technology*, Vol. 26 n^o 1, 2015.

[46] Kristensson E., Berrocal E. and Aldén M. “Two-pulse structured illumination imaging”. *Optics Letters*, Vol. 39 n^o 9, pp. 2584–2587, 2014.

[47] Reitz R.D. and Bracco F.V. “Mechanism of atomization of a liquid jet”. *Physics of Fluids*, Vol. 25, pp. 1730–1742, 1982.

[48] Reitz R.D. and Bracco F.V. *Mechanisms of Breakup of Round Liquid Jets. The Encyclopedia of Fluid Mechanics*, volume 3, capítulo 10, pp. 233–249. Gulf Publishing, 1986.

[49] Smallwood G.J. and Gülder O.L. "Views on the Structure of Transient Diesel Sprays". *Atomization and Sprays*, Vol. 10, pp. 355–386, 2000.

[50] Van de Hulst H.C. *Light Scattering by small particles*. John Wiley & Sons, N. Y., 1957.

[51] Bohren C.F. and Huffman D.R. *Absorption and scattering of light by small particles*. John Wiley & Sons, New York, 1983.

[52] Zhao H. and Ladommatos N. "Engine combustion instrumentation and diagnostics". *Warrendale, PA: Society of Automotive Engineers, 2001. 842*, 2001.

[53] Hodges J.T., Baritaud T.A. and Heinze T.A. "Planar liquid and gas fuel and droplet size visualization in a di diesel engine". *SAE Technical Papers*, 1991.

[54] Espey C. and Dec J.E. "The effect of TDC temperature and density on the liquid-phase fuel penetration in a D. I. diesel engine". *SAE Technical Papers*, 1995.

[55] Siebers D.L. "Liquid-phase fuel penetration in diesel sprays". *SAE Technical Papers*, 1998.

[56] Musculus M.P.B. "Multiple simultaneous optical diagnostic imaging of early-injection low-temperature combustion in a heavy-duty diesel engine". *SAE Technical Papers*, 2006.

[57] Lee Jinwoo and Bae Choongsik. "Application of JP-8 in a heavy duty diesel engine". *Fuel*, Vol. 90 n^o 5, pp. 1762 – 1770, 2011.

[58] Pastor J.V., García-Oliver J.M., Nerva J.-G. and Giménez B. "Fuel effect on the liquid-phase penetration of an evaporating spray under transient diesel-like conditions". *Fuel*, Vol. 90 n^o 11, pp. 3369–3381, 2011.

[59] Pastor J.V., Payri R., García-Oliver J.M. and Briceño F.J. "Analysis of transient liquid and vapor phase penetration for diesel sprays under variable injection conditions". *Atomization and Sprays*, Vol. 21 n^o 6, pp. 503–520, 2011.

[60] Kook S. and Pickett L.M. "Liquid length and vapor penetration of conventional, Fischer-Tropsch, coal-derived, and surrogate fuel sprays at high-temperature and high-pressure ambient conditions". *Fuel*, Vol. 93, pp. 539 – 548, 2012.

[61] Lequien G., Berrocal E., Gallo Y., Thermudo e Mello A., Andersson O. and Johansson B. "Effect of jet-jet interactions on the liquid fuel penetration in an optical heavy-duty di diesel engine". *SAE Technical Papers*, 2013.

[62] Pastor J.V., García-Oliver J.M., Bermúdez V. and Micó C. "Spray characterization for pure fuel and binary blends under non-reacting conditions". *SAE Technical Papers*, 2014.

[63] Browne K.R., Partridge I.M. and Greeves G. "Fuel property effects on fuel/air mixing in an experimental diesel engine". *SAE Technical Papers*, 1986.

[64] Kamimoto T., Yokota H. and Kobayashi H. "Effect of high pressure injection on soot formation processes in a rapid compression machine to simulate diesel flames". *SAE Technical Papers*, 1987.

[65] Siebers D.L. "Scaling liquid-phase fuel penetration in diesel sprays based on mixing-limited vaporization". *SAE Technical Papers*, 1999.

[66] Higgins B.S., Mueller C.J. and Siebers D.L. "Measurements of fuel effects on liquid-phase penetration in di sprays 1". *SAE Technical Papers*, 1999.

[67] Palomares A. *Análisis de imágenes de chorros Diesel.* Doctoral Thesis, Universitat Politècnica de València, Departamento de Máquinas y Motores Térmicos, 2001.

[68] Payri R., Gimeno J., Viera J.P. and Plazas A.H. "Needle lift profile influence on the vapor phase penetration for a prototype diesel direct acting piezoelectric injector". *Fuel*, Vol. 113, pp. 257–265, 2013.

[69] Rabenstein F., Egermann J. and Leipertz A. "Quantitative Analysis of Vapor Phase Structures in Transient Liquid Fuel Sprays". *The 4th International Symposium COMODIA 98*, 1998.

[70] Seasholtz M.B., Archibald D.D., Lorber A. and Kowalski B.R. "Quantitative analysis of liquid fuel mixtures with the use of Fourier transform near-IR Raman spectroscopy". *Applied Spectroscopy*, Vol. 43 n^o 6, pp. 1067–1072, 1989.

[71] Brands T., Hottenbach P., Koss H.-J., Grünefeld G., Pischinger S. and Adomeit P. "Quantitative fuel-air-mixing measurements in diesel-like sprays emanating from convergent and divergent multi-layer nozzles". *SAE Technical Papers*, 2012.

[72] Zhao H. *Laser Diagnostics and Optical Measurement Techniques in Internal Combustion Engines.* SAE International, Warrendale, 2012.

[73] Espey C., Dec J.E., Litzinger T.A. and Santavicca D.A. "Planar laser Rayleigh scattering for quantitative vapor-fuel imaging in a diesel jet". *Combustion and Flame*, Vol. 109 n^o 1-2, pp. 65–86, 1997.

[74] Idicheria C.A. and Pickett L.M. "Quantitative mixing measurements in a vaporizing diesel spray by rayleigh imaging". *SAE Technical Papers*, 2007.

[75] Myong K.-J., Suzuki H., Senda J. and Fujimoto H. "Spray inner structure of evaporating multi-component fuel". *Fuel*, Vol. 87 n^o 2, pp. 202–210, 2008.

[76] Pickett L.M., Manin J., Genzale C.L., Siebers D.L., Musculus M.P.B. and Idicheria C.A. "Relationship Between Diesel Fuel Spray Vapor Penetration/Dispersion and Local Fuel Mixture Fraction". *SAE International Journal of Engines*, Vol. 4 n^o 1, pp. 764–799, 2011.

[77] Schulz C. and Sick V. "Tracer-LIF diagnostics: Quantitative measurement of fuel concentration, temperature and fuel/air ratio in practical combustion systems". *Progress in Energy and Combustion Science*, Vol. 31 n^o 1, pp. 75–121, 2005.

[78] Juliá J.E. *Medida de concentraciones de combustible en chorros diesel mediante técnicas de fluorescencia inducida por láser.* Doctoral Thesis, CMT-Motores Térmicos, Universitat Politècnica de València, 2003.

[79] Matsuoka H., Yamashita H., Hayashi T. and Kitano K. "Effects of Fuel Properties on Diesel Spray Behavior under High Temperature and High Pressure Conditions". *SAE Technical Paper*, 2009.

[80] Williams B., Ewart P., Wangb X., Stone R., Mac H., Walmsley H., Cracknell R., Stevens R., Richardson D., Fu H. and Wallace S. "Quantitative planar laser-induced fluorescence imaging of multi-component fuel/air mixing in a firing gasoline-direct-injection engine: Effects of residual exhaust gas on quantitative PLIF". *Combustion and Flame*, Vol. 157, pp. 1866–1878, 2010.

[81] Chraplyvy A.R. "Nonintruvisve measurements of vapor concentrations inside sprays". *Applied Optics*, Vol. 20 n^o 15, pp. 2620–2624, 1981.

[82] Billings T. P. and Drallmeier J. A. "A detailed assessment of the infrared extinction technique for hydrocarbon vapor measurements in a controlled two-phase flow". *Atomization and Sprays*, Vol. 4 n^o 1, pp. 99–121, 1994.

[83] Winklhofer E. and Plimon A. "Monitoring of hydrocarbon fuel-air mixtures by means of a light extinction technique in optiaclly accessed research engines". *Optical Engineering*, Vol. 30, pp. 1262–1268, 1991.

[84] Suzuki M., Nishida K. and Hiroyasu H. "Simultaneous concentration measurement of vapor and liquid in an evaporating diesel spray". *SAE Technical Paper*, 1993.

[85] Zhang Y.-Y., Yoshizaki T. and Nishida K. "Imaging of Droplets and Vapor Distributions in a Diesel Fuel Spray by Means of a Laser Absorption–Scattering Technique". *Applied Optics*, Vol. 39 n^o 33, pp. 6221–6229, 2000.

[86] Zhang Y. Y. and Nishida K. "Vapor distribution measurement of higher and lower volatile components in an evaporating fuel spray via laser absorption scattering (LAS) technique". *Combustion Science and Technology*, Vol. 179 n^o 5, pp. 863–881, 2007.

[87] Gao J., Nishida K., Moon S. and Matsumoto Y. "Characteristics of Evaporating Diesel Spray: A comparison of laser measurements and empirical/theoretical predictions". *SAE Technical Paper*, 2009.

[88] Chato M., Fukuda S., Sato K., Fujikawa T., Chen R., Li Z., Tian J. and Nishida K. "Fuel Spray Evaporation and Mixture Formation Processes of Ethanol/Gasoline Blend Injected by Hole-Type Nozzle for DISI Engine". *SAE International Journal of Engines*, pp. 1836–1846, 2012.

[89] Edwards C., Siebers D. and Hoskin D. "A Study of the Autoignition Process of a Diesel Spray via High Speed Visualization". *SAE Technical Paper*, 1992.

[90] Dec J. and Coy E. "OH Radical Imaging in a DI Diesel Engine and the Structure of the Early Diffusion Flame". *SAE Technical Paper*, 1996.

[91] Dec J. and Espey C. "Chemiluminescence Imaging of Autoignition in a DI Diesel Engine". *SAE Technical Paper*, 1998.

[92] Higgins B., Siebers D. and Aradi A. "Diesel-Spray Ignition and Premixed-Burn Behavior". *SAE Technical Paper*, 2000.

[93] Pickett L.M., Kook S. and Williams T.C. "Visualization of Diesel Spray Penetration, Cool-Flame, Ignition, High-Temperature Combustion, and Soot Formation Using High-Speed Imaging". *SAE Technical Paper*, 2009.

[94] Gaydon A. G. *The Spectroscopy of Flames.* Springer Netherlands, 1974.

[95] Aldén M., Bood J., Li Z. and Richter M. "Visualization and understanding of combustion processes using spatially and temporally resolved laser diagnostic techniques". *Proceedings of the Combustion Institute*, Vol. 33 n^o 1, pp. 69–97, 2011.

[96] Bruneaux G. "Combustion structure of free and wall-impinging diesel jets by simultaneous laser-induced fluorescence of formaldehyde, poly-aromatic hydrocarbons, and hydroxides". *International Journal of Engine Research*, Vol. 9 n^o 3, pp. 249–265, 2008.

[97] Kosaka H., Aizawa T. and Kamimoto T. "Two-dimensional imaging of ignition and soot formation processes in a diesel flame". *International Journal of Engine Research*, Vol. 6 n^o 1, pp. 21–42, 2005.

[98] Bobba M. K. and Musculus M.P. "Laser diagnostics of soot precursors in a heavy-duty diesel engine at low-temperature combustion conditions". *Combustion and Flame*, Vol. 159, pp. 832 – 842, 2011.

[99] Musculus M.P.B. "Effects of the in-cylinder environment on diffusion flame lift-off in a di diesel engine". *SAE Technical Papers*, 2003.

[100] Singh S., Musculus M.P.B. and Reitz R.D. “Mixing and flame structures inferred from OH-PLIF for conventional and low-temperature diesel engine combustion”. *Combustion and Flame*, Vol. 156 n^o 10, pp. 1898–1908, 2009.

[101] Slabaugh C.D., Pratt A.C. and Lucht R.P. “Simultaneous 5 kHz OH-PLIF/PIV for the study of turbulent combustion at engine conditions”. *Applied Physics B: Lasers and Optics*, 2014.

[102] Ma X., Xu H., Jiang C. and Shuai S. “Ultra-high speed imaging and OH-LIF study of DMF and MF combustion in a DISI optical engine”. *Applied Energy*, Vol. 122, pp. 247–260, 2014.

[103] Merola S. S., Vaglieco B. M. and Corcione, F. E.and Mancaruso E. “In-Cylinder Combustion Analysis by Flame Emission Spectroscopy of Transparent CR Diesel Engine”. *SAE Technical Paper*, 2003.

[104] Merola S.S., Vaglieco B.M. and Mancaruso E. “Analysis of combustion process in a transparent common rail diesel engine by 2D digital imaging and flame emission spectroscopy”. *American Society of Mechanical Engineers, Internal Combustion Engine Division (Publication) ICE*, Vol. 40, pp. 649–660, 2003.

[105] Tornatore C., Merola S., Valentino G. and Marchitto L. “In-cylinder spectroscopic measurements of combustion process in a SI engine fuelled with butanol-gasoline blend”. *SAE Technical Papers*, 2013.

[106] Pastor J.V., García-Oliver J.M., García A., Micó C. and Durrett R. “A spectroscopy study of gasoline partially premixed compression ignition spark assisted combustion”. *Applied Energy*, Vol. 104, pp. 568–575, 2013.

[107] Merola S.S., Vaglieco B.M. and Mancaruso E. “Multiwavelength ultraviolet absorption spectroscopy of NO and OH radical concentration applied to a high-swirl diesel-like system”. *Experimental Thermal and Fluid Science*, Vol. 28 n^o 4, pp. 355–367, 2004.

[108] Glassman I. and Yetter R. A. *Combustion.* Elsevier Inc., 2008.

[109] Lyn W.T. “Study of burning rate and nature of combustion in diesel engines”. *Symposium (International) on Combustion*, Vol. 9 n^o 1, pp. 1069–1082, 1963.

[110] Plee S. and Ahmad T. “Relative Roles of Premixed and Diffusion Burning in Diesel Combustion”. *SAE Technical Paper*, 1983.

[111] Pickett L.M., Kook S., Persson H. and Andersson Ö. “Diesel fuel jet lift-off stabilization in the presence of laser-induced plasma ignition”. *Proceedings of the Combustion Institute*, Vol. 32 II, pp. 2793–2800, 2009.

[112] Siebers D. and Higgins B. “Flame lift-off on direct-injection diesel sprays under quiescent conditions”. *SAE Technical Papers*, 2001.

[113] Jing W., Roberts W.L. and Fang T. “Spray combustion of Jet-A and diesel fuels in a constant volume combustion chamber”. *Energy Conversion and Management*, Vol. 89, pp. 525–540, 2015.

[114] Flynn P.F., Durrett R.P., Hunter G.L., Zur Loye A.O., Akinyemi O.C., Dec J.E. and Westbrook C.K. “Diesel combustion: An integrated view combining laser diagnostics, chemical kinetics, and empirical validation”. *SAE Technical Papers*, 1999.

[115] Pickett L.M. and Siebers D.L. “Fuel Effects on Soot Processes of Fuel Jets at DI Diesel Conditions”. *SAE Technical Papers*, 10 2003.

[116] Pickett L.M. and Siebers D.L. “Soot in diesel fuel jets: effects of ambient temperature, ambient density, and injection pressure”. *Combustion and Flame*, Vol. 138, pp. 114 – 135, 2004.

[117] Tree D.R. and Svensson K.I. “Soot processes in compression ignition engines”. *Progress in Energy and Combustion Science*, Vol. 33 n^o 3, pp. 272–309, 2007.

[118] Bartok W. and Sarofim A. *Fossil Fuel Combustion: A Source Book.* John Wiley & Sons, N. Y., 1991.

[119] Haynes B.S. and Wagner H.G. “Soot formation”. *Progress in Energy and Combustion Science*, Vol. 7 n^o 4, pp. 229 – 273, 1981.

[120] Dec J.E. and Canaan R.E. “PLIF imaging of no formation in a di diesel engine 1”. *SAE Technical Papers*, 1998.

[121] J.E. Dec. “Soot Distribution in a D.I. Diesel Engine Using 2-D Imaging of Laser-induced Incandescence, Elastic Scattering, and Flame Luminosity”. *SAE Technical paper series*, 1992.

[122] Ito T., Hosaka T., Ueda M., Senda J. and Fujimoto H. “Detailed kinetic modeling and laser diagnostics of soot formation process in diesel jet flame”. *SAE Technical Papers*, 2004.

[123] Lee K., Han Y., Lee W., Chung J. and Lee C. “Quantitative measurements of soot particles in a laminar diffusion flame using a LII/LIS technique”. *Measurement Science and Technology*, Vol. 16 n^o 2, pp. 519–528, 2005.

[124] He X., Ma X. and Wang J.-X. “Quantitative soot concentration measurement of flame by laser induced incandescence”. *Ranshao Kexue Yu Jishu/Journal of Combustion Science and Technology*, Vol. 15 n^o 4, pp. 344–349, 2009.

[125] Schulz C., Kock B.F., Hofmann M., Michelsen H., Will S., Bougie B., Suntz R. and Smallwood G. “Laser-induced incandescence: Recent trends and current questions”. *Applied Physics B: Lasers and Optics*, Vol. 83 n^o 3, pp. 333–354, 2006.

[126] Pastor J.V., García J.M., Pastor J.M. and Buitrago J.E. “Analysis of calibration techniques for laser-induced incandescence measurements in flames”. *Measurement Science and Technology*, Vol. 17 n^o 12, pp. 3279–3288, 2006.

[127] Kook S. and Pickett L.M. “Soot volume fraction and morphology of conventional and surrogate jet fuel sprays at 1000-K and 6.7-MPa ambient conditions”. *Proceedings of the Combustion Institute*, Vol. 33 n^o 2, pp. 2911 – 2918, 2011.

[128] de Francqueville L., Bruneaux G. and Thirouard B. “Soot Volume Fraction Measurements in a Gasoline Direct Injection Engine by Combined Laser Induced Incandescence and Laser Extinction Method”. *SAE Int. J. Engines 3*, Vol. 1, pp. 163–182, 2010.

[129] Henriksen T.L., Nathan G.J., Alwahabi Z.T., Qamar N., Ring T.A. and Eddings E.G. “Planar measurements of soot volume fraction and OH in a JP-8 pool fire”. *Combustion and Flame*, Vol. 156 n^o 7, pp. 1480–1492, 2009.

[130] Kook S. and Pickett L.M. “Effect of fuel volatility and ignition quality on combustion and soot formation at fixed premixing conditions”. *SAE Technical Papers*, 2009.

[131] Cenker E., Bruneaux G., Pickett L. and Schulz C. “Study of soot formation and oxidation in the engine combustion network (ECN), spray A: Effects of ambient temperature and oxygen concentration”. *SAE International Journal of Engines*, Vol. 6 n^o 1, pp. 352–365, 2013.

[132] Schraml S., Dankers S., Bader K., Will S. and Leipertz A. “Soot temperature measurements and implications for time-resolved laser-induced incandescence (TIRE-LII)”. *Combustion and Flame*, Vol. 120 n^o 4, pp. 439–450, 2000.

[133] Kock B.F., Tribalet B., Schulz C. and Roth P. "Two-color time-resolved LII applied to soot particle sizing in the cylinder of a Diesel engine". *Combustion and Flame*, Vol. 147 n^o 1-2, pp. 79–92, 2006.

[134] Charwath M., Suntz R. and Bockhorn H. "Constraints of two-colour TiRe-LII at elevated pressures". *Applied Physics B: Lasers and Optics*, Vol. 104 n^o 2, pp. 427–438, 2011.

[135] Cenker E., Bruneaux G., Dreier T. and Schulz C. "Determination of small soot particles in the presence of large ones from time-resolved laser-induced incandescence". *Applied Physics B: Lasers and Optics*, 2014.

[136] Sjöholm J., Wellander R., Bladh H., Richter M., Bengtsson P.-E., Alden M., Aronsson U., Chartier C., Andersson Ö. and Johansson B. "Challenges for In-Cylinder High-Speed Two-Dimensional Laser-Induced Incandescence Measurements of Soot". *SAE International Journal of Engines*, Vol. 4 n^o 1, pp. 1607–1622, 2011.

[137] Yan J. and Borman G.L. "Analysis and in-cylinder measurement of particulate radiant emissions and temperature in a direct injection diesel engine". *SAE Technical Papers*, 1988.

[138] Quoc H.X., Vignon J.-M. and Brun M. "A new approach of the two-color method for determining local instantaneous soot concentration and temperature in a D.I. Diesel combustion chamber". *SAE Technical Papers*, 1991.

[139] Zhao H. and Ladommatos N. "Optical diagnostics for soot and temperature measurement in diesel engines". *Progress in Energy and Combustion Science*, Vol. 24 n^o 3, pp. 221–255, 1998.

[140] Vattulainen J., Nummela V., Hernberg R. and Kytölä J. "A system for quantitative imaging diagnostics and its application to pyrometric in-cylinder flame-temperature measurements in large diesel engines". *Measurement Science and Technology*, Vol. 11 n^o 2, pp. 103–119, 2000.

[141] Svensson K.I., MacKrory A.J., Richards M.J. and Tree D.R. "Calibration of an RGB, CCD camera and interpretation of its two-color images for KL and temperature". *SAE Technical Papers*, 2005.

[142] Payri F., Pastor J.V., García-Oliver J.M. and Pastor J.M. "Contribution to the application of two-colour imaging to diesel combustion". *Measurement Science and Technology*, Vol. 18 n^o 8, pp. 2579–2598, 2007.

[143] Musculus M.P., Singh S. and Reitz R.D. "Gradient effects on two-color soot optical pyrometry in a heavy-duty DI diesel engine". *Combustion and Flame*, Vol. 153 n^o 1-2, pp. 216–227, 2008.

[144] Zhang J., Jing W., Roberts W.L. and Fang T. "Soot temperature and KL factor for biodiesel and diesel spray combustion in a constant volume combustion chamber". *Applied Energy*, Vol. 107, pp. 52–65, 2013.

[145] Jing W., Roberts W. and Fang T. "Comparison of soot formation for diesel and jet-a in a constant volume combustion chamber using two-color pyrometry". *SAE Technical Papers*, 2014.

[146] Snelling D.R., Thomson K.A., Smallwood G.J., Gülder O.L., Weckman E.J. and Fraser R.A. "Spectrally resolved measurement of flame radiation to determine soot temperature and concentration". *AIAA Journal*, Vol. 40 n^o 9, pp. 1789–1795, 2002.

[147] Liu F., Thomson K.A. and Smallwood G.J. “Soot temperature and volume fraction retrieval from spectrally resolved flame emission measurement in laminar axisymmetric coflow diffusion flames: Effect of self-absorption”. *Combustion and Flame*, Vol. 160 n^o 9, pp. 1693–1705, 2013.

[148] Musculus M.P., Dec J.E. and Tree D.R. “Effects of fuel parameters and diffusion flame lift-off on soot formation in a heavy-duty di diesel engine”. *SAE Technical Papers*, 2002.

[149] Musculus M.P. and Pickettm L.M. “Diagnostic considerations for optical laser-extinction measurements of soot in high-pressure transient combustion environments”. *Combustion and Flame*, Vol. 141 n^o 4, pp. 371 – 391, 2005.

[150] Manin J., Pickett L.M. and Skeen S.A. “Two-Color Diffused Back-Illumination Imaging as a Diagnostic for Time-Resolved Soot Measurements in Reacting Sprays”. *SAE International Journal of Engines*, Vol. 6 n^o 4, 2013.

[151] Musculus M.P., Miles P.C. and Pickett L.M. “Conceptual models for partially premixed low-temperature diesel combustion”. *Progress in Energy and Combustion Science*, Vol. 39 n^o 2-3, pp. 246–283, 2013.

Chapter 3

Tools and Methodology

Contents

3.1 Introduction

In the previous chapters, the objectives and framework of the current thesis have been defined. Then, a description of the main experimental and theoretical tools is presented in this chapter. As it has been highlighted previously, optical techniques have played a major role on the development of this thesis. Not only as experimental tools, but also as targets of the study. For this reason, all the experimental work was carried out in an optically accessible test rig. It is based on a two-stroke single cylinder engine, which made it possible to achieve a wide variety of thermodynamic conditions similar to those found within a diesel engine. Besides, some parts of the work have been complemented with theoretical calculations made with a one-dimensional model (1D-Model). As it is described in following chapters, these calculations were utilized both as part of the data processing algorithm and for experimental result validation.

The experimental work was divided in two main groups: mixture formation (inert conditions) and combustion (reactive conditions). In the first case, one of the most relevant parts of the work is the development and validation of the UV-VIS LAS technique. In the second case, a complex optical arrangement was used to compare three different soot-measuring techniques to determine the advantages and limitations of each of them. Thus, there is a close relation between these experimental tools and the different results presented. For this reason, it has been decided to not include the optical diagnostic techniques as tools in this chapter and the corresponding detailed descriptions have been included in chapters 4 and 5. Besides, this outline is also motivated by the complexity of the two groups of experiments, each one involving a specific optical set-up and computational processing.

The current chapter starts with a description of the test rig. Information regarding hardware, working principle and thermodynamic conditions within the combustion chamber is presented. This section includes the definition of the operating conditions chosen for each of the two main experiment blocks. Moreover, a detailed characterization of the airflow is presented, which represents a contribution of this thesis in reference to others carried out in the same test rig. Next, the fuel main properties (including hydraulic characterization) are presented. The chapter ends with an exposition of the basis of the 1D-Model spray used for theoretical calculations.

3.2 Hot spray test rig

3.2.1 Hardware description

Tests were performed in an optically accessible single cylinder engine, whose detailed description can be found in [1]. The facility is based on a 2-stroke single cylinder engine (Jenbach JW 50), with three litres displacement.

The engine was designed for research purposes as the large displacement limits the effect of endothermic (liquid vaporization) and exothermic (spray combustion) processes on the pressure trace. However, it is not able to develop enough work each cycle to keep running by itself. Therefore, an asynchronous electric motor (37 kW) is utilized to start and keep the desired working conditions. The engine is motored at low speed (500 rpm), to minimize the variation of in-cylinder conditions during a relatively long period (compared with typical DI diesel injection durations).

A scheme of the engine is depicted in figure 3.1. Both air intake and exhaust are handled by transfers on the cylinder liner. The cylinder head was specially designed to provide optical access to the combustion chamber. It is cylindrical in shape, to avoid wall impingement when single hole nozzles are used. The effective compression ratio was kept at 15.7. The chamber presents an upper port, where the injector is mounted, and four lateral accesses. A pressure transducer is installed in one of them, whereas the other three are equipped with oval-shaped quartz windows (88 mm long, 37 mm large and 28 mm thick). The cylinder head and the block temperature are controlled by a coolant recirculation system. Their temperature was set to 353 K, to guarantee good lubricity.

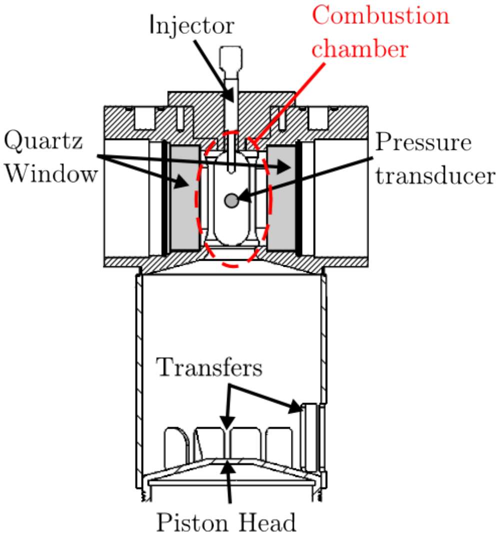

Figure 3.1. *Scheme of the arrangement of the cylinder head and the liner.*

According to the needs of this study, the facility can be operated in two different working modes to achieve both inert and reactive operating conditions:

- *Reactive conditions*: A roots compressor takes atmospheric air and sends it into the cylinder, where the thermodynamic cycle takes place. The air goes through two conditioning units, which heat it and remove any liquid or particle before reaching the intake port. After combustion, the exhaust gases are expelled to the atmosphere again.
- *Inert conditions*: The working fluid is nitrogen, to avoid any combustion reaction while keeping similar physical properties as the atmospheric air. For this purpose, the facility works under a closed loop scheme. When the exhaust gases (nitrogen + fuel) leave the cylinder, they flow through an intercooler and a cyclonic filter, to remove rests of fuel and oil out of the recirculated gas stream. This ensures proper operating conditions for a roots compressor, which is used to assist the air management of the engine. Then, nitrogen is impulsed into the cylinder, through the same conditioning units as the ones used for the reactive configuration. The circuit is refilled through an electronic valve to achieve the desired intake pressure and compensate blow-by and leakages.

For both configurations, the engine is usually operated under skip-fired mode, so that in-cylinder conditions are not influenced by the remaining residual gases from previous combustion cycles. An injection takes place every 30 cycles, which guarantees that ambient conditions are kept constant between consecutive repetitions, and temperature transients are avoided.

3.2.2 Operating conditions

In-cylinder thermodynamic conditions are controlled by the intake gas temperature and pressure. To determine the values required to achieve any combination of pressure and temperature at top dead centre (TDC), a characterization of the engine has to be performed. A detailed description can be found in [2]. The procedure is based on determining thermodynamic conditions inside the cylinder, for a variety of points that covers the entire operating range of the engine. In-cylinder temperature (T_c) and density (ρ_c) are calculated from in-cylinder pressure (p_c), using a first-law thermodynamic analysis and accounting for blow-by, heat transfer and mechanical stress [1, 3]. First, the trapped mass is estimated using intake pressure, temperature and volume at exhaust vent closure (EVC). Once the trapped mass is known, T_c and ρ_c are estimated for the whole cycle using the equation of state. The blow-by leakage mass is angularly distributed along the cycle as a linear function of in-cylinder pressure. Mechanical stress can lead to deformations which should be taken into account. However, in this particular engine, deformations were estimated to be negligible. Once angular-resolved thermodynamic conditions of the set of points are obtained, the exact intake conditions required for a defined test plan can be calculated by interpolating between the values available. The maximum T_c usually presents a linear response to intake temperature (T_{int}), independently from intake pressure (p_{int}). In order to achieve a desired ρ_c, the required value of p_{int} is calculated by interpolation for each T_{int} of the designed test plan.

The influence of fuel evaporation over in-cylinder conditions has been previously studied by Nerva [2]. Based on previous observations with multi-hole nozzles at the same test rig, the author decided to analyse the real influence of fuel evaporation over thermodynamic conditions inside the combustion chamber when a single hole nozzle was utilized. Despite finding small differences between cycles with and without injections, he concluded that the cooling effect (caused by the enthalpy absorbed by the fuel for vaporization) was insignificant at any condition of the test matrix. Therefore, it can be concluded that the characterization process is applicable for engine cycles with and without injection.

Based on these results, it was possible to define a test matrix for the current study. According to chapter 2, in-cylinder conditions as well as injection pressure (p_{inj}) play a significant role at all stages of the spray and combustion development. Therefore, sweeps of T_c, ρ_c (p_c) and p_{inj} where considered. Due to the transitory nature of in-cylinder conditions within the engine cycle, each operating point is identified in this document by its thermodynamic conditions at TDC. In this way, the test matrix is formed by a combination of two T_c values at TDC (i.e. 760 and 880 K) and three different p_c at TDC (i.e. 4.3, 5.3 and 7.3 MPa). Besides, for each operating point, three p_{inj} where evaluated: 50, 100 and 150 MPa. The resulting test matrix is summarized in figure 3.2, together with the corresponding evolution of in-cylinder thermodynamic conditions (p_c and ρ_c) for each operating point. The injection event was located near TDC, to minimize the variation of thermodynamic conditions. A typical mass flow rate trace has been included in figure 3.2, as an example.

The different complexity of each group of experiments forced to modify the original test matrix when necessary. For this reason, the entire matrix was only considered for the macroscopic characterization of the spray under inert conditions (section 4.2). It was simplified for the microscopic characterization (section 4.3) and the combustion studies (chapter 5) as presented in figure 3.3. For the reactive test, the ambient gas was changed from pure nitrogen to atmospheric air. Moreover, the lower temperature for the reactive study was

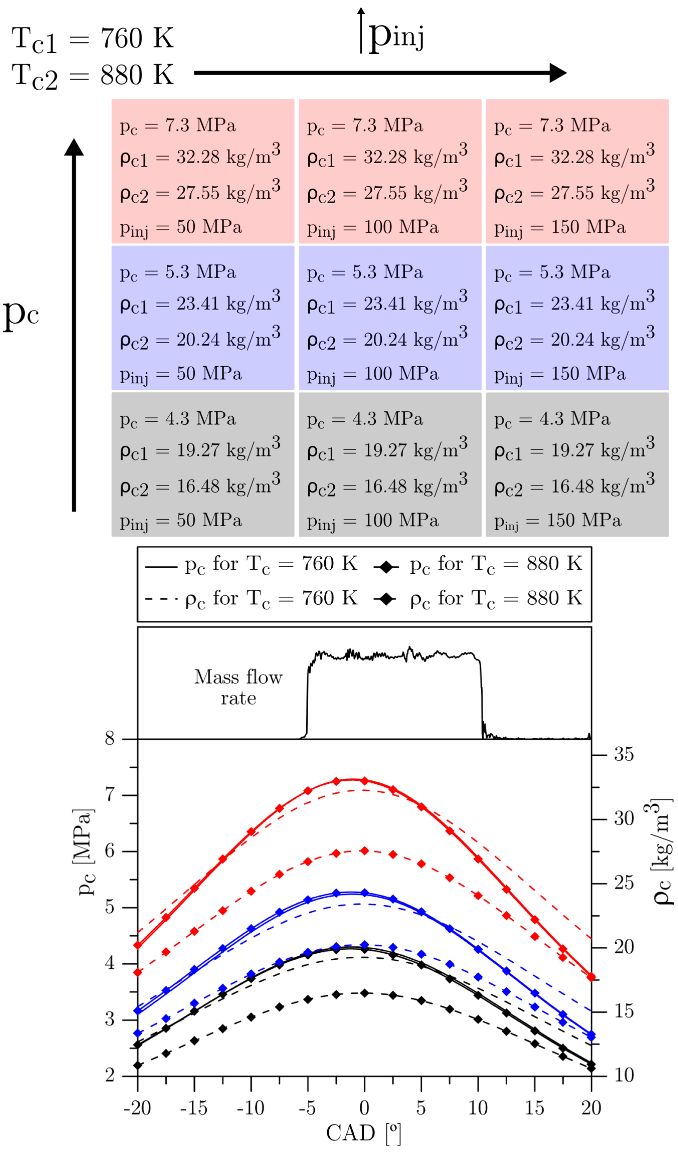

$p_c = 7.3$ MPa $\rho_{c1} = 32.28$ kg/m^3 $\rho_{c2} = 27.55$ kg/m^3 $p_{inj} = 50$ MPa	$p_c = 7.3$ MPa $\rho_{c1} = 32.28$ kg/m^3 $\rho_{c2} = 27.55$ kg/m^3 $p_{inj} = 100$ MPa	$p_c = 7.3$ MPa $\rho_{c1} = 32.28$ kg/m^3 $\rho_{c2} = 27.55$ kg/m^3 $p_{inj} = 150$ MPa
$p_c = 5.3$ MPa $\rho_{c1} = 23.41$ kg/m^3 $\rho_{c2} = 20.24$ kg/m^3 $p_{inj} = 50$ MPa	$p_c = 5.3$ MPa $\rho_{c1} = 23.41$ kg/m^3 $\rho_{c2} = 20.24$ kg/m^3 $p_{inj} = 100$ MPa	$p_c = 5.3$ MPa $\rho_{c1} = 23.41$ kg/m^3 $\rho_{c2} = 20.24$ kg/m^3 $p_{inj} = 150$ MPa
$p_c = 4.3$ MPa $\rho_{c1} = 19.27$ kg/m^3 $\rho_{c2} = 16.48$ kg/m^3 $p_{inj} = 50$ MPa	$p_c = 4.3$ MPa $\rho_{c1} = 19.27$ kg/m^3 $\rho_{c2} = 16.48$ kg/m^3 $p_{inj} = 100$ MPa	$p_c = 4.3$ MPa $\rho_{c1} = 19.27$ kg/m^3 $\rho_{c2} = 16.48$ kg/m^3 $p_{inj} = 150$ MPa

Figure 3.2. *Full test matrix for the current study (top) and the equivalent in-cylinder thermodynamic conditions (bottom).*

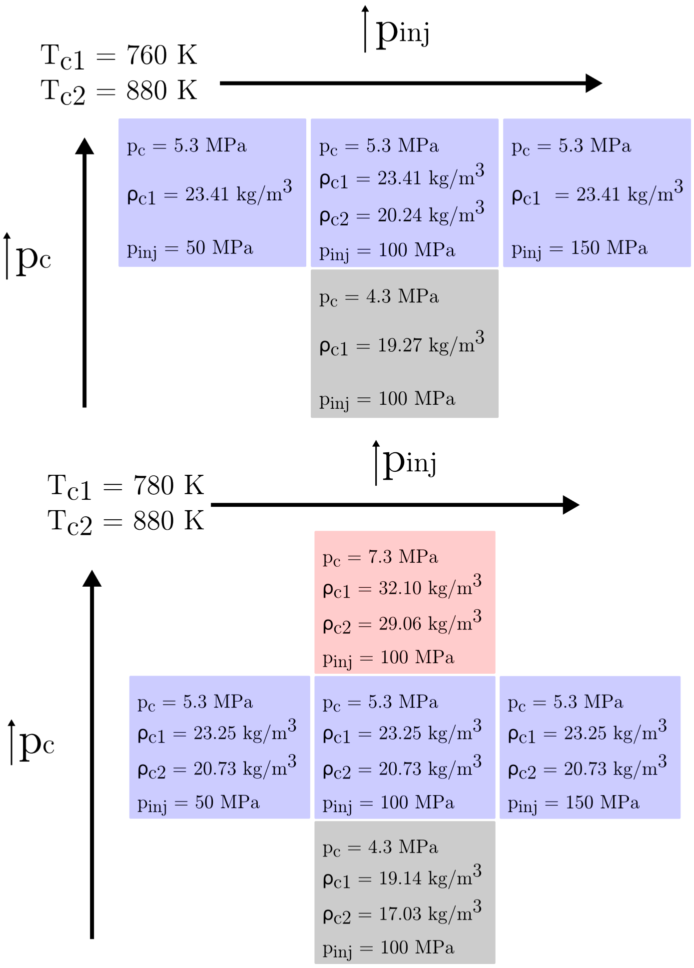

Figure 3.3. *Test matrix defined for microscopic spray characterization (top) and combustion studies (bottom).*

increased to 780 K, to ensure the proper combustion of all the fuels at any operating condition.

3.2.3 Fuel injection temperature

Despite the engine cooling water keeps the injector holder at constant temperature, the nozzle (which protrudes into the combustion chamber) can be heated by the much hotter in-cylinder gases. The heat transfer in the nozzle body can increase the temperature of the fuel before it is injected. This temperature (T_{inj}) is a parameter of interest as it influences the evaporation process. If the fuel is injected at higher temperature, less enthalpy is required to completely evaporate it. For this reason, T_{inj} is one of the input parameters of the one-dimensional spray mixing model. Therefore a reliable T_{inj} value is required, in order to get the more accurate theoretical estimations of the spray mixing process.

A methodology was followed, based on a previous work presented by Payri et al. [4]. A modified Bosch piezoelectric CR 3.1 injector was mounted, replacing the original injector of the study. The injector body and nozzle were "emptied", in order to introduce a thermocouple reaching the nozzle tip (figure 3.4). Besides, the nozzle orifices were blocked by welding, so the direct contact between in-cylinder gases and the thermocouple tip was avoided. The geometry of this injector was similar to the one utilized in the study. Thus, it could be expected that the seating on the injector holder and the heat transfer were similar.

Figure 3.4. *A thermocouple introduced in a modified Bosh piezoelectric injector.*

It was estimated that the inside volume of the original injector stored an amount of fuel equivalent to 12 injections. Therefore, the time that the fuel remains inside the injector (considering the low injection rate used in this study) was long enough so its temperature would not be sensitive to instantaneous variations of in-cylinder thermodynamic conditions. This allows using the time-averaged temperature values provided by the thermocouple (due to its low time response) as representative values.

Two different sets of measurements were performed. In the first one, temperature at the nozzle tip was measured for all the operating conditions described in figure 3.2. For each case, the temperature value was registered after it stabilized. Results are summarized in figure 3.5. It is possible to see that the measured values for all operating conditions were between 80 and 150 C degrees higher than the engine cooling water temperature. Besides, there is a clear trend with in-cylinder pressure and temperature. As both magnitudes increase, the temperature measured at the nozzle tip also increases.

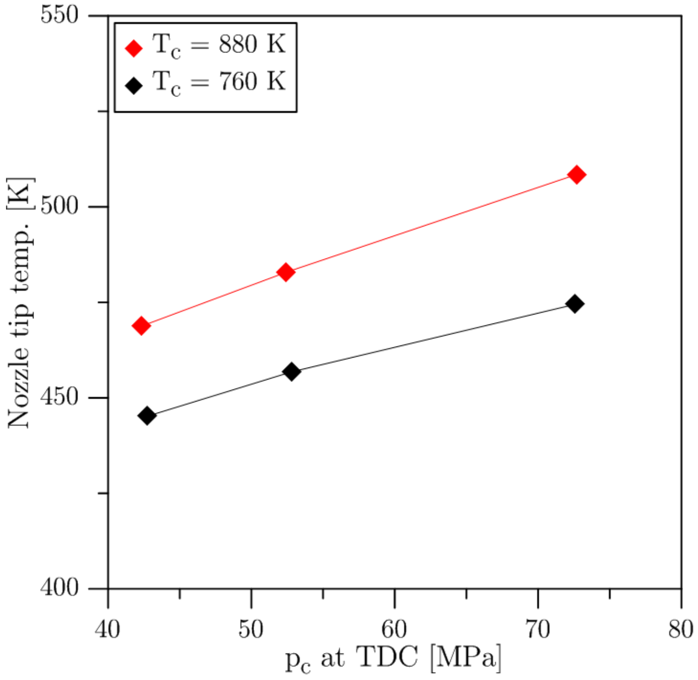

Figure 3.5. *Temperature at the nozzle tip as a function of in-cylinder pressure and temperature at TDC.*

The second set of measurements was focused on analysing the evolution of temperature inside the nozzle. In this case, temperature was registered while the thermocouple was gradually separated from the nozzle tip. As it was described previously, temperature at each point was registered after it stabilized. Results are summarized in figure 3.6. Thermodynamic conditions correspond to $p_c = 4.3\ MPa$ and $T_c = 760\ K$ at TDC. In this figure, it can be observed that the measured temperature decreased when the thermocouple was separated a few millimetres from the nozzle.

This characterization offers relevant information regarding the temperature of the nozzle tip and the injected fuel. On the one hand, it proves that the nozzle tip is heated by the in-cylinder gases, and reaches higher temperatures than that of the engine cooling water. Besides, it has been observed that the nozzle was not uniformly heated despite measured temperatures were close to the one measured at the nozzle tip. Another fact that has to be taken into

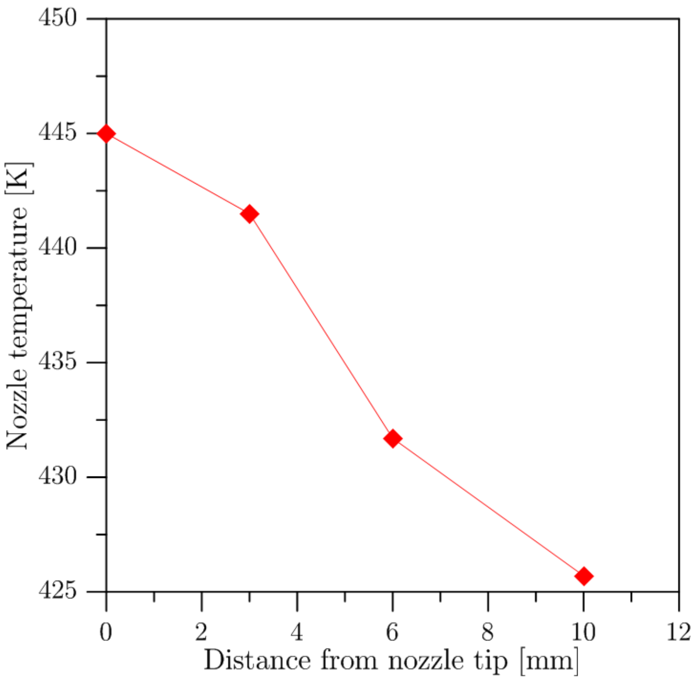

Figure 3.6. *Temperature inside the nozzle as a function of the distance to the nozzle tip.*

account is that the heat transfer within the original injector could be different than for the modified one. The presence of the different components and the fuel could make a difference in this regard. Considering all the foregoing, the temperature values presented in the previous figures should be used with caution. The author considers that they provide an estimation of the real temperature of the nozzle, but it could be different when considering the fuel. Nevertheless, they should be closer to the real values than the engine cooling water temperature.

3.2.4 In-cylinder Airflow

The test rig described in this section has been utilized previously for a wide variety of studies, as it can be found in literature [2, 3, 5–9]. However, in recent years, concerns about the high cycle-to-cycle variability have raised. For example, Payri et al. [3] were the first who analysed in detail and quantified the variability of the flame lift-off length. During the tests that conform the current thesis, a large variability was also observed. Besides, schlieren visualization and the spray penetration results provided more insight into this problem. This technique showed that the in-cylinder gas motion interaction with the spray was not negligible and, moreover, the behaviour seemed to vary from cycle-to-cycle.

Aiming to better understand such fluctuations in the spray behaviour, it was decided to characterize the airflow movement within the combustion chamber by means of *Particle Image Velocimetry* (PIV). This technique is based on measuring the displacement of a cloud of particles between two consecutive images. For this purpose, a pulsed laser is usually employed to create an intense light sheet that illuminates the particles. The scattered light is registered by a CCD camera. A more detailed description of this technique can be found in [10]. The optical set-up is depicted in figure 3.7. A double-head pulsed Nd:YAG (2 lamps) laser was utilized to generate two pulses at 532 nm. The laser beam was guided to the combustion chamber by means of a laser line mirror, while a cylindrical lens (-10 mm focal length) was used to transform the beam into a laser sheet. An spherical lens (1000 mm focal length) was utilized to minimize the beam waist at the region of interest. The light scattered by particles was registered by a CCD camera, working under "frame-straddling" mode [11].

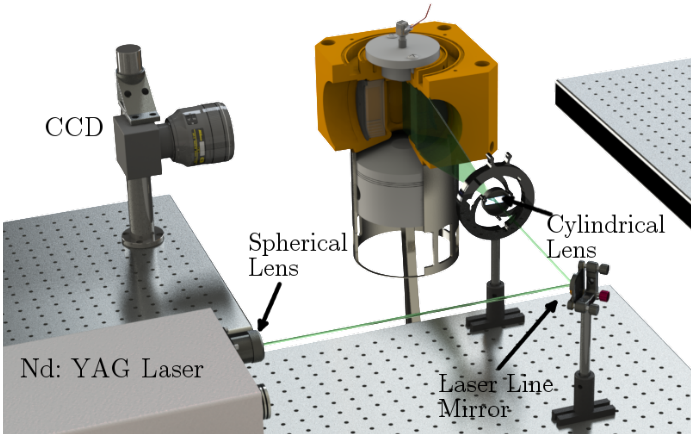

Figure 3.7. *Scheme of the optical set-up utilized for PIV measurements.*

Measurements were performed under thermodynamic conditions corresponding to $\rho_c = 19.27\ kg/m^3$ and $T_c = 760\ K$ at TDC, under non-reactive atmosphere. The air was seeded with test fluid, by means of a long injection performed just after the EVC. After several tests, it was proved that the oil droplets did not evaporate before reaching TDC, contrarily to what occurs when diesel fuel is injected for seeding purposes. Injection pressure was set to 100 MPa, so a good agreement between uniformity and quality of the images was obtained. Taking into account the range of velocities existing in the combustion chamber for the conditions chosen, the two laser pulses were separated 10 μs. Six different planes within the combustion chamber were measured. In figure 3.8, a scheme of the distribution of the region of interest is shown. As it can be observed, two perpendicular planes crossing the injector axis were chosen (labelled as C and CC respectively), together with the corresponding parallel planes separated 10 mm at both sides of the combustion chamber and labelled as L (left), R (right), F (front) and B (back), respectively. Therefore, it was possible to determine not only the flow pattern, but also any possible asymmetry. Measurements were performed between -10 and 15 CAD, with 1 CAD increments. For each plane and CAD, 75 cycles were recorded.

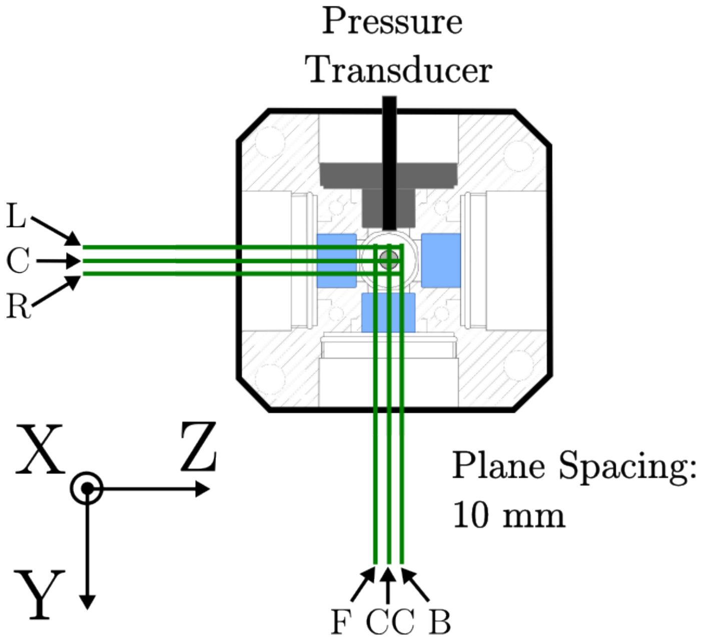

Figure 3.8. *Scheme of the distribution of the PIV measuring planes.*

3.2.4.1 Average flow field

In figure 3.9, velocity fields corresponding to the plane CC are shown. They have been obtained by averaging the velocity magnitude from 75 repetitions. It has been decided to show one plot each 3 CAD, as representative of the global behaviour. The colormap corresponds to the velocity magnitude (i.e. the modulus of the 2D projection of the velocity vector on the measurement plane), while the black lines represent the flow stream lines. As it can be observed, at -10 CAD the airflow is entering into the combustion chamber at almost 30 m/s, whilst at the upper part of the combustion chamber the speed is reduced to 5 m/s approximately. As CAD increases, velocity values decrease but it can be observed that the high speed region moves closer to the nozzle and towards the left part of the combustion chamber. Near TDC it decreases drastically, as expected. However, a clockwise vortex appears on the right part of the combustion chamber, whose rotational velocity is of the same order of magnitude as the airflow in the rest of the combustion chamber. Besides, this vortex seems to move towards the left part of the combustion chamber and disappears as the piston moves down and the outlet flow speed increases.

The evolution shown in figure 3.9 is representative of the average behaviour within the whole combustion chamber. However, differences in magnitude and distributions can be observed between the different measuring planes. For this reason, in figure 3.10 a comparison between the different planes is presented. Only flow fields at -5, 0 and 5 CAD have been included. The main conclusion that can be drawn from this comparison is that the flow field is not symmetric within the combustion chamber. Velocities at L and B are usually higher than at R and F respectively. Moreover, it is possible to see that the vortices which appear at the right part of F and B (0 CAD), are also visible at R (around 10 and -10 mm) but not at L or C. As the piston moves down (5 CAD), these vortices move to the centre of the combustion chamber and appear at C. This confirms the lack of symmetry in both Y and Z directions. However, the asymmetry seems to dilute as the piston approaches TDC.

The main consequence of these observations is that, since the spray is usually injected in the interval between -5 and +10 CAD (see figure 3.2), the spray tip can be slowed down by the airflow and even displaced towards one side of the combustion chamber. Despite low velocities have been measured at 0 CAD (as expected) the air momentum can be high in comparisons with the more diluted parts of the spray (its edges). This effect is discussed in chapter 4.

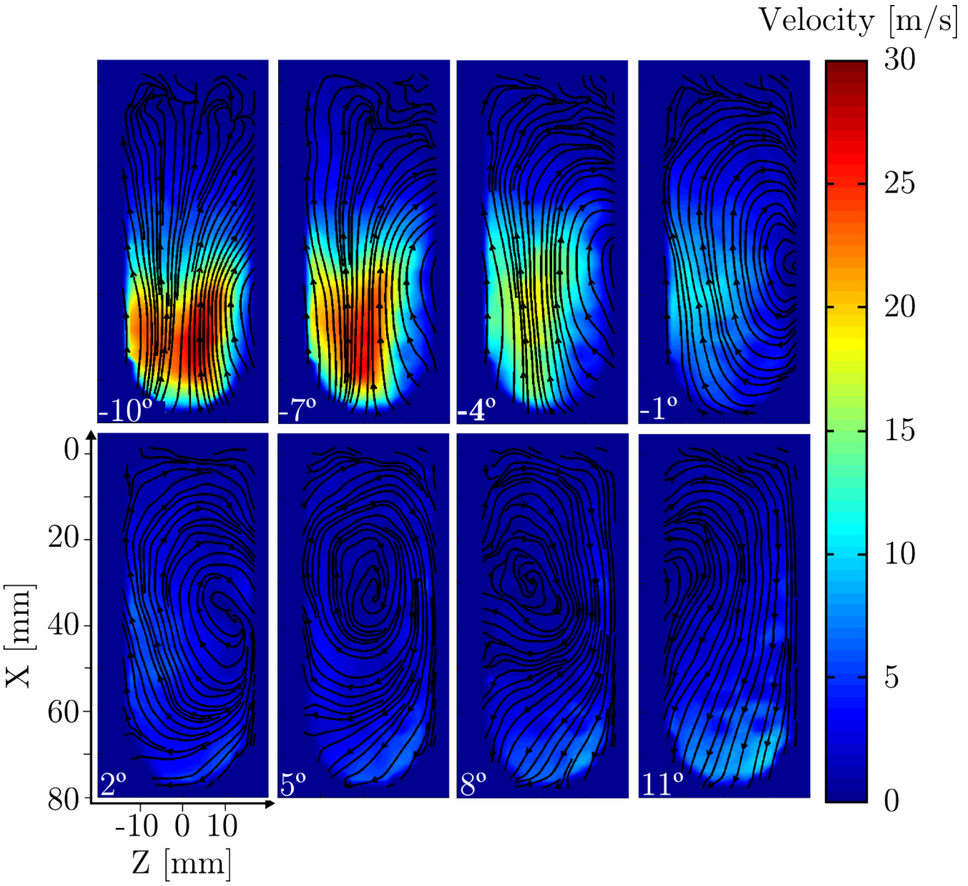

Figure 3.9. *Evolution of the average airflow velocity at plane CC.*

3.2.4.2 Cycle-to-cycle flow field

Images shown previously are the result of averaging 75 repetitions. They provide useful information about the flow distribution but not about the cycle-to-cycle variability. In this regard, standard deviation maps were calculated to quantify this effect. Firstly, it is worth mentioning that the experimental procedure was optimize to minimize measuring uncertainties and their influence over the calculated standard deviations should be small.

It has been distinguished between the velocity magnitude (M), the component aligned with spray axis (U) and the component perpendicular to spray axis (V). Thus, not only variations of the velocity magnitude but also on its direction could be described. In figure 3.11, the evolution of the standard deviation for M, V and U are shown for CC and C planes respectively.

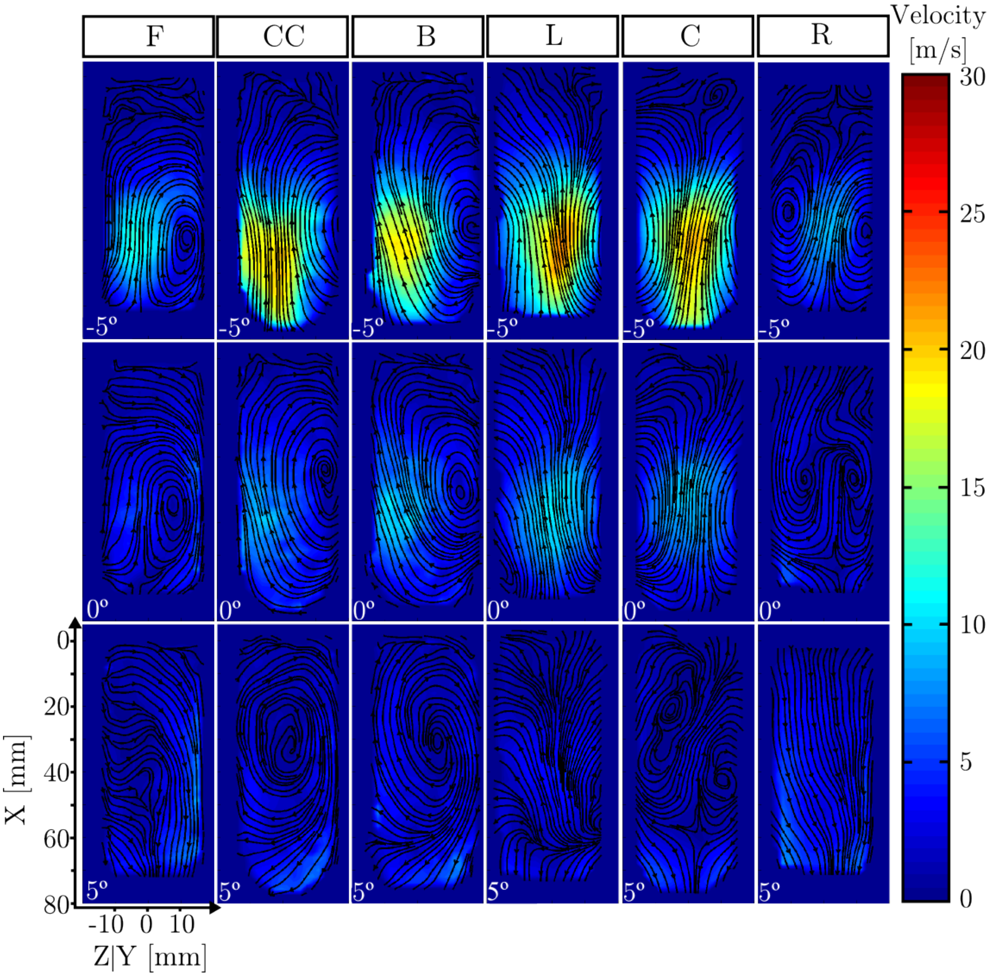

Figure 3.10. *Evolution of the airflow velocity at the 6 measuring planes.*

Between -10 and 0 CAD, M and U show similar values, as the X-axis is the main direction of propagation of the flow. In both cases, it is possible to see that the region of higher deviation moves towards the nozzle when increasing CAD. After 0 CAD, the flow field becomes more uniform and the variability decreases drastically. The deviation of component V is usually higher at the mid-lower part of the combustion chamber, specially during the compression stroke. This suggest that air entrainment into the combustion chamber is different from cycle-to-cycle, which could explain the differences observed in the rest of the combustion chamber. Finally, it has to be noted that the standard deviation reaches local values of the same order of magnitude as the corresponding average velocity.

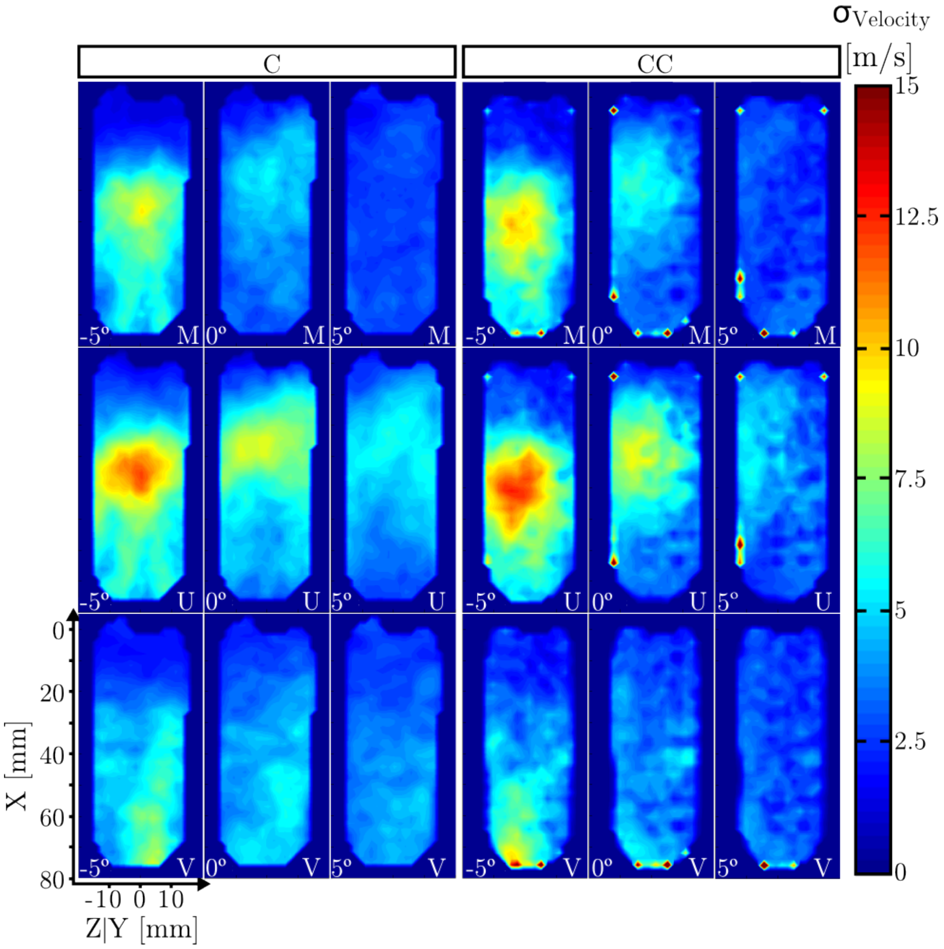

Figure 3.11. Evolution of the airflow standard deviation at C and CC, calculated from 75 cycles.

In order to illustrate the variability of the airflow, a set of single cycle images are shown in figure 3.12 (bottom), together with the corresponding average velocity magnitude and standard deviation (top). The colormap of the single-cycle images corresponds to the velocity magnitude, while the black lines with arrows represents the flow stream lines. Images correspond to plane CC, at -3 CAD (a typical injection location). It can be expected that the large scattering observed would cause variations on spray mixing and combustion development from cycle to cycle. Therefore, this effect should be taken into account for a proper analysis of later measurements.

3.3 Fuels

Two single-component fuels have been used in this study, namely n-Decane (DEC) and n-Hexadecane (HEX), together with two derived binary blends: 50% n-Decane/50% n-Hexadecane (50DEC) and 30% n-Decane/ 70% n-Hexadecane (30DEC). The blending percentages were defined in terms of mass. The main properties of the four fuels are summarized in table 3.3. The simplicity of the molecules considered (n-alkanes[1]) makes them suitable for the analysis and development of experimental tools, as it is the aim of this work.

	Temp. [O°C]	**DEC**	**50DEC**	**30DEC**	**HEX**
Density ρ_f **[kg/m^3]**	30°	723.4	745.3	753.9	767.0
	70°	692.8	716.2	725.4	739.3
	100°	669.2	693.9	703.7	718.5
Dynamic Viscosity μ_f **[mPa $\cdot$ s]**	30°	22.67	24.28	25.08	26.42
	70°	18.65	20.24	21.29	22.35
	100°	15.79	17.51	18.75	19.81
Vapour pressure [Pa]	30°	270	170	80	-
	70°	255	150	94	-
	100°	9.67	5.67	3.66	20
Derived Cetane Number [DCN]	-	65.9	82.8	85.4	92.9
C-C bonds	-	9	11.37	12.56	15
H/C	-	2.19	2.16	2.14	2.12
$(A/F)_{st}$	-	14.984	14.932	14.913	14.882

---

[1] Saturated hydrocarbon molecules, formed only by carbon and hydrogen atoms connected only by simple bonds, which always present non-cyclic forms

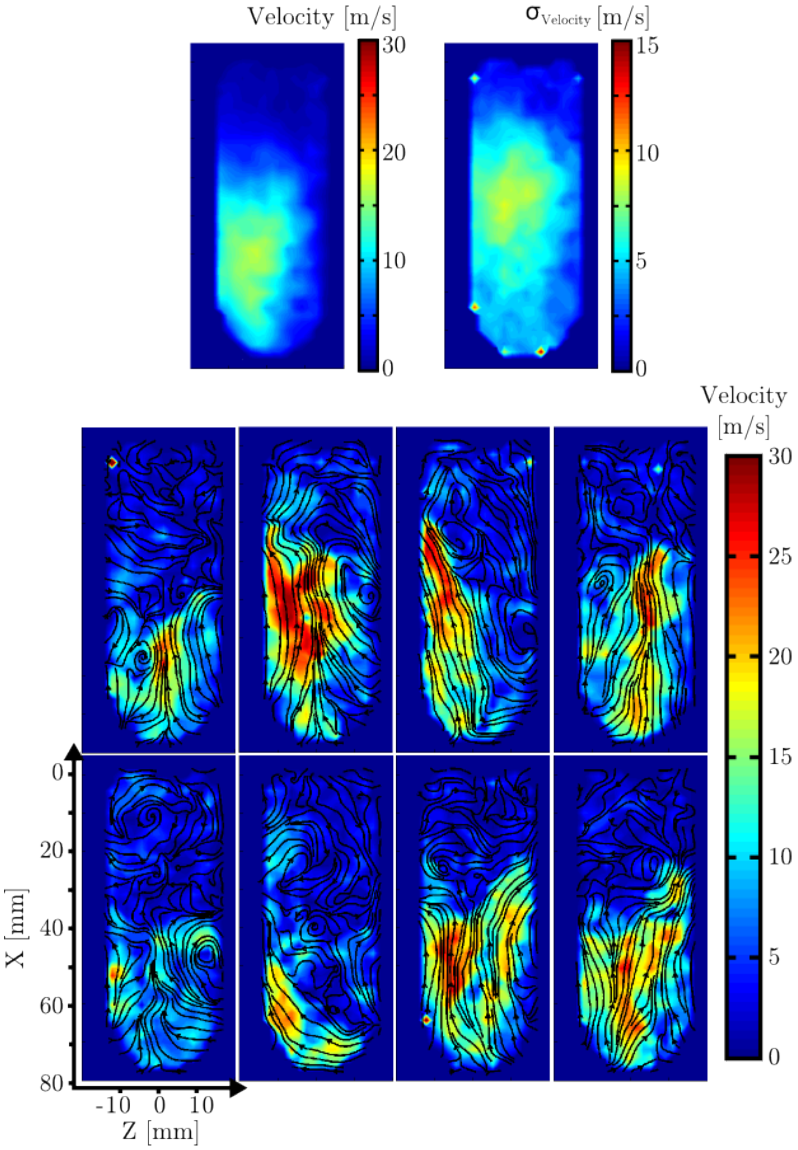

Figure 3.12. *Average and standard deviation of the airflow velocity module (top) at -3 CAD. Airflow velocity magnitude from 8 out of 75 cycles (bottom). Data corresponds to plane CC.*

The different molecule length affects both physical (density, viscosity and vapour pressure) and chemical (derived cetane number) properties. Therefore, some differences can be expected between the four fuels in terms of mixture formation and combustion. Regarding the fuel blends, it can be observed that the physical properties are gradually affected by the increase of HEX fraction. However, DCN shows a different behaviour. Even 50DEC is more similar to 30DEC and HEX than to DEC, despite it is a 50% blend. It suggests that ignition properties are dominated by the most reactive component. This discussion will be addressed in more detail in chapter 5.

With the aim of characterizing the volatility of each fuel, distillation curves were obtained at atmospheric pressure as specified by the ASTM D86-04b [12]. The curves of figure 3.13 show the percentage of the total mixture that was evaporated as the temperature of the fuel was slowly increased. It can be observed that the pure n-alkanes represent the upper and lower limits in terms of volatility, while the two blends are located between them.

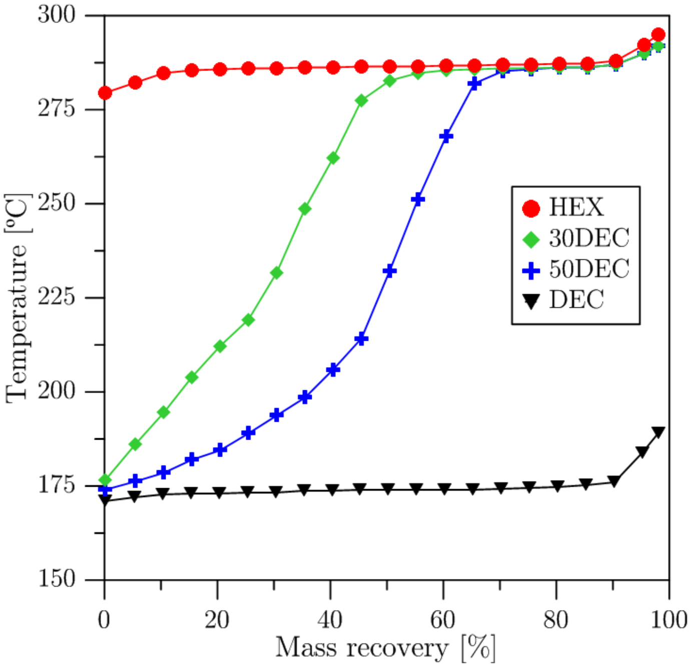

Figure 3.13. *Distillation curves of the four fuels obtained via ASTM D86-04b [12].*

3.4 Injection settings & hydraulic characterization

In the following paragraphs, a description of the injection system is presented. The hydraulic characterization for each of the fuels is included, based on the combination of mass flow rate and momentum flux measurements.

A 2^{nd} generation Bosch injector with piezoelectric actuation of the needle was connected to a standard common-rail from which a pressure transducer was measuring the fuel pressure and permitted its control through a proportional-integral-derivative (PID) system. The injector was equipped with a single-hole nozzle drilled axially. The nominal diameter of the orifice exit was 140 μm, with a conicity factor[2] (K_s) of 1.5. In this way, cavitation effects were avoided. The choice of this type of injector was mostly motivated by the simplicity of the mechanical arrangement necessary to house it in the test rig. Besides, it made it possible to maximize the free spray development (according to the design of the combustion chamber).

3.4.1 Mass flow rate and momentum flux

Mass flow rate ($\dot{m}_f$) measurements were carried out using a commercial Injection Discharge Rate Curve Indicator (IVA Model EVI2). This device measured the chronological sequence of an individual fuel injection event. The measurement of this magnitude has been subject of several Ph.D studies at CMT-Motores Térmicos so only a brief summary is given here. Nevertheless, further details can be found at [13, 14]. The measuring principle is the anechoic tube method [15], which consist of a fuel injector injecting into a fuel-filled measuring tube. Back pressure (p_{back}) is provided with a cavity filled with nitrogen while back pressure oscillations are avoided. The fuel discharge produces a pressure increase inside the tube, proportional to the amount of mass injected. The mass flow rate is related to such pressure increase through an equation derived from the Allievi relationship in stationary fluids:

$$\dot{m}_f = \frac{A_t \cdot \mathit{\Delta} P}{a} \tag{3.1}$$

where A_t is the transversal area of the tube, $\mathit{\Delta} P$ is the pressure increase with respect to the back pressure and a is the speed of sound within the fuel. The speed of sound is calculated through an empirical correlation as a function of temperature, obtained from standard diesel fuel. The mass of fuel injected is

---

[2] The conicity factor is defined as the ratio of the difference between the input and output diameters expressed in μm and a fixed number, 10.

accumulated and measured with a precision scale, so the resulting mass flow rate can be checked.

Measurements of the spray momentum flux ($\dot{\mathrm{M}}_f$) were carried out in a purposely-designed rig [14, 16]. Under a pressurized ambient, the force created by the spray impact on a plate is measured by means of a calibrated piezo-electric pressure sensor. The area of the plate and its position are selected so that spray impingement area is much smaller than the sensor. Under the assumption that the fuel is deflected perpendicularly to the propagating axis, and according to the hypothesis of momentum conservation, the force measured by the sensor is the same as the axial momentum flux at the orifice or at any other axial location when injection is stationary.

The combination of three injection pressures (50, 100 and 150 MPa) and three back pressures (4.3, 5.3 and 7.3 MPa) were tested, according to the table presented in figure 3.2. The energizing time was set to 3000 μs for the whole work, to ensure the stabilization of the mixing and combustion processes. Both $\dot{\mathrm{m}}_f$ and $\dot{\mathrm{M}}_f$ measurements were time-resolved, thanks to the 100 KHz sampling rate utilized. An example of both magnitudes as a function of time is shown in figure 3.14. Data correspond to DEC, 50DEC and HEX, at $p_{inj} = 100\ MPa$ and $p_{back} = 5.3\ MPa$. The origin of the time scale coincides with the start of energizing (SoE), i.e. the instant when the actuation pulse reaches the injector. For all the fuels, a similar delay is observed between SoE and the real start of injection (SoI), which is known as the *hydraulic delay.* It must be highlighted that, despite the energizing signal finishes at 3 ms after SoE (EoE), the injection event lasts around 5.5 ms (EoI). In this case, it is possible to see that the different viscosity of the fuels causes differences on the injector closure, as it has been previously reported by Payri et al. [17].

For such long injections, both $\dot{\mathrm{m}}_f$ and $\dot{\mathrm{M}}_f$ present a “top-hat” profile. Therefore it is possible to calculate a representative time-averaged value. As it is shown in figure 3.14, data has been averaged between 2 and 5 ms for the three fuels and all the test conditions. Accordingly, the results of the whole test matrix is represented in figure 3.15. Firstly, it can be observed that the three fuels present a similar response to ΔP variations. In general, an increase of this parameter either by increasing p_{inj} or reducing p_{back} produces both higher mass flow rate and spray momentum flux. Secondly, regarding the fuel effect it is possible to see that for each p_{inj}, $\dot{\mathrm{m}}_f$ varies between fuels according to their different densities (table 3.3). This is not the case for $\dot{\mathrm{M}}_f$, as no influence of the fuel properties can be detected.

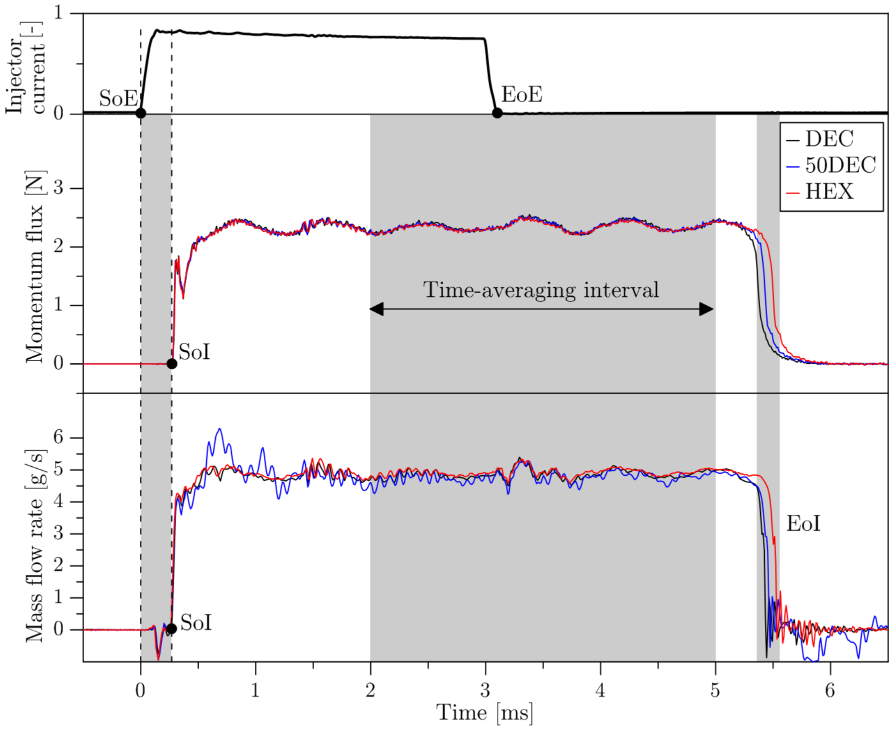

Figure 3.14. *Injector current signal, mass flow rate and momentum flux as a function of time for DEC, 50DEC and HEX, at* $p_{inj} = 100\ MPa$ *and* $p_{back} = 5.3\ MPa$.

3.4.2 Hydraulic characterization

The hydraulic characterization of a nozzle is derived from the association of the mass flow rate (equation 3.2) and spray momentum flux (equation 3.3) [18]. Their combination makes it possible to estimate the effective jet speed at the exit of the orifice and the effective section through which the fuel flows towards the chamber. The effective velocity (u_{eff}) can be related with the theoretical one (from Bernoulli's law) by means of the coefficient of velocity (C_v), as it is described in equation 3.4. In the same way, the effective area (A_{eff}) can be related with the geometric section (A_{geo}) through the coefficient of area (C_a), described in equation 3.5.

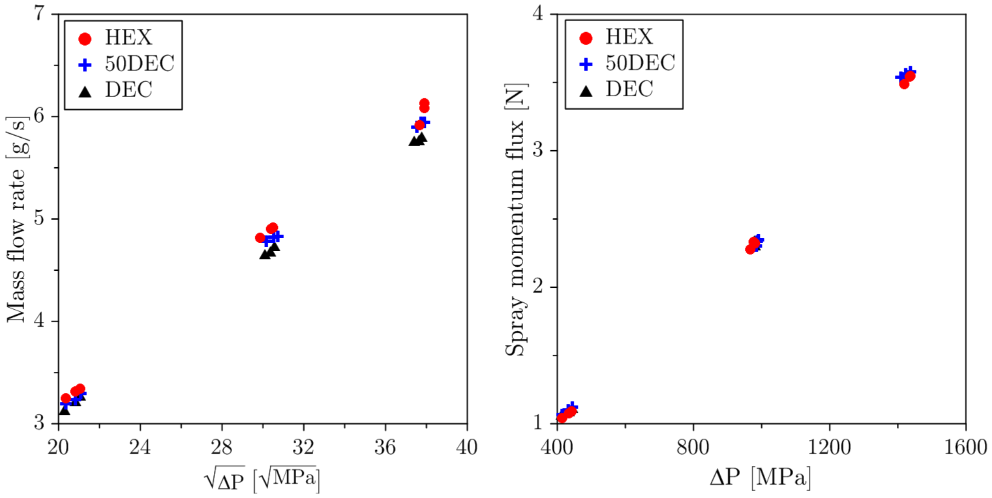

Figure 3.15. *Mass flow rate and momentum flux as a function of ΔP for DEC, 50DEC and HEX.*

$$\dot{m}_{eff} = u_{eff} \cdot \rho_f \cdot A_{eff} \tag{3.2}$$

$$\dot{M}_{eff} = u_{eff}^2 \cdot \rho_f \cdot A_{eff} \tag{3.3}$$

$$u_{eff} = C_v \cdot u_{th} = C_v \cdot \sqrt{\frac{2 \cdot (P_{inj} - P_{back})}{\rho_f}} \tag{3.4}$$

$$A_{eff} = C_a \cdot A_{geo} \tag{3.5}$$

Both virtual magnitudes (A_{eff} and u_{eff}) hypothesize a vector field of velocity at the output orifice of the nozzle, with uniform direction and magnitude and accounts for two main effects. The first one rather occurs at low Reynolds numbers, where velocity gradients are radially significant due to the interaction between the fuel and the wall of the conduct [19]. As the Reynolds number increases, the more important turbulent viscosity reduces such effect and homogenizes the velocity profile up to a point where the second effect, namely cavitation, comes into play. As velocity increases, pressure locally drops down to the fuel vapour pressure, forming “bubbles”. They are dragged by the flow to the nozzle exit and their low density virtually produces a contraction of the exit section.

C_a and C_v include effects of fuel compressibility and variations of both density and viscosity with temperature as it is not possible to isolate and quantify each effect separately. The product of these two coefficients gives the discharge coefficient (C_d), which has been historically used to relate the effective mass flow rate with the theoretical one provided by Bernoulli's principle (equation 3.6). However, some authors use the coefficient of momentum (C_M) to better analyse all the issues associated with that measurement, such as spray penetration or mixing. Its relation with C_a and C_v is presented in equation 3.7.

$$\dot{\mathrm{m}}_f = C_v \cdot C_a \cdot A_{geo} \cdot \sqrt{2\Delta P \rho_f} = C_d \cdot A_{geo} \cdot \sqrt{2\Delta P \rho_f} \tag{3.6}$$

$$\dot{\mathrm{M}}_f = C_v^2 \cdot C_a \cdot A_{geo} 2\Delta P = C_M \cdot A_{geo} \cdot 2\Delta P \tag{3.7}$$

The coefficients resulting from the previous measurements have been plotted in figure 3.16, as a function of the Reynolds number. As it can be observed, in the range considered in this work, minimum variations on both coefficients are observed. The fact that C_d is almost not varying suggests that the differences observed between fuels, in terms of $\dot{\mathrm{m}}_f$, are mainly caused by the fuel density (according to equation 3.6). Besides, the similar momentum flux suggest that no differences should be found between fuels in terms of spray penetration or air-fuel mixture formation [20]. Therefore, only volatility would make the difference. It must be noted that these conclusions are also valid for 30DEC as it presents similar physical properties as the other three fuels.

3.5 One-dimensional spray model

As it has been described in chapter 1, one of the main objectives of this work is the development and validation of an experimental methodology to characterize mixture formation (i.e. UV-VIS LAS). For this purpose, it was decided to draw on the use of spray modelling codes to validate measurements. The most powerful tools in this field are the Computer Fluid Dynamic (CFD) codes. However, as a simplification, one-dimensional (1D) spray models are also usually utilized for the prediction of free spray evolution under quiescent boundary conditions. Different models can be found in literature. For the current study, it has been decided to use a 1D-Model developed at CMT-Motores Térmicos [21], which has been previously utilized for similar purposes in different studies [4, 22, 23].

During recent years, the model has been extended to account for multi-component fuel capabilities [24], which makes it suitable for the current

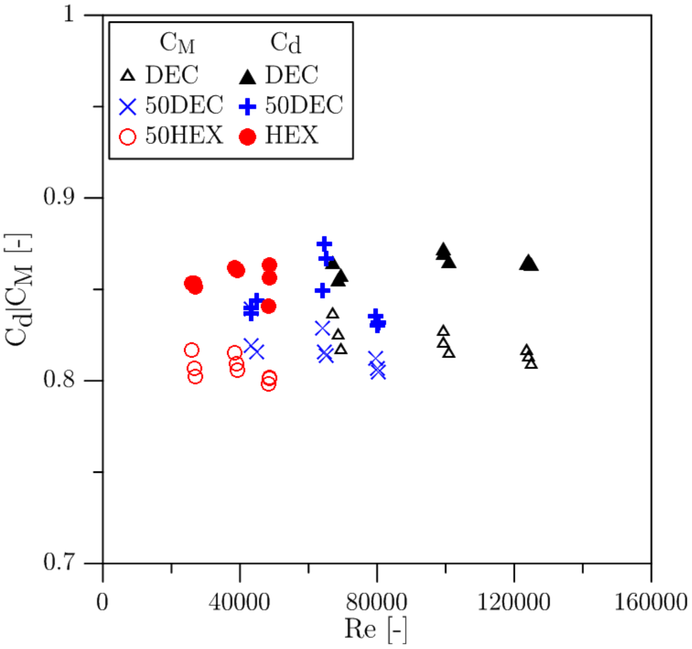

Figure 3.16. *Discharge coefficient and coefficient of momentum as a function of ΔP for DEC, 50DEC and HEX.*

application. Besides, the code calculates a thermodynamic description of the mixture (state relationship), which was also utilized in the UV-VIS LAS processing routine (according to section 4.3.3). Therefore, in the following paragraphs an overview of the model is presented, with emphasis on the state relationship. A more detailed description can be found in [21, 24].

3.5.1 General description of the model

The spray is assumed to be injected into a quiescent air volume, which is large enough so that flow evolution does not modify air conditions far away from the nozzle. Figure 3.17 shows a sketch of the basic configuration of this type of problem. Fuel stream is assumed to have a uniform velocity profile at the nozzle exit. This flow exchanges momentum with the ambient air and sets it in motion, so that it increases in width with the axial distance. The spray cone half-angle $\alpha/2$ defines this radial growth, and it is an input of the model. Together with the nozzle diameter d_0, the spray angle defines the virtual origin $x_0 = d_0/(2\tan(\alpha/x))$. The spray domain is divided axially into a number of cells with certain thickness Δx spanning the whole spray cross section. Each

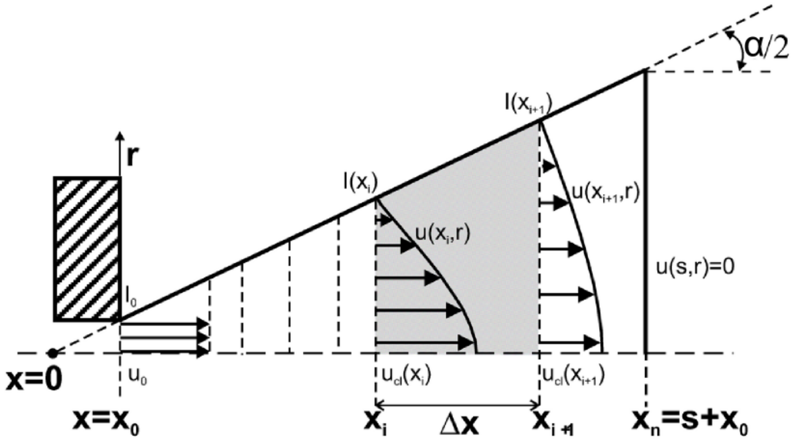

Figure 3.17. *1D-Model description. Source: [24].*

cell is delimited by the inlet and outlet sections (i and i+1, respectively) so that $x_{i+1} = x_i + \Delta x$. At every time instant, the spray size is defined in terms of the tip penetration S, which is the farthest cell from the nozzle where inlet velocity is different from zero and outlet velocity is zero.

The following hypotheses are made:

- Symmetry on the spray axis.
- A fully developed turbulent flow is assumed, which means that self-similar radial profiles can be defined for the conserved variables. In the present approach, a radial Gaussian profile is assumed.
- The spray cone angle is calculated from the spray contour, which is defined as the location where the axial velocity is $\zeta = 1\%$ of the value on the spray axis.
- Turbulent Lewis number is assumed to be equal to 1. Consequently, the local enthalpy can be expressed as

  $$h(x,r,t) = h_{a,\mathrm{inf}} + f(x,r,t)(h_{f,0} - h_{a,\mathrm{inf}}) \tag{3.8}$$

  where $f(x,r,t)$ is the local mixture fraction value and $h_{f,0}$ and $h_{a,\mathrm{inf}}$ are the enthalpy of the pure fuel (nozzle outlet conditions) and pure air (far away from nozzle), respectively. This relationship is independent of the general flow calculations, so that state relationship can be calculated a priori.

- Pressure is assumed to be constant all over the spray.
- Locally homogeneous flow is assumed, i.e., local equilibrium exist both in thermal and velocity conditions.

Conservation equations of axial momentum and fuel mass are formulated for each cell (figure 3.17). To solve them, a definition of local density has to be made. Formally, this is expressed as a function of the type $\rho = g(f)$, which falls into the category of so-called state relationships. In a more general way, such relationships define the local composition, temperature, and density of the spray in terms of mixture fraction (f), by means of an ideal adiabatic mixing process of pure fuel stream (nozzle conditions) and pure air. These boundary conditions can be considered either constant or variable with time. The calculation of the state relationships is independent of the solution of flow conservation equations.

These relationships are utilized to solve conservation equations at each cell, to obtain on-axis velocity and mixture fraction from which radial profiles can be defined. The required information consists on momentum ($\dot{\mathrm{M}}_0$) and mass ($\dot{\mathrm{m}}_0$) fluxes at the nozzle exit, and the radial integration of radial profiles coupled to the local density. To calculate such integrals, the spray cone angle (α) is needed as well as local density (ρ), which is obtained from state relationship. Eventually, once the mixture fraction f is obtained at one location, local temperature, density and composition can be calculated from state relationships.

3.5.2 State relationships for inert vaporizing sprays

The state relationship consists of composition (Y_i), temperature (T), and density (ρ) tabulations as a function of mixture fraction (f). To calculate these dependencies, the following general procedure is followed:

1. The main underlying assumption is that the mixture state corresponds to the result of an adiabatic mixing process. For inert sprays, this hypothesis results in:
    (a) Local mixture enthalpy is calculated by means of equation 3.8
    (b) Local composition can be obtained from the mixture fraction as:

$$Y_i = Y_{i,\mathrm{inf}} + f \cdot (Y_{i,0} - Y_{i,\mathrm{inf}}) \tag{3.9}$$

where Y_i is the mass fraction of species i in the mixture, when adding contribution of both liquid an vapour phases.

2. To define the local composition, the contribution of both liquid (Y_i^L) and vapour/gas (Y_i^V) phases to each of the components has to be found, with $Y_i = Y_i^L + Y_i^V$. If the mixture is in a single-phase region, the solution is trivial ($Y_i = Y_i^V$). In the liquid-vapour region, the spray is assumed to be in adiabatic saturation conditions, and therefore liquid and vapour phase conditions are those of bubble and dew curves, respectively. This requires a calculation of the L-V equilibrium, which can be found in detail in [24]. In practice, local composition for each phase is obtained from L-V flash calculation as a function of pressure, local temperature and mixture fraction.

3. A real-gas mixture is assumed by means of the following equation:

   $$h(T,f) = \sum_i Y_i \cdot \overline{h}_i(T) \tag{3.10}$$

   where $\overline{h}_i$ is the partial enthalpy of component i in the mixture. The partial enthalpy of each component is obtained by means of equation

   $$\overline{h}_i = h_i^0 - RT^2 \left(\frac{d \ln \hat{\phi}_i}{dT} \right)_{p,x_i} \tag{3.11}$$

   where h_i^0 is the perfect gas enthalpy, and $\hat{\phi}_i$ is the fugacity coefficient of component i in the mixture.

4. In the single-phase region of the spray, where composition is fully defined, local temperature is the only unknown when equating enthalpy from equation 3.8 to the real gas mixture enthalpy in equation 3.10. In the two-phase region, L-V equilibrium is coupled to the enthalpy calculation to fully resolve both temperature and composition for each phase.

5. Once temperature and composition are known, mixture density can be obtained by means of equation

   $$\frac{1}{\rho} = \frac{\sum_i Y_i^L}{\rho^L} + \frac{\sum_i Y_i^V}{\rho^V} \tag{3.12}$$

   where ρ^L and ρ^V are the liquid and vapour phase densities, respectively, which are obtained from local temperature, pressure, composition, and compressibility factors for each phase.

The previous formulation is valid for any equation of state (EoS), from which the following necessary parameters can be derived:

- Fugacity coefficient for each component
- Departure term in the real enthalpy calculation, i.e. $\left(d\ln(\hat{\phi}_i)/dT\right)_{p,x_i}$ in equation
- Compressibility factors of both phases

The model considered in this work utilizes the Peng-Robinson equation of state for both liquid and vapour phases. Detailed expressions can be found in [24].

3.6 Summary & conclusions

In this chapter, global methodology followed in this thesis has been outlined and all the tools used in the realization of this study have been presented. The experimental resources have been described, paying special attention on defining in detail the boundary conditions of the different test points. The main characteristics of the test-rig have been described together with the thermodynamic conditions in the combustion chamber. Besides, a detailed description of the airflow has been presented, which should be considered for the analysis of results. The most relevant properties of the fuels used in this study have been presented, as well as the corresponding main injection parameters. Finally, a spray mixing 1D-Model has been described, which has been used in chapter 4 to validate experimental results. Special attention has been paid on the state relationship, as it is required to apply the UV-VIS LAS technique. The description of the optical techniques, whose development was a target of this thesis, and the optical arrangements that have been used for the different parts of the research work are included in the following chapters.

Bibliography

[1] Bermúdez V., García J.M., Juliá E. and Martínez S. “Engine with optically accessible cylinder head: A research tool for injection and combustion processes”. *SAE Technical Papers*, 2003.

[2] Nerva J-G. *An assessment of fuel physical and chemical properties in the combustion of a Diesel spray.* Doctoral Thesis, Universitat Politècnica de València, Departamento de Máquinas y Motores Térmicos, 2013.

[3] Payri F., Pastor J.V., Nerva J.-G. and García-Oliver J.M. “Lift-Off Length and KL Extinction Measurements of Biodiesel and Fischer-Tropsch Fuels under Quasi-Steady Diesel Engine Conditions”. *SAE International Journal of Engines*, Vol. 4 n^o 2, pp. 2278–2297, 2011.

[4] Payri R., García-Oliver J.M., Bardi M. and Manin J. “Fuel temperature influence on diesel sprays in inert and reacting conditions”. *Applied Thermal Engineering*, Vol. 35 n^o 1, pp. 185–195, 2012. cited By 18.

[5] Payri F., Pastor J.V., García-Oliver J.M. and Pastor J.M. “Contribution to the application of two-colour imaging to diesel combustion”. *Measurement Science and Technology*, Vol. 18 n^o 8, pp. 2579–2598, 2007.

[6] Pastor J.V., Payri R., Gimeno J. and Nerva J.G. “Experimental study on RME blends: Liquid-phase fuel penetration, chemiluminescence, and soot luminosity in diesel-like conditions”. *Energy and Fuels*, Vol. 23 n^o 12, pp. 5899–5915, 2009.

[7] Pastor J.V., García-Oliver J.M., Nerva J.-G. and Giménez B. “Fuel effect on the liquid-phase penetration of an evaporating spray under transient diesel-like conditions”. *Fuel*, Vol. 90 n^o 11, pp. 3369–3381, 2011.

[8] Juliá J.E. *Medida de concentraciones de combustible en chorros diesel mediante técnicas de fluorescencia inducida por láser.* Doctoral Thesis, CMT-Motores Térmicos, Universitat Politècnica de València, 2003.

[9] García-Oliver J. M. *Aportaciones al estudio del proceso de combustión turbulenta de chorros en motores diesel de inyección directa.* Doctoral Thesis, Universitat Politècnica de València, Departamento de Máquinas y Motores Térmicos, 2004.

[10] Zhao H. *Laser Diagnostics and Optical Measurement Techniques in Internal Combustion Engines.* SAE International, Warrendale, 2012.

[11] “How Frame-Straddling works”. *Information available at http://www.tsi.com.*

[12] “Standard Test Method for Distillation of Petroleum Products at Atmospheric Pressure”. *Information available at http://www.astm.org.*

[13] Payri R., Salvador F.J., Gimeno J. and Bracho G. “A new methodology for correcting the signal cumulative phenomenon on injection rate measurements”. *Experimental Techniques*, Vol. 32 n^o 1, pp. 46–49, 2008.

[14] Gimeno J. *Desarrollo y Aplicación De La Medida Del Flujo De Cantidad de Movimiento De Un Chorro Diesel.* Doctoral Thesis, Universidad Politècnica de València, Departamento de Máquinas y Motores Térmicos, 2008.

[15] Bosch W. “The fuel rate indicator: A new measuring instrument for display of the characteristics of individual injection”. *SAE Technical Papers*, 1966.

[16] Desantes J. M., Payri R., Salvador F. J. and Gimeno J. “Measurements of Spray Momentum for the Study of Cavitation in Diesel Injection Nozzles”. *SAE Technical Paper*, 03 2003.

[17] Payri R., García A., Domenech V., Durrett R. and Plazas A.H. "An experimental study of gasoline effects on injection rate, momentum flux and spray characteristics using a common rail diesel injection system". *Fuel*, Vol. 97, pp. 390–399, 2012.

[18] Payri R., García J.M., Salvador F.J. and Gimeno J. "Using spray momentum flux measurements to understand the influence of diesel nozzle geometry on spray characteristics". *Fuel*, Vol. 84 n^o 5, pp. 551–561, 2005.

[19] Bracho G. *Experimental and theoretical study of the direct diesel injection process at low temperatures.* Doctoral Thesis, Universitat Politècnica de València, Departamento de Máquinas y Motores Térmicos, 2011.

[20] Kook S. and Pickett L.M. "Liquid length and vapor penetration of conventional, Fischer-Tropsch, coal-derived, and surrogate fuel sprays at high-temperature and high-pressure ambient conditions". *Fuel*, Vol. 93, pp. 539 – 548, 2012.

[21] Pastor J.V., López J. J., García J.M. and Pastor J.M. "A 1D model for the description of mixing-controlled inert diesel sprays". *Fuel*, Vol. 87 n^o 13-14, pp. 2871–2885, 2008.

[22] López J. J., García-Oliver J.M., García A. and Domenech V. "Gasoline effects on spray characteristics, mixing and auto-ignition processes in a {CI} engine under Partially Premixed Combustion conditions". *Applied Thermal Engineering*, Vol. 70 n^o 1, pp. 996 – 1006, 2014.

[23] Payri F., Payri R., Bardi M. and Carreres M. "Engine combustion network: Influence of the gas properties on the spray penetration and spreading angle". *Experimental Thermal and Fluid Science*, Vol. 53, pp. 236–243, 2014. The concentration of the second component was gradually increased so the absorption coefficient should also increase.

[24] Pastor J.V., Garcia-Oliver J.M., Pastor J.M. and Vera-Tudela W. "One-Dimensional diesel spray modeling of multicomponent fuels". *Atomization and Sprays*, Vol. 25 n^o 6, pp. 485–517, 2015.

Chapter 4

Evaporation and mixture formation

Contents

4.1 Introduction

As it was described in chapter 2, the evaporation and air-fuel mixture formation control the latter development of the diesel combustion. For this reason, the study of these phenomena is considered as an important step to describe the evolution of all processes and reactions that take place inside the cylinder, during the injection and combustion of a DI diesel spray.

The UV-VIS LAS technique has been proposed to determine the fuel vapour distribution, according to the advantages that it offers in comparison to other techniques (like Raman scattering or PRS). The application of this technique has been usually linked to the use of fuels with appropriate optical properties (i.e. high absorption coefficient in the UV range), but which are not commonly employed as surrogates fuels. In contrast, the fuels considered for this work (n-alkanes) have been traditionally used as surrogates (due to its simplicity), but their optical properties are not the most suitable for research purposes. Therefore, experimental procedure needs to be optimized. In this regard, a large portion of the chapter has been dedicated to the analysis and optimization of the UV-VIS LAS technique, to obtain the most accurate and reliable data from the fuels used in this work. A macroscopic characterization has been also included to complement the study, which provides a more basic description of the evolution of both liquid and vapour phases, to help understanding the results obtained regarding fuel vapour distribution.

The chapter begins with the macroscopic characterization of the spray, from the evolution of the liquid phase to the vaporized spray and its penetration into the combustion chamber. Then, a more detailed description of the air-fuel mixture is presented thanks to the UV-VIS LAS measurements. All the experimental tools, methodology and fuel properties have been described in chapter 3. Therefore, in the following paragraphs, only the optical techniques and the corresponding configurations are described.

4.2 Macroscopic Spray characterization

The macroscopic approach is a common way to address the study of the evaporation and mixture processes of a diesel spray. Obtaining the geometrical parameters that best define the jet (both liquid and vapour phases) allows describing its behaviour and the influence of different operating conditions [1, 2]. In this way, this study provides a first approach to the air-fuel mixing problem. However, at the same time, it makes it possible to link the injection characteristics with the fuel distributions that are presented in the next section.

4.2.1 Liquid phase visualization

The elastic interaction between light and liquid droplets has been traditionally used to visualize this portion of the spray. As it has been discussed in chapter 2, the most common techniques that can be found in literature are Backlight Illumination (BL) and Mie scattering (MIE) visualization. Despite the terminology usually employed, both techniques are based on the same phenomenon: elastic scattering of light by fuel droplets. In wave optics, this interaction is described by the Mie theory, which is a particular solution (Lorentz-Mie solution) to Maxwell's equations and quantifies the light scattered by spherical particles, whose size is at least one tenth of the incident wavelength.

If a liquid droplet is introduced between the light source and the detector, the scattering phenomenon would cause that less light arrives to the detector. Thus, a shadow will be generated by the droplet, while the rest of the field of view (without liquid droplets) will be not affected. When a cloud of droplets is considered (as the liquid spray), the Mie scattering will generate a shadow, equivalent to the projected area of the cloud. This is the basis for BL application. In contrast, if the detector is not positioned in the direction of propagation of light, no signal will be measured unless light is deviated. In this way, if a droplet interacts with light, it will be scattered in all directions and part of the light will arrive to the detector. Thus, if the portion of light is intense enough, it is possible to visualize a cloud of droplets like the liquid part of the diesel spray.

In the work presented here, the two aligned optical accesses were used for schlieren imaging whilst the third one, perpendicular to the others, was used to register simultaneously the light scattered by droplets in the Mie regime, as in [3].

4.2.2 Vapour phase visualization

Schlieren visualization has been chosen for the macroscopic characterization of the vapour phase of the spray, as it is one of the most common optical techniques that can be found in literature for this purpose. Its simplicity and sensitivity make it an option preferable to others (e.g. PLIF). The technique is based on the deviation suffered by a light beam, due to its refraction when crossing from one media to another, with different refractive index. This effect is known as *beam steering.* If a continuous non-homogeneous media is considered, the variation of the refractive index is represented by its gradient. Thus, it can be demonstrated that the deviation suffered by a light beam while traversing this media is proportional to the refractive index gradients within it [4].

For air and other gases, a linear relationship can be found between the gas density and its refractive index. For this reason, in the combustion chamber of a DI diesel engine, the fuel injection generates density gradients and the consequent refractive index gradients. If the spray is illuminated with a uniform collimated light beam, these gradients will bend rays' trajectories, generating a shadowgram. The direct visualization of this shadowgram is usually called *shadowgraphy.* However, sensitivity of this phenomenon is usually not enough for the study of diesel spray evaporation. For this reason, it is necessary to resort to *schlieren visualization.* While shadowgraphy only requires the use of a collimated light source, schlieren presents a more complex optical set-up that makes it possible to increase the sensitivity of the technique. In summary, it can be said that shadowgraphy is sensitive to the displacement of light rays caused by the deflection angles associated to the refractive index gradients, while schlieren is sensitive to the deflection angles themselves.

A generic schlieren system is depicted in figure 4.1. It is formed by a light source, a collimating lens, a collecting lens, a knife-edge located at the focal plane of the collecting lens and a focusing lens. The basis of any schlieren system is that the light-source and knife-edge plane, as well as the test-area and the screen plane, form sets of conjugate optical planes. In this way, what appears in one also appears undistorted in the other (with a possible scale transformation). In the ideal case, the collimated light beam would be generated by a point light source, located at the focal distance of the collimating lens. However, this is not possible in practice, as the light source will present finite dimensions no matter how small it is. The main implication is that in these "collimated" light beams, the light rays are not parallel. Every point of the test area is illuminated by countless rays within a cone angle, limited by the physical dimensions of the light source. Besides, all light crossing each point of the test area will form an image of the light source at the knife-edge plane. Therefore, a composite image of the light-source is formed at this plane which is the result of the superposition of "weaker" elementary images of it. As a consequence, if the test area is blocked with a pinhole, an image of the light source at the knife-edge plane will still be formed, but with much less intensity than the original one.

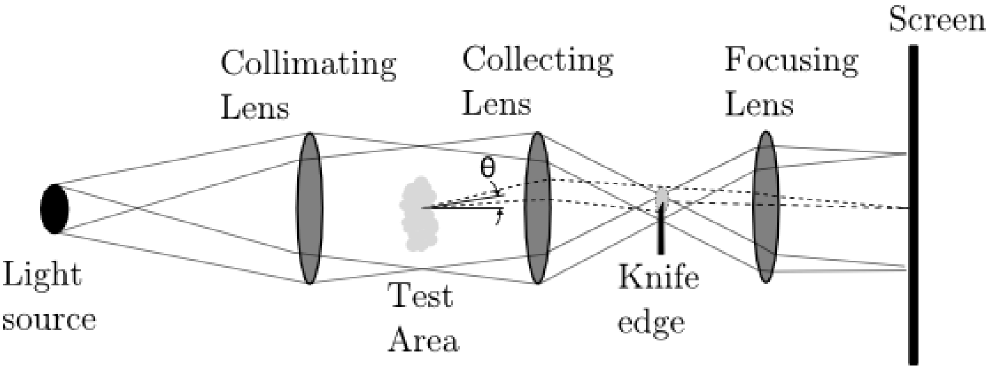

Figure 4.1. *Diagram of a generic schlieren system with a real light source. Source: Settles [4].*

If light traverses a media without refractive index gradients, all the elementary images of the light source will be formed at the same position. Therefore, the knife edge will cut all elementary images equally, and the image on the screen will darken uniformly. However, when a bundle of light rays suffers refraction (dashed lines), they are deviated with the angle θ. They still form an elementary image of the light source at the knife-edge plane, but displaced from the original one due to the refraction effect. Despite this displacement, any bundle of rays coming from the test area will be focused at the same relative position at the screen, thanks to the focusing lens. Therefore, the system provides a way to spatially separate deviated and not-deviated light rays at the knife-edge plane. Moreover, for a certain position of the knife edge, each bundle of deviated light rays is marked with a different amount of cutoff and then recombined at the screen plane, yielding a variation of luminosity with respect to the background. In fact, here resides the major difference when comparing this system to an ideal point light source[1]. In this case, the image of the point light source (at the knife-edge plane) could not be partially marked by the cutoff, obtaining a binary schlieren image instead of a grey scale. It can be concluded that the consequence of the light source not being a point source is a smooth schlieren image. In the same way, it can be stated that the smaller the light source, the sharper the schlieren image.

---

[1] It has to be considered that, ideally, a point is an elementary unit without any dimensions

4.2.3 Optical Set-up

The use of a single hole nozzle made it possible to take advantage of all the optical accesses available in the engine and visualize simultaneously the liquid and the vapour phases, without requiring complex techniques like UV-VIS LAS or Exciplex PLIF. For this reason, a single optical set-up was employed, which represents a real advantage in comparison with previous studies carried out at the same test rig [1, 2]. The experimental arrangement is depicted in figure 4.2.

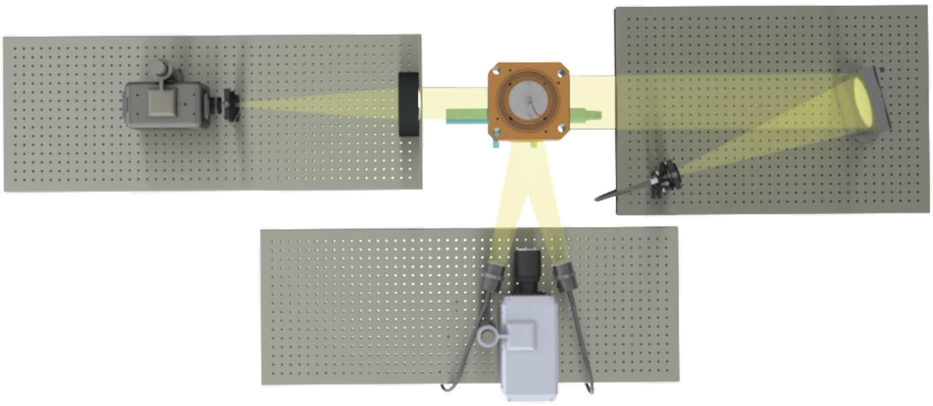

Figure 4.2. *Representation of the optical set-up utilized for schlieren and MIE visualization.*

A more detailed depiction of the schlieren system is presented in figure 4.3. An off-axis single-mirror set-up was utilized, through the two aligned optical accesses. A 150 mm diameter parabolic mirror created the collimated light beam, from a light source located at its focal length (610 mm). The light was generated by a continuous broadband 150 W Halogen Lamp and conducted with a liquid light guide (8 mm diameter) to the desired position. A diaphragm was placed at the output of the guide, to control the diameter of the resulting light source. As it can be seen in figure 4.2, at the other side of the combustion chamber, a 150 mm diameter lens was positioned to collect the outgoing light. A second diaphragm was located at the focal distance of this lens (the knife-edge plane). The rounded geometry of the cutting element was chosen so light deviated in any direction was removed. Finally, the light was registered by a high-speed CMOS camera Phantom V12.1. It was set to record at 34000 fps and 160x512 pixels resolution, with 1 μs exposure time. The camera was equipped with a photographic lens, with $f/\# = 1.8$ and 50 mm focal length.

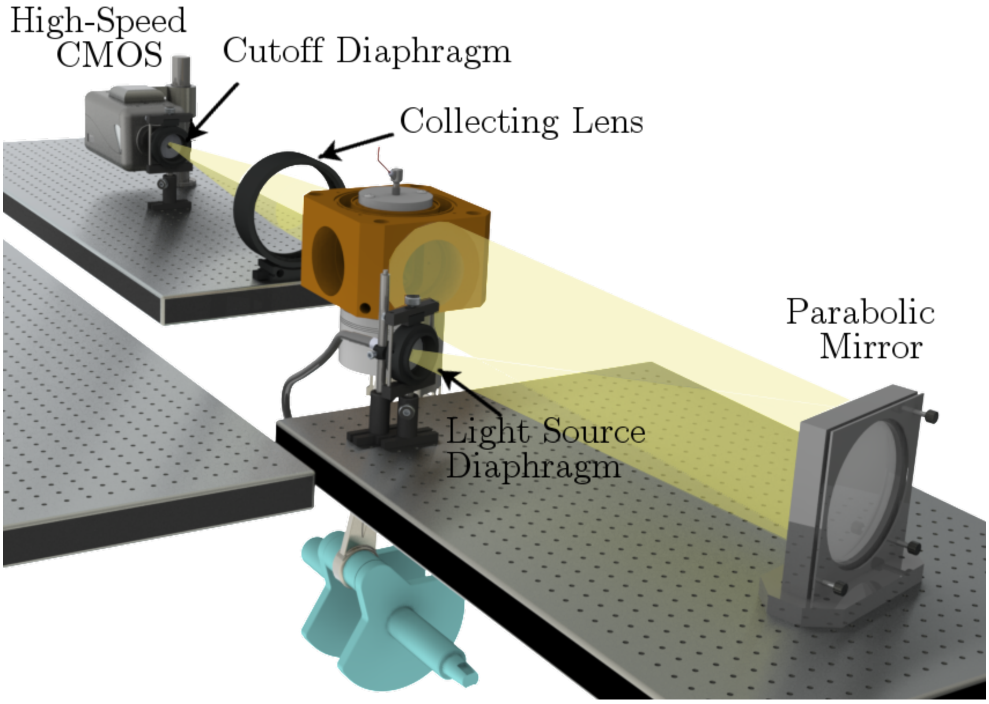

Figure 4.3. *Depiction of the optical set-up utilized for schlieren visualization.*

The aperture of both diaphragms can control the sensitivity of the technique. On the one hand, the cutoff diameter (ϕ_{CO}) directly affects the amount of deviated light rays that arrive to the camera and thus, the intensity with which the regions of the test area that are affected by beam steering are reconstructed. On the other hand, the light-source diameter (ϕ_{LS}) determines the total amount of light arriving to the detector and the efficiency of ϕ_{CO}. A study of the influence of these diameters was performed to optimize the optical set-up. A comparison between different combinations is presented in figure 4.4. It can be observed that, as expected, a decrease of ϕ_{CO} increases drastically the sensitivity of the technique. For $\phi_{CO} = 6\ mm$, the sensitivity is too low as it is even difficult to detect the fully vaporized part of the spray. As this diameter is reduced, this part becomes darker and, in consequence, more visible. In terms of ϕ_{LS}, the images suggest that it affects the sensitivity of the schlieren system to ϕ_{CO}. The effect of varying this diameter is lower for $\phi_{LS} = 6\,mm$ than for $\phi_{LS} = 2\,mm$.

One could consider that the maximum sensitivity has to be pursued always. However, for the current application, this would not be the best solution. For example, if the combination of $\phi_{LS} = 2$ mm and $\phi_{CO} = 2$ mm is observed, it is possible to see that even the density gradients caused by the in-cylinder air movement are detected, and it is difficult to distinguish them from the spray. This suggest that, when working with a test rig like the one utilized in this work, the user has to look for a compromise to get enough sensitivity to properly characterize the spray without detecting the "air structures". For this reason, the values $\phi_{CO} = 4\,mm$ and $\phi_{LS} = 2\,mm$ were chosen for this study. This configuration still allowed detecting "air structures", but most of them were removed by the processing routine.

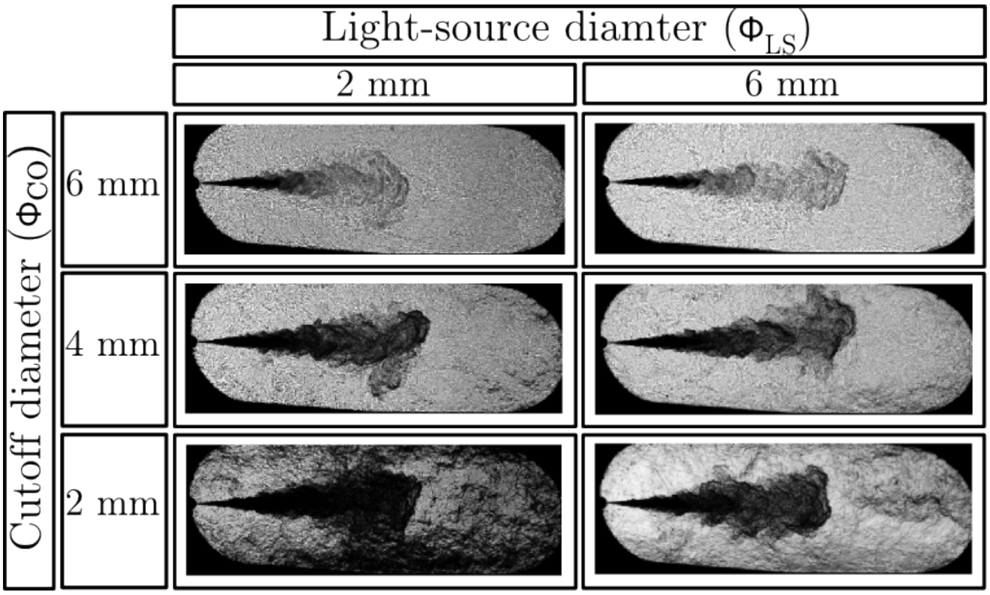

Figure 4.4. *Comparison between different combinations of ϕ_{CO} and ϕ_{LS}. Images correspond to DEC at 1500 μs aSoE, $\rho_c = 23.41\,kg/m^3$ at TDC and $p_{inj} = 100\,MPa$.*

As it has been depicted in figure 4.2, MIE visualization was performed through the remaining access of the cylinder head. A more detailed depiction of the optical set-up is presented in figure 4.5. Two continuous broadband light sources (300 W Xenon Arc Lamp) were utilized, connected to the respective liquid light guides (8 mm diameter). Each guide was coupled to a collimator, which minimized light spreading and ensured the maximum light intensity at the region of interest. Light beam direction was tilted in reference to the camera to avoid reflections from the quartz window of the optical access. For this reason, two light sources were necessary to minimize the shadows generated by the liquid core of the spray, which would difficult the latter image processing. Light scattered by fuel droplets was registered by a high-speed CMOS camera Photron SA5, recording at 30000 fps with 196x576 pixels resolution and 33 μs exposure time. The camera was equipped with a photographic lens, with $f/\# = 2.8$ and 24-70 mm focal length. It has to be noted that the exposure time is more than 30 times larger than the one used for schlieren visualization. This is due to the low intensity of the scattered signal, in comparison with the intensity of the background light of the other technique. However, this is an advantage as it ensures that for this type of optical configuration, schlieren images will be almost not contaminated with the light used for the MIE arrangement (and scattered by droplets).

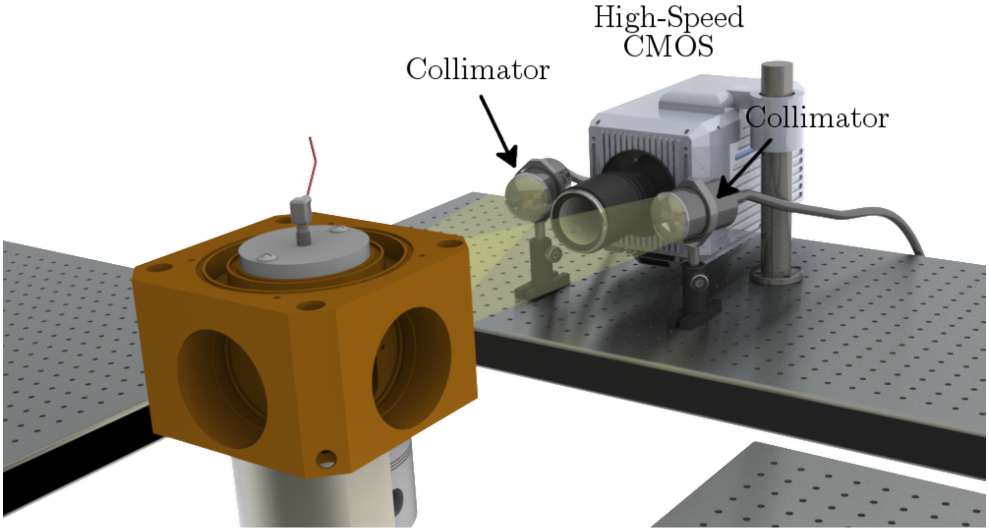

Figure 4.5. *Depiction of the optical set-up utilized for MIE visualization.*

4.2.4 Geometry analysis

In order to determine the most relevant parameters of the spray geometry, firstly the contour of the spray has to be defined. For this purpose, a spray-background segmentation algorithm was implemented as part of the digital processing routine. Different segmentation strategies can be found in literature for diesel spray images. However, the best compromise between results and computational costs are obtained with statistical methods of pattern recognition and classification [5]. The methodology followed in this work is based on the *log-likelihood ratio test* (LRT), which has been described in detail in appendix 4.A.

A time sequence of both MIE (left) and schlieren (right) images is shown in figure 4.6. In the first case, the spray corresponds to the brightest area within the combustion chamber, while for the second one the spray is the darkest region within the combustion chamber. For both techniques, specially schlieren, the background region is not uniform and presents noise, which can interfere in the segmentation process. For this reason, a background reference image was always calculated and subtracted from all the images. It has to be noted that, in the case of schlieren visualization, the spray images were subtracted from the background reference. In this way, the resulting images presented the spray as the brightest area, while the background was dark (more similar to MIE). This is important for the application of the LRT algorithm, as one of the hypothesis on which it is based is that the background levels are located at the lowest part of the digital-level histogram.

Each spray image is segmented according to the optimum threshold obtained with the LRT. The result is a binary image in which pixels belonging to the spray are distinguished from those which are part of background. However, despite using the optimum threshold, the binarized images usually present some noise, which corresponds to the existence of certain regions/pixels of background that cannot be distinguished form the spray in terms of digital levels. It usually appears scattered and separated from the spray area, which makes it possible to filter it out using mathematical morphology analysis and *pixel connectivity* [6, 7] criterion. Thus, the class (spray or background) of each pixel is finally determined according to their neighbours. Then, once the spray is segmented, it is possible to identify its edge. In figure 4.6, the contour detected for both MIE (left) and schlieren (right) images is represented by the red points.

The analysis of the spray contour makes it possible to characterize its geometry. In this regard the most interesting metrics are:

- *Spray cone angle* (α): It is calculated as the angle formed by two regression lines, fitted to each half of the spray contour (divided by the spray axis). They are calculated by applying least square fitting to all the points of the contour located upstream a certain percentage of the spray penetration (figure 4.7 -left-).

- *Liquid and vapour penetration* (LL and S): These magnitudes are calculated as the average distance to the nozzle of a group of points of the spray contour (liquid or vapour phases respectively), located at the tip of the spray and near the spray axis. This axis is defined as the bisector of the two regression lines previously mentioned. The aim of using a group of points is to avoid errors caused by atypical geometries. More specifically, according to Palomares' criteria [8], this group consists of all the points located further than 80% of the distance between the nozzle and the axis-contour intersection, and less than 1 mm from the spray axis (figure 4.7 -right-).

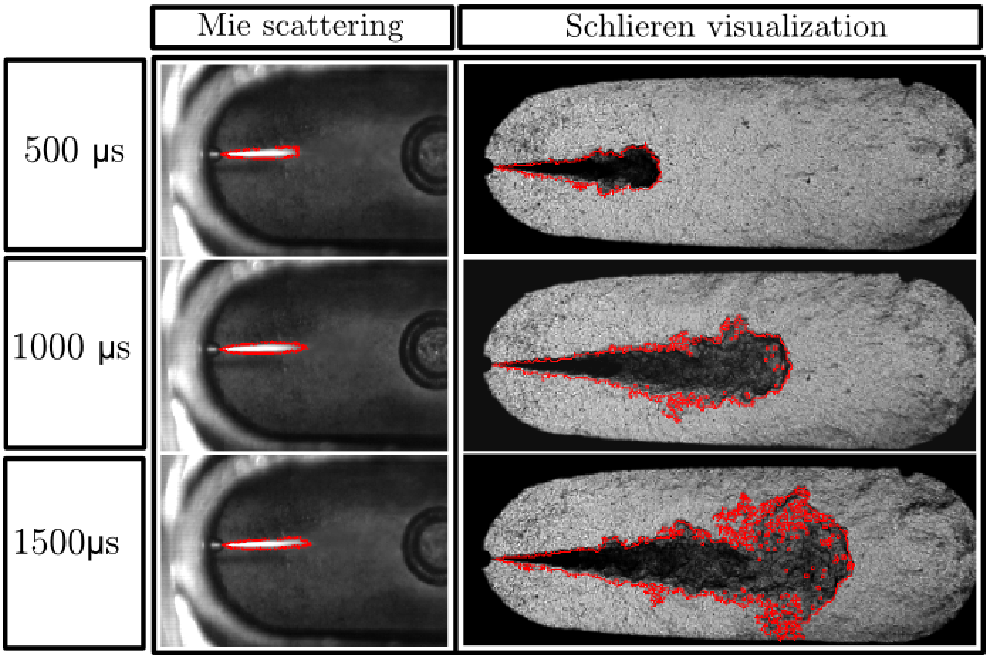

Figure 4.6. *Time sequence of MIE (left) and schlieren (right). The spray contour detected is represented by the red points. Data correspond to DEC at* $\rho_c = 23.41\ kg/m^3$ *at TDC and* $p_{inj} = 100\ MPa$.

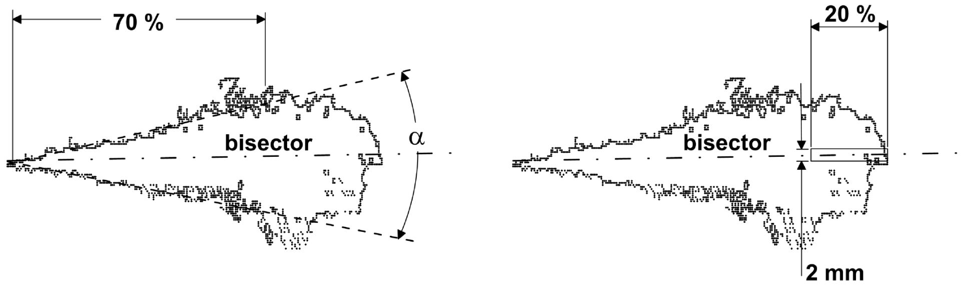

Figure 4.7. *Example of the calculation of spray cone angle (left) and tip penetration (right) from its contour.*

4.2.5 Results and discussion

The spray development was characterized for the four fuels described in chapter 3. For each test condition, ten consecutive repetitions were recorded. Each of them was formed by more than 150 images of both MIE and schlieren visualization. Then, the procedure described in the previous paragraphs was applied to every image to obtain the liquid length, the spray tip penetration and the spray cone angle. In figure 4.8 an example of results is shown, corresponding to DEC at $\rho_C = 23.41\ kg/m^3$ at TDC and $p_{inj} = 100\ MPa$. The left part of the figure shows the liquid length measurement, while at the right part the spray penetration and cone angle are plotted. The symbols represent values obtained from single images, while the continuous line and the error bars correspond to the average value and two times the standard deviation respectively. In this figure, the whole injection event is shown. However, as it can be observed, the spray reached the optical access limit at around 3000 μs aSoE. Besides, for later instants, it is possible to see that the change of thermodynamic conditions (due to the piston movement) “re-adjusts”maximum LL. This effect has been already reported by Pastor et al. [9]. For this reason, in the following figures only values up to 2000 μs aSoE have been plotted. This time interval is long enough to guarantee that spray achieves a steady stage (once the maximum LL is reached). Something that attracts attention from figure 4.8 is the large scattering reported. It is specially noticeable for the spray penetration and cone angle, and it increases with S. In fact, for the case shown here, the coefficient of variation[2] (CoV) of LL varies between 1% and 5%, while for S it ranges from 3% to 10%.

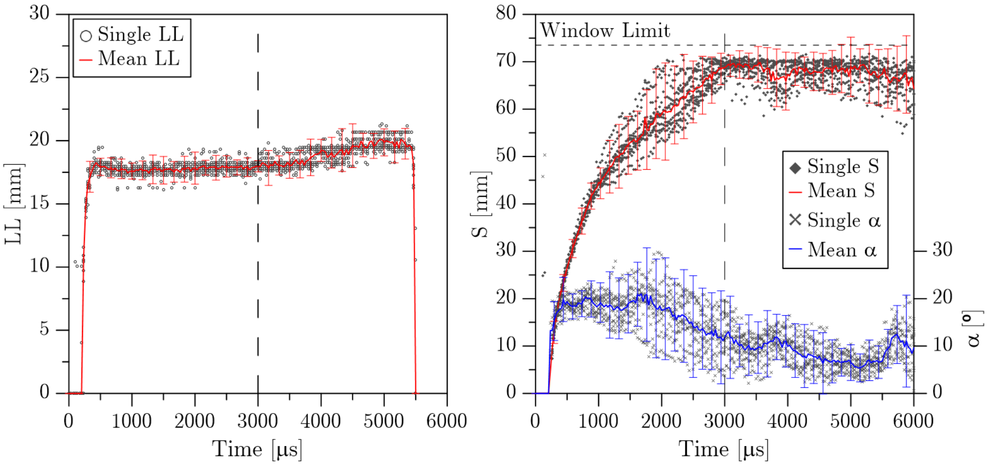

Figure 4.8. *Example of liquid length, spray penetration and spray cone angle measurements. Data correspond to DEC at* $\rho_c = 23.41\ kg/m^3$ *at TDC and* $p_{inj} = 100\ MPa$.

In chapter 3, the in-cylinder airflow was described in detail. It was observed that the cycle-to-cycle variability was not negligible and it could explain the scattering observed on results. At the first millimetres of the spray, where air velocity is low and spray momentum is high, the jet is almost not affected by this interaction. For this reason, LL variation is very small. However, when the spray penetrates into the combustion chamber, it achieves regions where the in-cylinder airflow is more important. Moreover, spray cross-section increases while local fuel momentum decreases (according to the hypothesis of spray momentum flux conservation). At this point, the interaction with air becomes relevant and it slows-down or even deviates part of the spray from its original direction of propagation. This effect can be observed in figure 4.9, where five out of ten repetitions are compared at different instants aSoE. The images shown correspond to data presented in figure 4.8. At 1000 μs the spray tip has almost reached half of the combustion chamber and the scattering between repetitions is minimum. However, at 2000 μs, the tip is around 60 mm from nozzle and the spray width has increased. Thus, it is possible to see an important variability between repetitions as a consequence of the interaction between the airflow in the chamber and the fuel moving at

---

[2] The coefficient of variation is defined as the ratio between standard deviation and the mean value of the measurement

low speed at the spray tip. What is more, for some of the injection events the spray's shape is not even conical, which specially affects the spray angle calculation. Some authors propose alternative methodologies to calculate this parameter [10], which are not very sensitive to the contour local morphology. They reduce data scattering, but a lot of information of the actual shape of the spray is lost. For this reason, these kind of solutions were not considered in this study. Instead, the use of average images was evaluated. For each instant, all repetitions were averaged pixel by pixel. Then, the same processing algorithm was applied to the resulting image, to obtain S and α. An example of these averaged images is shown in the right part of figure 4.9. Results obtained from instantaneous and averaged images have been compared and discussed in the following paragraphs.

4.2.5.1 Liquid phase

In the following section, results of LL are presented for the four fuels and all the test conditions listed in figure 3.2. Due to the "stationary nature" of the liquid length during the steady stage of the injection, it has been decided to represent the mean value of LL ($\overline{LL}$), calculated between 1000 and 2000 μs aSoE. In figure 4.10, the effect of injection pressure over this parameter is shown. Data correspond to $T_c = 760\ K$ at TDC, and two in-cylinder gas densities (namely 19.27 kg/m^3 and 32.28 kg/m^3). Therefore, not all the results are included in this figure, but the trends represented here can be extrapolated to the whole data set. A minor or even negligible decrease of the liquid length can be observed among all the fuels when injection pressure is increased. This effect is similar to the one reported by Pastor et al. [9] and Siebers [11], for Fischer-Tropsch diesel and biodiesel fuels. They suggest that the small variation could be the result of a slight increase of the spray angle [11, 12] when increasing injection pressure.

In the previous figure, the effect of both fuel properties and in-cylinder pressure are noticeable. Significant differences can be observed between HEX and DEC, which represent the upper and lower boundaries of the tested fuels in terms of volatility. In figure 4.11, the effect of in-cylinder temperature and pressure as well as fuel volatility are summarized for all the test conditions studied. Since injection pressure showed a small impact over LL, only results corresponding to $p_{inj} = 100\ MPa$ have been depicted. In this figure, it is possible to identify different effects. On the one hand, an increase of in-cylinder temperature and pressure clearly reduces the liquid length for all the cases. A higher gas density improves the air-fuel mixing process, while an

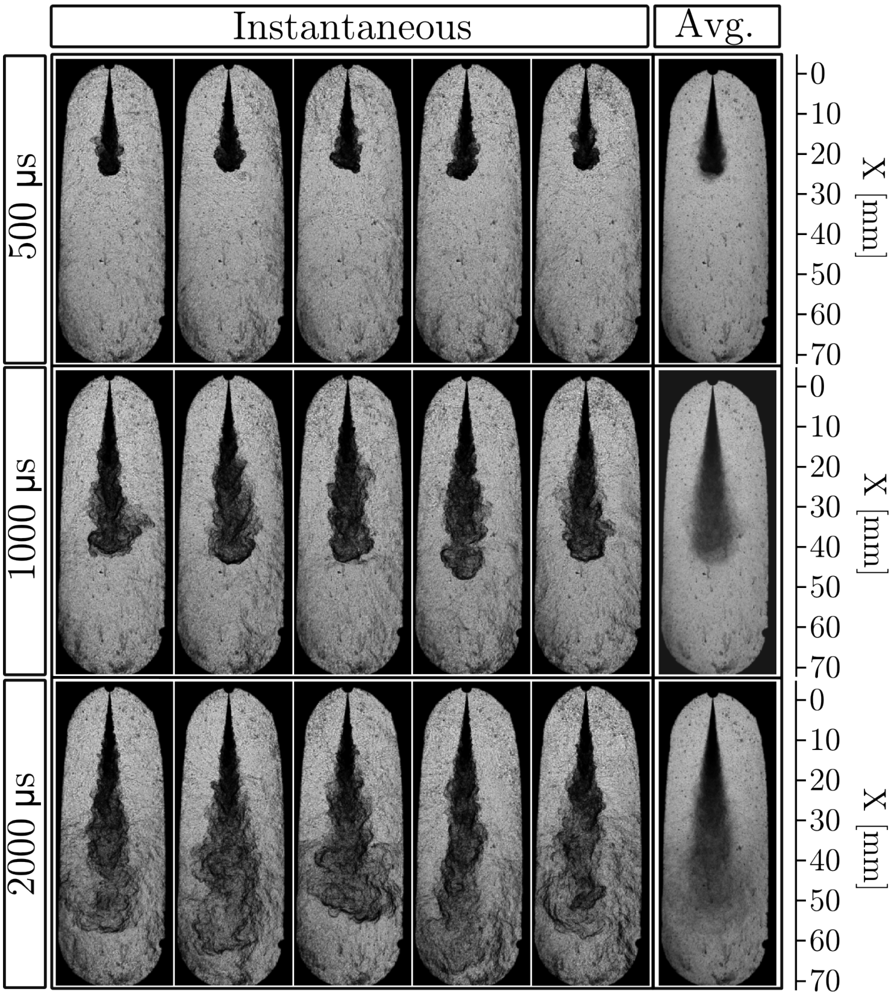

Figure 4.9. *Sequence of schlieren images (500, 1000 and 2000 μs aSoE) for 5 different injections. Images corresponds to DEC at $\rho_c = 23.41\ kg/m^3$ at TDC and $p_{inj} = 100\ MPa$.*

ambient with higher temperature provides more energy to heat and evaporate the fuel. On the other hand, a clear relation between fuel volatility and liquid-phase penetration can be observed. The pure fuels represent the upper and lower boundaries in terms of LL, and the results obtained for the mixtures are allocated between them. This trend is similar to the one shown by the distillation curve (figure 3.13) as it could be expected, since the association between liquid length and distillation curves has been widely defended in literature [9, 11, 13, 14]. In this regard, Siebers [11] suggests that the liquid

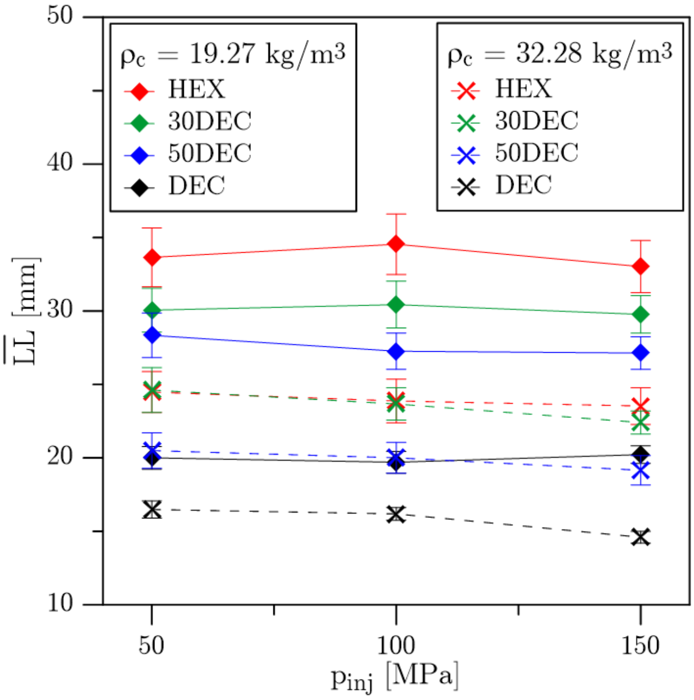

Figure 4.10. *Injection pressure effect on liquid length for the four studied fuels, at* $T_C = 760$ *K at TDC and two in-cylinder gas densities.*

length is controlled by the less volatile fraction, as he reports that LL is scaled with the 80% point of the distillation curve. However, the results obtained here are more likely in agreement with Higgins et al. [13] and Pastor et al. [9], who concluded that the liquid length is rather linked with the average volatility (the 50% point). Anyhow, all of them report that the differences caused by this property get reduced when in-cylinder pressure and/or temperature is increased. In this study, LL seems to be linearly scaled with the DEC blend fraction. However, when in-cylinder pressure is increased, the trend changes and even HEX and 30DEC report similar LL values. The similarities between both distillation curves (figure 3.13), in combination with the effect of thermodynamic conditions, could explain the minimum differences observed between both fuels.

The maximum liquid length can be interpreted as the axial location where the energy supplied from the entrained air is high enough to fully vaporize the liquid fuel [13, 15, 16]. Based on a mass and energy balance, this location can be related with a specific fuel mass fraction, which has been named hereafter

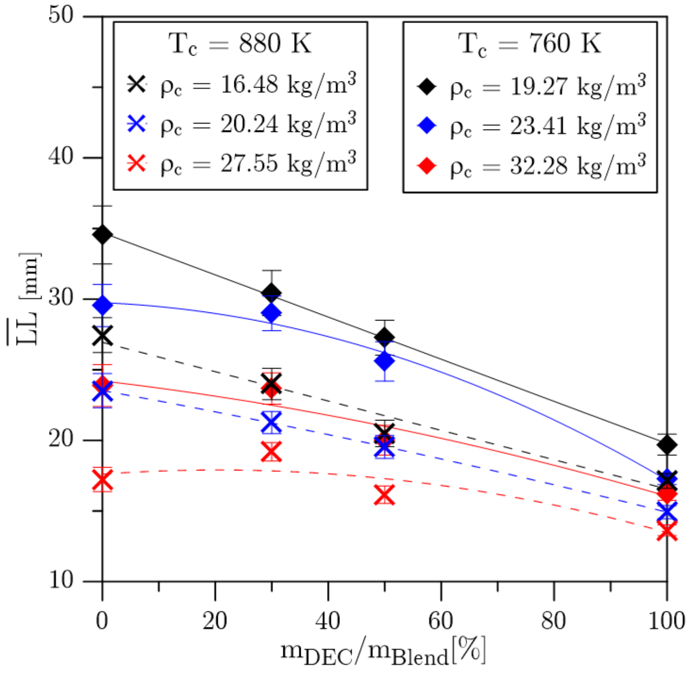

Figure 4.11. *Liquid length vs n-Decane mass fraction, for the different test conditions proposed in figure 3.2 and p_{inj} = 100 MPa.*

as $Y_{f,evap}$. Following this hypothesis, a scaling-law for liquid length can be derived based on turbulent spray mixing considerations. Thus, the liquid length at the steady stage of the diesel spray can be expressed as [17]:

$$LL = K_{LL} \left(d_0 \sqrt{\frac{\rho_f}{\rho_c^{1.4}}} \right) \frac{1}{Y_{f,evap}} \tag{4.1}$$

where d_0 is the nozzle diameter, ρ_f is the fuel density at injection conditions, ρ_c is the in-cylinder ambient density and K_{LL} is a proportionality constant, which can be considered independent of the fuel properties. The term in brackets characterizes the spray mixing scales. Such "mixing factor" considers both in-cylinder and fuel physics, by including the ratio of both densities. The last term of equation 4.1 is usually referred as the *energy factor*, as it accounts for the spray vaporization processes. The value of $Y_{f,evap}$ depends on both fuel properties and ambient thermodynamic conditions [15–17].

When in-cylinder temperature and/or pressure is varied, not only ρ_c is affected but also ρ_f (due to the heat transferred to the injector) and $Y_{f,evap}$ (energy balance). Considering the range of thermodynamic conditions chosen for this study, it is possible to obtain the value of all theses parameters for each fuel. Thus, using equation 4.1, it is possible to estimate the effect of varying in-cylinder conditions over LL. In this regard, some calculations have been carried out, which are summarized in table 4.1. When p_c is increased, the ambient density also increases while $Y_{f,evap}$ and ρ_f decreases. The combined variation of these three parameters predicts differences in liquid length between 14% and 37%. In contrast, when T_c is increased, ρ_c and ρ_f decrease while $Y_{f,evap}$ rises. In this case, a variation of LL between 13% and 26% could be expected. According to results presented in figure 4.11, experimentally measured variations are in general in the same range as predictions (table 4.1). However, the effect of in-cylinder pressure is being overestimated. The reason could be the influence that this parameter could have over the spray angle, which would modify the value of K_{LL} and which has not been considered here. This has been discussed in more detail in section 4.2.5.2. From this calculations, it can be also observed that the effect of temperature is larger than that of in-cylinder pressure. Increasing p_c by 70% causes a maximum LL variation of around 37%. However, an increase of 15% on T_c causes variations of LL up to 26%.

According to equation 4.1, a change of fuel is reflected in ρ_f and $Y_{f,evap}$. In this way, LL should vary between 34% and 43% between DEC and HEX. This is in agreement with the experimental data, which presents variations between 21% and 43%. A similar comparison has been performed between HEX and 30DEC, which states that differences from 0.6% to 6% could be expected between these two fuels. This is in agreement with the similarities observed from experimental data. In this case, a negative variation has been reported, which reflects certain experimental condition where measured LL from 30DEC was slightly larger than that of HEX. This could be explained by the uncertainties on the measurements, as previously discussed, fir experimental conditions where LL of both fuels is similar. It has to be noted that the main parameter that controls the LL is $Y_{f,evap}$. This means that thermodynamic properties related to evaporation, like the latent heat of evaporation or the boiling point, controls the maximum penetration of the liquid phase. An increase in content of HEX (the less volatile fraction) affects the evaporation process as it increases the amount of energy required to completely evaporate the fuel.

4.2.5.2 Vapour phase geometry

In this second part of the study, the spray tip penetration (S) and cone angle (α) are presented and analysed. As it was concluded from figures 4.8 and

Parameter	**Controlling term**	**$\mathbf{LL_{prediction}}$ variation**	**$\mathbf{LL_{experiment}}$ variation**
$\uparrow p_c$	$\uparrow \rho_c(23\% - 70\%)$ $\downarrow Y_{f,evap}(0\% - 7\%)$ $\downarrow \rho_f(1\% - 5\%)$	↓14% - 37%	↓5% - 28%
$\uparrow T_c$	$\downarrow \rho_c(15\%)$ $\uparrow Y_{f,evap}(27\% - 50\%)$ $\downarrow \rho_f(1\% - 3\%)$	↓13% - 26%	↓13% - 28%
↑Fuel Volatility HEX→DEC	$\downarrow \rho_f(6\%)$ $\uparrow Y_{f,evap}(46\% - 71\%)$	↓34% - 43%	↓21% - 43%
↑Fuel Volatility HEX→30DEC	$\downarrow \rho_f(2\%)$ $\uparrow Y_{f,evap}(0\% - 6\%)$	0.6% - 6%	↓ −4% - 12%

Table 4.1. *Theoretical and experimental estimation of the effect of p_c, T_c and fuel volatility over the spray liquid length.*

4.9, the spray geometry is conditioned by its interaction with the in-cylinder airflow. It causes large cycle-to-cycle variations as well as the appearance of local structures at the margins of the spray which hinder the accurate measurement of both S and α. For this reason, it has been proposed to work with average images instead of single ones. These average sprays present softened edges, where deformations and deflections are minimum (figure 4.9). Spray penetration and cone angle, obtained from the two type of images, are compared in figure 4.12. They correspond to DEC, at $\rho_c = 23.41\ kg/m^3$ at TDC and $p_{inj} = 100\ MPa$. The red lines represent data obtained from single images and averaging the result (sng); the black lines represent data obtained from averaged spray images (avg). Ten consecutive repetitions have been considered for this comparison. It is possible to see that spray penetration in both cases is similar , despite S_{sng} is around 1 mm lower than S_{avg}. Larger differences can be observed for the spray cone angle, where α_{avg} is clearly higher than α_{sng}.

In figure 4.13, a comparison between the average and single image contour is shown. They correspond to the data included in figure 4.12. Black points represent the detected contour of an average image (AVG). Red points are

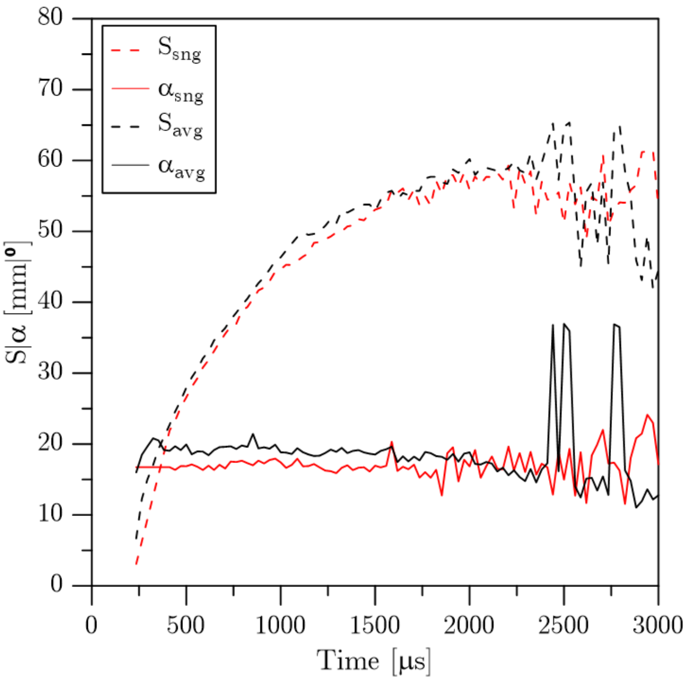

Figure 4.12. *S and α obtained from processing average images or single repetitions. Data correspond to DEC, at $\rho_c = 23.41\ kg/m^3$ at TDC and $p_{inj} = 100\ MPa$.*

the result of averaging the coordinate at the R-axis of the contour of all repetitions, at each coordinate at the X-axis (SNG). This comparison makes it possible to identify, in a first instance, differences between the two ways of processing. At the first half of the spray, both AVG and SNG coincides. However, at the second half, some differences are noticeable as AVG is wider than SNG. In figure 4.9, it is possible to see that the average spray presents a grey-level degradation towards the edges of the spray, which is specially visible downstream the 50% of S. In fact, this degradation appears at the region where scattering between repetitions is larger. Then, the LRT finds an optimum threshold that includes the major part of this “degradation region”, resulting on the definition of a wider spray contour. This effect is specially relevant for the calculation of the spray cone angle, but it can also affect the spray penetration (as it has been shown in figure 4.12). The differences between the first and second half of the spray are reflected on the calculation of α when different percentages of the spray penetration are considered. In figure 4.13 the linear regressions obtained for 30% and 60% of S are depicted. It is possible to see that for the first part of the spray, both processing methodologies (AVG and SNG) provide similar values of α. However, when the percentage increases, α_{avg} becomes larger than α_{sng}.

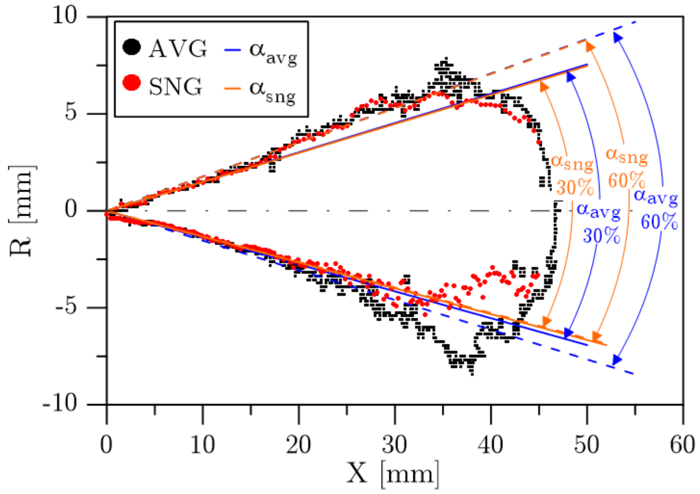

Figure 4.13. *Comparison between the contour of an average (AVG) and single spray image (SNG). The straight lines represent the fits utilized to calculate α, for points below 30% and 60% of the spray penetration. Data correspond to DEC, at 1000 μs aSoE, $\rho_c = 23.41\ kg/m^3$ at TDC and $p_{inj} = 100\ MPa$.*

The comparison of the spray cone angle, from AVG and SNG contours, provides information about how the spray geometry can be affected by the cycle-to-cycle variation of the test rig. More precisely, the comparison between α_{avg} and α_{sng} obtained for different percentages of S can give some insight into the real influence that the airflow variability could have over the spray geometry, at different regions downstream the nozzle. The ratio between α_{avg} and α_{sng} versus the value of α_{sng} is shown in figure 4.14. Data correspond to DEC, at all the in-cylinder conditions proposed in figure 3.2. The angles depicted here correspond to the average of instantaneous values, calculated between 500 and 1500 μs aSoE. This time interval has been chosen in order to avoid the first transitory evolution of the spray cone angle and the wrong values obtained when the average spray is large enough to occupy almost the whole optical access. The main conclusion that can be extracted from this comparison is that even the first millimetres of the spray are affected. The ratio between α_{avg} and α_{sng} is near one, but the cone angle of the average spray is usually higher. Differences increase with the percentage of S as it could be expected.

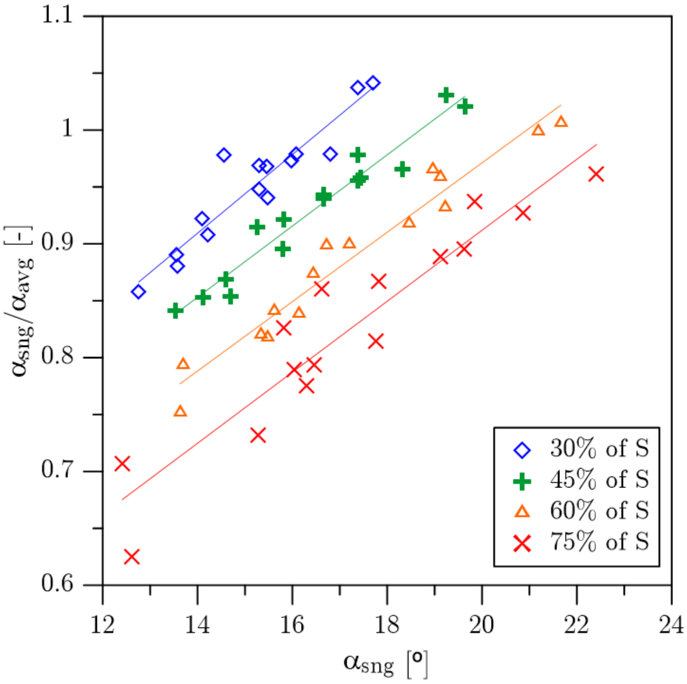

Figure 4.14. *Ratio between* α_{avg} *and* α_{sng} *vs* α_{sng}. *Data correspond to DEC, for the test conditions proposed in figure 3.2, and averaged between 500 and 1500* μs.

Considering all the foregoing, it is difficult to select the “best” approach to characterize the spray geometry. The use of average images seems to soften the spray edges, making it easier to calculate the spray cone angle. However, their metrics are affected by the cycle-to-cycle airflow variability of the test rig, resulting on larger α values than the ones obtained for single repetitions. Regarding the usefulness of results (e.g. for CFD tuning or validation), the SNG contours would provide more accurate values. Hence, values of S and α presented in the following paragraphs were obtained by processing single repetitions separately and averaging results. However, it has been shown that α_{sng} can be also affected by the spray deformation and deflection if the percentage of penetration considered for its calculation is large enough. For this reason, the author suggests that 30% of the spray penetration represents a good reference for spray cone angle calculation.

Spray geometry was characterized for the four fuels of study, at the test conditions defined in figure 3.2. In figure 4.15, the effects of p_c and T_c over S and α are shown. Data correspond to DEC (left) and HEX (right), injected at $p_{inj} = 100\ MPa$. Both parameters have a clear effect over the in-cylinder ambient density. Therefore, whereas injection properties ($\dot{m}_f$ and $\dot{M}_f$) are almost not modified, a reduction of the ambient density would make it easier for the spray to penetrate into the combustion chamber. For the same reason, the spray would be less spread radially and thus the cone angle would be reduced. This behaviour is observed for both fuels, as the reduction of ρ_c (either by increasing T_c or decreasing p_c) causes an increment of S and a decrease of α. However, it is possible to see that the range of variation of T_c does not cause much effect over the spray geometry. In figure 4.16, the evolution of S and α is shown for DEC (left) and HEX (right), at three different injection pressures and $\rho_c = 23.41\ kg/m^3$. It can be observed that S increases with p_{inj}, while α is almost not affected. The higher momentum flux (and fuel velocity) at the output nozzle orifice, thanks to the higher injection pressure, makes it possible for the fuel to penetrate faster into the combustion chamber. These results coincide with the ones reported by Naber and Siebers [10] or the information available at the *Engine Combustion Network* [18] (for Spray-A conditions).

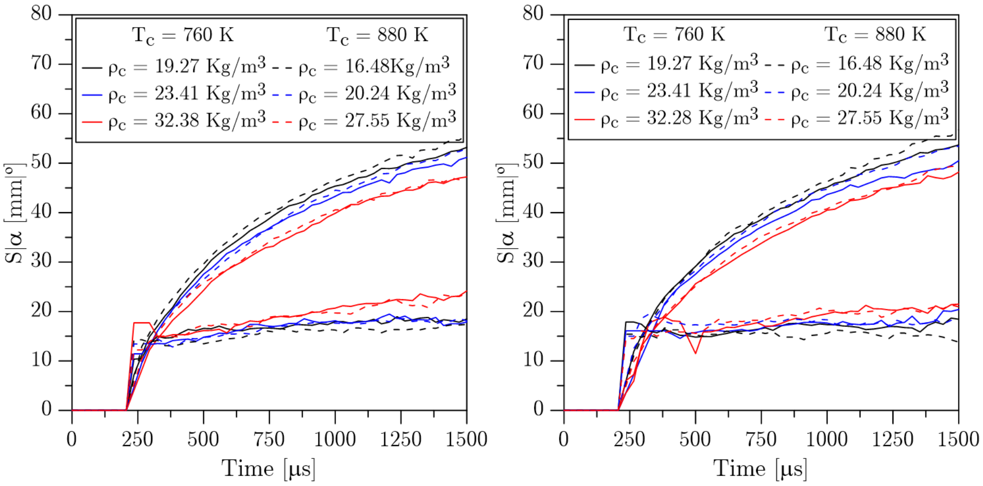

Figure 4.15. *Effect of in-cylinder conditions over spray penetration and cone angle, for DEC (left) and HEX (right). Data correspond to* $p_{inj} = 100\ MPa$.

Finally, a comparison between fuels is depicted in figure 4.17. The spray penetration and cone angle of DEC, 50DEC, 30DEC and HEX are compared, for $\rho_c = 23.41\ kg/m^3$ and $p_{inj} = 100\ MPa$. Moreover, measurement uncertainties of DEC are also included as an example, for both S and α. They have been calculated as $\mu_{DEC} \pm \sigma_{DEC}$, and are represented by both shaded areas. In this figure, it is possible to see that the four fuels present similar

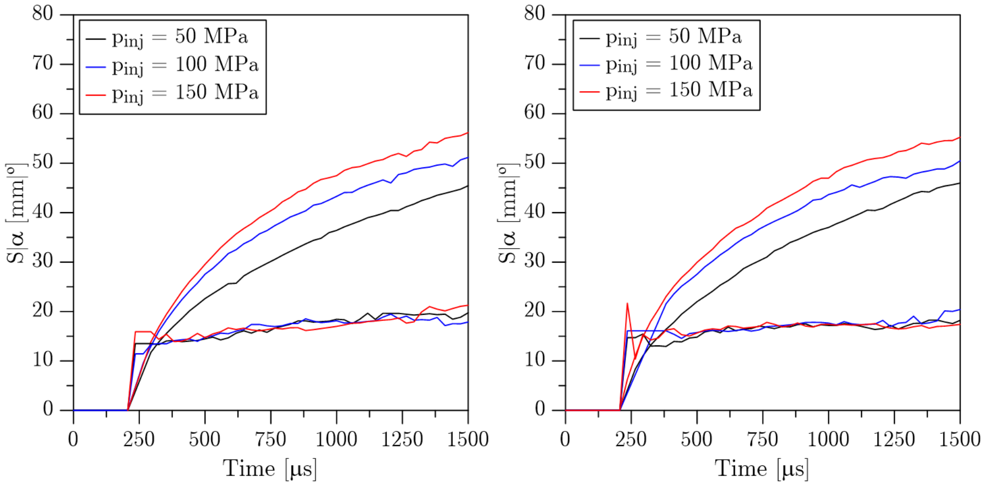

Figure 4.16. *Effect of injection pressure over spray penetration and cone angle, for DEC (left) and HEX (right). Data correspond to* $\rho_c = 23.41\ kg/m^3$.

spray penetration and cone angle, despite certain discrepancies arise after 1250 μs aSoE. However, they are within the range delimited by the measurement uncertainties, so it cannot be stated that they represent real differences and no clear trend can be extracted. The independence of the spray geometry with the fuel properties is in agreement with the hydraulic characterization presented in section 3.4, as almost no differences were reported for the momentum flux between the four fuels at any injection pressure. A similar comparison is reported by Kook and Picket [19], for conventional, Fischer-Tropsch, coal-derived and surrogate fuels. Moreover, Payri et al. [20] obtained a similar result when comparing gasoline and diesel injections, both performed with the same common-rail injection system.

A theoretical analysis is proposed with the aim of supporting the reported trends. For this purpose, three main hypotheses have been considered [17, 21]: injection and in-cylinder conditions are assumed to be constant; spray momentum flux is conserved along the spray axis; instantaneous spray penetration is derived from the average spray velocity. These hypotheses lead to the following equation [16]:

$$\begin{aligned} S &= K_S \cdot M_{0f}^{1/4} \cdot \rho_c^{-1/4} [\tan{(\alpha/2)}]^{-1/2} \cdot t^{1/2} \\ &\approx K_S^* \cdot M_{0f}^{1/4} \cdot \rho_c^{-0.35} \cdot t^{1/2} \end{aligned} \tag{4.2}$$

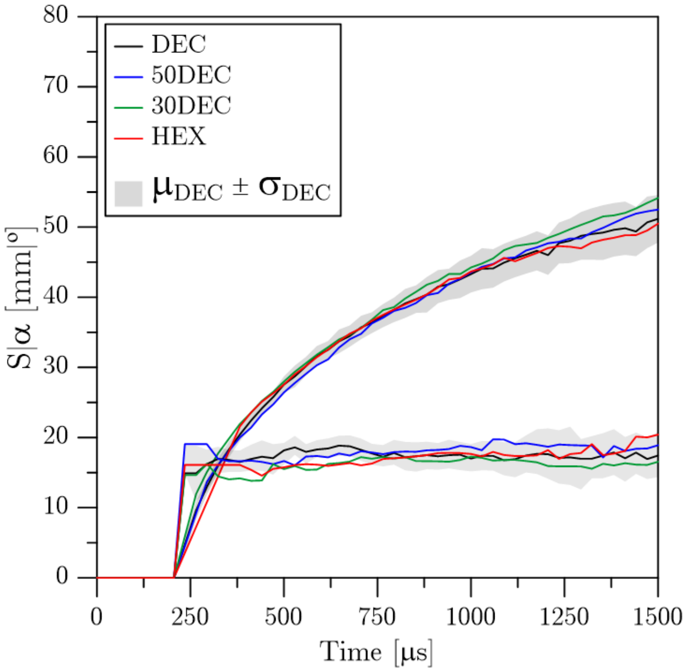

Figure 4.17. *Effect of fuel properties over spray penetration and cone angle. Data correspond to* $\rho_c = 23.41\ kg/m^3$ *and* $p_{inj} = 100\ MPa$.

where K_S^* is a proportionality constant, M_{0f} is the spray momentum flux and t is time aSoI.

A summary of the effects predicted and measured for each parameter is presented in table 4.2. The experimental data corresponds to DEC, between 500 and 1500 μs aSoE. On the one hand, an increment of ρ_c (either by increasing p_c and/or decreasing T_c) would cause a reduction of S, according to the negative exponent that goes with this parameter. On the other hand, when rising p_{inj}, the spray momentum flux is also increased and this is reflected on a larger penetration for a certain time aSoE. Finally, according to equation 4.2, the only way that the fuel properties could have an effect on the spray penetration is through the momentum flux. In section 3.4, it has been stated that this parameter is related with the dynamic viscosity. However, differences between fuels were not large enough to cause variations on $\dot{\mathrm{M}}_f$. Thus, it can be stated that the fuels considered in this study should not present differences on neither S nor α. There is an agreement for the major part of the cases between theoretical and experimental trends. However, it should be noted that the effect of the spray angle is not being considered for these calculations, as it has been observed that any influence on this parameter was minimum (only noticeable when varying p_c).

Parameter	**Controlling term**	$\mathbf{S_{prediction}}$ **variation**	$\mathbf{S_{experiment}}$ **variation**
$\uparrow p_c$	$\uparrow \rho_c$(23% - 70%)	↓7% - 17%	↓4% - 14%
$\uparrow T_c$	$\downarrow \rho_c$(15%)	↑5%	↑3%
$\uparrow p_{inj}$	$\uparrow \dot{M}_f$(317%)	↑20% - 33%	↑20% - 30%
↓Fuel Viscosity	$\approx \dot{M}_f$	≈	≈

Table 4.2. *Theoretical and experimental estimation of the effect of p_c, T_c, p_{inj} and fuel viscosity over the spray penetration. Experimental data corresponds to DEC, between 500 and 1500 μs aSoE.*

In summary, the measured effect of test conditions over LL, S and α is similar for the four fuels considered in this study, which is consistent with other works previously published. The effect of fuel properties over the spray development was also analysed. In this regard, a dependence of fuel volatility with the maximum liquid penetration was detected. It was found that LL scales with the content of the lowest volatile fraction. However, results suggested that it is more related with the average volatility (50% point of the distillation curve) rather than to the heavier component volatility. In contrast, no dependence was found between S and fuel properties. The differences on viscosity between them are not high enough to affect the momentum flux. Therefore, it can be concluded that when fuels with different physical properties (density, viscosity or boiling point) are injected into a high-density and high-temperature atmosphere (i.e. in the combustion chamber of a diesel engine), they may evaporate differently resulting on different liquid lengths. Despite this, similar vapour penetration and cone angles could be expected, indicating virtually the same total amount of ambient gas entrainment and fuel-air mixing.

4.3 Microscopic spray characterization

The spray penetration and cone angle have been traditionally used provide a good overview of the air-fuel mixing process. However, a more detailed knowledge about it is usually required. Many studies in literature go further in detail, and seek to characterize the local distribution of fuel within the spray. For this purpose, current work proposes the use of *UV-VIS Light Absorption and Scattering*, to the detriment of other renowned techniques (i.e. PRS or PLIF).

As it has been previously mentioned, the use of this technique with n-alkanes, like the ones considered in this study, has not been previously addressed in literature. Therefore, the application and optimization of UV-VIS LAS to this kind of fuels is described in the following paragraphs. The study is focused in two of the fuels (i.e. DEC and 50DEC) as, according to the macroscopic characterization, no differences should be expected between them downstream the liquid length. A new methodology to characterize on-line the absorption properties of each fuel is described, together with the processing algorithm. Finally, the reliability and usefulness of UV-VIS LAS has been analysed and discussed, for the conditions proposed in this study.

4.3.1 UV-VIS Light Absorption and Scattering fundamentals

When light is transmitted through a mixture of vapour and droplets, it is attenuated according to the Bouguer-Lambert-Beer law as follows:

$$\ln\left(\frac{I_0}{I}\right) = \int_0^L \frac{1}{MW}\varepsilon(\lambda)\rho_{vf}100dx + \int_0^L Q_{ext}(\lambda)dx \tag{4.3}$$

where λ is wavelength, ε is the absorption coefficient of vapour fuel ($l \cdot mol^{-1} \cdot cm^{-1}$), ρ_{vf} is the vapour fuel partial density (kg/m^3), MW is the molecular weight of the fuel (g/mol), L is the optical path length (m) and Q_{ext} is the extinction coefficient of a cloud of droplets. The first term on the right side of equation 4.3 corresponds to light attenuation due to absorption by vapour molecules, while the second term is the attenuation due to droplets, which includes scattering and absorption losses.

UV-VIS LAS is based on the combination of attenuation measurements at two wavelengths, the first one in the ultraviolet range (UV) and the other in the visible range (VIS). In this work, 280 nm and 560 nm were chosen as the working wavelengths. The main underlying hypotheses are: fuel molecules will not absorb light in the visible range neither in the form of droplets nor in vapour phase; UV absorption by fuel droplets is negligible compared to scattering. Suzuki et al. [22] evaluated the drop optical thickness for 280 nm and 560 nm for α-dimethylnaphtalene and concluded that the hypothesis of non-absorbance from liquid droplets can be applied. Close to the nozzle region, a certain error can affect the measurement since the droplet number density is too high. However, it is minimized if vapour optical thickness dominates the total extinction. Considering this, attenuation for both wavelengths can be described as follows:

$$\ln\left(\frac{I_0}{I}\right)_{UV} = \ln\left(\frac{I_0}{I}\right)_{VapAbs,UV} + \ln\left(\frac{I_0}{I}\right)_{DropScatt,UV} \tag{4.4}$$

$$\ln\left(\frac{I_0}{I}\right)_{VIS} = \ln\left(\frac{I_0}{I}\right)_{DropScatt,VIS} \tag{4.5}$$

Equations 4.3, 4.4 and 4.5 can be combined to obtain the following expression, for line-of-sight averaged vapour fuel partial density:

$$\overline{\rho_{vf}} = \frac{MW}{100 \cdot \varepsilon(\lambda_{UV})}\left[\ln\left(\frac{I_0}{I}\right)_{UV} - R\ln\left(\frac{I_0}{I}\right)_{VIS}\right] \tag{4.6}$$

where $\overline{\rho_{vf}}$ is the average vapour fuel partial density along the optical path, as LAS technique is based on Line-of-Sight (LoS) measurements. The R term is the ratio of the droplet optical thickness for the two wavelengths. From now on, the term within brackets will be referred as *absorption*. Billings et al. [23] examined the variation of the droplet optical thickness for their application at 3390 nm and 632 nm. Results showed that $R \approx 1$ for droplets larger than 30 μm, while for smaller droplets the error was lower than 10%. Calculations conducted for the present work (discussed in following section) provided similar results in the UV-VIS range.

The optical set-up utilized is presented in figure 4.18. A continuous broadband 1000 W Hg (Xenon) Arc lamp was utilized, in combination with a diaphragm and a diffuser to create a uniform point light source. This lamp is characterized by a continuous emission spectra from 250 to 2400 nm (figure 4.19), with enough intensity to replace the commonly used Nd:YAG pulsed laser [24–29]. A parabolic mirror of 150 mm diameter, with aluminium coating, was employed to create a collimated light beam which crossed the combustion chamber. The light beam was collected at the other side of the engine by a quartz lens of 75 mm diameter, which focused light on both detectors. A square beam splitter (50 mm side) was positioned just after the lens, to divide light in two different beams. It was chosen so that 50% of the light was reflected (UV channel) and 50% transmitted (VIS channel). For both UV and VIS wavelengths, a digital ICCD image system Andor iStar was utilized. Light was filtered just prior to the detectors by two interference filters centred at 280 and 560 nm respectively (10 nm FWHM and 50% peak transmittance).

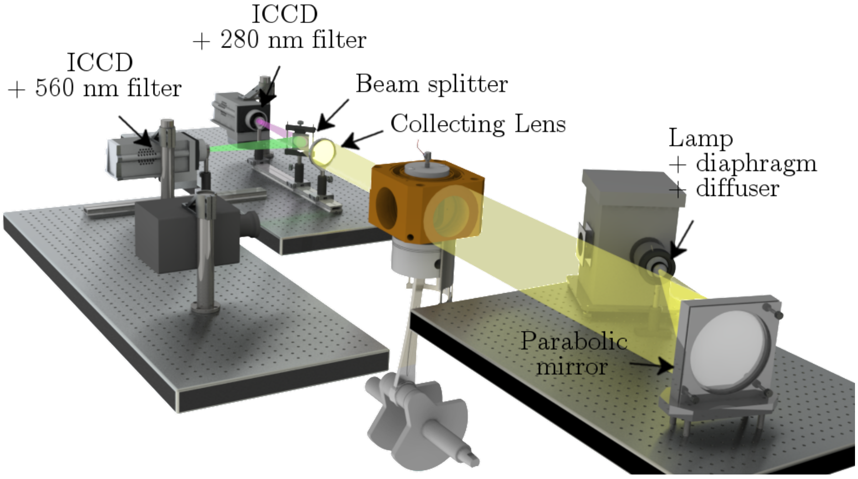

Figure 4.18. *Scheme of the UV-VIS LAS optical set-up.*

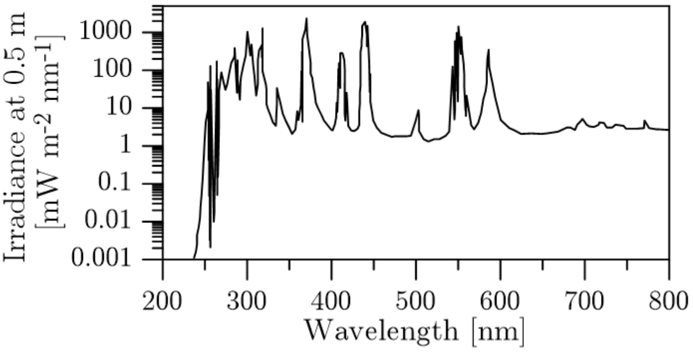

Figure 4.19. *Hg (Xenon) lamp emission spectrum.*

Simultaneously to LAS measurements, MIE from the liquid droplets was registered. In this regard, a third ICCD image system (LaVision Dynamight) was utilized, due to the low intensity of the collimated light beam, which made the function of MIE light source in this case. Images were processed following the same procedure as described in section 4.2.4.

4.3.2 Absorption coefficient calibration

According to equation 4.6, one requirement to obtain quantitative results with LAS technique is knowing the absorption coefficient (ε) of the fuel of study. Depending on the molecule, some information can be extracted from literature survey. In most of the cases, data available has been obtained at low temperature and pressure, and may not be valid for the conditions that can be found in the combustion chamber of a diesel engine since the absorption coefficient can be strongly affected by thermodynamic conditions [25, 30]. Thus, usually these values cannot be extrapolated to higher temperatures and pressures. Besides, significant differences in sensitivity to thermodynamic conditions have been observed between fuels. For this reason, it becomes necessary to characterize the absorptivity of each fuel under test conditions. A methodology is proposed in the current work, based on creating a homogeneous mixture inside the cylinder with known concentration, temperature and pressure. Therefore, if light absorption is measured, it is possible to apply equation 4.6 to obtain the absorption coefficient at in-cylinder thermodynamic conditions.

Trapped air mass and in-cylinder density were derived from the pressure signal (section 3.2.2), while the amount of fuel injected was previously measured for all the fuels, as described at section 3.4. Then, the average fuel mass fraction ($\overline{Y_f}$) inside the cylinder was calculated and hence $\overline{\rho_{vf}} = \overline{Y_f} \cdot \rho_c$. In order to achieve the homogeneous mixture, fuel was injected early in the cycle, just after the transfers were blocked by the piston (at -80.5 CAD). Long energizing times and high injection pressures were required to introduce enough mass of fuel to obtain a measurable fuel concentration (due to the large displacement of the engine).

In order to evaluate the accuracy of the methodology, three mixtures of n-Heptane (HEP) and a high absorptive fuel[3] (HAF) were characterized. Hereafter they have been named as HEPB1, HEPB2 and HEPB3, respectively. Both fuels where chosen so the absorptivity of the first one is negligible in comparison with the second one. In this way, the concentration of the second component was gradually increased so the absorption coefficient should also increase. The main properties of the three mixtures are presented in table 4.3. This mixtures were characterized under thermodynamic conditions corresponding to $\rho_c = 19.27\ kg/m^3$ at TDC. In this case, mass flow rate was only measured for HEPB3 and scaled for the other two, based on each mixture density.

---

[3] Fuel composed by a blend of n-alkanes and aromatic compounds

Fuel	**X_f HAF**	**Y_f HAF**	**ρ_f (303 K) [kg/m^3]**	MW **[g/mol]**
HEPB1	0.023	0.047	715.637	105.303
HEPB2	0.032	0.065	717.896	107.346
HEPB3	0.041	0.083	720.054	109.295

Table 4.3. *Main properties of the three mixtures of HEP and HAF.*

Apart from this, a more detailed characterization was performed for HEPB3, DEC and 50DEC. Corresponding operating conditions are summarized in table 4.4. Light absorption was measured at different CADs after TDC, which made it possible to calculate ε for different combinations of pressure and temperature. Moreover, measurements were performed at different in-cylinder conditions (at TDC) but same CADs. Thus, it was possible to compare points with the same pressure but different temperature or vice versa. Two values of energizing time were tested for the low absorption fuels (DEC and 50DEC). The aim was to corroborate that no systematic error related to the calculation of $\overline{\rho_{vf}}$ was introduced. For each test conditions, 50 images of the light beam with fuel (I) and without fuel (I_0) were registered alternatively. Each set of images was averaged and then the vapour absorption was calculated.

Fuel	ρ_c [kg/m^3]	**p_{inj} [MPa]**	**Energizing Time [μs]**	**Total injected mass [mg/cc]**	**CAD of interest**
DEC	19.27 - 20.24 - 23.41	150	4500 - 9000	37.53 - 54.37	0 - 6 - 12 - 18
50DEC	19.27 - 20.24 - 23.41	150	4500 - 9000	39.70 - 64.03	0 - 6 - 12 - 18
HEPB3	19.27 - 20.24 - 23.41	150	9000	60.25	0 - 6 - 12 - 18 - 24 - 30

Table 4.4. *Test conditions for the absorption coefficient calibration.*

Finally, the absorption spectrum and the absorption coefficient (at 280 nm) were measured at standard temperature and pressure (STP), for all the fuels employed in the calibration process. The same light source as the one described previously was used, while absorption was measured with a UV-VIS spectrometer AvaSpec 2048 L and quartz sample cell of 5 mm width.

4.3.3 Vapour fuel distribution

A long energizing time was set so the spray was stabilized before the injection finished. The light was registered at -3 CAD (1000 μs aSoE) and 0 CAD (2000 μs aSoE) before TDC. Latter times were not considered due to the expected interaction between the airflow and the spray that has been previously reported.

The reduced size of the beam splitter limited the field of view, so all the receiving optics were spatially shifted to measure the whole spray, with a precision translational stage. Light was registered at three positions along the spray axis. The effective length of the field of view was 45 mm, while the optics were displaced 25 mm between two consecutive positions. Thus, an overlap of 20 mm was ensured, which was the base to assembly the three images into a single one. In figure 4.20, an example of the image assembly is shown, corresponding to DEC at $\rho_c = 19.27\ kg/m^3$ at TDC. For each test condition and measuring position, 50 images of the light beam with injection (I) and without injection (I_0) were registered. Each set of images was averaged and then the mean images were assembled. Finally, attenuation was calculated.

A scheme of the image processing flow is depicted in figure 4.21. Firstly, the images of spray (I) and background (I_0) are coupled to calculate the attenuation for each wavelength (UV Att. and VIS Att.) pixel by pixel. The reference and attenuated intensities were measured alternately, so the influence of light source variations and window fouling was minimized. Then, the vapour absorption signal is calculated ($\ln{(I_0/I)_{UV}} - R\ln{(I_0/I)_{VIS}}$). The signal corresponding to the visible wavelength is spatially transformed to obtain the best correspondence pixel by pixel with the UV signal. This transformation comprises translation, rotation and scaling. At this point, the absorption is line-off-sight integrated. Thus, a deconvolution (inversion) algorithm is required to obtain the corresponding signal at the symmetry plane of the spray. For this purpose, the absorption signal is divided in two halves (along its axis), which are averaged to apply properly the deconvolution algorithm. Then, equation 4.6 is utilized to calculate the vapour fuel partial density (ρ_{vf}) pixel by pixel. It has to be noted that the form at which this equation has been presented corresponds to the calculation of the LoS averaged partial density

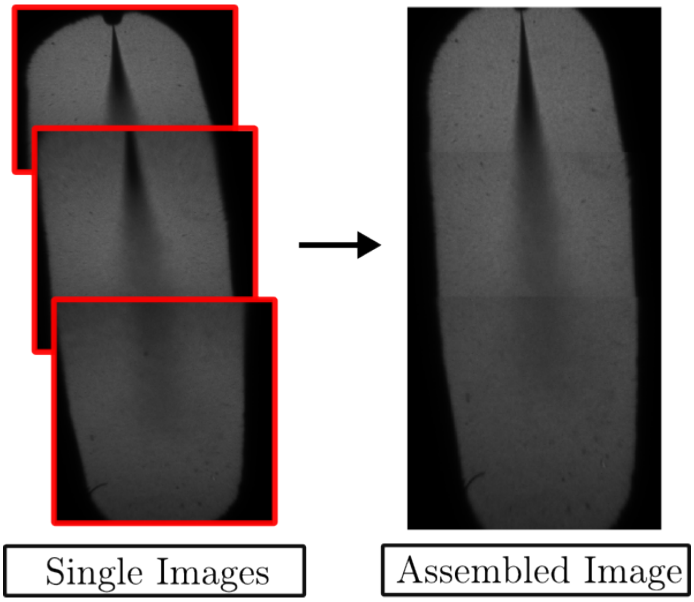

Figure 4.20. *Single images (left) compared with their final assembly (right). Images correspond to DEC, at* $\rho_c = 19.27\ Kg/m^3$ *at TDC and 2000* μs *aSoE.*

($\overline{\rho_{vf}}$). When applying this equation to the symmetry plane, the optical path (L) considered is the minimum spatial unit (i.e. 1 pixel).

Application of equation 4.6 requires the use of certain parameters, whose values have to be determined previously. The first one is the constant R, which can be defined as the ratio between the extinction coefficient (Q_{ext}) of the droplet cloud at 280 and 560 nm. Different approaches can be found in literature [31, 32], which provide similar results. For current work, van de Hulst approximation was followed, which is deeply described in [31] and summarized in figure 4.22. Assuming that the imaginary part of the refractive index is negligible [33] (i.e. there is no absorption by liquid droplets), and considering that the diameter of droplets (d) is large in comparison with the working wavelengths ($\chi = \pi d/\lambda \gg 1$), the following equation can be applied to estimate the absorption coefficient:

$$Q^*_{ext} = 2 - \frac{4\sin\rho}{\rho} + \frac{4(1-\cos\rho)}{\rho^2} \tag{4.7}$$

where $\rho = 2\chi(n-1)$ for this equation, and n is the real part of the complex refractive index.

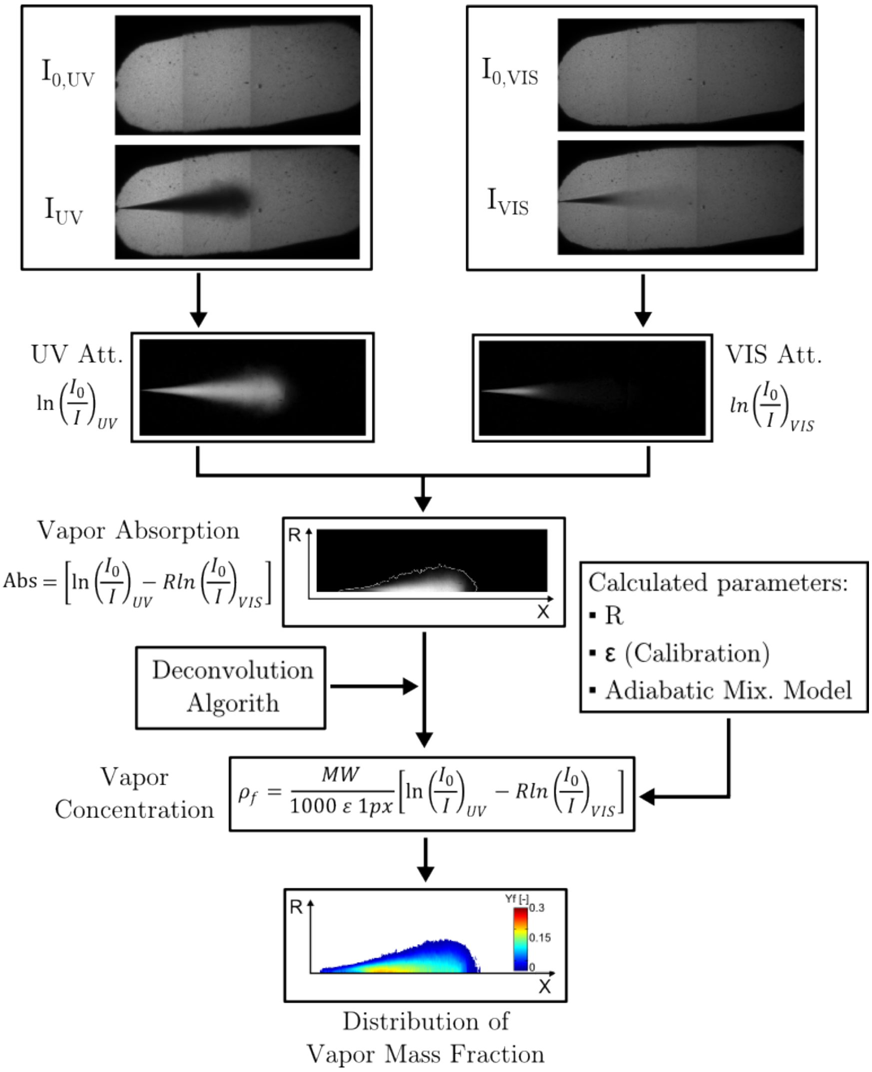

Figure 4.21. *Scheme of the processing flow of LAS images.*

In the region of the first maximum of the Q_{ext} curve (i.e. when d is around 10-15 μm), a correction term can be introduced to improve accuracy in the estimation of Q_{ext} as given by equation 4.8. For the fuels considered in this work, the value of the refractive index was $n \approx 1.4$ - 1.44 , depending on the precise composition and the values of pressure and temperature. It was observed that variations of n within this range caused differences below 1%

over R. Consequently, variations of the refractive index were neglected and a constant value of $n = 1.42$ was considered in all the cases.

$$Q_{ext} = \left(1.1 + \frac{n - 1.2}{3}\right) Q^*_{ext} \tag{4.8}$$

The extinction coefficient of each wavelength was corrected by an efficiency parameter that accounted for the effect of the solid angle subtended between the spray and the detection system [34]. For this application, and considering the distances between the different optics and their diameters, it was observed that the most restrictive element was the focusing lens for both wavelengths. Then, the correction factor was calculated as:

$$\xi_{ext} = \frac{1 + [J_0(x\theta/2)]^2 + [J_1(x\theta/2)]^2}{2} \tag{4.9}$$

where θ is the half-angle subtended between the detection system and the spray, while J_0 and J_1 are the Bessel functions of order zero and one respectively. θ is expressed in radians, and is assumed to be small enough so that $\theta \approx \sin\theta$. For the optical set-up utilized in this work, the subtended angle between the lens and the spray was 0.083 rad. Finally, the value of R was calculated as:

$$R = \frac{Q_{ext,UV} \cdot \xi_{ext,UV}}{Q_{ext,VIS} \cdot \xi_{ext,VIS}} \tag{4.10}$$

In figure 4.22, the extinction coefficient (left) and the corresponding correction factor (right) are shown for each wavelength, as a function of the droplet diameter. It was considered that the size of fuel droplets, under diesel-like conditions, could vary between 10 and 60 μm. Therefore, an average value of $R = 0.975$ was used in the region of the images where any attenuation by Mie scattering of the liquid fuel could be observed. The largest error committed with this approach is below 10% within the defined range of diameters. For the rest of the spray, a value of R = 1 was utilized.

The other parameter required for the application of equation 4.6 is the absorption coefficient (ε). This parameter was measured for each fuel, according to the methodology described previously. However, as it has been reported in literature [24], the value of ε could depend on pressure and temperature. It has been assumed that the pressure along the whole spray is the same as the surrounding gases but the local temperature varies within it. For this reason, an adiabatic mixing model (state relationship) was utilized

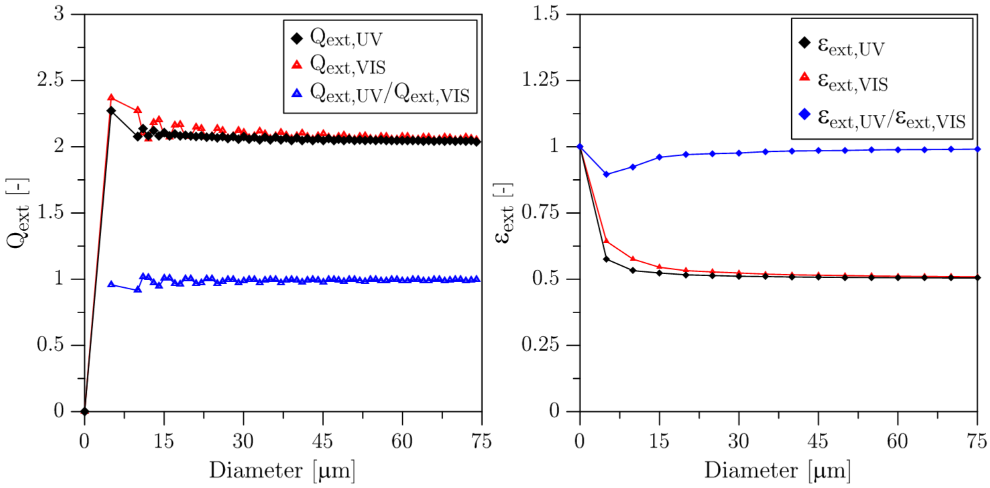

Figure 4.22. *Extinction coefficient (left) and correction factor (right) for 280 and 560 nm and different droplet diameters.*

(section 3.5). It is able to correlate the local fuel partial density with the local temperature of the mixture. Thus, a two-equation system was built to determine both local vapour partial density and temperature. The last step was the calculation of the vapour fuel mass fraction (Y_f). Once the partial density was obtained, the same adiabatic mixing model was utilized to calculate the vapour fuel mass fraction along the spray. It has been decided to work with this magnitude, as it is more used and referred in literature than ρ_{vf}.

4.3.3.1 Deconvolution algorithm

The UV-VIS LAS technique is based on line-of-sight (LoS) measurements, which integrates all the information along the optical path (projected data). However, in the case of sprays, information at the symmetry plane is of interest. Therefore, a numerical deconvolution (inversion) algorithm is required to reconstruct the fuel distribution at the symmetry plane. The simplest and most commonly used algorithm is the *Onion-Peeling method* [24, 25, 28, 35, 36] (OP). However, Dasch [37] states that the *Three-Point Abel inversion* (A3P) is the most recommendable due to the low noise and computational cost. Nevertheless, this kind of inversion techniques are characterized by a large numerical instability. This causes that small errors in the projected data are magnified by the deconvolution process. When low absorption fuels are considered, this could be a major issue as measurements would present a low signal-to-noise ratio. In order to solve this, a regularization method is proposed, known as *Tikhonov regularization* [36, 38] (TR). It is based on generating solutions to a sequence of well-posed problems, which satisfy the original problem with a very small residual. The value of this residual depends on a regularization parameter, which has to be optimized for each problem in order to obtain a good agreement between accuracy and noise. In the current work, an automatic selection method was employed, proposed by Åkesson et al. [38].

In figure 4.23 (right), an example of application is presented to compare the A3P with and without TR. A theoretical Gaussian curve (C) was numerically integrated to obtain the LoS projection of the profile (Att). Moreover, random noise was introduced to simulate measurement noise (figure 4.23 -left-). Then, the projected profile was deconvoluted to reconstruct the theoretical Gaussian curve (C) again. It is possible to see that, without TR, the reconstructed profile is strongly affected by the random noise. The use of the regularization algorithm clearly minimizes this problem. However, it is also possible to see that discrepancies tend to accumulate at the inner layers of the profile.

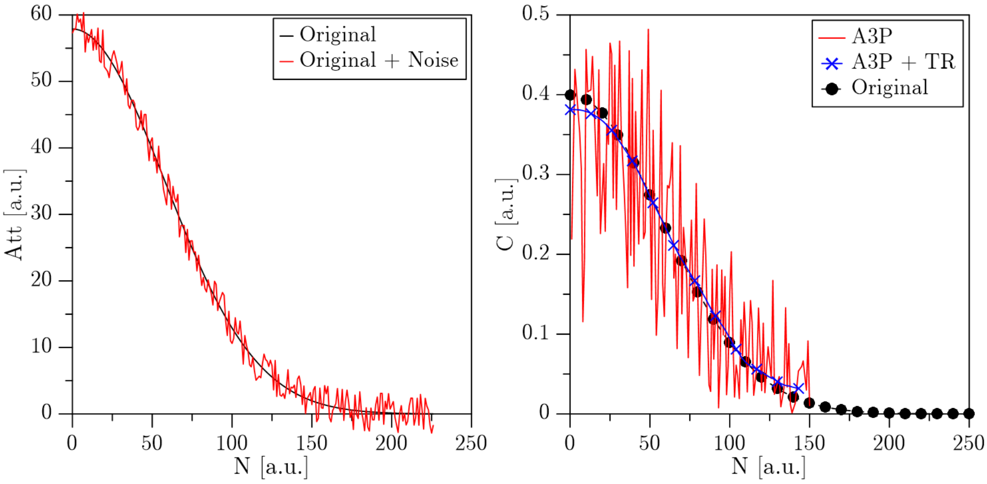

Figure 4.23. *Line-of-sight projection of a theoretical Gaussian profile with artificial noise (left) and its deconvolution, by means of A3P, with and without TR (right).*

Dasch [37] suggests that one of the most common mistakes when using the traditional deconvolution algorithms is the oversampling. When the spacing between points is decreased, the real difference between adjacent LoS projections becomes small. When this difference is comparable with the measuring noise, the deconvolution is highly inaccurate. Moreover, he provides an expression for the total error committed by the deconvolution algorithm, which suggest that it is inversely proportional to the data spacing (ΔN). Therefore, one could propose that a simpler solution to reduce the effect of the measuring noise would be considering just one pixel out of n. In this way, if resolution is reduced to 1/n, data spacing would increase directly, reducing the sensitivity to noise. However, when signal-to-noise ratio is low (as it will be discussed later), the required spacing is too large and sometimes it is not even possible to completely remove the influence of noise. Besides, there is not a clear criterion to select the data spacing and if it is too high, information regarding the original shape of the profile can be lost.

One of the main drawbacks of the TR algorithm is that the computational cost is high. In this regard, one possibility is to combine TR with an increase of data spacing. A comparison between increased and original data spacing is shown in figure 4.24. The theoretical profile and the deconvolution process are the same as described for figure 4.23. It is possible to see that without using TR, the influence of noise has been reduced but not completely. Besides, when TR is utilized, the differences between varying and not varying data spacing is minimum. Considering all the foregoing, the deconvolution algorithm utilized in the current work was a combination of the Three-Point Abel Inversion and the Tikhonov regularization. Moreover, the data spacing was increased to $\Delta N = 10$, to reduce the computational costs. The new resolution corresponds to 0.5 mm spacing between adjacent points, according to the pixel/mm ratio obtained with the optical set-up.

4.3.3.2 Precision analysis

Before the deconvolution algorithm is applied, the absorption signal from all repetitions is averaged ($\overline{Abs}$), to minimize the relative importance of the noise. In order to obtain an estimation of the precision of the measurement, the corresponding standard deviation (σ_{Abs}) was calculated. The uncertainty at each calculation step was obtained according to the theory of propagation of uncertainties. For a non-linear combination (f) of independent variables (x and y), the standard deviation propagation can be expressed as:

$$\sigma_f = \sqrt{\left(\frac{\delta f}{\delta x}\right)^2 \sigma_x^2 + \left(\frac{\delta f}{\delta y}\right)^2 \sigma_y^2} \tag{4.11}$$

Then, applying equation 4.11 to the calculation of light attenuation ($Att = \ln(I_0/I)$), the following expression can be obtained for the corresponding standard deviation (σ_{Att}) at each wavelength:

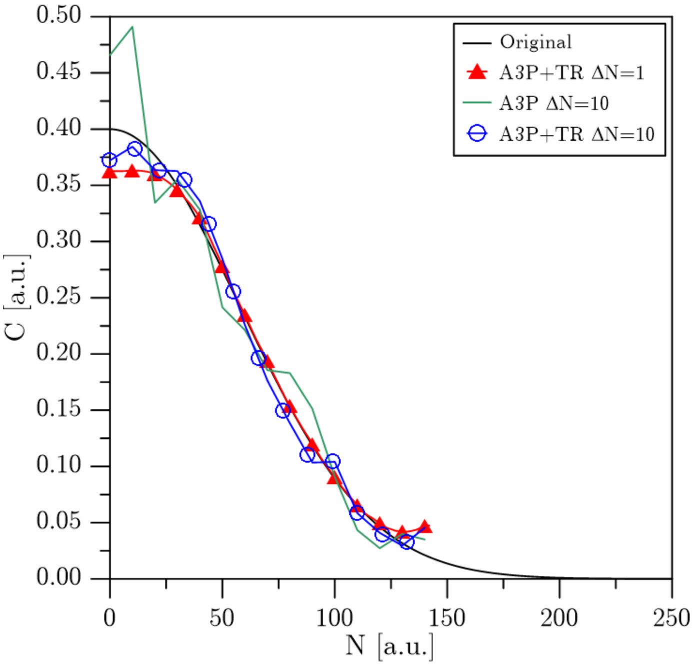

Figure 4.24. *Example of application of TR and data spacing (ΔN) increase.*

$$\sigma_{Att} = \sqrt{\left(\frac{1}{I_0}\right)^2 \sigma_{I0}^2 + \left(-\frac{1}{I}\right)^2 \sigma_I^2} \tag{4.12}$$

where σ_I and σ_{I0} are the standard deviation of all the repetitions, with and without injection respectively. Once attenuation at each wavelength is calculated, the vapour absorption signal can be obtained (equation 4.6) and the corresponding standard deviation (σ_{Abs}) is:

$$\sigma_{Abs} = \sqrt{\sigma_{Att,UV}^2 + (-R)^2 \sigma_{Att,VIS}^2} \tag{4.13}$$

where $\sigma_{Att,UV}$ and $\sigma_{Att,VIS}$ are the standard deviation of the UV and VIS attenuation signals respectively. Finally, as it has been described previously, the vapour absorption signal was divided in two halves, which were averaged. Therefore, the resulting standard deviation (σ_{Abs}^*) can be calculated by means of equation 4.14:

$$\sigma^*_{Abs} = \sqrt{\left(\frac{1}{2}\right)^2 \sigma^2_{Abs,1} + \left(\frac{1}{2}\right)^2 \sigma^2_{Abs,2}} \tag{4.14}$$

Finally, once the standard deviation is known, it is possible to calculate the Coefficient of Variation (CoV) as:

$$CoV = \frac{\sigma^*_{Abs}}{\overline{Abs}} \tag{4.15}$$

4.3.4 Results and discussion

In the current section, results for both absorption coefficient calibration and fuel distribution are presented. Firstly, the absorption coefficient measurements are discussed to determine the accuracy and reliability of the procedure and the results. Secondly, the fuel mass fraction distribution for DEC, 50DEC and HEPB3 are compared in order to highlight the limitations of UV-VIS LAS technique when low absorption fuels are employed.

4.3.4.1 Absorption coefficient

As commented before, to determine the absorption coefficient of the fuel, an homogeneous air-fuel mixture was generated in the combustion chamber by injecting fuel early in the compression stroke, just after the transfers were blocked by the piston. To ensure homogeneity of the mixture, measurements were performed after TDC according to table 4.4. In figure 4.25, a series of assembled images of attenuation at 280 nm is shown. It was obtained by injecting 54.37 mg of DEC, at in-cylinder conditions corresponding to $\rho_c = 19.27\ kg/m^3$ at TDC. As it can be seen, the distribution of attenuation is practically homogeneous along the whole combustion chamber, so that optics shifting was not necessary for calibration.

For each fuel and test condition, attenuation at 280 nm and 560 nm was measured at the middle position (see figure 4.20). For all cases, measured attenuation at the visible wavelength was in the range of background noise, which confirmed that no absorption was taking place at this wavelength. In figure 4.26 (left), ε values are presented for the three mixtures of HEP and HAF, as well as for the low absorption fuels. The first point (lowest temperature) of each series correspond to the value obtained at 0.1 MPa and 298 K (STP), measured with the spectrometer. The rest of the points

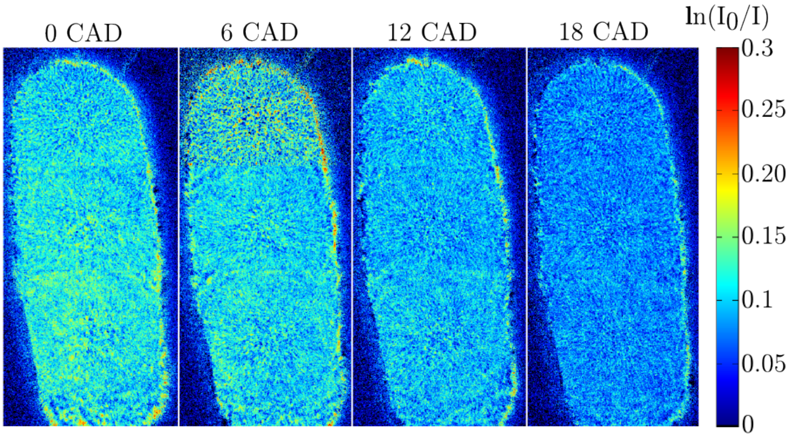

Figure 4.25. *Example of in-cylinder homogeneous attenuation for DEC, at* $\rho_c = 19.27\ kg/m^3$ *at TDC.*

correspond to different combinations of mean temperature and pressure inside the cylinder at the moment of image acquisition. The comparison of two series with similar in-cylinder pressure at TDC enables the analysis of the temperature influence, while the comparison of two series with similar in-cylinder temperature at TDC makes it possible to study the effect of pressure. In figure 4.26 (right), the correlation of attenuation and vapour molar concentration is also shown.

As it can be observed, the absorption coefficient increases with the HAF fraction while DEC and 50DEC present significantly lower ε values. For all the fuels, a decrease of ε between STP and engine conditions is observed. This is coherent with results presented by Zhang et al. [24], who reported a large reduction of the absorption coefficient when pressure and temperature increased. However, at certain level (p_c over 3 MPa and T_c over 650 K) this sensitivity tends to decrease. Moreover, it seems to depend on the type of molecule, as they report variations of the absorption coefficient around 10% for 1,3-Dimethylnaphtalene and 60% for α-Methylnaphtalene, when temperature changed from 575 to 650 K at $p_c = 3\ MPa$. In the same line, Yamakawa et al. [25] reported that the absorption coefficient of p-xylene is almost not affected by thermodynamic conditions above 1.5 MPa and even only 400 K. Anyhow, all of them conclude that the sensitivity of ε to both in-cylinder pressure and temperature tends to minimize or even disappear at high pressures and temperatures. This is consistent with the results presented in this work.

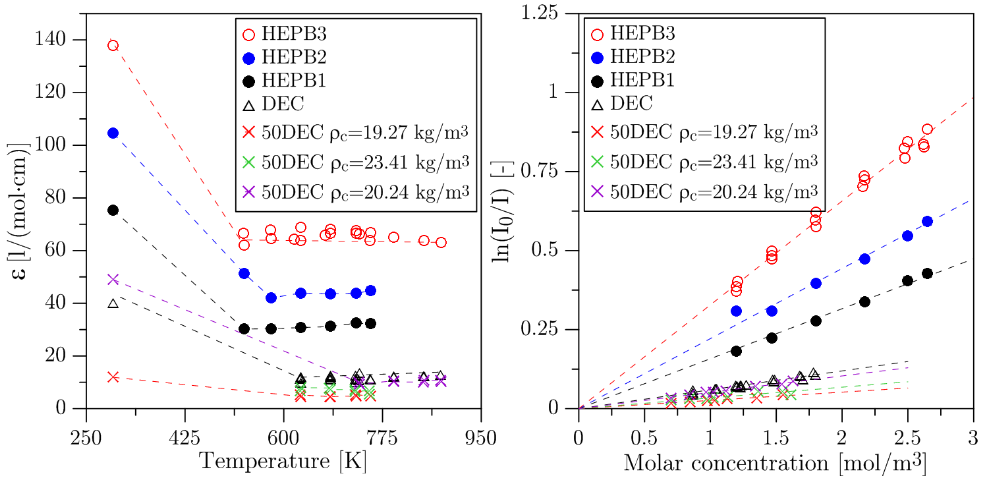

Figure 4.26. *Absorption coefficient versus temperature for all the fuels, at different engine conditions (left). Correlation between attenuation and molar concentration for all the fuels and different engine conditions (right).*

In the case of DEC and 50DEC, attenuation values were obtained for different masses of fuel injected in the cylinder. The consistency of all measured points shown in figure 4.26 (left) suggests that the hypothesis of complete evaporation of the fuel is valid in all the cases considered here and discards any systematic error over $\overline{\rho_{vf}}$ calculation. For all the cases, absorption is in direct proportion to the molar concentration inside the cylinder, as it is shown in figure 4.26 (right), which confirms that the Lambert-Beer's law is followed.

The data presented in figure 4.26 for DEC and HEPB3 show that the influence of thermodynamic conditions is low and even negligible under the test conditions defined in figure 3.3. Therefore, it can be concluded that the absorption properties of both fuels do not depend neither on pressure nor on temperature (within the range considered in this work) and the validity of this argument will be discussed later.

Contrary, for 50DEC clear discrepancies can be observed between different datasets (i.e. data obtained for each ρ_c at TDC). Nevertheless, if it is analysed in detail, it is possible to see that this variability is not caused by thermodynamic conditions. The three datasets presented in figure 4.26 for this fuel are formed by sets of points, obtained at different combinations of pressure and temperature within the same thermodynamic cycle. In this way, if each dataset is considered separately, no clear dependence between

ε and thermodynamic conditions can be deduced. If the pressure of the cycle is increased (i.e. from 19.27 kg/m^3 to 23.41 kg/m^3 at TDC), an increase of the absorption coefficient is reported. In the same way, if the temperature of the cycle is increased (i.e. from 23.41 kg/m^3 to 20.24 kg/m^3 at TDC) an increase of ε is also reported. However, both trends are contrary to the ones described previously for other hydrocarbons [24, 25]. Moreover, the variation of ε is also detected in the data corresponding to STP, which corroborates that it could not be caused by thermodynamic conditions. According to the experimental procedure followed, the increase of the absorption coefficient coincides with the temporal sequence of tests carried out. Thus, the author considers that the main cause of the variation of the optical properties is a degradation/contamination of the fuel. A later analysis by Fourier-Transformed Infrared Spectroscopy (FTIR) (A2 Technologies PAL) and Nuclear Magnetic Resonance (Varian Unity-300 NMT Spectrometer) detected the presence of a new specie in the aged fuel, but in low concentrations. However, it was not possible to identify it.

4.3.4.2 Signal-to-noise considerations

Once the absorption coefficient is obtained with the calibration procedure, the state relationship (section 3.5) can be used to calculate the distribution of the vaporized fuel mass fraction (Y_f) at the symmetry plane of the spray. In figure 4.27, an example is shown for HEPB3, DEC and 50DEC, obtained at $\rho_c = 23.41\ kg/m^3$ at TDC. The edge of the liquid region (from MIE visualization) has been depicted as a red curve in the plots. In the three maps it can be observed that Y_f starts increasing at the first millimetres, until it reaches a local maximum value ($Y_{f,evap}$). In this figure, the first differences between low (i.e. DEC and 50DEC) and high absorption fuels (i.e. HEPB3) arise. The amount of noise (data scattering) seems to increase as the absorption coefficient of the fuel decreases, especially in presence of liquid.

In order to better understand the differences between the two types of fuels considered in this study, the attenuation caused by them can be directly compared. In figure 4.28, the LoS attenuation signal along the spray axis is shown, for HEPB3 (left) and 50DEC (right), at 280 and 560 nm. Besides, the resulting vapour absorption signal is also depicted. Data correspond to 2000 μs aSoE, at $\rho_c = 23.41\ kg/m^3$ at TDC and $p_{inj} = 100\ MPa$. When both fuels are compared, it is possible to see that the vapour absorption of 50DEC is significantly lower than that of HEPB3. Besides, it is of the same

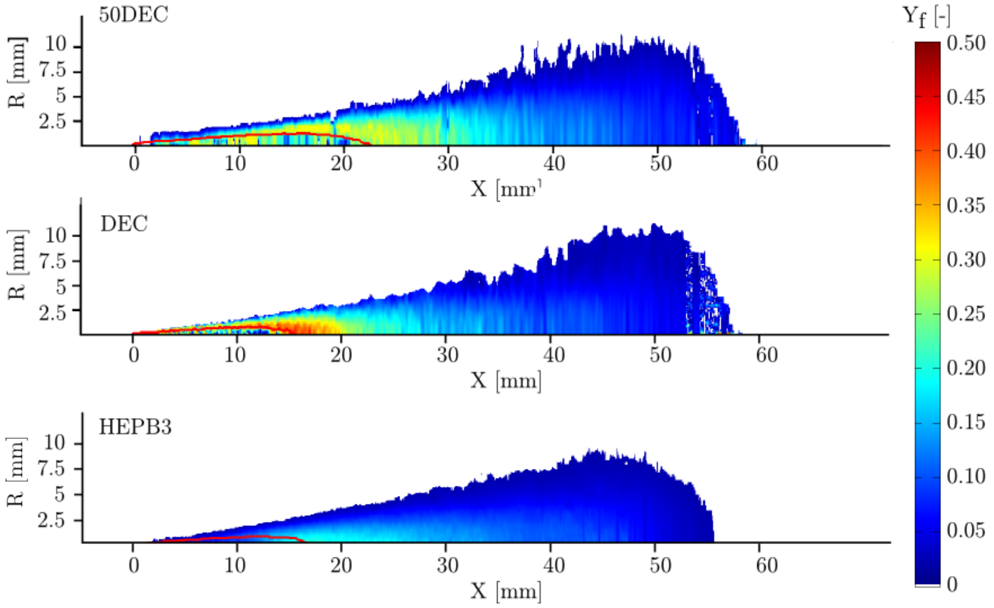

Figure 4.27. *Fuel mass fraction distribution for HEPB3, DEC, 50DEC at the symmetry plane. The red line represents the limits of the liquid fuel region. Data correspond to 2000 µs aSoE at* $\rho_c = 23.41\ kg/m^3$ *at TDC and* $p_{inj} = 100\ MPa$.

order of magnitude as the attenuation obtained for the visible wavelength. If this last signal is considered as noise (mainly caused by beam steering), the corresponding signal-to-noise ratio (calculated between 25 and 50 mm) is 1.80. In contrast, the attenuation of HEPB3 at 280 nm is in general one order of magnitude higher and even at the first millimetres, where the dense liquid region is located, some vapour absorption signal can be detected. In this case, the signal-to-noise ratio is 26.46. Regarding DEC, a similar calculation was performed resulting on a signal-to-noise ratio of 4.89, which is closer to 50DEC than HEPB3.

With the average vapour absorption ($\overline{Abs}$) signal and the corresponding standard deviation (σ^*_{Abs}), the coefficient of variation can be calculated for each fuel. In figure 4.29, an example of the CoV distribution for each of them is presented. Data correspond to $\rho_c = 23.41\ kg/m^3$ at TDC and $p_{inj} = 100\ MPa$, but it can be considered as representative of all test conditions. It is possible to see that CoV increases in the regions where the signal level decreases (i.e. the dense liquid region and the edge of the spray). Moreover, a similar behaviour can be observed when the absorption coefficient decreases. At the outer layers of the spray, CoV rises for the three fuels.

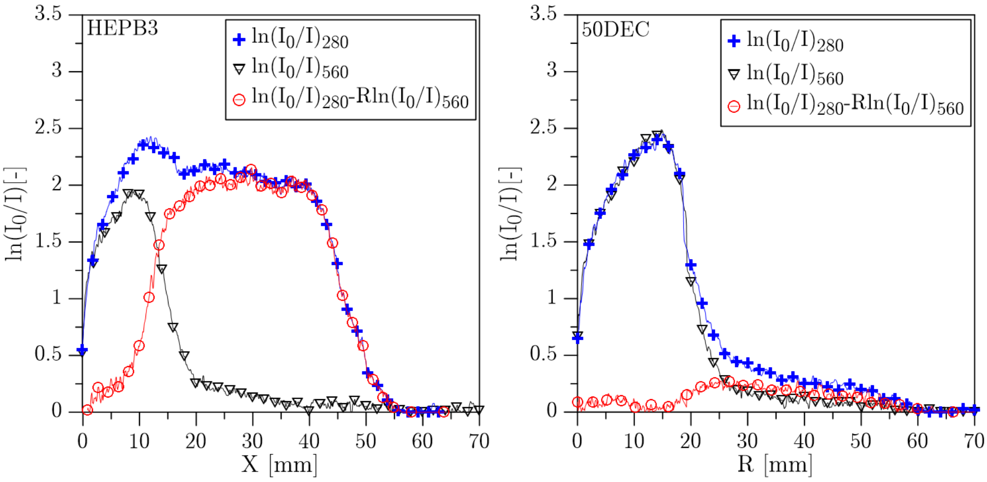

Figure 4.28. *On-axis LoS attenuation for HEPB3 (left) and 50DEC (right). Data correspond to HEPB3 and 50DEC, at* $\rho_c = 23.41\ kg/m^3$ *at TDC and* $p_{inj} = 100\ MPa$.

However, this rapid increase is reached sooner for the low absorption fuels. This suggest that, for these fuels, the data scattering at the outer part of the spray could be important in comparison with the average signal, which would reduce the accuracy and precision of the results. Moreover, the deconvolution algorithm can spread these uncertainties to the whole radial profile.

All the foregoing information remarks the drawbacks of working with low absorption fuels, in comparison with other hydrocarbon molecules with more suitable optical properties. The large data scattering and low signal-to-noise ratio could limit the applicability of this technique, and both should be considered when analysing the results presented in the following paragraphs.

4.3.4.3 Spray measurements

The ε calibration procedure had to be validated to guarantee the reliability of results. For this purpose, vapour fuel distribution was measured for the three HEPB# blends, at $\rho_c = 19.27\ kg/m^3$ at TDC, $p_{inj} = 100\ MPa$ and 2000 μs aSoE. Its comparison is depicted in figure 4.30 (left), where the on-axis vapour absorption at the symmetry plane of the spray is shown. The corresponding partial density (ρ_{vf}) is included in figure 4.30 (right). Similar fuel distributions could be expected as mass flow

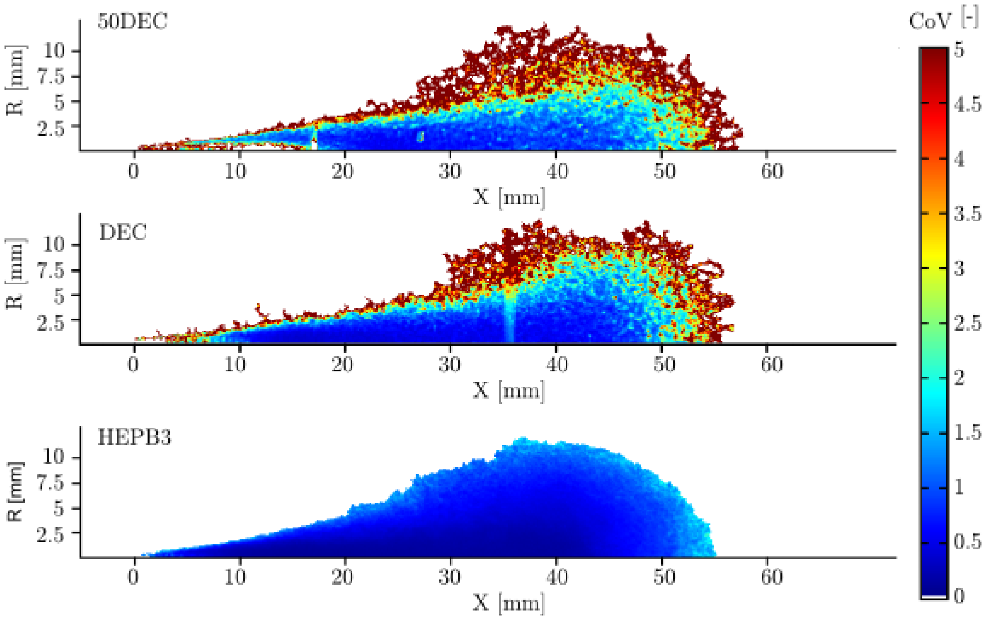

Figure 4.29. *Coefficient of variation of the LoS absorption signal for 50DEC, DEC and HEPB3. Data correspond to 2000 μs aSoE, at* $\rho_c = 23.41\ kg/m^3$ *at TDC and* $p_{inj} = 100\ MPa$.

rate and spray momentum flux should barely change [39] between blends. Thus, as it can be seen, consistent results were obtained at the completely vaporized region (downstream the maximum peak). It has to be noted that the absorption coefficient was measured for the completely vaporized fuel, with known HEP/HAF fraction. As long as liquid length is not reached, the local fraction of each component is unknown and thus the absorption coefficient cannot be strictly applied. Therefore, in the case of fuels with more than one component, ε should be strictly only applied to the completely vaporized part of the spray, where it is supposed that the composition is the same as the original blend [40]. For this reason, differences larger than expected are observable before the maximum peak is reached.

The second aspect that needed to be validated was the sensitivity of ε to in-cylinder pressure and temperature. According to the results presented in figure 4.26, a constant ε value was used to obtain Y_f for each fuel, under different thermodynamic conditions. It is worth mentioning the case of 50DEC, whose the absorption coefficient was varied according to its progressive degradation. The vapour fuel mass fraction of HEPB3 is shown in figure 4.31, for the three ambient gas densities proposed in figure 3.3. Data

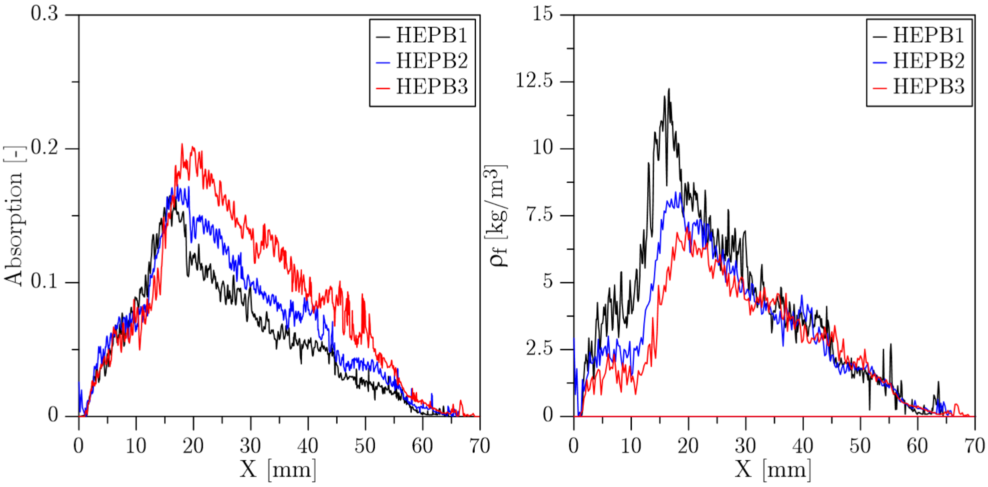

Figure 4.30. *Vapour absorption (left) and* ρ_{vf} *at the symmetry plane of the spray for the three mixtures of HEP and HAF, along its axis. Data correspond to 2000* μs *aSoE,* $\rho_c = 19.27\ kg/m^3$ *at TDC and* $p_{inj} = 100\ MPa$*.*

correspond to the value along the spray axis. The X-coordinate of each curve has been normalized with the equivalent diameter [41], which is defined as $\phi_{eq} = d_0\sqrt{\rho_f/\rho_c}$, where d_0 is the nozzle exit diameter, ρ_f is the fuel density and ρ_c is the ambient gas density. It can be observed that the three distributions collapse when the X-coordinate is normalized, which confirms that results are consistent. Thus, it can be stated that ε is independent of thermodynamic conditions for the fuels utilized in this study, as expected.

The ε values shown in figure 4.26 were utilized to obtain the fuel vapour distribution of DEC, 50DEC and HEPB3. In figures 4.32 (1000 μs aSoE) and 4.33 (2000 μs aSoE), on-axis vapour mass fraction at the symmetry plane of the spray is shown for the three fuels, at the three ambient densities defined in figure 3.3 and $p_{inj} = 100\ MPa$. In the highly dense liquid region (i.e. first 10 - 20 mm), data for 50DEC is not plotted due to the extremely high noise observed. The low amount of fuel evaporated, in combination with a low absorption coefficient, leads to large uncertainties on the experimental data (low signal-to-noise ratio and high CoV). Thus, despite offering promising results with DEC, it can be stated that the methodology described in this work is not sensitive enough to characterize this region if fuels with absorption properties as 50DEC are considered. Nevertheless, it is important to highlight that near the maximum liquid length, the technique is able to measure the vapour fuel distribution in presence of liquid, even for 50DEC. This

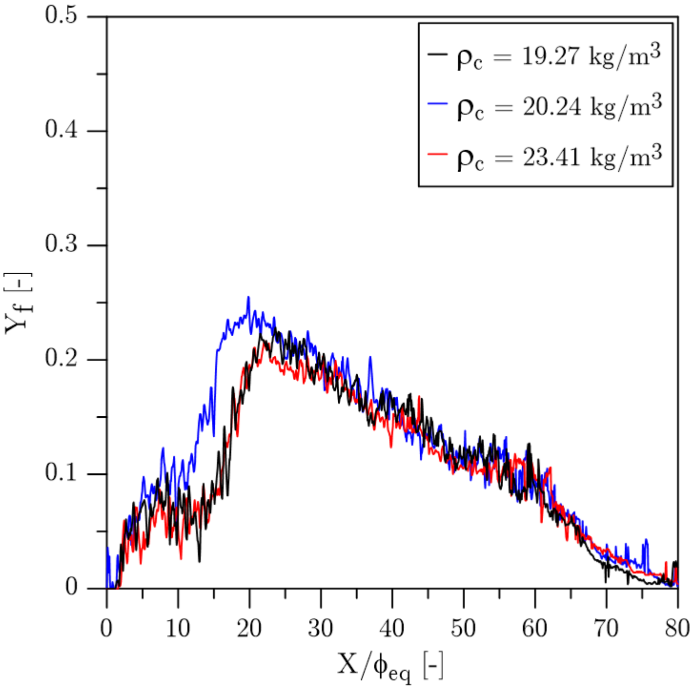

Figure 4.31. *Y_f distribution of HEPB3 at the symmetry plane, along spray axis. Data correspond to 2000 μs aSoE, at the thermodynamic conditions defined in figure 3.3 and $p_{inj} = 100\ MPa$.*

represents a major advantage when compared, for example, with Rayleigh scattering or PLIF. Downstream of the maximum vapour mass fraction, liquid is completely evaporated. From this point onwards, air entrainment continues and fuel mass fraction decreases until the tip of the spray is reached. At the completely vaporized region, mass fraction distribution for both HEPB3 and DEC coincide. However, it is not the case for 50DEC. For $\rho_c = 23.41\ kg/m^3$ and $\rho_c = 19.27\ kg/m^3$ cases, higher values of Y_f were obtained for this fuel in comparison with the other two. When 50DEC and HEPB3 are compared (from 25 to 50 mm), these differences are around 20% for $\rho_c = 23.41\ kg/m^3$ and 40% for $\rho_c = 19.27\ kg/m^3$. In terms of time evolution, the comparison do not show any difference between 1000 and 2000 μs aSoE.

It has been stated in the previous section that the calibration methodology was able to characterize low ε values. However, it can be observed (figure 4.26) that all the fuels present a similar standard deviation, despite value of ε can be more than one order of magnitude different. The main consequence is that, while for HEPB3 the deviation accounts for a maximum of 5% of the mean

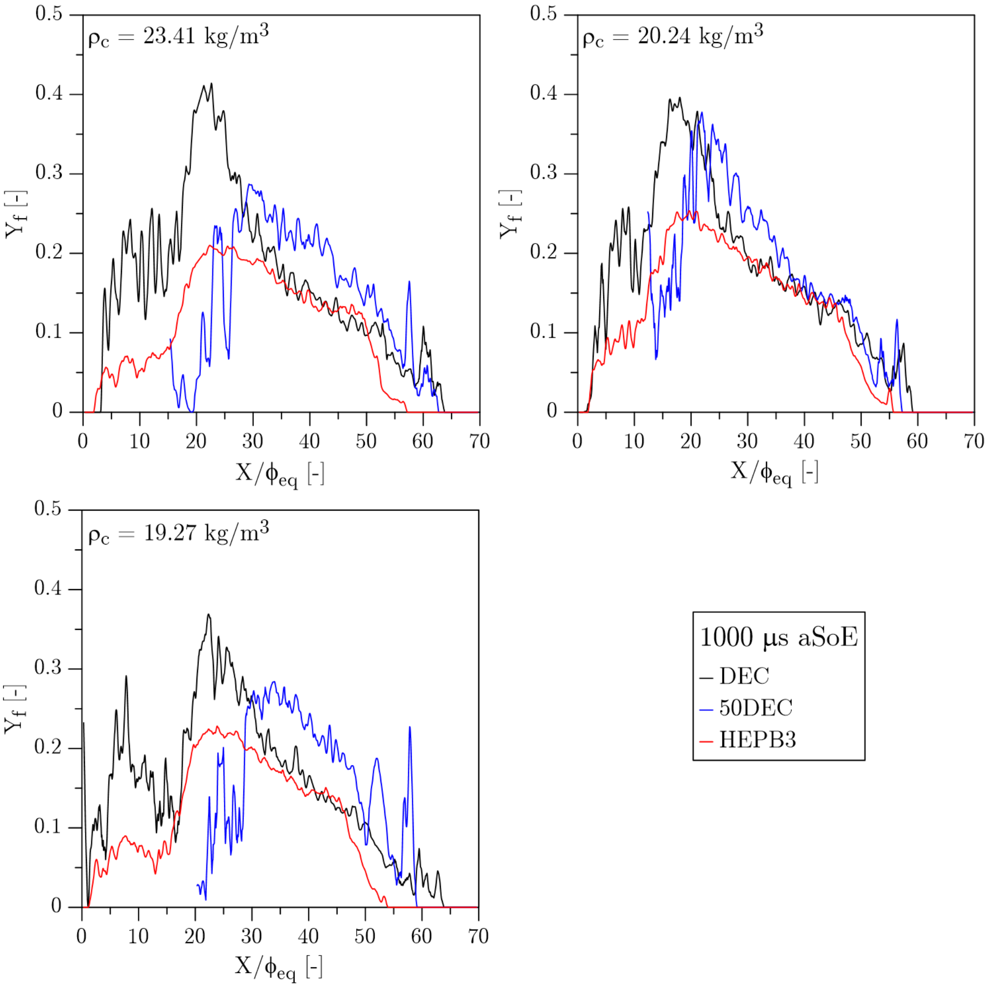

Figure 4.32. *Y_f distribution of DEC, 50DEC and HEPB3 at the symmetry plane, along spray axis. Data correspond to 1000 μs aSoE, at the thermodynamic conditions defined in figure 3.3 and p_{inj} = 100 MPa.*

value, in the case of 50DEC the standard deviation reaches almost 50% of the mean value. This leaves much uncertainty over the calculated average value of ε, which directly affects Y_f distribution estimations.

According to the mixing theory of sprays [42] it can be expected that, at the stabilized region[4] of the spray, Y_f radial profiles should be self-similar when

---

[4] This term refers to the region where fuel has been completely evaporated, avoiding the region near the tip of the spray which is strongly affected by the interaction with the airflow within the combustion chamber

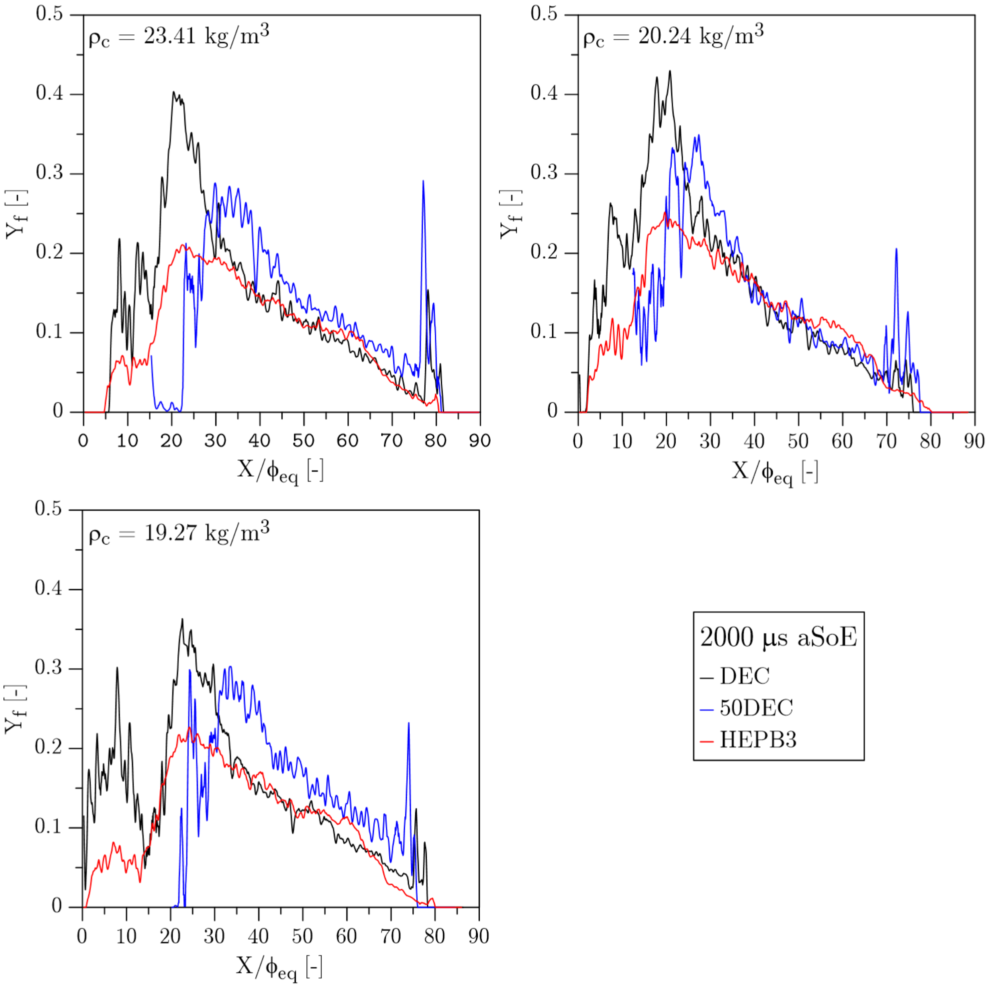

Figure 4.33. *Y_f distribution of DEC, 50DEC and HEPB3 at the symmetry plane, along spray axis. Data correspond to 2000 μs aSoE, at the thermodynamic conditions defined in 3.3 and $p_{inj} = 100\ MPa$.*

they are normalized in the abscissa axis by Y_f at the centre line ($Y_f/Y_{f,cl}$) and in the ordinate axis by the distance to the nozzle tip (R/X). This approach has been followed to compare the radial distributions obtained for the three fuels. For this purpose, only information from 1000 μs aSoE was considered, to minimize the influence of the spray-airflow interaction. At this time the maximum LL was reached for all test conditions, while the spray development should be less affected by the airflow than it could be at 2000 μs aSoE. Besides, only the stabilized region of the spray (i.e. between 25 and

35 mm from nozzle) has been included in the analysis. Normalized profiles were calculated within this range, together with the radii where 15%, 50% and 90% of $Y_{f,cl}$ were located. In figure 4.34, these radii are presented for DEC, 50DEC and HEPB3 and the three test conditions included in figure 4.32 ($p_{inj} = 100\ MPa$). Data below 15% have not been considered in this analysis due to the large uncertainties observed in these regions and the low signal-to-noise ratio, especially for the low absorption fuels. This made it difficult to calculate accurately the radius corresponding to values below this percentage.

The first thing that one can notice is that the scattering is, in general, smaller for HEPB3 than for the other two fuels. Nevertheless, for 90%, certain variability is observed for all of them. As it has been discussed previously, the deconvolution algorithm introduces errors at this part of the radial profiles. A second aspect to note is that, in general, values for the three fuels are similar. This suggests that the discrepancies found for 50DEC, reported in figures 4.32 and 4.33, are related to the value of the absorption coefficient. In this work, ε acts like a proportionality constant as it has no dependence with neither pressure nor temperature. Therefore, when profiles are normalized, the effect of the absorption coefficient is removed and the three fuels are similar. Finally, it is worthy to note that the flat trends observed for the normalized plots confirm that the measured profiles are self-similar when moving along the spray axis.

Taking into account the foregoing analysis, data corresponding to DEC has been utilized to analyse the effect of the different boundary conditions. In figure 4.35 (left), the Y_f on-axis distribution at the symmetry plane of the spray is shown for the three ambient densities proposed in figure 3.3. To analyse the fuel radial spread, normalized radial profiles (see figure 4.34) between 25 and 35 mm from nozzle have been averaged and the result is plotted in figure 4.35 (right). When in-cylinder pressure is decreased, it can be seen that the Y_f peak moves further from the nozzle and decreases its value. This is coherent with the trends presented in figure 4.11, as it was observed that reducing p_c increases LL (which coincides with the Y_f peak). However, this variation seems to not affect the $Y_{f,evap}$ value. From this point, at any X-coordinate within the stabilized region of the spray, Y_f seems to decrease locally when increasing p_c (and so ρ_c). Besides, it also makes the spray to spread radially. This is coherent with the increase of the spray angle observed with the schlieren visualization (figure 4.15). When T_c increases, LL decreases and so it does the distance of the Y_f peak to the nozzle. An increase of $Y_{f,evap}$ could be expected as less air should be necessary to reach the complete

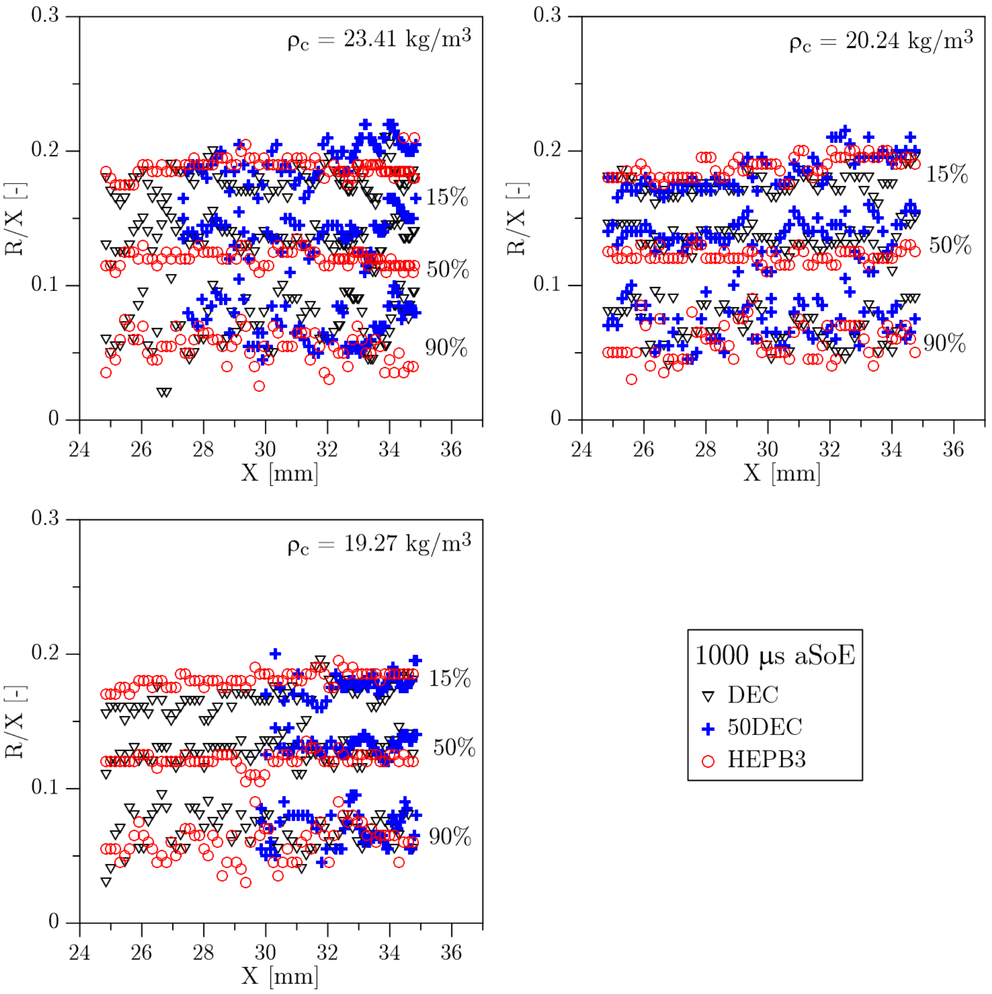

Figure 4.34. *Radii for 15%, 50% and 90% of $Y_{f,cl}$ fir DEC, 50DEC and HEPB3 along the spray axis. Data correspond to 1000 μs aSoE, at the three ambient densities proposed in figure 3.3 and $p_{inj} = 100\ MPa$.*

evaporation. However, this is not observed in the experimental data. At the fully vaporized region, a slightly increase of Y_f when increasing temperature is observed, which is coherent with the decrease of the in-cylinder density (the spray should penetrate “easier”, reducing the radial spread). However, a corresponding effect is not observed for the radial profiles. Nevertheless, this is coherent with the minimum variations reported for S and α when T_c was varied.

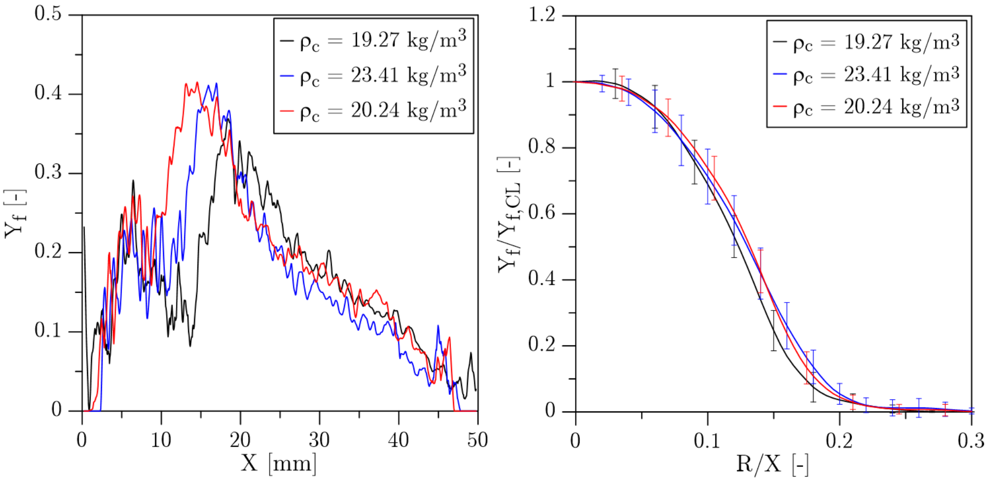

Figure 4.35. *Effect of in-cylinder temperature and pressure over on-axis (left) and radial (right)* Y_f *distribution. Data correspond to DEC, at 1000* μs *aSoE and* $p_{inj} = 100\ MPa$.

In figure 4.36, the fuel distribution is compared for the three injection pressures considered in this work. In this case, it is possible to see that the spray penetration varies, but no differences are visible in terms of Y_f. The location of the maximum peak coincides, which is coherent with the independence of LL with p_{inj} reported previously. Moreover, the same $Y_{f,evap}$ has been obtained for the three cases. A higher injection pressure causes an increase of mass flow rate, which is compensated by an increase of air entrainment. In terms of radial distributions, no differences are observable when comparing the normalized profiles within the stabilized region of the spray. The macroscopic characterization confirms this result, as no differences on the spray cone angle were detected when varying p_{inj}.

Finally, the problems reported for 50DEC difficult the analysis of the effect of fuel properties. Based on the foregoing information, the macroscopic characterization can provide some insight in this regard. It was reported in the previous section that these fuels present different LL, but similar α and S. Therefore, it was concluded that main differences should be expected before LL is reached but, downstream this point, similar fuel distribution should be obtained. However, as it has been discussed in the previous paragraphs, this is not observed when 50DEC and DEC are compared. A more detailed analysis have been included in the following paragraphs.

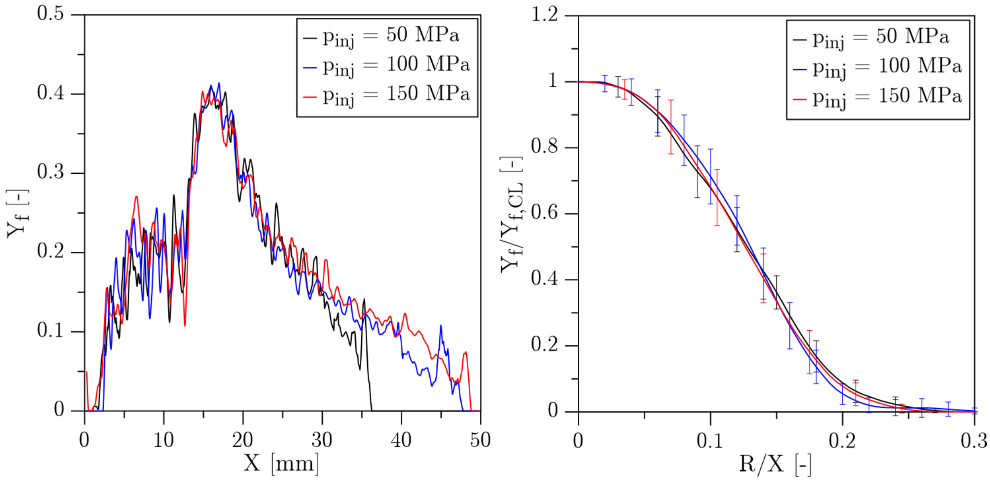

Figure 4.36. *Effect of injection pressure over Y_f on-axis (left) and radial (right) distribution. Data correspond to DEC, at 1000 µs aSoE and $\rho_c = 23.41$ kg/m^3.*

4.3.5 Comparison with other data sources

It is not common to find in literature a direct comparison between UV-VIS LAS measurements and other data sources, like theoretical models or other optical techniques. For this reason, it was decided to carry out a comparison between LAS, a 1D-Model (see section 3.5) and the ECN [18] database. In a first instance, a more detailed comparison has been performed focused on DEC measurements corresponding to $\rho_c = 23.41$ kg/m^3. Then, the 1D-Model has been utilized to validate the trends described in the previous paragraphs.

The ECN data corresponds to Planar Rayleigh Scattering (PRS) measurements performed in a spray of n-Dodecane (DOD), injected at 150 MPa into an ambient density of 22.8 kg/m^3. The nominal nozzle outlet diameter was 0.090 mm while the real diameter was 0.0837 mm, according to measurements with optical microscopy. The area contraction coefficient (C_a) for this orifice was 0.98. The fuel density at the injection conditions was 713 kg/m^3.

The 1D-Model calculations were performed under variable boundary conditions, to resemble the real injection and mixing processes as close as possible. Experimentally measured in-cylinder pressure and derived density were utilized to define the ambient gas conditions, while the injection characteristics were obtained from the hydraulic characterization of the injection system (section 3.4). An specific calibration procedure of the

1D-Model had to be followed, to adjust it as much as possible to the particularities of the test rig. As discussed in section 3.5, one of the main hypotheses of the model is that the spray is injected into a quiescent ambient gas. However, this is not strictly applicable to the whole combustion chamber and this fact has to be considered for a proper calibration. Two spray cone angles (α_1 and α_2) are required as inputs according to the variable spreading angle proposed by Pickett et al. [43]. These authors suggest that the spray cone angle is not necessarily constant with the axial direction. In fact, it is smaller in the near field of the jet compared to the far field. Based on this, they propose a 1D-Model which defines two spray regions, with different spray cone angle. The concept has been schematized in figure 4.37.

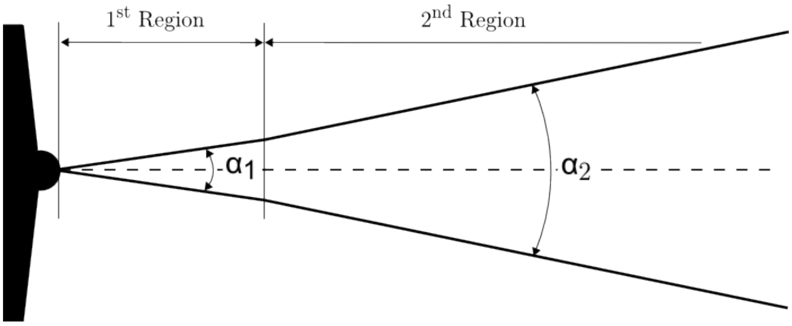

Figure 4.37. *Depiction of the variable spray cone angle hypothesis.*

In a first instance, just one angle (α_1) is optimized to get a predicted spray penetration similar to the experimental one. It was considered only the time interval between SoI and the instant when maximum LL was reached, to avoid the penetration decay due to the in-cylinder airflow interaction. Afterwards, keeping the first angle fixed, the second one (α_2) is adjusted comparing the predicted penetration with a largest range of the experimental one. Besides the inflection point between the two regions represented in figure 4.37 has to be also defined. For this study, the inflection point was arbitrary fixed at 15 mm from nozzle for all the test conditions. Experimental data corresponding to $\rho_c = 23.41\ kg/m^3$ at TDC and $p_{inj} = 100\ MPa$ was used as reference to optimize both angles. The first one was kept constant for all conditions, while the second one was scaled with the in-cylinder density according to equation 4.16 [44].

$$\tan(\theta/2) \propto (\rho_c/\rho_f)^{0.19} \tag{4.16}$$

In figure 4.38, a comparison between predicted and experimental penetrations is depicted. It is possible to see that, even for the most optimized angles, differences arise above 1000 μs aSoE. This is a consequence of the air-fuel interaction that has been described in chapter 3, as the slow-down suffered by the spray is not considered by the 1D-Model. Thus, the comparison between calculated and measured data will be performed for 1000 μs aSoE. In this figure it is also possible to see that, under certain conditions, LL is underpredicted.

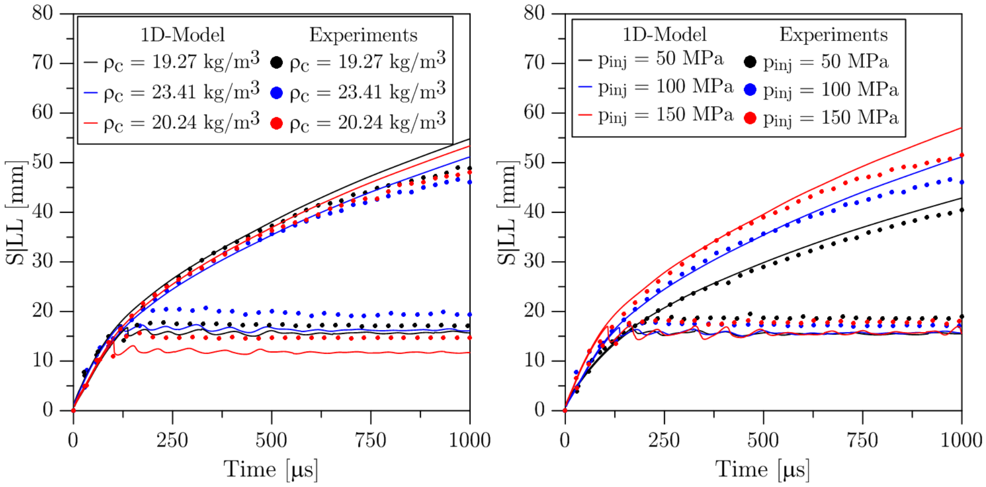

Figure 4.38. *Comparison between calculated and experimental S and LL, for different* ρ_c *(left) and* p_{inj} *(right). Data correspond to DEC, at* $T_c = 765\ K$.

Fuel injection temperature (T_{inj}) is another input parameter of the model. However, it cannot be determined with accuracy for this test rig. Despite the temperature of the cylinder head and the injector holder were kept constant, it was proved (see section 3.2.3) that the temperature of the injector tip reached higher values, depending on the in-cylinder thermodynamic conditions. A proper definition of the injection temperature is important, as LL and $Y_{f,evap}$ are strongly related with this parameter. An example of the influence of T_{inj} over the 1D-Model calculation is presented in figure 4.39. Spray penetration (S and LL) and the Y_f on-axis distribution at the symmetry plane have been calculated for two injection temperatures: 373 K, which is similar to the cooling temperature; and 457 K, according to measurements performed at the tip of the injector. In the figure, it is possible to see that S is not affected by this parameter. However, the effect over LL and $Y_{f,evap}$ is not negligible. In fact, if fuel were injected at higher temperature it would require less heat to vaporize, and thus less mixing time. The comparison presented in this figure provides a clear idea of the range within calculations could vary, which should be considered for a proper analysis as it is not possible to determine the real value of T_{inj} with accuracy.

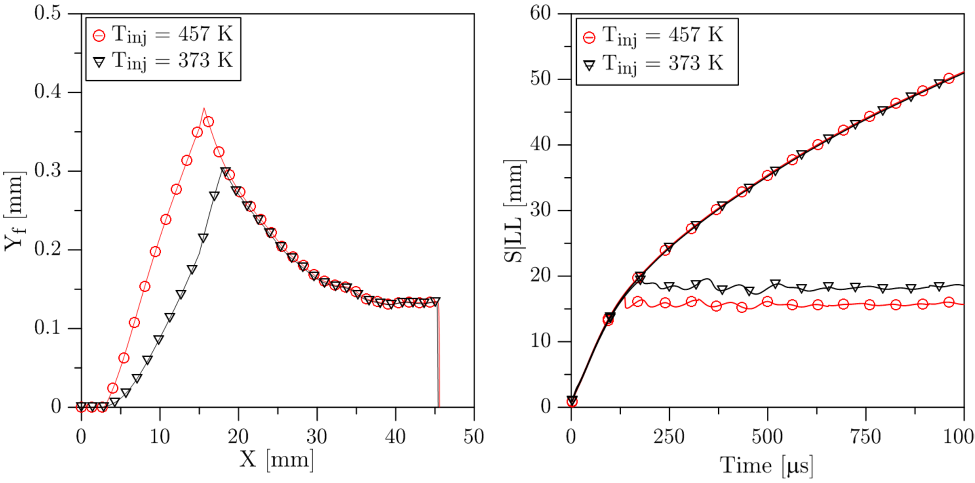

Figure 4.39. *Comparison between predicted on-axis Y_f distribution (left), S and LL (right) for DEC at $\rho_c = 23.41\ kg/m^3$ at TDC, $p_{inj} = 100\ MPa$ and two different T_{inj} values (373 and 457 K).*

The calculations presented in the following figures were performed with T_{inj} determined by the characterization described in section 3.2.3. In this way, they were consistent with the state relationships utilized for the LAS processing, which were also calculated with the same injection temperature. The angles utilized for each condition are listed in table 4.5.

In figure 4.40, the on-axis vapour mass fraction at the symmetry plane is shown for DOD, and DEC (both predicted and measured). The continuous lines represent the LAS data, while the dashed lines correspond to the distribution obtained with the 1D-Model. For DOD, the mean and standard deviation have been represented. Both LAS and calculation data correspond to 1000 μs aSoE, at $\rho_c = 23.41\ kg/m^3$ at TDC and $p_{inj} = 150\ MPa$. This injection pressure has been chosen to maximize the spray penetration and the spatial overlap between LAS measurements and the ECN data. The X-coordinate has been normalized with the corresponding equivalent diameter. A good agreement can be observed between LAS, 1D-Model calculations and PRS data. However, two regions can be identified where discrepancies are

ρ_c [kg/m^3]	P_{inj} [MPa]	α_1 [°]	α_2 [°]	T_{inj} [K]
19.27	100	15.00	25.447	445
23.41	50	15.00	26.75	457
23.41	100	15.00	26.75	457
23.41	150	15.00	26.75	457
20.24	100	15.00	25.806	483

Table 4.5. *Input angles and T_{inj} values for 1D-Model calculations.*

important: the near-nozzle region and the tip of the spray. This could be caused by the weak signal and the strong scattering and noise observed on the measurements (especially the near-nozzle region). However, neither PRS nor the theoretical model provide a realistic representation of the spray tip. On the one hand, PRS data corresponds to part of the stabilized region of the spray and not its tip. On the other hand, the 1D-Model is not able to predict the effects of the airflow-spray interaction, which is specially noticeable at the furthest regions of the spray. Thus it cannot be concluded that this part of the spray was not properly characterized with LAS (nor the opposite). From this comparison, it has to be highlighted the good agreement between LAS and the 1D-Model, even for the liquid region of the spray (despite the low absorption coefficient).

A more detailed comparison between the three data sources is presented in figure 4.41 (right). In this case, the representation has been limited between 30 to 45 mm from nozzle (between 40 to 60 in normalized coordinates), where LAS can be compared with both PRS and the 1D-Model simultaneously. The aim is to identify small differences that are not observable in the previous figure. In this case, it is possible to see that LAS is generally smaller than the corresponding prediction or PRS results, and the difference increase when moving downstream. This discrepancy can be attributed to the deconvolution algorithm, as it has been previously reported that it tends to accumulate errors at the inner and outer parts of the inverted profiles (figure 4.23). According to Palomares [8], an exponential curve (equation 4.20) can be fitted to the experimental data, to reconstruct the real Y_f profile. This profile shape has been considered also in this work as it is commonly used in literature. Considering only the range defined by $0.9 \geqslant Y_f/Y_{f,cl} \geqslant 0.15$, it should be possible to reconstruct the complete profile while avoiding the affected

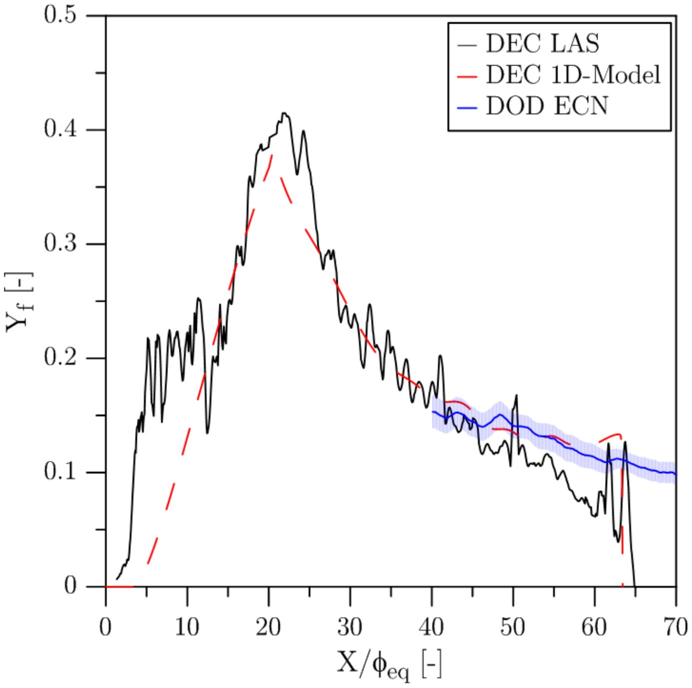

Figure 4.40. *Comparison of the on-axis Y_f distributions obtained with UV-VIS LAS, PRS and the 1D-Model. DEC measured and predicted data corresponds to 1000 μs aSoE, $\rho_c = 23.41\ kg/m^3$ at TDC and $p_{inj} = 150\ MPa$.*

regions. The fitting algorithm is based on the *maximum gradient descent methodology*, which is described in detail in appendix 4.B. An example of the fitted curves is shown in figure 4.41 (left), which corresponds to DEC at 30 and 40 mm from nozzle. The corresponding fitted on-axis distribution is depicted in figure 4.41 (right), together with the original (LAS), predicted (1D-Model) and PRS data. In this figure, it can be observed that the agreement between the fitted LAS and the other two data sources has improved in comparison with the original LAS distribution. Moving downstream the liquid length, the CoV_{abs} increases and the signal-to-noise ratio decreases. Therefore, the relative weight of the noise increases, and so it does the error introduced by the deconvolution algorithm.

The agreement between the 1D-Model and LAS data makes it possible to utilize the first one to validate the experimental trends reported previously. In figure 4.42, the evolution of on-axis Y_f when varying in-cylinder density (left) and injection pressure (right) are depicted. Experimental data corresponding to DEC, at $\rho_c = 23.41\ kg/m^3$ at TDC and $p_{inj} = 100\ MPa$ has been

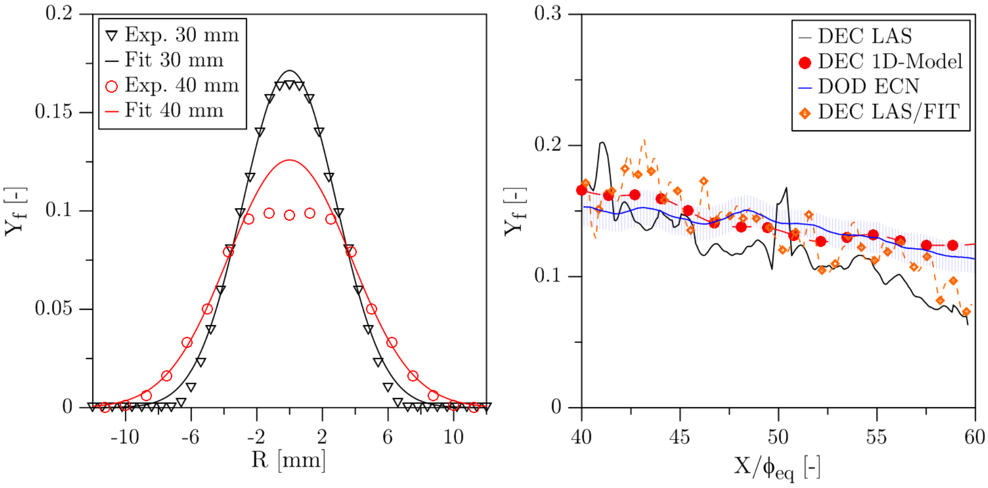

Figure 4.41. *Comparison between experimental and fitted exponential curve for DEC, at 30 and 40 mm from nozzle (left). Comparison of the on-axis Y_f distributions obtained with UV-VIS LAS (original and fitted profiles), PRS and the 1D-Model, between 40 and 60 in normalized coordinates. DEC measured and predicted data corresponds 1000 μs aSoE, $\rho_c = 23.41\ kg/m^3$ at TDC and $p_{inj} = 150\ MPa$.*

included as reference. From this comparison, it is possible to see that there is a general agreement between trends obtained with the 1D-Model and the ones reported in figures 4.35 and 4.36. An increase of p_{inj} increases the fuel penetration but does not vary the local Y_f values. In contrast, when in-cylinder density is varied, the Y_f distribution is also modified. When temperature is increased (23.41 → 20.24 kg/m^3), the 1D-Model predicts a decrease of the maximum LL and an increase of $Y_{f,evap}$. On the other hand, when in-cylinder pressure is reduced (23.41 → 19.27 kg/m^3), the maximum LL slightly increases while $Y_{f,evap}$ is almost constant. In the vapour region of the spray, local Y_f generally increases when reducing ρ_c. These trends are consistent with the ones obtained experimentally. Moreover, the decays observed on the calculations are similar to the ones reported by the experiments, taking into account that the tip of the spray is usually not well predicted. Therefore, the UV-VIS LAS technique (and the methodology described in this study) is sensitive enough to characterize the effect of the boundary conditions over the fuel distributions, even for low absorption fuels as DEC. The magnitude of the predicted variations at the liquid region of the spray does not coincide with the experimental measurements. On the one hand, the accuracy of the 1D-Model in this region of the spray is jeopardised by the definition of T_{inj}

(figure 4.39). On the other hand, this region is critical for the LAS technique due to the high CoV and low signal-to-noise ratio of the measurements.

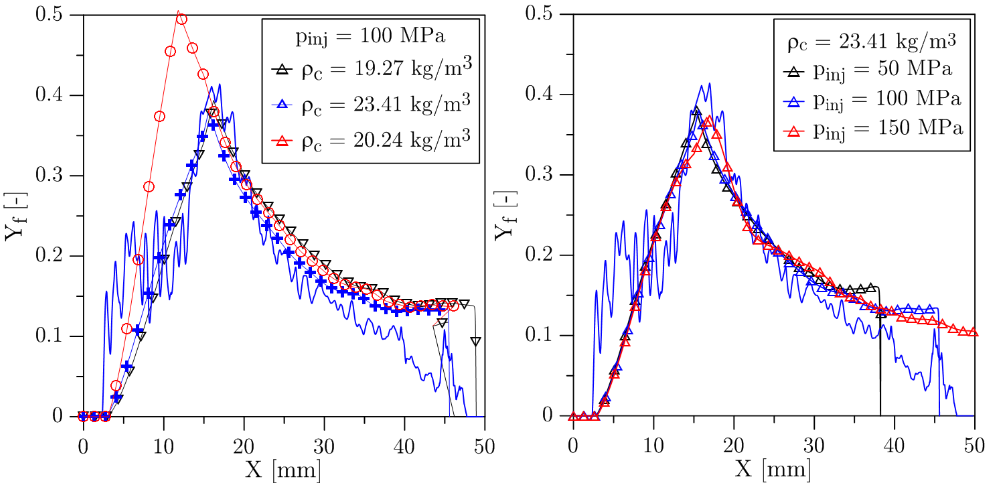

Figure 4.42. *Comparison between experimental and predicted on-axis* Y_f *distributions of DEC, for the three in-cylinder densities (left) and the three injection pressures (right) utilized in this study. Experimental conditions correspond to* $\rho_c = 23.41\ kg/m^3$ *at TDC and* $p_{inj} = 100\ MPa$*.*

The 1D-Model was also utilized to validate the differences between fuels reported previously. For 50DEC calculations, the corresponding mass flow rate and momentum flux were used as inputs, while the same angles and T_{inj} as the ones listed in table 4.5 were considered. The comparison between 50DEC and DEC is presented in figure 4.43. It can be observed that, according to the macroscopic characterization, the 1D-Model predicts a similar Y_f distribution for both fuels at the vaporized region of the spray. As it was discussed previously, this is not observed with the LAS data. Only for $\rho_c = 20.24\ Kg/m^3$, it is possible to see certain similarities between experimental and predicted distributions. The author considers that this agreement is not by chance, as this case is the one that shows the largest absorption coefficient (figure 4.26) out of the three cases depicted for 50DEC. The corresponding ε value in this case was more similar to the one reported for DEC.

The radial Y_f distributions from the different data sources are compared in figure 4.44. For this purpose, they have been normalized and averaged between 25 and 35 mm (as in figure 4.35). LAS (original) is compared with PRS and LAS fitted distributions, as described in the previous paragraphs. The

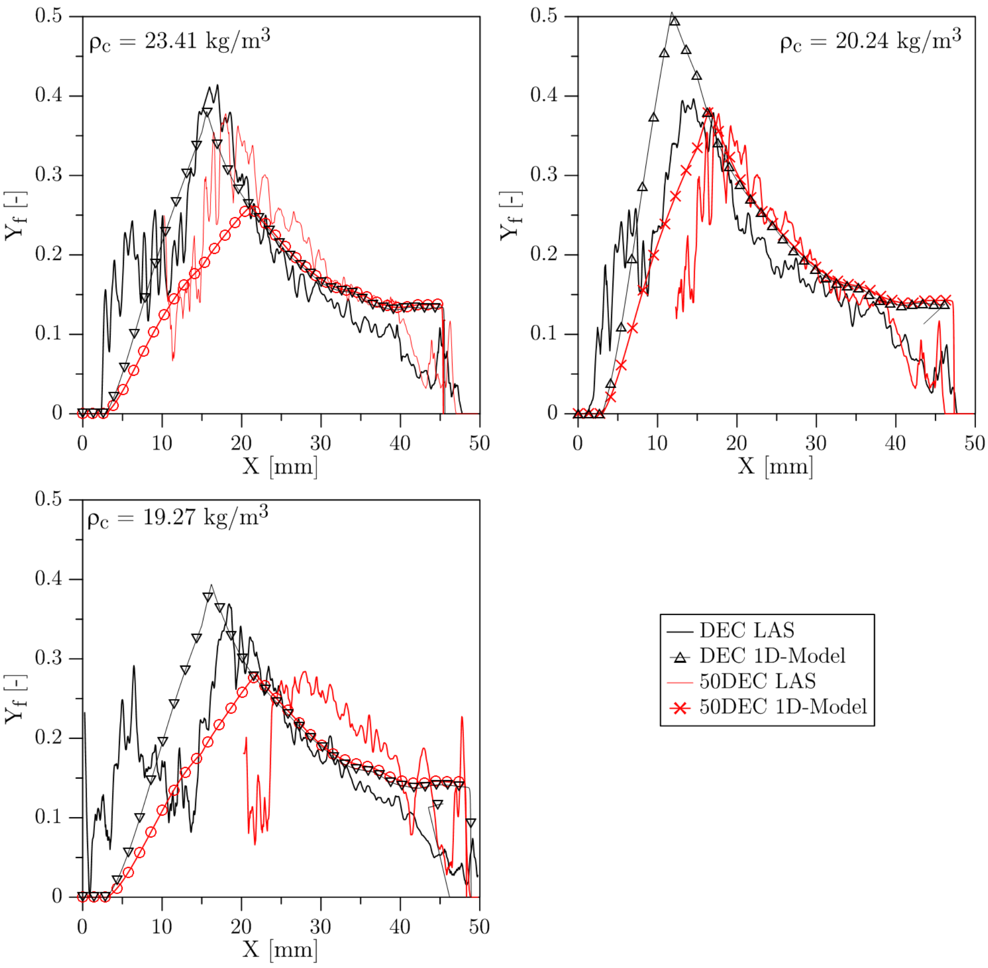

Figure 4.43. *Comparison between experimental and predicted on-axis* Y_f *distributions of DEC and 50DEC, for the three in-cylinder densities proposed in figure 3.3.*

1D-Model is represented by an exponential curve, according to the spray angle utilized for the calculations. From the comparison, it is possible to see that original LAS profiles are wider than the other two sources. Moreover, the scattering shown in the figure suggests that there is more variability between profiles in the case of LAS than PRS. When the fitted profile is considered, it is possible to see that differences are lower but not negligible.

In summary, the comparison highlights the reliability of the technique when it is applied with low absorption fuels, like DEC in this case.

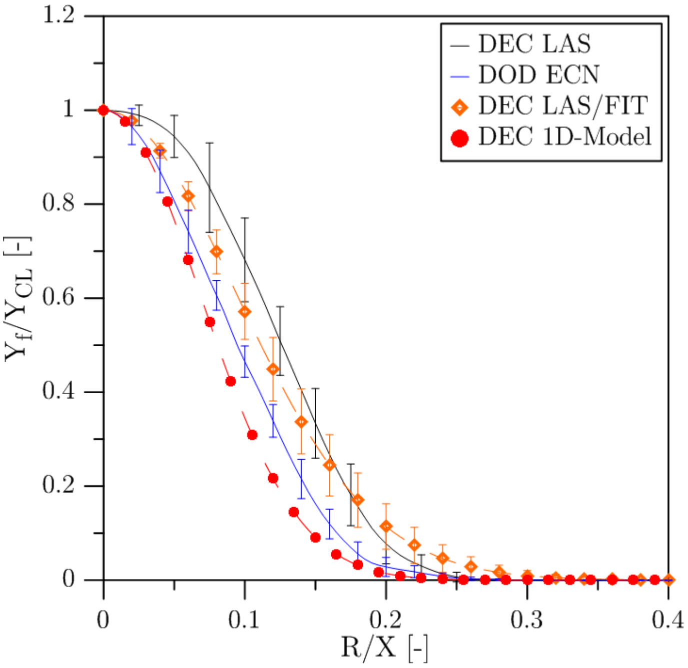

Figure 4.44. *Averaged normalized profiles from LAS (original and fitted profiles), PRS and 1D-Model, calculated between 30 and 40 mm. DEC measured and predicted data corresponds 1000 μs aSoE, $\rho_c = 23.41\ kg/m^3$ at TDC and $p_{inj} = 150\ MPa$.*

It has been observed that similar Y_f fraction distributions are obtained with LAS, PRS and the 1D-Model. Moreover, the experimental trends reported previously have been corroborated with the corresponding theoretical calculation. However, PRS measurements and predictions provide slightly higher values of Y_f at the spray axis, while presenting narrower radial profiles than LAS. It has been shown that the errors introduced by the deconvolution algorithm are partially causing the reported discrepancies, but they do not explain them completely. Therefore, a more detailed analysis of the different uncertainty sources is needed, and presented in the next section.

4.3.6 Analysis of uncertainties

Errors associated to generic physical phenomena, such as beam steering through the medium, as well as some other uncertainties specifically related to the particular experimental setup (e.g. airflow motion in the rig) or procedures (e.g. absorption coefficient calibration) are considered in this analysis. However, it must the taken into account that the objective is to analyse the main error sources in a qualitative way, rather than to provide a rigorous uncertainties quantification.

4.3.6.1 Beam Steering Effect

A collimated light beam was used in the current work. All light rays, which are more or less parallel to each other, are collected by a lens after traversing the combustion chamber (figure 4.18) and directed to the ICCD. When these rays cross the spray, they are attenuated mainly due to vapour absorption and/or liquid scattering. Ideally, each attenuated ray would leave the combustion chamber and illuminate the same pixel of the ICCD, but with less intensity. Therefore, the calculation of attenuation would require just a comparison between the measured intensity with and without spray interaction, pixel by pixel (as it has been done in this work). However, the collimated beam is affected by a steering effect, caused by the density gradients within the spray and combustion chamber gases (section 4.2.2). Thus, whenever density gradients exist and in particular when fuel is injected, the direction of propagation of the light rays is modified. This could affect the vapour absorption calculations.

The contribution of the beam steering to the extinction signal has been previously analysed by Thomson et al. [45]. They identify this effect as an error source and propose a variation of the traditional two-dimensional line-of-sight light extinction method for soot concentration measurements (which is a problem similar to the one addressed here). In this case, the collimated light beam is replaced by a diffuse source, imaged at a given plane within the medium (i.e. the symmetry plane of the flame), and at the same time imaged onto the CCD with a second imaging system which aperture is physically limited. A comparison between both configurations is presented in figure 4.45. These authors state that the main difference lies upon the fact that, with the collimated light, the signal depends on individual rays; with the diffuse light, it depends on a bundle of light rays that propagate with different directions. In the first case, they suggest that there is a path variation caused by beam steering and its effect is enhanced rather than cancelled when raw and attenuated signals are divided. In contrast, when using a diffuse light source, the beam steering effect is compensated. Any bundle of rays, associated with any chord through the flame, overfills the aperture of the imaging lens. Thus, despite they are affected by beam steering, the optical path travelled by the rays that reach the detector does not vary (considering that the deviated bundle of rays still overfills the aperture of the lens). In this case, the uncertainties are more related with the lack of uniformity of the light source. The authors present an experimental comparison and conclude that the main differences are the uncertainty of the measurement, while the mean extinction values are similar.

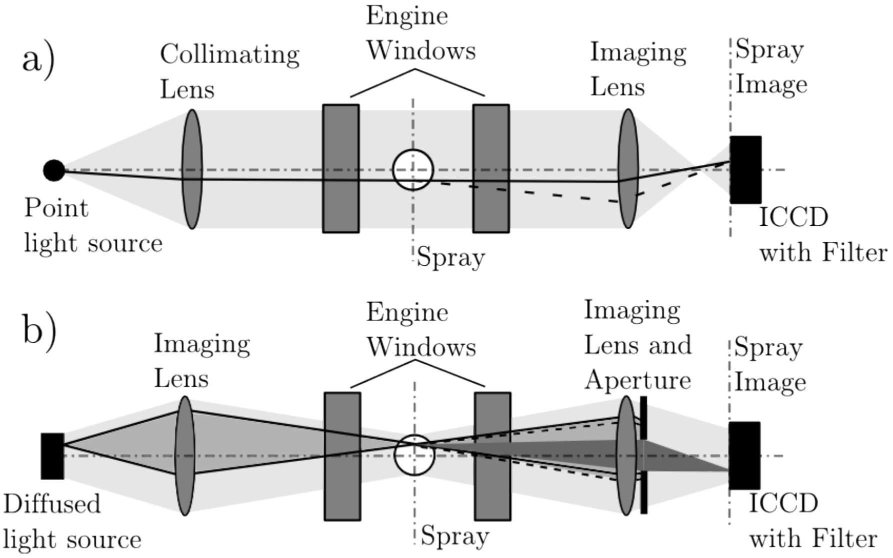

Figure 4.45. *Collimated (a) and diffuse (b) illumination experimental set-up. The solid and dashed lines represent the light path without and with beam-steering respectively. The darkest area at (b) represents the portion of light that is imaged over the ICCD.*

This analysis was performed for laminar flames at atmospheric pressure. However, the authors suggest that differences could be larger when working under high pressure and/or turbulent flames. A similar experimental solution has been also applied by Manin et al. [46] for 2D soot measurements. On the other side, Nishida and Chato et al. [29, 30, 35] report the use of a diffuser located just before the test rig, to reduce the beam steering influence. In this case, the optical set-up is different to the one proposed by Thomson et al. [45] and the real effect of the diffuser is not analysed. For this reason, it was decided to evaluate the uncertainties introduced due to the use of a collimated light source, with the test conditions and the fuels utilized in this work.

Firstly, the influence of the spray density gradients was evaluated through a set of simplified calculations which are described in detail in appendix 4.C. In this approach, a theoretical distribution of vapour fuel mass fraction was used to calculate the corresponding refractive index gradients. Thus, it was possible to obtain the deviation suffered by the light rays while crossing the spray. At the same time, the attenuation suffered by light (absorption) was calculated for the original trajectory (I_{Orig}) and the deviated one (I_{BS}), which are compared at figure 4.46. Calculations were performed for DEC, and correspond to the case of $\rho_c = 23.41\ kg/m^3$ at TDC and $p_{inj} = 100\ MPa$. The main conclusion that can be extracted from the small values obtained from these calculations is that the deviation suffered by the light rays within the spray should not cause a significant variation of the optical path, as attenuation seems to be almost not affected. The collecting lens (figure 4.18) helps to keep this effect small, as it guarantees that the major part of the light rays reach the detector even if they are deviated.

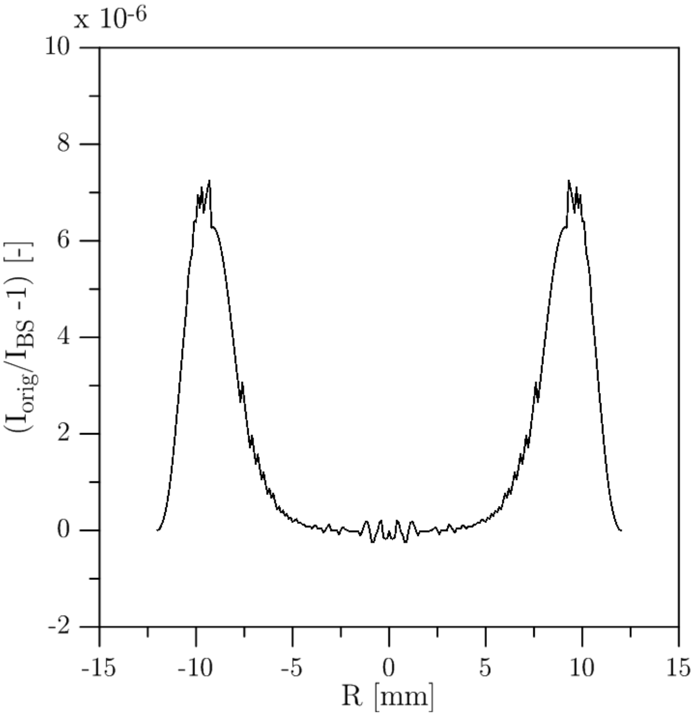

Figure 4.46. *Ratio between the absorption suffered by light when its direction of propagation is affected or not by beam steering. Data correspond to 34 mm from nozzle.*

However, these calculations do not take into account the effect of the ambient gas. The local heterogeneities[5] observed during the airflow characterization could cause important deviation of the light rays. Therefore,

---

[5] Density gradients increased by local turbulences, generated by airflow and convective effects caused by the spray injection

in order to validate the conclusions obtained from calculations, the collimated and diffuse light sources were compared experimentally. The original configuration was modified to create the image of a diffuse light source at the symmetry plane of the spray, according to the solution proposed in [45]. Therefore, a diffuser was introduced just after the light source and its distance to the parabolic mirror was modified, as this element was used as the focusing lens. In this case, the optical access of the engine limited the aperture of the receiving optics (Window + Lens + filter). In figure 4.47, Y_f obtained with the collimated (COL) and diffuse light source (DIFF) are compared, where the on-axis distribution at the symmetry plane is shown. Data correspond to DEC at 1000 μs and 2000 μs aSoE, $\rho_c = 23.41\ kg/m^3$ at TDC and $p_{inj} = 100\ MPa$. Both DIFF and COL represent similar vapour distributions despite the first one is, in general, slightly lower. The main differences are observable near the Y_f maximum peak, which is a critical region (specially for low absorption fuels). The vicinity of maximum LL is where the largest density gradients are located within the spray. Thus, this region could be specially affected by the beam steering effect. However, the own variability of the test rig (specially in terms of T_{inj}) and not the experimental procedure could also explain such differences.

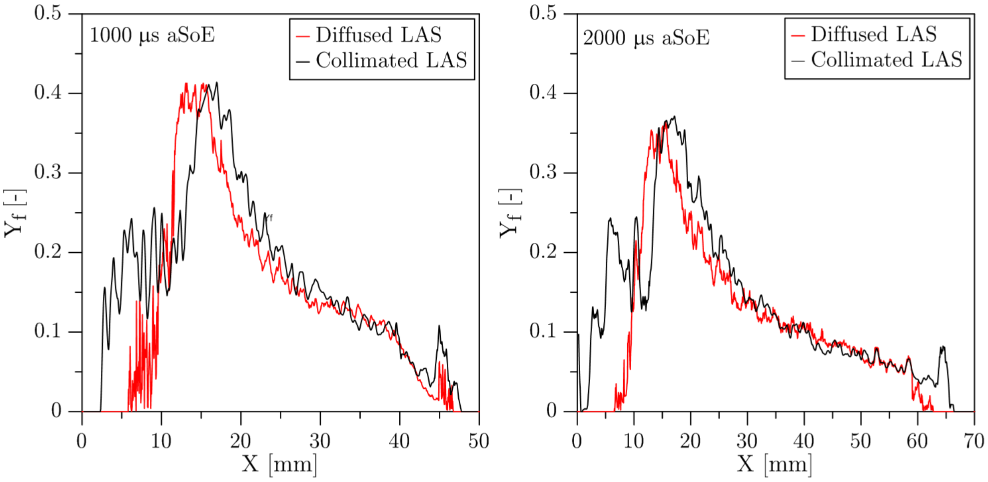

Figure 4.47. *On-axis Y_f distribution at the symmetry plane obtained with collimated and diffuse light source respectively. Data correspond to DEC, at 1000 (left) and 2000 (right) μs aSoE, $\rho_c = 23.41\ kg/m^3$ at TDC and $p_{inj} = 100\ MPa$.*

This comparison is consistent with results presented by Thomson et al. [45], as they also reported certain agreement between results obtained by means of both illumination schemes. However, they highlight that main differences arise when considering uncertainty of measurements. In this regard, the coefficient of variation of the diffuse-light absorption $CoV_{Abs,DIFF}$ was calculated and is presented in figure 4.48, where it is compared with the CoV_{Abs} (obtained with the collimated light source). It can be clearly seen that CoV is drastically reduced, which should improve accuracy of results.

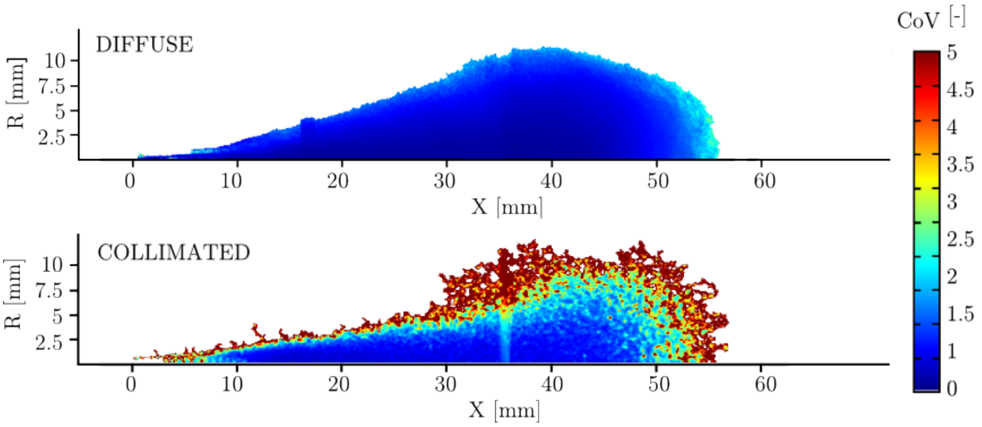

Figure 4.48. Coefficient of variation of the line-off-sight absorption signal obtained with a diffuse (up) and collimated (down) light source. Data correspond to DEC, at 2000 µs aSoE, $\rho_c = 23.41\ kg/m^3$ and $p_{inj} = 100\ MPa$.

The benefit of the reduction of CoV is appreciable when comparing the radial Y_f distribution along the spray axis for collimated and diffuse light sources. In figure 4.49 (left) Y_f distribution at certain distances from nozzle is presented, together with the corresponding exponential curves which have been fitted to the experimental data (according to appendix 4.B). In this plot, difference between both illumination systems are visible, specially for the profiles closer to the nozzle. Besides, when comparing experimental (LAS) and fitted distributions (LAS/FIT), it is possible to see that they are more similar for DIFF data than for COL. The differences are mainly visible near the spray axis, but also at the outer part of the profiles. The relatively larger noise observable at the COL absorption signal introduces larger errors during the deconvolution process. The plot on the right represents the average normalized profiles (as in figure 4.44) for both experimental and fitted distributions. When the radial distribution is normalized, DIFF and COL are more similar, which suggest that the differences observed for the absolute Y_f could be mainly caused by the variability of the test rig. However, COL data presents larger scattering than DIFF.

In summary, it has been concluded that the use of either a collimated or diffuse light source should not cause important differences on the measured fuel distribution, as it has been theoretically and experimentally demonstrated. However, as Thomson et al. [45] reported, important differences arise when considering the measurement uncertainty. The diffuse light clearly improves the CoV, which is a critical issue when working with low absorption fuels like the ones considered in this study. For this reason, the author suggests that this experimental configuration should be considered in future works.

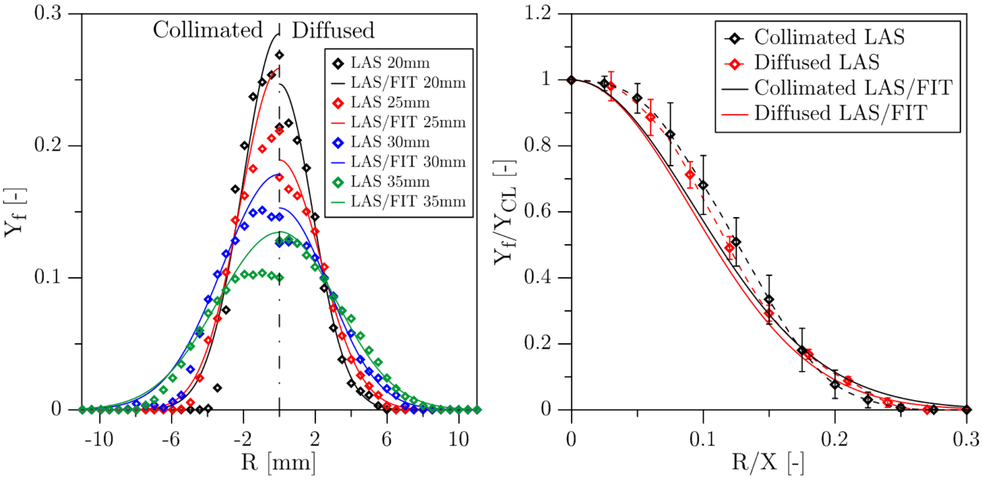

Figure 4.49. *Comparison between collimated and diffuse-light based measurements: Y_f radial distributions (symmetry plane) at different distances from nozzle (left) and average normalized profiles (right), calculated between 25 and 35 mm. Data correspond to DEC, at 1000 μs aSoE, $\rho_c = 23.41\ kg/m^3$ at TDC and $p_{inj} = 100\ MPa$. The LAS/FIT data refers to the exponential curve fitted to experimental LAS data.*

4.3.6.2 Absorption coefficient

A new methodology was utilized to measure the absorption coefficient of the fuels of study. As it has been described previously and according to other publications, it could be expected that ε presents certain dependence with thermodynamic conditions, which tends to reduce when pressure and temperature increase. However, it has been observed that the fuels studied here present no dependence, at least in the working range defined for this work.

Considering the trends reported by Zhang and Yamakawa et al. [24, 25], it could be expected that an increase of temperature and/or pressure would cause a decrease of the absorption coefficient. If this were the case for any of the fuels used in this work, errors would be introduced when using a fixed ε, due to the local variations of temperature within the spray. More specifically, some discrepancies would be observable when moving along the spray axis and toward the edges (perpendicular to the spray axis). Downstream the nozzle, the mixture increases its temperature gradually. Therefore, the absorption coefficient would decrease while increasing consequently on-axis ρ_{vf} (according to equation 4.6) and hence Y_f in comparison with the fixed ε case. One could consider that this explains the differences observed in figure 4.40 between the experimental and modelled results. However, at any point of the spray axis, temperature also rises when moving from the centre to the edges. This would cause a decrease of the absorption coefficient and an increase of the Y_f value, in comparison with the fixed ε case. As temperatures at the outer layers of the spray are higher than at the spray axis, the ratio $Y_f/Y_{f,cl}$ would be larger than with a constant absorption coefficient, resulting on wider normalized profiles than the ones reported in figure 4.41. Besides that, it has been also proved that the same absorption coefficient, applied at different thermodynamic conditions, offered consistent results. Some discrepancies have been reported for 50DEC, but they have been related to a degradation of the fuel, as they were also observed at standard conditions.

Finally, another issue that has to be taken into account is the precision of the absorption coefficient. It has been discussed previously that the methodology followed in this work seems to present an inherent uncertainty level that can be important in reference to the ε mean value, when fuel optical properties are in the limit of what is acceptable. As the fuel partial density is inversely proportional to ε, this lack of accuracy could strongly affect results. It has been considered that this issue is causing the discrepancies observed when comparing 50DEC, with DEC and HEPB3.

4.3.6.3 Interaction between spray and airflow

The characteristics of the airflow within the combustion chamber of the test rig have been described in detail in chapter 3. An issue that has been reported is the lack of symmetry of the airflow, relative to the spray axis. This could cause the mixing process to be not similar throughout the whole spray. Therefore, the spray would not be axisymmetric, which is one of the main hypotheses when applying a deconvolution algorithm [37]. In order to evaluate the influence of this asymmetry over the fuel distribution, the spray (absorption signal) was splitted in two halves through its axis, to calculate the ratio between them. The result is shown in figure 4.50, for HEPB3 and

DEC$_{DIFF}$ (with the diffuse light source). Data was obtained at 1000 and 2000 μs aSoE, $\rho_c = 23.41\ kg/m^3$ at TDC and $p_{inj} = 100\ MPa$. These cases with the lowest CoV have been chosen as reference, to minimize the influence of the measurement uncertainties on this comparison. The maps shown in this figure can be considered as representative of all the $\overline{Abs}$ distributions obtained in this work. From these maps it can be observed, in general, that the spray is not perfectly axisymmetric. Around the spray axis the ratio is near 1, but differences arise near the edges. At 1000 μs aSoE, these regions are more located near the edge of the spray. However, at 2000 μs they extend to inner regions of the spray. Moreover, it can be observed that these areas can be found also at the first 20 mm of the spray, where it was supposed at first that the airflow-spray interaction could interfere less.

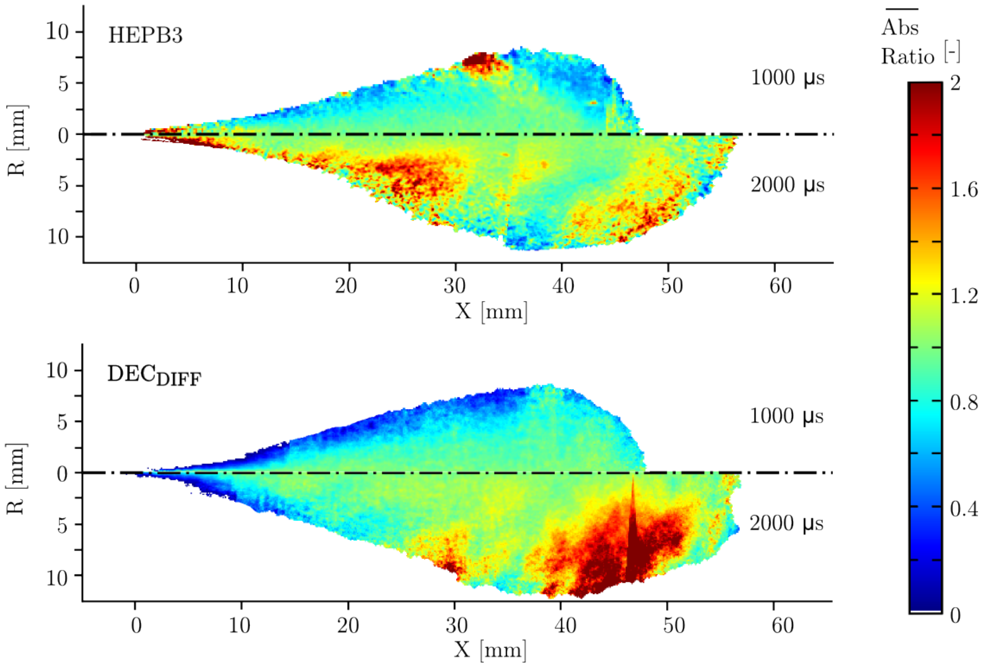

Figure 4.50. *Ratio between LoS absorption of each half of the spray, for HEPB3 (up) and DEC$_{DIFF}$. Data correspond to $\rho_f = 23.41\ kg/m^3$ and $p_{inj} = 100\ MPa$.*

Apart from the asymmetry of the average air-flow patterns, the large cycle-to-cycle variability could interfere on the spray characterization. The different spray development between repetitions could be reflected in a larger measurement uncertainty (specially problematic when working with low absorptive fuels) and even, at the extreme, the average signal could not be considered as representative of the spray behaviour within the combustion chamber. In order to provide a detailed view of the cycle-to-cycle variability, the radial distribution of UV-attenuation at 30 mm from nozzle was analysed repetition per repetition. In figure 4.51, the normalized[6] profiles for the 50 repetitions are depicted. Data correspond to DEC at 1000 μs aSoE, $\rho_c = 23.41\ kg/m^3$ at TDC and $p_{inj} = 100\ MPa$, obtained with diffuse (left) and collimated (right) light source. In order to characterize this scattering, the relative location of the percentile 97% of each profile (P97), in reference to the average spray axis, and its Full-Width Half-Maximum (FWHM) were calculated. Moreover, both magnitudes were normalized with the distance to the nozzle (P97* and FWHM*) to allow a direct comparison between these values and the normalized profiles shown previously. In figure 4.52, the value of both parameters are shown for each repetition. The trends reported in this figure can be considered as representative of the spray behaviour for all test conditions.

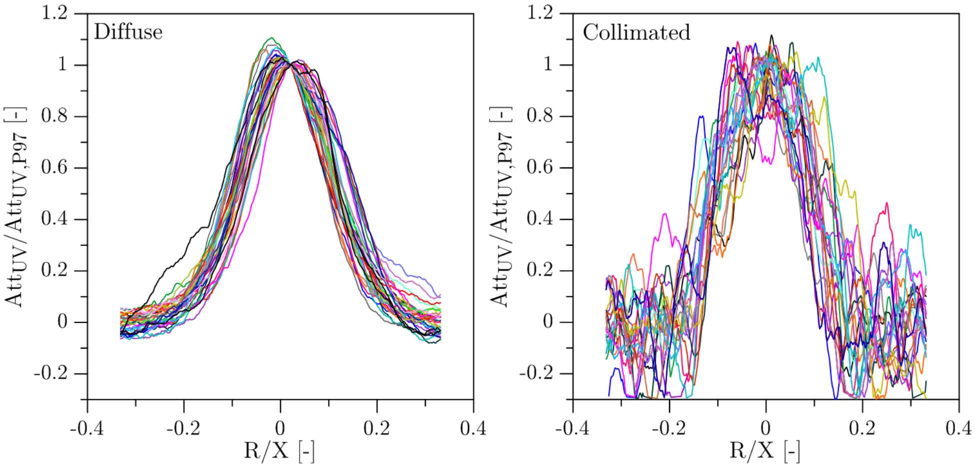

Figure 4.51. *Normalized radial distribution of LoS UV-attenuation at 30 mm from nozzle, using a diffuse (left) and collimated (right) light source. Data correspond to DEC at 1000 μs aSoE, $\rho_c = 23.41\ kg/m^3$ at TDC and $p_{inj} = 100\ MPa$.*

The cycle-to-cycle variability is clearly represented by the last two figures and it can be stated that the scattering is in the same order of magnitude as the differences observed between LAS profiles and Rayleigh (see figure 4.44). Considering the cycle-to-cycle variability of P97*, a certain misalignment of the spray between repetitions can be observed. Nevertheless, it is not possible

---

[6] Each profile was divided by its percentile 97%, while the radial coordinate was divided by the distance to the nozzle

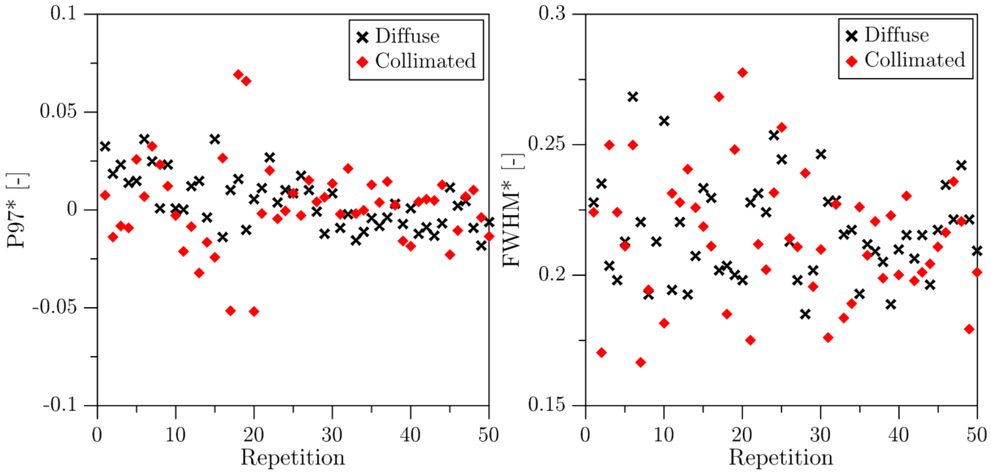

Figure 4.52. *Location of the percentile 97% (left), in reference to the average spray axis, and the corresponding FWHM (right) for UV-attenuation radial profile at 30 mm form nozzle of each repetition. Data correspond to DEC (both COL and DIFF) at 1000 μs aSoE, $\rho_c = 23.41\ kg/m^3$ at TDC and $p_{inj} = 100\ MPa$.*

to identify a clear trend towards any side of the combustion chamber. The scattering shown by FWHM* is even larger, which suggests that the mixing process (radial spread) is affected by the airflow variability. The fact that sprays are not clearly deviated towards any side of the combustion chamber suggest that the net effect of the asymmetric flow on the mean spray structure is negligible and is unlikely to be causing the asymmetry depicted in figure 4.50. However, the large cycle-to-cycle variations of the airflow seem to be causing the large scattering of the data presented here. In figure 4.51, it is possible to see that the effect is specially harmful when a collimated light source is utilized. Moreover, it could be the reason for the shape of the deconvoluted profiles not to be exactly Gaussian.

4.4 Summary and conclusions

This chapter has been focused on the study of the fuel mixing process. For this purpose, the spray was characterized macroscopically and microscopically. For the former, MIE and schlieren visualization were applied simultaneously to obtain the most relevant metrics of the spray geometry. For the latter, UV-VIS LAS was chosen to measure the fuel vapour distribution within the spray.

The visualization and analysis of both liquid and vapour phases made it possible to determine the influence of different engine parameters (ρ_c, T_c and p_{inj}) and the fuel properties over the spray development. The small differences in viscosity and density between the four fuels provided nearly the same vapour penetration and spread angle, which suggest that the air entrainment is similar. In contrast, the maximum liquid length was found to be proportional to the volatility of the fuel (more specifically to the central point the distillation curve of the fuel), as this property is indicative of the amount of energy required by each fuel to completely evaporate. Therefore, it can be concluded that once the maximum liquid length is reached, the fuel distribution should be similar for the four fuels of the study. Upstream this point, differences should be expected as the evaporation rate depends on the fuel. The variations observed for the different test conditions agreed with the ones predicted by theoretical models widely used in literature.

The macroscopic characterization made it possible also to identify a certain influence of the in-cylinder airflow. The cycle-to-cycle variability caused large scattering on the spray penetration and cone angle measures. A first analysis suggested that the interaction generated local structures at the edge of the spray, which even hindered the proper calculation of the spray cone angle. In this regard, the use of average images (calculated with all repetitions) was evaluated to obtain the spray metrics. However, some difficulties where found to define with accuracy the real spray contour. The large scattering observed, not only for the spray cone angle but also for the spray penetration, suggests that the air-fuel mixing process should be affected by the airflow inside the cylinder.

The microscopic characterization of the spray was carried out by means of UV-VIS LAS technique and it is the first time that this technique was proposed to be used with low absorption fuels. A calibration procedure was designed to obtain in-situ measurements of the absorption coefficient of each fuel, using exactly the same optical set-up as the one used for spray measurements. The main hypothesis of this calibration procedure is the formation of a completely homogeneous mixture between fuel and air, fact which was corroborated. Moreover, the fuel concentration estimation was validated as it was demonstrated that the values obtained were independent of the injected mass, according to the Lambert-Beer's Law. The sensitivity and accuracy of the calibration methodology was evaluated by characterizing three different mixtures of HEP and HAF (with high absorptive properties at the UV range). Results confirmed that the calibration methodology was sensitive to fuel optical properties. This was also corroborated with the comparison of the spray fuel distributions obtained for each of these three mixtures. Besides, the absorption coefficient was measured for different combinations of in-cylinder pressure and temperature. In this regard, results for all the fuels suggested that the sensitivity of ε to thermodynamic conditions was very small, which was coherent with results reported by other authors for other types of fuels. Moreover, this conclusion was experimentally validated by the comparison of fuel mass fraction distributions obtained at different in-cylinder pressures and temperatures. Finally, the calibration procedure made it possible to measure the low absorption coefficient of both DEC and 50DEC. However, it was observed that results presented uncertainties which could be important in comparison with the mean value.

The absorption coefficients were utilized to obtain the vapour fuel mass fraction distribution of HEPB3, DEC and 50DEC. The absorption signal measured for the two low absorption fuels was characterized by a high coefficient of variation. However, it was shown that in the case of DEC it was not affecting the accuracy of results, as the distribution coincided with that of HEPB3. Some major discrepancies were reported for 50DEC, which showed differences with the other two fuels higher than expected, considering the previous macroscopic characterization of the spray. However, it was shown that for the three fuels the radial profiles were (Y_f) self-similar, which suggested that the lack of accuracy of 50DEC was more related to the absorption coefficient utilized and not the application of the LAS technique itself.

Considering all the foregoing, the methodology described in this work is limited to characterize fuels with similar absorption properties as 50DEC. However, this is not the case for DEC. Its increase in absorption coefficient when comparing with 50DEC seems to improve accuracy of results. In fact, it is not by chance that the higher the ε of 50DEC the lower the differences between this fuel and the other two. Based on these, it can be stated that fuels with $\varepsilon > 11\ lmol^{-1}cm^{-1}$ (as DEC) are suitable for the methodology presented here. However, it is clear that larger ε could increase accuracy of results.

The effect of test conditions over the fuel distributions where characterized for DEC, which agreed with the trends identified during the macroscopic characterization of the spray. These results were validated with a theoretical 1D-Model and experimental data from the ECN [18] database. In this regard, similar on-axis distributions were reported, confirming the trends extracted from the LAS data. From this comparison, it must be also highlighted the agreement obtained in the vicinity of liquid fuel, which is a clear advantage in comparison with Rayleigh scattering and Laser Induced Flourescence technique. It also made it possible to detect the location of the $Y_{f,evap}$ and measure its value.

However, it was observed that the fuel mass fraction obtained at the spray axis was, in general, slightly lower than the values reported by the other data sources. Moreover, when comparing normalized radial distributions, it was shown that UV-VIS LAS provided wider profiles. In a first instance, it was considered that differences were caused by the errors introduced by the deconvolution algorithm. However, they did not justify all the differences observed. For this reason, a more detailed analysis of uncertainties was proposed. Three main uncertainty sources were identified: absorption coefficient calibration, beam steering effect and interaction between airflow and spray. A detailed discussion was presented in this regard, which concluded that the discrepancies observed between LAS measurements, 1D-Model and PRS data could be caused by the peculiarities of the airflow more than other uncertainty sources inherent to the methodology utilized. Nevertheless, the beam steering was also identified as an important noise source, especially for low absorption fuels like DEC. An alternative optical set-up, based on a diffuse light source, was evaluated. The results showed that it clearly improves the level of uncertainty of the signal, which is critical for the test conditions considered in this work and presents a clear potential which should be evaluated in future works, beyond the scope of this thesis.

4.A Application of the Log-Likelihood Ratio Test to diesel sprays segmentation

The difficulty on defining a threshold value for the spray segmentation is the identification of the different classes present in the image. For this specific application, the statistical distributions of the digital levels of each class are overlapped. For this reason, algorithms for statistical pattern recognition are useful to determine the optimum threshold value for spray segmentation.

The histogram of each image can be considered as an estimation of the digital level probability density function p(x). This function is the weighted sum of two unimodal probability density functions[7], one for the spray ($p_S(x)$)and another one for background ($p_B(x)$). It has to be noted that from now on everything related with the spray and background have been referred as S and B respectively. Based on this, the log-likelihood ratio test can be utilized to find the optimum threshold value to separate spray from background. The algorithm can be summarized with the following equation [5, 8, 47]:

$$h(x) = -\ln p_S(x) + \ln p_B(x) - \ln \frac{P_S}{P_B} \tag{4.17}$$

where P_S and P_B are *a priori probabilities* of the spray and background respectively. It can be demonstrated [47] that the value of x that makes equation 4.17 equal to zero minimizes the probability of error of the segmentation algorithm. Thus, this value is the optimum threshold T between the spray and background.

For the current application, it was considered that the digital level of both background and spray followed a Gaussian distribution. In order to estimate the characteristic parameters of the two probability density functions (PDF), these are the steps that were followed [5, 47]:

- *Image pre-processing*: this step comprises the application of filters, spatial transformations and/or noise removal. Besides, a background reference image is subtracted to correct partially the nonuniform background level. After this operation, an arbitrary constant (1000 in this case) is added to avoid any negative value in the subtracted image, which could difficult the analysis of the histogram.

---

[7] A diesel spray image contain only two principal regions: the one occupied by the spray and the corresponding to background

- *Background PDF (PDF_B)*: A first estimation of the mean value of the background distribution (μ') is obtained from the maximum of the histogram (the mode). It has to be considered that, while background represents the lowest digital levels of the images, the mode should be located near the arbitrary value added in the previous step. However, care must be taken when large sprays are considered, as its area could be larger than that of the background and thus the mode of the histogram would correspond to the spray. The estimation of the standard deviation (σ') is calculated with the values of the histogram at the left of μ'. In this way, any possible influence from pixels of the spray is avoided. Then, the mean μ_B and standard deviation σ_B of PDF_B are calculated considering the range of the histogram that presents larger frequencies than those corresponding to $\mu' \pm n\sigma'$. The value of n is usually set at 2, to consider the 95% of the first estimation.

- *A priory threshold and Spray PDF (PDF_S)*: Once the PDF_B is defined, it is possible to obtain an a priori estimation of the threshold value (Th_{ap}). It is calculated from the cumulative distribution function (CDF) of the background , obtained integrating the PDF_B. Thus, Th_{ap} is defined as the digital level where CDF = 95%. This value is utilized to define PDF_S, which is characterized by the μ_S and σ_S of the values of the histogram at the right side of Th_{ap}.

Once the PDFs are defined, equation 4.17 can be applied. The following expression is obtained:

$$\frac{(Th-\mu_B)^2}{2\sigma_B^2} - \frac{(Th-\mu_S)^2}{2\sigma_S^2} + \ln\frac{\sigma_B P_S}{\sigma_S P_B} = 0 \tag{4.18}$$

where Th is the optimum threshold value and P_S and P_B are the a priori probabilities of belonging to spray and background, respectively. They are calculated with the CDF of both probability distributions, considering Th_{ap} as the calculation limit.

4.B Maximum Gradient Descent methodology

The gradient of a scalar function is a vector that indicates the direction of the greatest rate of increase (in the space defined by the parameters of the function). The opposite direction corresponds to the maximum rate of decrease. The gradient descent method is an iterative optimization algorithm, which takes steps proportional to the negative of the gradient of a function to determine at each iteration "j" the new value of the parameters $(A_{j+1}, B_{j+1}, \dots)$ that minimize an error function E_j. This function has to be defined for each problem. Thus, each new iteration can be calculated as:

$$(A_{j+1}, B_{j+1}, \dots) = (A_j, B_j, \dots) - \Psi \frac{\nabla E_j}{|\nabla E_j|} \tag{4.19}$$

where Ψ is the so called step factor and defines the size of the step for each iteration. Large values of this factor makes the algorithm to converge rapidly but limits the accuracy of the final parameters. Low values of the step factor makes the algorithm to converge slowly but makes it possible to obtain results that are more accurate. In order to obtain the parameters of a Gaussian curve (equation 4.20) that best fits the experimental data, the following error function (quadratic error) can be defined (equation 4.21):

$$Y_f = A \exp -bx^2 \tag{4.20}$$

$$E(A, b) = \sum_{i=1}^{m} \big(A \exp(-bx^2) - C(i)\big)^2 \tag{4.21}$$

where A and b are the parameters to determine, i represents the distance in pixels to the axis of the spray and C(i) are the experimental normalized fuel mass fraction values $(Y_f/Y_{f,cl})$. Hence, the gradient of equation 4.21 can be expressed as:

$$\begin{aligned}\nabla E &= \frac{\partial E}{\partial A}\overline{u_A} + \frac{\partial E}{\partial b}\overline{u_b} \\ &= \sum_{i=1}^{m} 2 \exp -bi^2 \cdot \big(A \exp(-bi^2) - C(i)\big) \cdot \big(\overline{u_a} - 2Ai^2\overline{u_b}\big)\end{aligned} \tag{4.22}$$

where $\overline{u_A}$ and $\overline{u_b}$ are unit vectors pointing to A and b directions. The parameters for tuning the algorithm are the step factor and the number of iterations. For this work, $\Psi = 0.01$ and 5000 iterations were chosen as they offered good accuracy and relatively low computational time.

4.C Beam Steering Model

The deviation suffered by a light ray that crosses a defined air-fuel mixture field has been described by means of a geometric approach. It must be noted that this is just an approximation to the more-complete physical optics approach, but is sufficient for the present purpose. When a collimated light beam moves through a media that presents refractive index gradients, it is deviated in direction and quantity according to the unit vector and module of the gradient. A simplified representation of the phenomenon is depicted in figure 4.53. A planar wavefront, defined by the collimated light beam (I), propagates from r_1 to r_2 covering a differential distance dr in a differential time dT. The original direction of propagation of I has be named as X. Moreover, for simplicity, it has been assumed a negative vertical refractive-index gradient, in the direction of axis Y.

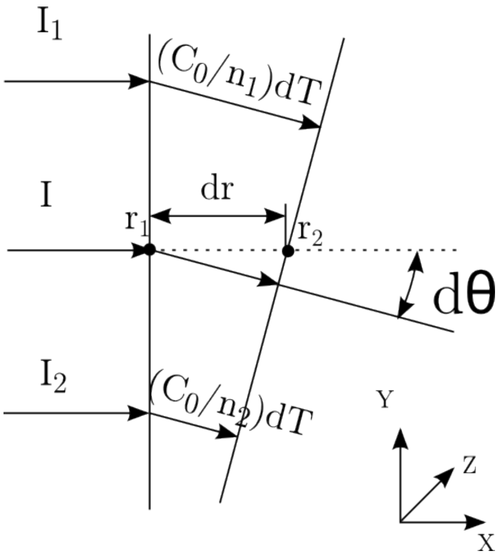

Figure 4.53. *Scheme of the geometrical approach to calculate beam steering.*

The local refractive index can be defined as the ratio between the speed of light in the vacuum (C_0) and the local value of the speed of light (C). Thus, the distance travelled by an individual light ray can be expressed as:

$$dr = \frac{C_0}{n_{local}} dt \tag{4.23}$$

where n_{local} is the local refractive index. From this expression, one can see that the distance travelled by each light ray depends on the local refractive index. This effect is represented in figure 4.53, by I_1 and I_2. The refractive index n_1 is lower than n_2 and dr_1 is consequently larger than dr_2. Since light rays always point normal to the wavefront, the original beam passing through r_1 is refracted a differential angle dE.

It can be demonstrated [4] that, based on the current approach, the ray curvature can be expressed as:

$$\frac{\partial^2 y}{\partial^2 x} = \frac{1}{n}\frac{\partial n}{\partial y} \tag{4.24}$$

If equation 4.24 is integrated in the direction of propagation, the angular ray deflection (θ_y) can be obtained:

$$\theta_y = \frac{1}{n}\int_{r_1}^{r_2} \frac{\partial n}{\partial y}\partial r = \frac{L}{n_0}\frac{\partial n}{\partial y} \tag{4.25}$$

where L is the distance along the optical axis and n_0 is the refractive index of the surrounding medium. It is important to remark that equation 4.25 is applicable to calculate the angle of deviation of a light ray, which propagates through a direction perpendicular to the refractive index gradient. A similar expression can be utilized to calculate the angle of deviation in the Z-axis direction.

For the current study, an air-fuel mixture field was defined, based on experimental results obtained for DEC at $\rho_c = 23.41\ kg/m^3$ at TDC and $p_{inj} = 100\ MPa$ (figure 4.35). A parabolic curve was fitted to the on-axis experimental data in the vaporized region. Moreover, a Gaussian profile was considered for the radial distribution, and a theoretical spray cone angle of 23.5° was chosen. Firstly, the molar refractivity (A) of DEC was calculated and utilized to obtain the refractive index at standard conditions. The molar refractivity is defined as a measure of the total polarizability of a mole of a substance, and is dependent on the temperature, pressure and refractive index. Vickery and Denbigh [48] propose a simple system of molecular bond refractions to calculate the molar refractivity of n-alkanes. In this regard, A of a normal n-alkane containing N carbon atoms can be obtained with equation 4.26:

$$A = a + b(N-2) \tag{4.26}$$

The values of a and b are calculated combining molecular bond refractions as follows:

$$b = [CC] + 2[CH] \tag{4.27}$$

$$a = [CC] + 6[CH] \tag{4.28}$$

where $[CC] = 1.296$ and $[CH] = 1.674$ are the C-C and C-H bond refractions. Thus, the value of molar refractivity of DEC is 48.492 cm^3/mol. The refractive index and the molar refractivity are related through the Lorentz-Lorenz equation 4.29 [49]. At standard pressure and temperature, this equation can be expressed as:

$$n = \sqrt{\frac{V_M + 2A}{V_M - A}} \tag{4.29}$$

where V_M is the molar volume calculated as the ratio between Avogadro's and Loschmidt's constants. Thus, a refractive index of 1.00324697 was obtained for vaporized DEC, at standard conditions. In the case of nitrogen, a value of 1.0002989 was obtained from [50]. In order to calculate the refractive index field, two main hypotheses were considered: the variations of refractive index are caused mainly by the nitrogen/fuel mixture field, while the effect of the thermodynamic conditions is neglected; both DEC and nitrogen are considered as ideal gases. The first hypothesis implies that constant refractive indexes are considered for each specie for the whole distribution, without taking into account local thermodynamic conditions. The second hypothesis is related with the calculation of the refractive index of the mixture. In this regard, several mixture rules can be found in literature [51], to determine the refractive index of a dilution. For the current work, the Lorentz-Lorenz formulation was chosen as it is the most extended (equation 4.30).

$$\frac{n_m^2 - 1}{n_m^2 + 2} = \sum_i \phi_i \frac{n_i^2 - 1}{n_i^2 + 2} \tag{4.30}$$

The parameter n_m represents the refractive index of the mixture, n_i is the refractive index of each component and ϕ_i is the volume fraction of each component. This parameter was considered equal to the molar fraction, according to the second hypothesis. Thus, the molar fraction was directly obtained from the fuel mass fraction, which simplified the calculation process. An example of the refractive index distribution (left) is shown in figure 4.54, together with the corresponding refractive index gradients (right) in the X (axial) and R (radial) directions. The data presented correspond to the symmetry plane of the spray (Z = 0 mm) and one perpendicular section (X = 34 mm). The coordinate system was chosen to coincide with all the results presented in chapter 4. Therefore the X-axis is aligned with the spray axis, the R-axis is perpendicular to the spray axis and the Z-axis is perpendicular to the plane defined by X and R. For beam steering calculations, it was supposed that light rays originally propagate parallel to the Z-axis (as depicted in figure 4.54) and they are deviated due to the refractive index gradients in the other two axes.

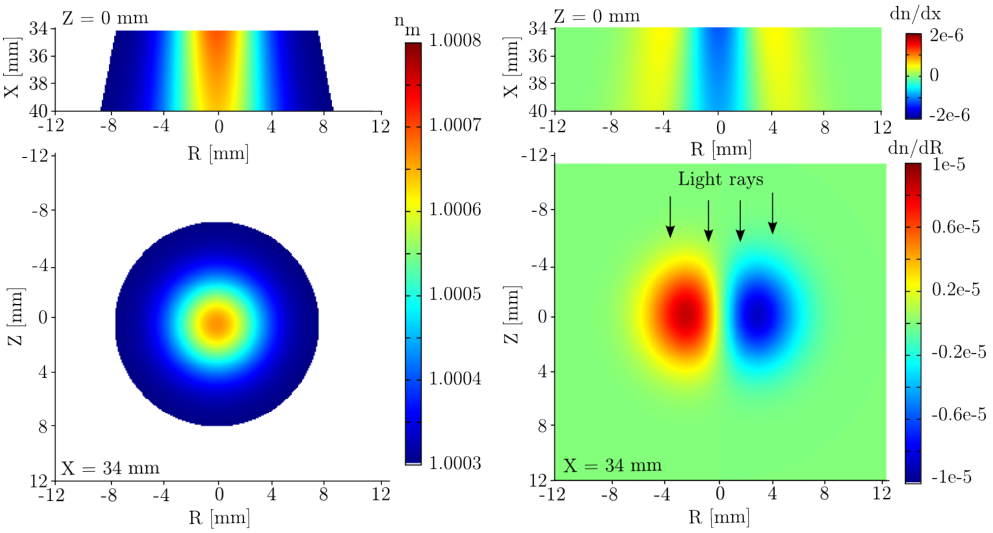

Figure 4.54. *Refractive index distribution for DEC, at the symmetry plane of the spray (Z = 0 mm) and the cross-section corresponding to X = 34 mm from nozzle (left); the corresponding gradients in the X and R directions respectively (right).*

The calculation process considers that every light ray arrives to the gradient field with 0° incidence. As it moves on, the trajectory changes due to the different gradients with which it interacts. When it reaches the margin of the spray, the resulting direction of propagation is forming an angle with the Z-axis (the original direction), which is the accumulation of the successive calculated deviations. This procedure is applied to a finite number of light rays, spread along the R-axis. The refractive index field is discretized in several calculation surfaces. They are parallel to the plane defined by the X-axis and the R-axis, and are sepaced 0.2 mm in the direction of the Z-axis. In this sense, for an individual light ray, equation 4.25 is applied to calculate θ_R and θ_x between two consecutive calculation surfaces. Each couple of calculation surfaces would correspond to r_1 and r_2 in figure 4.53. The value of n_0 is the refractive index at r_1. The value of the refractive index gradient at that point was also utilized for the calculation as it can be considered as a good approach of the gradient at the calculation region. Once θ_y and θ_x are calculated, the intersection between the light ray and the next calculation surface can be obtained. Then, this new point becomes r_1 and the calculation process continues. This procedure is repeated as the light ray moves along the refractive index field, until it achieves its margin. It has to be noted that the angle obtained between two consecutive calculation surfaces is added to the angle of incidence of the light ray over the first surface.

Bibliography

[1] García-Oliver J. M. *Aportaciones al estudio del proceso de combustión turbulenta de chorros en motores diesel de inyección directa.* Doctoral Thesis, Universitat Politècnica de València, Departamento de Máquinas y Motores Térmicos, 2004.

[2] Nerva J-G. *An assessment of fuel physical and chemical properties in the combustion of a Diesel spray.* Doctoral Thesis, Universitat Politècnica de València, Departamento de Máquinas y Motores Térmicos, 2013.

[3] Pastor J.V., Payri R., García-Oliver J.M. and Briceño F.J. "Analysis of transient liquid and vapor phase penetration for diesel sprays under variable injection conditions". *Atomization and Sprays*, Vol. 21 n^o 6, pp. 503–520, 2011.

[4] Settles G.S. *Schlieren and Shadowgraph Techniques.* Springer-Verlag Berlin Heidelberg New York, 2001.

[5] Pastor J.V., Arrégle J. and Palomares A. "Diesel spray image segmentation with a likelihood ratio test". *Applied Optics*, Vol. 40 n^o 17, pp. 2876–2885, 2001.

[6] González R. C. and Woods R. E. *Digital image processing.* Prentice Hall, 2002.

[7] Pratt W. K. *Digital image processing.* Wiley-Interscience Publication, 2001.

[8] Palomares A. *Análisis de imágenes de chorros Diesel.* Doctoral Thesis, Universitat Politècnica de València, Departamento de Máquinas y Motores Térmicos, 2001.

[9] Pastor J.V., García-Oliver J.M., Nerva J.-G. and Giménez B. "Fuel effect on the liquid-phase penetration of an evaporating spray under transient diesel-like conditions". *Fuel*, Vol. 90 n^o 11, pp. 3369–3381, 2011.

[10] Naber, J.D.Siebers D.L. "Effects of Gas Density and Vaporization on Penetration and Dispersion of Diesel Sprays". *SAE Technical Paper*, 1996.

[11] Siebers D.L. "Liquid-phase fuel penetration in diesel sprays". *SAE Technical Papers*, 1998.

[12] Allocca L., Montanaro A., Cipolla G. and Vassallo A. "Spatial-Temporal Characterization of Alternative Fuel Sprays from a Second-Generation Common-Rail Fuel Injection System for Euro4 Passenger Car Application". *SAE Technical Paper*, 2009.

[13] Higgins B.S., Mueller C.J. and Siebers D.L. "Measurements of fuel effects on liquid-phase penetration in di sprays 1". *SAE Technical Papers*, 1999.

[14] Browne K.R., Partridge I.M. and Greeves G. "Fuel property effects on fuel/air mixing in an experimental diesel engine". *SAE Technical Papers*, 1986.

[15] Siebers D.L. "Scaling liquid-phase fuel penetration in diesel sprays based on mixing-limited vaporization". *SAE Technical Papers*, 1999.

[16] Pastor J.V., López J. J., García J.M. and Pastor J.M. "A 1D model for the description of mixing-controlled inert diesel sprays". *Fuel*, Vol. 87 n^o 13-14, pp. 2871–2885, 2008.

[17] Desantes J.M., Pastor J.V., Payri R. and Pastor J.M. "Experimental characterization of internal nozzle flow and diesel spray behavior. Part II: Evaporative conditions". *Atomization and Sprays*, Vol. 15 n^o 5, pp. 517–543, 2005.

[18] "Engine Combustion Network". *Information available at http://www.sandia.gov/ecn/.*

[19] Kook S. and Pickett L.M. "Liquid length and vapor penetration of conventional, Fischer-Tropsch, coal-derived, and surrogate fuel sprays at high-temperature and high-pressure ambient conditions". *Fuel*, Vol. 93, pp. 539 – 548, 2012.

[20] Payri R., García A., Domenech V., Durrett R. and Plazas A.H. "An experimental study of gasoline effects on injection rate, momentum flux and spray characteristics using a common rail diesel injection system". *Fuel*, Vol. 97, pp. 390–399, 2012.

[21] Desantes J. M., Payri R., Salvador F. J. and Soare V. "Study of the Influence of Geometrical and Injection Parameters on Diesel Sprays Characteristics in Isothermal Conditions". In *SAE Technical Paper*. SAE International, 2005.

[22] Suzuki M., Nishida K. and Hiroyasu H. "Simultaneous concentration measurement of vapor and liquid in an evaporating diesel spray". *SAE Technical Paper*, 1993.

[23] Billings T. P. and Drallmeier J. A. "A detailed assessment of the infrared extinction technique for hydrocarbon vapor measurements in a controlled two-phase flow". *Atomization and Sprays*, Vol. 4 n^o 1, pp. 99–121, 1994.

[24] Zhang Y.-Y., Yoshizaki T. and Nishida K. "Imaging of Droplets and Vapor Distributions in a Diesel Fuel Spray by Means of a Laser Absorption–Scattering Technique". *Applied Optics*, Vol. 39 n^o 33, pp. 6221–6229, 2000.

[25] Yamakawa M., Takaki D., Li T., Zhang Y.-Y. and Nishida K. "Quantitative Measurement of Liquid and Vapor Phase Concentration Distribution in a D.I. Gasoline Spray by the Laser Absortion Scattering (LAS) Technique". *SAE Technical Paper*, 2002.

[26] Zhang Y.-Y., Nishida K. and Yoshizaki T. "Characterization of Droplets and Vapor Concetration Distributions in Split-Injection Diesel Sprays by Processing UV and Visible Images". *JSME International Journal, Series B: Fluids and Thermal Engineering*, Vol. 46, pp. 100–108, 2003.

[27] Zhang Y. Y. and Nishida K. "Vapor distribution measurement of higher and lower volatile components in an evaporating fuel spray via laser absorption scattering (LAS) technique". *Combustion Science and Technology*, Vol. 179 n^o 5, pp. 863–881, 2007.

[28] Moon S., Gao J. and Nishida K. "Entrainment, Evaporation and Mixing Characteristics of Diesel Sprays around End-of-Injection". *SAE Technical Paper*, 2009.

[29] Chato M., Fukuda S., Sato K., Fujikawa T., Chen R., Li Z., Tian J. and Nishida K. "Fuel Spray Evaporation and Mixture Formation Processes of Ethanol/Gasoline Blend Injected by Hole-Type Nozzle for DISI Engine". *SAE International Journal of Engines*, pp. 1836–1846, 2012.

[30] Gao J. and Nishida K. "Laser absorption-scattering technique applied to asymmetric evaporating fuel sprays for simultaneous measurement of vapor/liquid mass distributions". *Applied Physics B: Lasers and Optics*, pp. 1–11, 2010.

[31] Kokhanovsky A.A. and Zege E.P. "Optical properties of aerosol particles: A review of approximate analytical solutions". *Journal of Aerosol Science*, Vol. 28 n^o 1, pp. 1–21, 1997.

[32] Zhang H. "Approximate calculation of extinction coefficient". *Journal of Physics D: Applied Physics*, Vol. 23 n^o 12, pp. 1735–1737, 1990.

[33] Hecht E. and Zajac A. *Optics*. Addison Wesley, 2003.

[34] Gumprecht R.O. and Sliepcevich C.M. "Scattering of light by large spherical particles". *Journal of physical chemistry*, Vol. 57 n^o 1, pp. 90–95, 1953.

[35] Nishida K., Gao J., Manabe T. and Zhang Y. "Spray and mixture properties of evaporating fuel spray injected by hole-type direct injection diesel injector". *International Journal of Engine Research*, Vol. 9, pp. 347–360, 2008.

[36] Daun K.J., Thomson K.A., Liu F. and Smallwood G.J. "Deconvolution of axisymmetric flame properties using Tikhonov regularization". *Applied Optics*, Vol. 45, pp. 4638–4646, 2006.

[37] Dasch C.J. "One-dimensional tomography: a comparison of Abel, onio-peeling, and filtered backprojection methods". *Applied Optics*, Vol. 31, pp. 1146–1152, 1992.

[38] Akesson E.O. and Daun K.J. "Parameter selection methods for axisymmetric flame tomography through Tikhonov regularizaron". *Applied Optics*, Vol. 47 n^o 3, pp. 407–416, 2008.

[39] Pastor J.V., García-Oliver J.M., Bermúdez V. and Micó C. "Spray characterization for pure fuel and binary blends under non-reacting conditions". *SAE Technical Papers*, 2014.

[40] Pastor J.V., Garcia-Oliver J.M., Pastor J.M. and Vera-Tudela W. "One-Dimensional diesel spray modeling of multicomponent fuels". *Atomization and Sprays*, Vol. 25 n^o 6, pp. 485–517, 2015.

[41] Thring M.W. and Newby M.P. "Combustion length of enclosed turbulent jet flames". *Symposium (International) on Combustion*, Vol. 4 n^o 1, pp. 789 – 796, 1953.

[42] Spalding D. B. *Combustion and mass transfer.* 1979.

[43] Pickett L.M., Manin J., Payri R., Bardi M. and Gimeno J. "Transient Rate of Injection Effects on Spray Development". *SAE Technical Paper*, 2013.

[44] Abramovich G.N. *The theory of turbulent sets.* MIT Press, 1963.

[45] Thomson K.A., Johnson M.R., Snelling D.R. and Smallwood G.J. "Diffuse-light two-dimensional line-of-sight attenuation for soot concentration measurements". *Applied Optics*, Vol. 47 n^o 5, pp. 694–703, 2008.

[46] Manin J., Pickett L.M. and Skeen S.A. "Two-Color Diffused Back-Illumination Imaging as a Diagnostic for Time-Resolved Soot Measurements in Reacting Sprays". *SAE International Journal of Engines*, Vol. 6 n^o 4, 2013.

[47] Zapata L.D. *Caracterización de los Procesos de Inyecciónn-Combustiónn Diesel Mediante Visualización y Procesado Digital de Imágenes.* Doctoral Thesis, Universitat Politècnica de València, Departamento de Máquinas y Motores Térmicos, 2010.

[48] Vickery B.C. and Denbigh K.G. "The Polarisabilities of Bonds Part II: Bond Refractions in the Alkanes". *Transaction of the Faraday Society*, Vol. 45, pp. 61–81, 1949.

[49] Manin J. *Analysis of Mixing Processes in Liquid and Vaporized Diesel Sprays Through LIF and Rayleigh Scattering Measurements.* Doctoral Thesis, Universitat Politècnica de València, Departamento de Máquinas y Motores Térmicos, 2011.

[50] "Vaxa Software Educational Resources". *information available at http://www.vaxasoftware.com.*

[51] Heller W. "Remarks on refractive index mixture rules". *Journal of Physical Chemistry*, Vol. 69 n^o 4, pp. 1123–1129, 1965.

Chapter 5

Combustion and soot formation

Contents

5.1 Introduction

This chapter is focused on the characterization of combustion and soot formation. For this purpose, a wide variety of measuring techniques were combined to analyse spray autoignition, flame lift-off length and soot formation. Naturally, results and conclusions from the previous chapter have been accounted to determine the effect of the different parameters over combustion development and the consistence of the results presented in the following paragraphs.

Special attention has been paid to soot measurements, as it is one the most challenging topics in the field of compression ignition engines. As it has been discussed in chapter 2, three main optical techniques can be found in literature for this purpose, namely LII, 2C and LEM. Therefore, it was decide to compare them to determine their strengths and limitations, while providing guidelines for future works in this field. A complex optical set-up was used, where the three techniques were applied simultaneously. The aim was to obtain the most reliable results.

The chapter begins with the description of the optical set-up, as all measurements were carried out simultaneously. Following, the first part of the analysis is presented, which includes ignition delay and lift-off length characterization. The second part of the chapter is focused on soot measurements. The fundamentals of each of the three techniques is described, together with the strategy followed to compare results. Then, measurements are presented and the effect of fuel properties is analysed. Finally, a discussion regarding the experimental methodology has been included.

5.2 Optical System

The study under reactive conditions was carried out with four different optical techniques and the in-cylinder pressure measurements. The four optical accesses available in the cylinder head (chapter 3) made it possible to apply all measurements simultaneously. In figure 5.1, a scheme of the optical arrangement is depicted. All the elements have been numbered and the corresponding list can be found below the figure. More detailed descriptions of the different parts of the optical set-up are included in the following sections.

In figure 5.2, a sketch of the acquisition timing with the different techniques is given for the baseline injection conditions. The injector energizing time was set to 3 ms for all conditions, which results in an approximate 6 ms (18 CAD) real injection duration, considering electrical and hydraulic delays. Injector was triggered at 6 CAD before TDC (SoE) so that variations of the in-cylinder conditions during the injection event were minimized. 2C and LEM are able to measure soot formation during the whole combustion event, thanks to the high sampling rate of the detectors. At the same time, for each injection event, one image of both OH*-chemiluminescence and LII were recorded. The first one

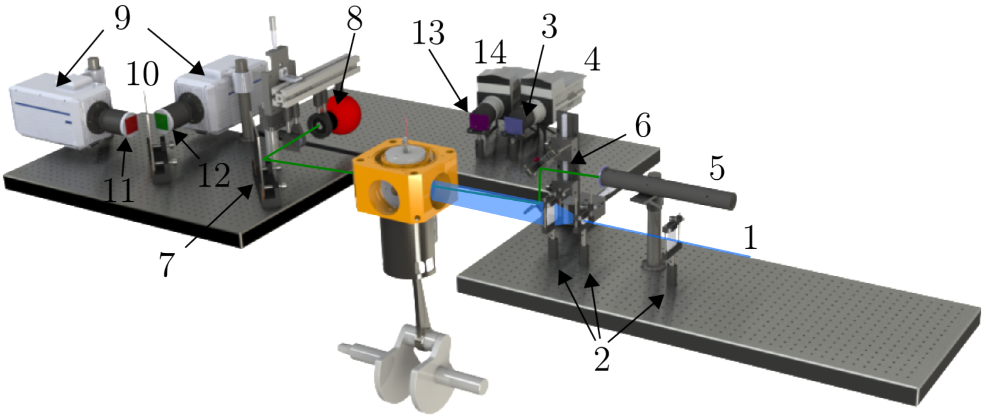

LII	LEM	2C	OH* - chem.
1 - Nd:YAG Laser Beam	5 - Laser fiber optics	9 - High-Speed CMOS cameras	13 - 310 nm filter
2 - Sheet-shaping lenses	6 - Mirrors and kinematic mounts	10 - Beam splitter	14 - ICCD camera
3 - Low-pass filter	7 - Beam splitter	11 - 650 nm filter	
4 - ICCD camera	8 - Recieving optics	12 - 550 nm filter	

Figure 5.1. *Scheme of the optical arrangement for test carried out under reactive conditions.*

was registered between 2200 and 3000 μs (0.6 to 3 CAD after TDC), during the stabilized stage of the flame. For the second one, a Nd:YAG laser was fired at 3 CAD after TDC to heat the soot particles. The LEM laser beam was aligned perpendicular to, and intersecting, the flame axis. The LII laser sheet was aligned with the spray axis.

As LEM is a point measuring technique, the corresponding optics were shifted along the flame axis to measure at different points. Therefore, light extinction was measured at 33, 42, 51 and 60 mm from the nozzle for two nominal conditions corresponding to $p_c = 5.3\ MPa$ at TDC and $p_{inj} = 100\ MPa$, for the two in-cylinder temperatures defined in chapter 3. For the rest of the operating conditions, light extinction was measured only at 33 and 51 mm from nozzle. Accordingly, the laser sheet was aligned to obtain LII signal from 22 to 67 mm from the injector. Finally, for each test condition, 15 repetitions were recorded for all the techniques.

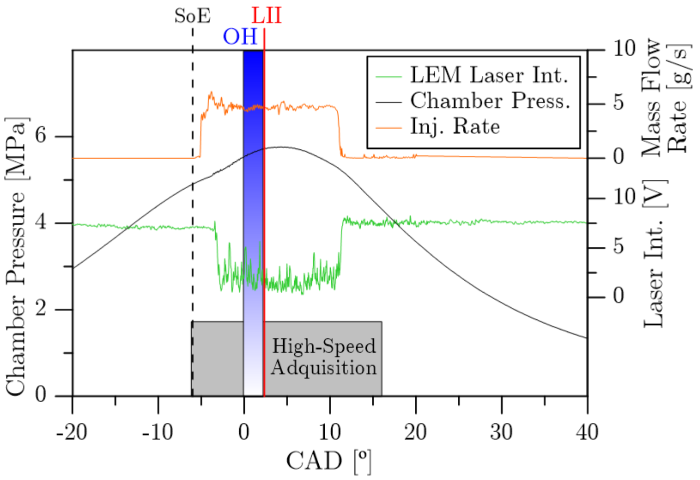

Figure 5.2. *Measuring sequence followed for test under reactive conditions.*

5.3 Ignition delay

According to chapter 2, the first stage of combustion is the autoignition process. Once fuel is mixed with the surrounding air and gets evaporated, the first low-temperature reactions take place. The time interval between the start of injection and the appearance of these reactions is known as ignition delay (ID), and depends on both chemical and physical properties of the fuel. Different methodologies can be found in the literature to characterize this parameter. Some of them are based on the detection of the first radiation, originated in the combustion chamber. The main benefit is that these methodologies make it possible to determine not only when low-temperature reactions take place but also its position within the combustion chamber (if a 2D sensor is used). Nevertheless, intensity of radiation of these reactions is low and makes it difficult to characterize the ignition delay with accuracy. In contrast, they cause an increase of pressure [1] in the combustion chamber that can be detected and used to measure the ID [2].

This approach has been followed in this work. In-cylinder pressure was measured by means of a pressure transducer (Kistler 6125B) an recorded at a sampling frequency of 100 kHz. Such resolution ensured an accurate measurement of ID, which was calculated for each injection event. The acquisition chain was configured so the motored cycle prior to the one with combustion was also registered. Therefore, it was possible to calculate in-cylinder pressure difference between combustion and motored cycles ($\mathit{\Delta P}$).

ID was defined as the time elapsed between de real start of injection (SoI) and the first instant when pressure rise exceeds two times the standard deviation of the time-averaged (ΔP) calculated between 35 and 10 CAD before TDC.

An example of the ID calculations is shown in figure 5.3, which corresponds to DEC at $\rho_c = 23.25\ kg/m^3$ at TDC. ΔP calculated for 15 repetitions is shown, with the corresponding ID values. As it can be observed, certain scattering occurs between repetitions. However, this behaviour could be expected considering the cycle-to-cycle variability of the test rig, which has been discussed in previous chapters. In order to provide more insight into how ID is affected, the histograms of measurements corresponding to $\rho_c = 23.25\ kg/m^3$ and $\rho_c = 20.73\ kg/m^3$ at TDC and $p_{inj} = 100\ MPa$ are shown in figure 5.4 for the four fuels. As it can be observed, scattering is similar for the four fuels and differences are only observable when comparing both operating conditions. When in-cylinder temperature is increased, ID scattering gets reduced for all the cases. Besides, in general, the four fuels present distributions similar to the typical Gaussian shape. Accordingly, ID can be represented by its mean value and standard deviation.

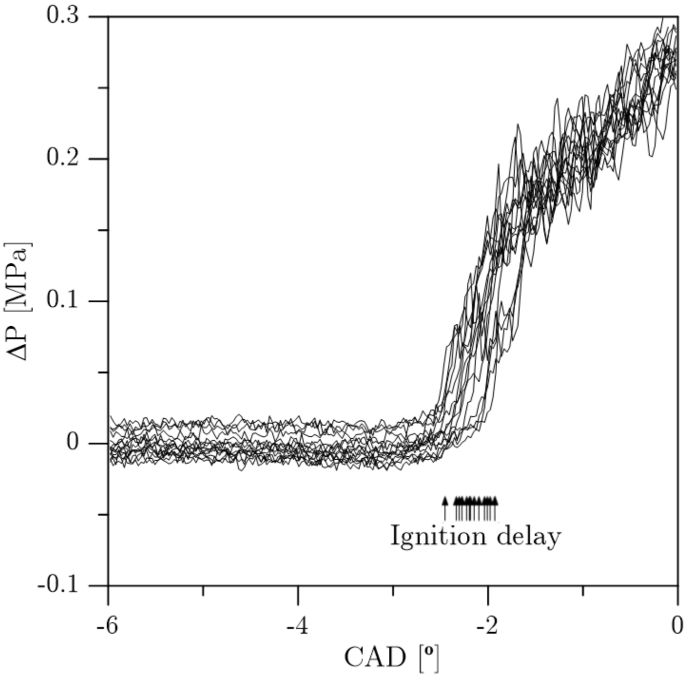

Figure 5.3. *ΔP calculated for 15 consecutive repetitions, with the corresponding ignition delay values measured for DEC, at $\rho_c = 23.25\ kg/m^3$ at TDC and $p_{inj} = 100\ MPa$.*

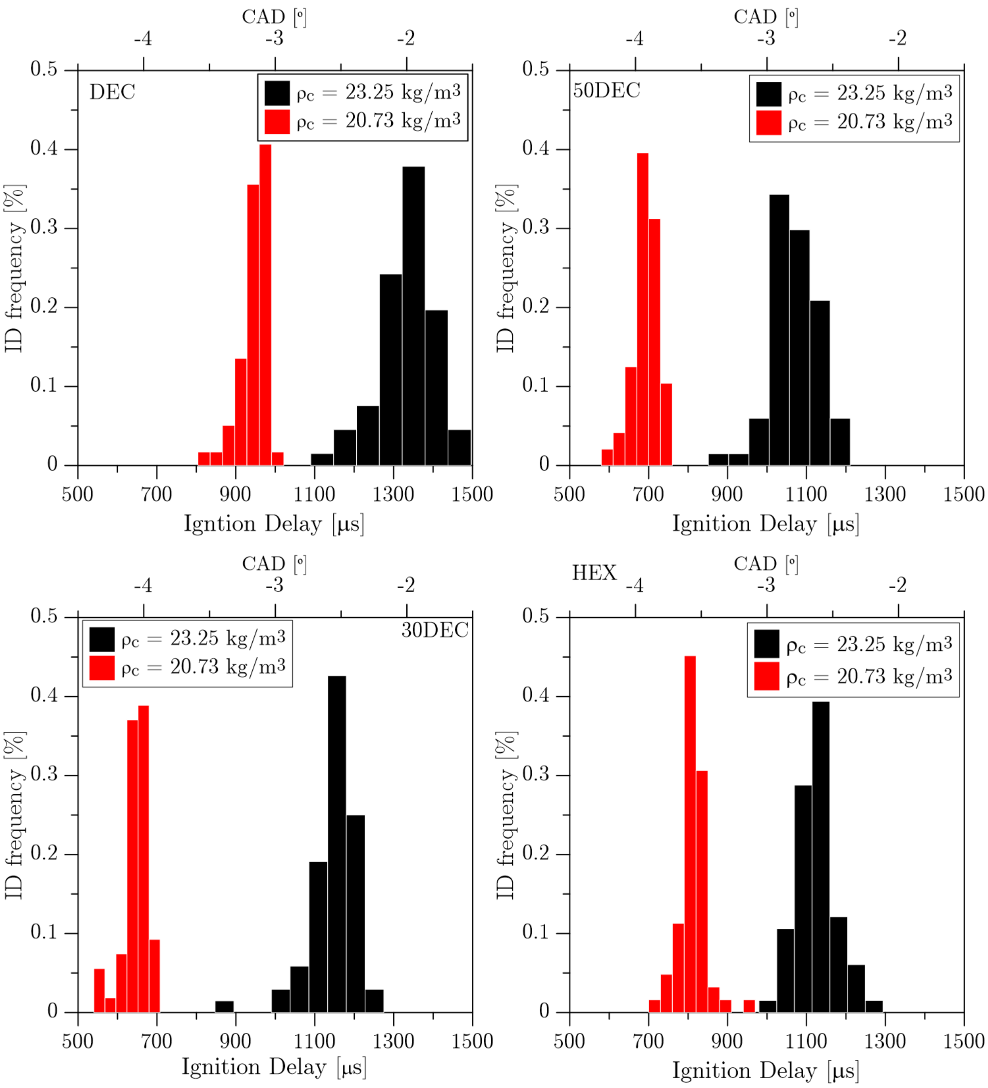

Figure 5.4. *Histograms of measurements of ignition delay for the four fuels. Data correspond to* $\rho_c = 23.25\ kg/m^3$ *at TDC and* $p_{inj} = 100\ MPa$.

In figure 5.5, ID is presented as a function of the fuel composition for the three injection pressures (left) and the three in-cylinder pressures proposed in figure 3.3, at both in-cylinder temperatures. Each fuel is represented by its content in n-Decane (%DEC). The first thing that can be observed is that ID is scaled with the CN of each fuel (see table 3.3), as expected, since this parameter is indicative of the reactivity of the fuel. The second fact that can be extracted from the figure is that the relationship between ID and %DEC is not linear. HEX seems to dominate the autoignition process as, even for 50DEC, ID is significantly lower than for DEC.

For all the fuels, an increase of p_{inj}, p_c and T_c produce a reduction of the ignition delay as they improve chemical kinetics. An improvement of the mixing process and an increase of the energy available in the surrounding gas boosts the development of the first chemical reactions. However, it is possible to see that sensitivity of all the fuels is not the same. As %DEC increases, the fuel seems to be more affected by operating condition variations (specially temperature). However, the effect of p_{inj}, p_c and the influence of fuel properties are soften when increasing T_c.

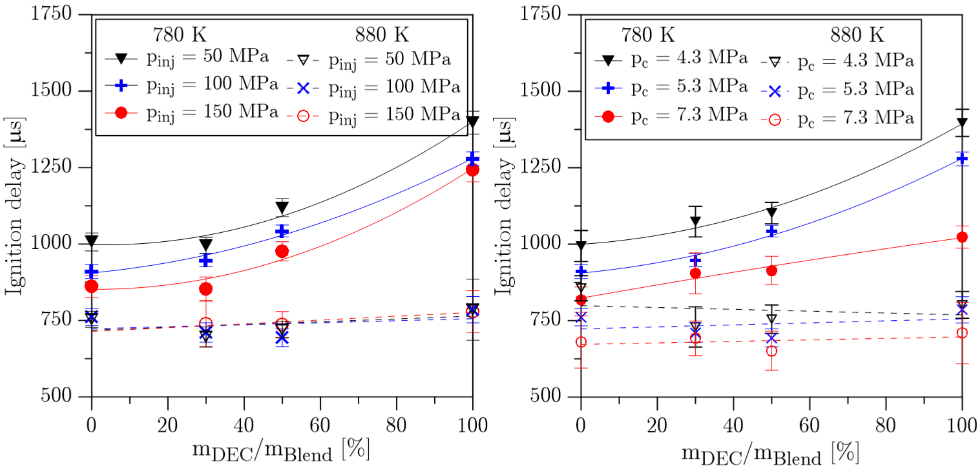

Figure 5.5. *Ignition delay as a function of fuel composition, for the three injection pressures (left) and the three in-cylinder pressures (right), and 780 and 880 K in-cylinder temperature at TDC.*

5.4 Lift-off length

The lift-off length (LOL) is an important parameter for diesel combustion understanding, as different studies have proved its relationship with soot formation [3–5]. All of them state that this parameter is related with the amount of oxygen entrained upstream of the region where high temperature heat release takes place. The visualization of line-off-sight OH*-chemiluminescence at the base of the flame makes it possible to measure the LOL, defined as the distance between the nozzle and the first chemiluminescence signal.

A gated 16-bit intensified CCD camera (Andor iStar) was used, equipped with a UV f/4 100 mm focal length lens. An interference filter centred at 310 nm (10 FWHM) was placed in front of the camera to remove the major part of the radiation of the flame while keeping OH*-chemiluminescence. The camera was triggered at 6.6 CAD after SoE while the intensifier was gated during 800 μs (i.e. 2.4 CAD in this case) and the gain was set to use the complete dynamic range of the camera without saturating it. Background segmentation was applied, based on a threshold value (D_{thresh}) calculated as a percentage (β) of the difference between the maximum (D_{max}) and the minimum (D_{min}) intensity level found in the image. This criteria is described by the following equation:

$$D_{thresh} = D_{min} + \beta(D_{max} - Dmin) \tag{5.1}$$

The value of β was arbitrarily set to 10%, as it offered a good compromise for all the different test conditions. Then lift-off length was defined as the average distance between the nozzle and the ten nearest pixels of the flame. The flame was divided axially due to its "double-lip" shape (figure 5.6) and each half-flame was processed independently. Then, LOL from the two halves was averaged.

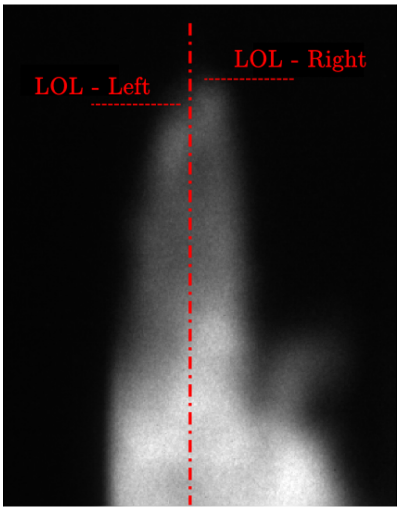

Figure 5.6. *Example of lift-off length detection for OH*-chemiluminescence of DEC at $\rho_c = 20.73\ kg/m^3$ at TDC and $p_{inj} = 100\ MPa$.*

The cycle-to-cycle LOL scattering is analysed in figure 5.7. The histograms depicted here correspond to $\rho_c = 23.25\ kg/m^3$ and $\rho_c = 20.73\ kg/m^3$ at TDC, and p_{inj} = 100 MPa. In this case, it has been decided to show only data of DEC and HEX to keep clarity in the figure. However, they can be considered as representative of the other two fuels. Unlike ID measurements, the scattering observed for LOL was significant from one cycle to other. The coefficient of variation (CoV) of these measurements varies between 3% and 15%, while for ID the maximum CoV calculated was below 10%. For all the cases shown in this figure, histograms are similar to Gaussian distributions. Therefore, each dataset can be characterized by its mean value and standard deviation.

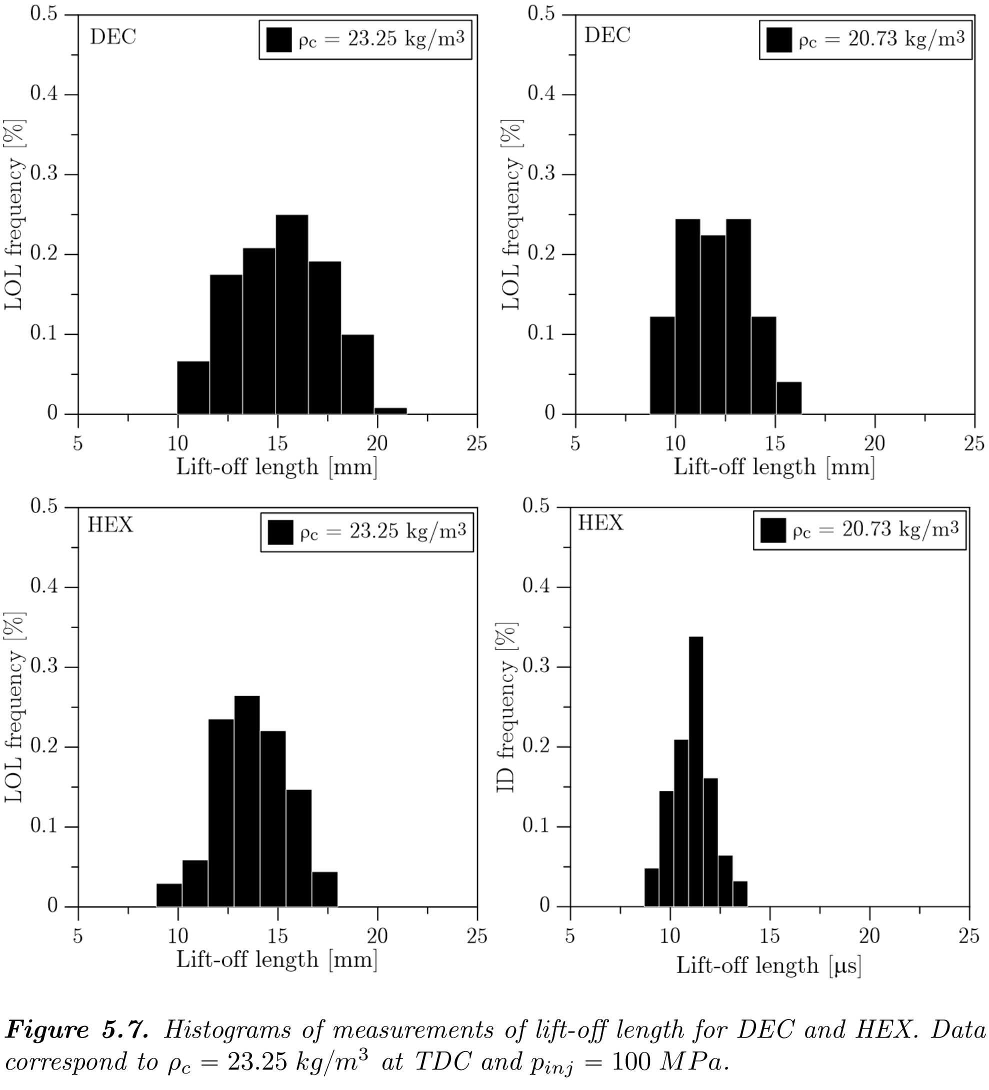

Figure 5.7. *Histograms of measurements of lift-off length for DEC and HEX. Data correspond to* $\rho_c = 23.25\ kg/m^3$ *at TDC and* $p_{inj} = 100\ MPa$.

In figure 5.8, LOL is plotted as a function of the fuel composition, for the three injection pressures (left) and in-cylinder pressures (right) proposed in figure 3.3, at both in-cylinder temperatures. Each fuel is represented by its content in n-Decane (%DEC). It is possible to see that LOL increases with the DEC fraction. This is consistent with the trends obtained for ID, as a less reactive fuel should ignite later and further from the nozzle than a more reactive one. In contrast with ID measurements, it is more difficult to state whether the relationship between %DEC and LOL is linear or not. For all the fuels, an increase of p_{inj} produces an increases of the LOL. In contrast, an increase of either in-cylinder pressure or temperature produces a reduction of LOL as it improves chemical kinetics. The reader can be referred to chapter 2, for more references in this regard.

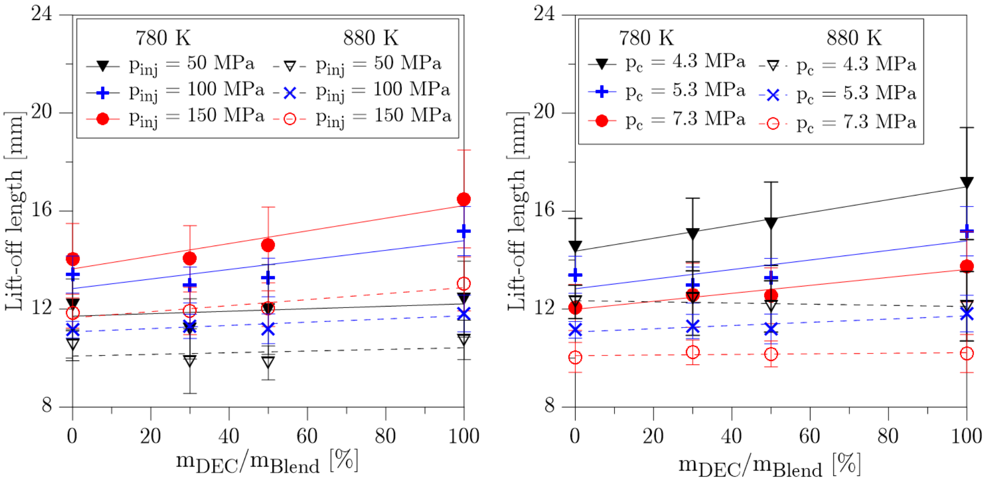

Figure 5.8. *Lift-off length as a function of fuel composition, for the three injection pressures (left) and the three in-cylinder pressures (right), and 780 and 880 K in-cylinder temperature at TDC.*

Considering all the foregoing, it is obvious that ID and LOL are related. It has been shown that, when chemical kinetics are favoured, both parameters decrease. This relationship is represented in figure 5.9, where LOL is plotted as a function of ID, for all the operating conditions of the test matrix (figure 3.2). In the left part of the figure, the whole dataset is depicted in series for the three levels of injection pressure. In the right part, data have been separated in the four fuels. In this case, only $p_c = 5.3\ MPa$ has been depicted for clarity, but it can be considered as representative of the rest of the test matrix. Two main effects are summarized in this figure. Firstly, the existence of a relationship in which LOL depends on ID and injection pressure (fuel velocity). Hence, the faster the fuel is injected and the longer it takes to ignite the larger the resulting LOL will be. Secondly, the stratification of both parameters due to fuel properties. All these results are consistent with conclusions previously reported by Pickett el al. [6] and Nerva [2].

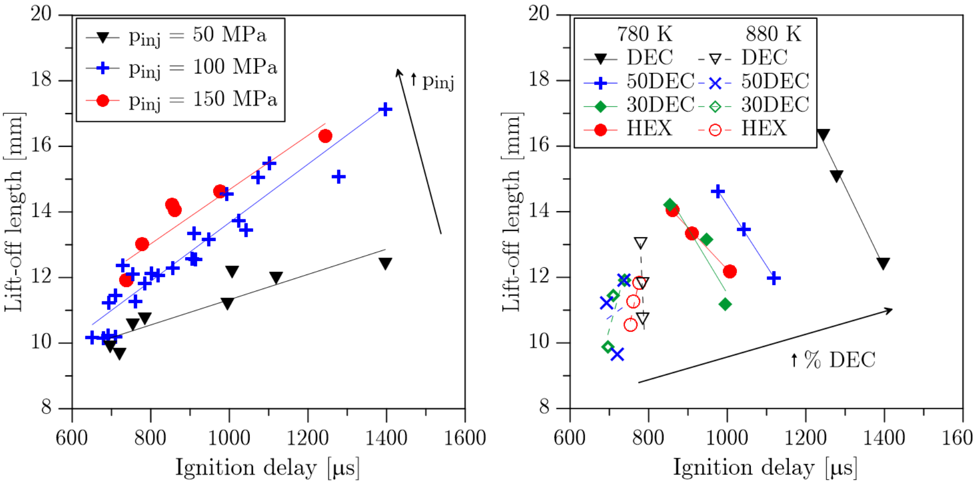

Figure 5.9. *Lift-off length as a function of ignition delay. Results from the four fuels under the entire test matrix are presented in the left plot, while only the temperature and injection pressure sweep are shown in the right plot, for* $p_c = 5.3\ MPa$.

In summary, according to results obtained for ignition delay and lift-off length, it can be stated that HEX is more prone to form soot than DEC. Its higher reactivity leads to shorter LOL and ID, which decreases the amount of oxygen entrained before high temperature reactions are reached. Regarding the two blends, results suggest that both ID and LOL are highly influenced by the most reactive fraction (i.e. HEX). The comparison presented in figure 5.9 (left) shows that 30DEC presents similar behaviour as HEX, while results for 50DEC lie between both pure fuels.

5.5 Soot Formation

The fundamentals of the three techniques used for the study of soot formation, namely Laser Extinction Method, 2 Colour Pyrometry and Laser Induced Incandescence are treated in the following subsections. Then a discussion is held to define the parameters to allow comparison of the outputs of the three techniques. Finally results of the parametric studies are presented and discussed, enhancing strengths and weaknesses of each technique and their combination.

5.5.1 Laser Extinction Method

The Laser Extinction Method (LEM) is based on the attenuation that a light beam undergoes when it traverses a soot cloud. It is caused both by scattering and absorption, which can be described by the Lambert-Beer's law. When the extinction properties of soot are considered as constant along the soot cloud, light extinction can be expressed as:

$$I = I_0 \exp\left(-K_{LEM} L\right) \tag{5.2}$$

where I and I_0 are the attenuated and original intensities, K_{LEM} is the dimensional extinction coefficient of the cloud of particles and L is the path length, which corresponds to the size of the cloud in the direction of the light beam. The extinction coefficient depends on the soot concentration and it can be expressed as:

$$K_{LEM} = \frac{k_{soot} Y_{soot}}{\lambda} \tag{5.3}$$

where Y_{soot} is the soot volume fraction, λ is the laser wavelength and k_{soot} is the dimensionless extinction coefficient, whose value will be discussed later. A continuous Argon-Ion laser was set to cross the combustion chamber through two aligned optical accesses (figure 5.1). The laser was tuned at 514.5 nm with 400 mW and oriented with a small angle of incidence in relation to the entrance quartz window due to space and optics limitations. Besides, it was observed that this orientation made it possible to remove any influence of the etalon effect on the measurements [7]. In order to minimize the divergence of the laser, a 500 mm focal length lens was set just at the output of the fiber optics that were used to guide the beam from the laser output towards the test rig (figure 5.10). The minimum beam waist (300 μm diameter) was located in the region of the flame and the laser beam was aligned in a way that it was crossing the flame axis. Two laser line mirrors with precision kinematic mounts were used to control the position of the beam for the measurement of light extinction at different positions along flame's axis (figure 5.10). Once the laser left the combustion chamber, it was reflected by a beam splitter (60% Transmission - 40% Reflection) towards the collection optics. This was necessary to keep an optical access free for simultaneous 2-Colour pyrometry measurements. Thus, the size of the beam splitter was large enough (127 x 178 mm) to cover the optical access.

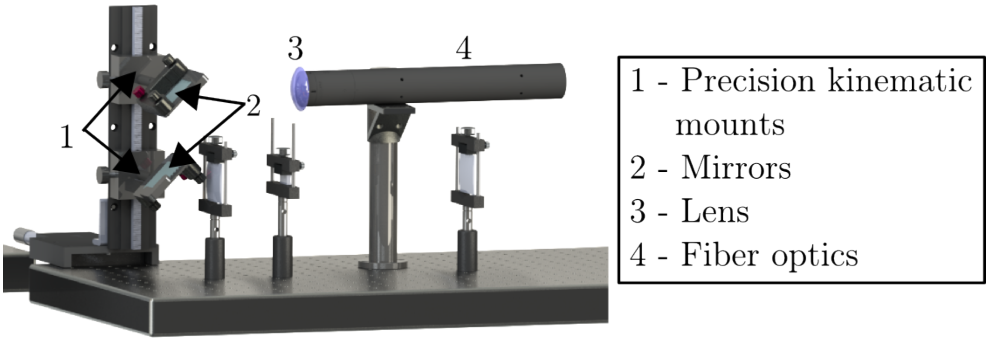

Figure 5.10. *Scheme of the emission optics for the Laser Extinction Method.*

Musculus et al. [7] presented an extended analysis of several uncertainty sources that must be considered when LEM is applied. Two major issues were identified: beam steering and the contamination of the measurement by light coming from the flame. The first one is a consequence of the refractive index gradients inside the combustion chamber due to fuel evaporation and combustion. In order to minimize this effect, a 50 mm diameter lens was placed just after the beam splitter (figure 5.11), to collect deviated rays up to a maximum divergence angle of 150 mrad. If the maximum divergence angle collected is too large, the light emitted by the flame can be also registered leading to an underestimation of the light extinction. In this sense, a diaphragm was located at the focal plane of the lens to limit the maximum divergence angle to 100 mrad [30]. Finally, between the diaphragm and the detector, a bandpass filter was placed (centered at 514 nm with 10 nm FWHM) to reject most of the flame radiation. The detector is a fast response photodiode, connected directly to an integrating sphere.

In order to calculate the instantaneous transmissivity of the flame, the attenuated intensity from each combustion event is compared with the intensity registered in the previous motored cycle according to equation 5.2. This ensures that effects like window fouling or intensity variations from the laser do not affect measurements. In figure 5.12, an example of $K_{LEM}L$ evolution is presented. The black line shows the value of the $K_{LEM}L$ averaged for the 15 repetitions. The grey area represents the standard deviation, which is not negligible. A similar behaviour was previously reported by Payri et al. [5], where the authors analyse the scattering inherent to the test rig.

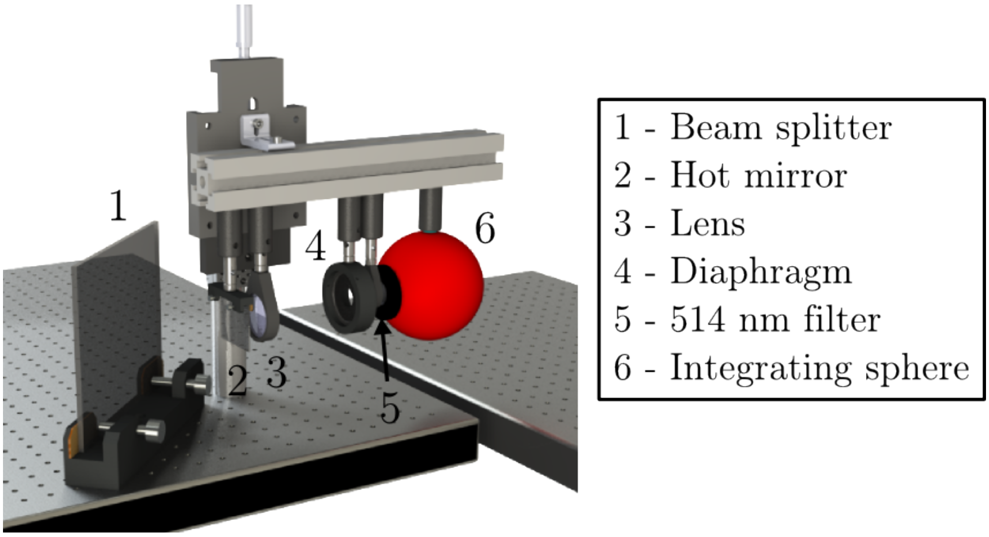

Figure 5.11. *Scheme of the receiving optics for the Laser Extinction Method.*

A minimum and maximum reliable $K_{LEM}L$ value were defined to verify LEM measurements. The I_0 signal presented certain noise even when the piston was at bottom dead center. At this point, density gradients inside the combustion chamber are minimal. Hence, if the laser is properly aligned, the measured noise can be attributed mainly to the measurement equipment (electronic source). This noise can be characterized by means of a standard deviation (σ). Thus, it is possible to define a minimum measurable $K_{LEM}L$ value with a confidence level of 95% by calculating $K_{LEM}L_{min} = \ln\left(I_0/(I_0 - 2\sigma)\right)$. Any value measured below this limit will not be considered as reliable. In the same way, in the ideal situation of complete attenuation, it is possible that measured laser intensity were not null due to the same noise source. In this situation, a similar standard deviation can be considered and a maximum measurable $K_{LEM}L$ value can be defined by calculating $K_{LEM}L_{min} = \ln I_0/2\sigma$, with a 95% confidence level. Higher $K_{LEM}L$ values will not be considered as reliable. The laser power and the photodiode amplifier were set so the baseline level was around 9 Volts (I_0). A representative value of 2σ for the major part of the tests was 0.13 Volts and therefore the corresponding minimum and maximum optical thickness to be accepted were found to be $K_{LEM}L_{min} = 0.015$ and $K_{LEM}L_{max} = 4.23$.

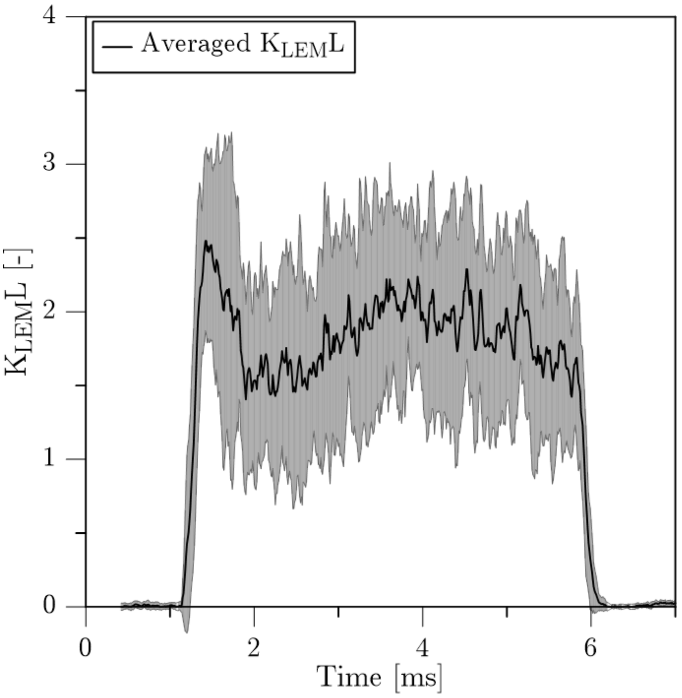

Figure 5.12. *Average* $K_{LEM}L$ *and standard deviation for* $p_c = 5.3\ MPa$, $T_c = 900\ K$ *and* $p_{inj} = 100\ MPa$, *at 50 mm from nozzle tip.*

5.5.2 2-Colour Pyrometry

The technique known as 2-Color Pyrometry (2C) is an optical thermometry technique that makes use of the presence of radiating soot inside the flame. The intensity of radiation emitted by soot particles (I_{soot}) is proportional to the radiation emitted by a black body at the same temperature (T). This proportionality is determined by the emissivity of the particles, which can be expressed in terms of soot concentration, working wavelength (λ) and a constant parameter (α) [8]. Therefore, I_{soot} can be expressed as the following equation:

$$I_{soot}(\lambda, T, K_{2C}L) = \left[1 - exp\left(-\frac{K_{2C}L}{\lambda^{\alpha}}\right)\right] \frac{1}{\lambda^5} \frac{c_1}{\left[exp\left(\frac{c_2}{\lambda T}\right) - 1\right]} \tag{5.4}$$

where $c_1 = 1.1910439 \cdot 10^{-16}\ Wm^2sr^{-1}$ and $c_2 = 1.4388 \cdot 10^{-2}\ mK$. Zhao et al. [9] reported that α values are less dependent to the wavelength in the visible range than in the infrared. In this regard, 550 and 650 nm were chosen for this work, so that $\alpha = 1.39$ for most of the fuels [10]. The dependence of the emissivity on the soot amount within the optical path is usually expressed in terms of $K_{2C}L$. This variable accounts for the total contribution of the soot along the optical path, no matter neither the soot distribution nor geometrical size.

In this work, two CMOS cameras were employed to measure soot radiation at two different wavelengths. The signal “S” registered by each sensor depends on the detector spectral response, the radiation intensity itself, the area A of the sooting flame within the field of view of the detector and the solid angle Ω subtended by the detector. Several simplifications can be applied [8], and a final expression is obtained for each wavelength:

$$S_\lambda = C_\lambda I_{soot}(\lambda, T, K_{2C}L) \tag{5.5}$$

where C_λ is a constant that takes into account A, Ω and λ. This parameter has to be calculated by means of a radiance calibration procedure. For this purpose, calibration curves were obtained by means of a previously calibrated light source, as it is described by Payri et al. [8]. For each electrical power condition and each camera settings used in the tests, 10 images of the lamp were recorded. Thus, a calibration curve was obtained per camera and acquisition settings. The slope of these curves is the transformation factor (C_λ) presented in equation 5.5.

The light emitted by the sooting flame crossed a first beam splitter (60% transmission - 40% reflection), which was placed to reflect the LEM laser (see figure 5.11). Then, a second beam splitter was used to transmit and reflect 50% of the soot radiation to each of the two high-speed CMOS cameras: a Phantom V12 for 650 nm and Photron SA5 for 550 nm. Both cameras were equipped with a 100 mm focal length and f/2 lens and an interference filter, centred at 650 nm and 550 nm respectively with 10 nm FWHM. In order to ensure frame-to-frame synchronization, both cameras were connected in a Master/Slave mode. They were set to record at 15000 fps, with 5 to 8 μs exposure time for 650 nm and 8 to 12 μs for the 550 nm, depending on the test conditions. A spatial transformation was required to match both images pixel by pixel. In this sense, a transformation matrix was calculated, considering translation, rotation and scaling. For both images, background segmentation was also applied with a thresholding procedure similar to that described previously in equation 5.1. The value of β was set to 5% for all the tests, which showed a good accuracy on the flame boundary detection for all the tests.

Once both images were coupled, equation 5.4 was applied for each wavelength and $K_{2C}L$ and temperature were obtained. In figure 5.13, an example of the application is shown. A colour composition of the soot natural luminosity for 550 nm and 650 nm is presented, together with the calculated map of $K_{2C}L$ and temperature. It is possible to see that the $K_{2C}L$ distribution is not homogeneous and even some spots of constant $K_{2C}L = 3$ are observed. These spots were artificially introduced, as they are formed by pixels where the combination of radiation at the two wavelengths leads to no-physical solution. In figure 5.14, intensity of radiation at 550 and 650 nm for each pixel of the flame shown in figure 5.13 is presented. Moreover, three curves are plotted which represent the different combinations of radiation that lead to $K_{2C}L = 0.1$ (green), $K_{2C}L = 0.5$ (blue) and $K_{2C}L = 3$ (red). When $K_{2C}L$ increases, its emissivity tends asymptotically to 1 (black body). For $K_{2C}L = 3$, the corresponding emissivity at 550 nm is 0.999. Therefore, the red curve can be interpreted as a frontier of the 2C methodology.

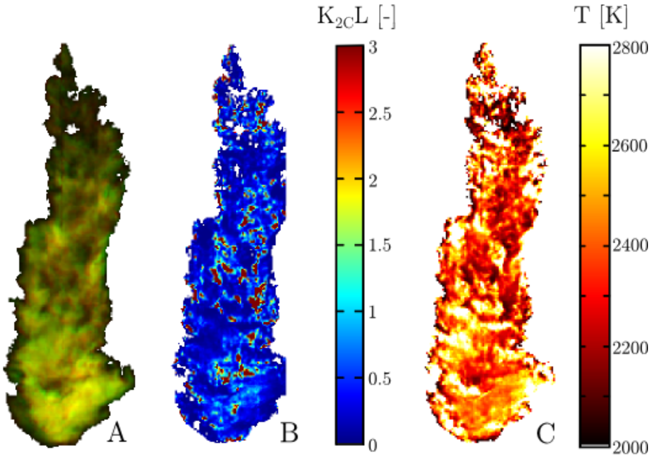

Figure 5.13. *Composition of instantaneous soot natural luminosity at 550 and 650 nm (A) and the corresponding* $K_{2C}L$ *(B) and Temperature (C) distributions. Data correspond to DEC, at* $\rho_c = 20.73\ kg/m^3$ *at TDC and* $p_{inj} = 100\ MPa$*.*

Different uncertainty sources [8, 11] can lead to a combination of intensities of radiation located in the red region of figure 5.14, which lead to a non-physical solution. When this happens, it is not possible to obtain a value of $K_{2C}L$ for these pixels and maximum $K_{2C}L = 3$ was assigned in this work. A similar heterogeneous distribution was previously reported by other authors [11–13]. Svensson et al. [11] suggest that the heterogeneity is real and not caused by uncertainty sources. However, Payri et al. [8] conclude that the influence of the different uncertainty sources is not negligible, leading to variations of $K_{2C}L$ up to 20%.

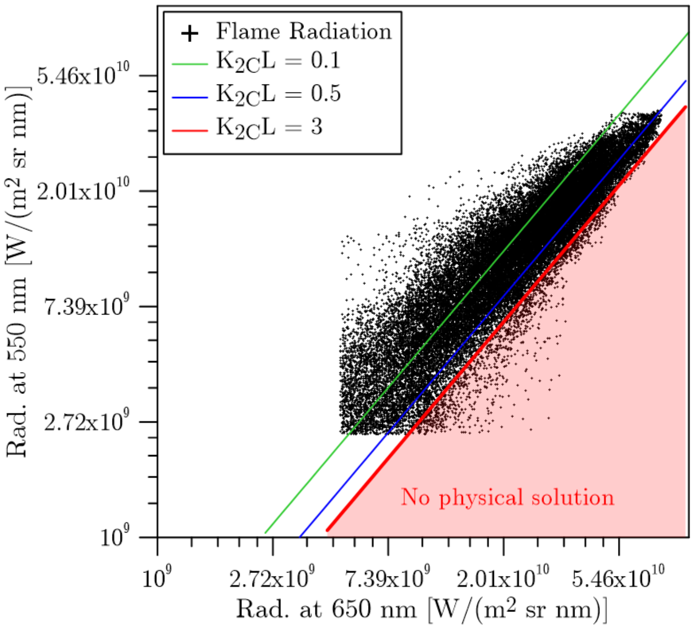

Figure 5.14. *Intensity of radiation for each pixel of a flame, at 550 and 650 nm. Data correspond to DEC, at* $\rho_c = 20.73\ kg/m^3$ *at TDC and* $p_{inj} = 100\ MPa$.

In order to reduce the influence of the different uncertainties over the final solution, an approach was followed based on the work presented by Yan et al. [14]: the intensity of radiation from all repetitions was averaged and the corresponding $K_{2C}L$ was calculated. In figure 5.15 the colour composition of the averaged natural soot radiation at 650 and 550 nm is shown (A), along with the $K_{2C}L$ obtained from the averaged radiances (B). The third $K_{2C}L$ map (C) was obtained by averaging the $K_{2C}L$ of the 15 repetitions, like the one shown in figure 5.13. When both $K_{2C}L$ distributions are compared, it is possible to see that values are similar but some differences are observable. This result is coherent with the analysis presented in [14] where the authors suggested that, despite no differences were observed, they should be expected due to the non-linearity of equations used. However, such differences seem to be more noticeable when the procedure is applied to images than when radiation is integrated from the whole combustion chamber by means of photodiodes.

Considering the previous analysis, and the lack of criteria to decide which way of calculating $K_{2C}L$ is the most reliable, it was decided to keep in the following sections the value derived from averaged soot radiation images. With

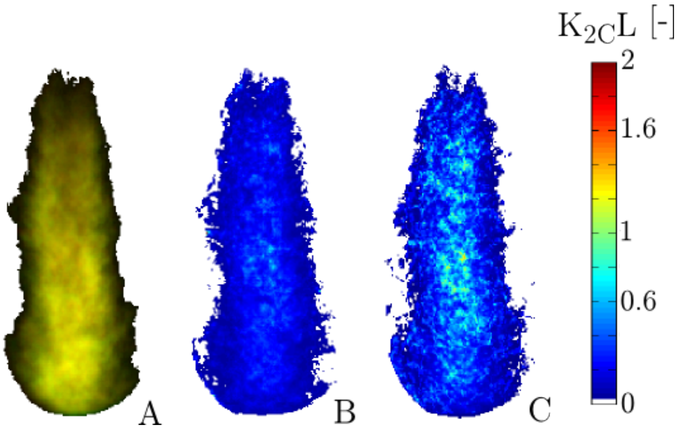

Figure 5.15. *Effect of averaging two colour pyrometry results: (A) Composition of averaged natural soot radiation (A) for 650 and 550 nm; (B) $K_{2C}L$ maps calculated from average images; (C) Map obtained as the average of the 15 individual $K_{2C}L$ maps. Data correspond to DEC, at $\rho_c = 20.73\ kg/m^3$ at TDC and $p_{inj} = 100\ MPa$.*

this methodology, the influence of measurement uncertainties such as read noise are minimized. Moreover, non-physical solutions as the ones described previously are avoided. Finally, it was important to remark that the processing time consumption is drastically reduced. This is an important issue, especially when high-speed imaging is applied due to the large amount of experimental data that is generated[1].

5.5.3 Laser-Induced Incandescence

The Laser-Induced Incandescence technique (LII) is based on the thermal radiation emitted by a soot cloud, when it is irradiated with an intense laser pulse. Soot particles absorb the laser light and are heated to higher temperatures than the surrounding gases and radiation from such particles is much more intense than that emitted by the particles at flame temperature. Therefore, it is possible to register the LII signal and remove the natural luminosity of the flame.

A laser sheet was created to heat the soot particles at the symmetry plane of the flame. A Nd:YAG laser pulse at 1064 nm was used, with 600 mJ/pulse and a Gaussian intensity profile. The main wavelength of this laser was chosen to avoid the PAH fluorescence, as it has been previously reported by Bobba

---

[1] In the experiments corresponding to the test matrix presented in chapter 3, a total of 108000 images were obtained

et al. [15]. Three cylindrical lenses were used to obtain a 45 x 0.35 mm^2 collimated laser sheet (see figure 5.10), with 450 mJ/pulse at the entrance of the combustion chamber. The equivalent energy fluence was calculated as 2.87 J/cm^2, which is large enough to get a signal independent of the laser pulse energy as it has been previously reported by other authors [15–17]. However, care must be taken during analysis as this high energy fluence could evaporate the smallest soot particles. The laser sheet was located to obtain LII signal from 22 to 67 mm from the injector nozzle, covering a similar range as the LEM measurement. The signal was registered by a 16-bit intensified CCD camera (LaVision Dynamight), equipped with a 100 mm focal length, f/2 UV lens. A low pass filter with the cutting wavelength at 400 nm was placed in front of the detector, to improve the separation between LII and natural luminosity from the flame. Nevertheless, for each test, the background radiation was measured and removed from the LII signal. In this regard, five images of the natural luminosity of the flame were registered and averaged to obtain the background signal. Background levels were found to be around 10% of the LII signal (varying between regions with intense or weak LII signal). It must be noted that this procedure is not an instantaneous correction. Therefore, it can be introducing local errors when single repetitions are considered. A 50 ns gate width was chosen, short enough to minimize the influence of ambient conditions but far larger than the jitter between the laser pulse and the intensifier window.

5.5.4 Evaluation strategy for soot measuring techniques

KL values (optical thickness) have been chosen as the metric of soot measurements, as it has been used extensively in literature [3, 5, 7, 18]. In this sense, a discussion regarding soot optical properties is omitted here. According to the literature survey, LEM measurements have been chosen as the reference technique for measurement of soot in flames, so performance and limitations of 2C and LII can be analysed relative to this technique.

The KL value obtained by means of LEM corresponds to the absorption cross-section (optical thickness) of the soot particles inside the flame. This parameter is proportional to the soot concentration and to the flame width. Considering Kirchhoff's law, under thermal equilibrium the emissivity ε equals absorptivity α. Moreover, if the interaction between light and soot particles were in the Rayleigh regime (i.e. if the particles are far smaller than the light wavelength), absorption would be dominant and scattering could be disregarded. Under this assumption, the emissivity of the 2-Colour Pyrometry and LEM absorption can be compared as follows:

$$1 - \exp\left(-K_{LEM}L\right) = 1 - \exp\left(\frac{-K_{2C}L}{\lambda^{\alpha}}\right) \tag{5.6}$$

where $K_{LEM}L$ is the optical thickness obtained by means of LEM. To compare both techniques, the same physical magnitude has to be used. At this point, nomenclature in the literature is sometimes inconsistent, as both extinction and 2C derived results are often defined as KL. Therefore, a new parameter (K^*_{2C}) will be used in this work, which has been defined as $K^*_{2C} = K_{2C}/\lambda^{\alpha}$ and should enable a direct comparison of the optical thickness of the flame obtained by means of 2C and LEM measurements, i.e. $K^*_{2C} = K_{LEM}$. Hence, considering that the wavelength used for laser extinction was 514.5 nm and $\alpha = 1.39$, the following relationship can be derived in the particular case of the measurements performed in this work:

$$K_{LEM} = K^*_{2C} = 2.519 \cdot K_{2C} \tag{5.7}$$

Note that the right-hand side of equation 5.7 is a semi-empirical derivation where λ is to be expressed in μm.

In order to provide optical thickness values from the LII signal, firstly it has to be converted to soot volume fraction. It can be found in the literature [9] that LII signal is proportional to the soot volume fraction, as it is expressed by equation 5.8:

$$Y_{soot} = C \cdot I_{LII} \tag{5.8}$$

where Y_{soot} is the soot volume fraction, C is a constant and I_{LII} is the registered LII signal intensity. The calculation of C can be addressed in two different ways. The first one is based on numerical approaches to characterize all the physical phenomena involved in the process. Different theoretical models can be found in the literature [19]. However, all of them show high complexity especially under engine conditions. The second procedure is based on an empirical calibration by means of an additional experimental technique. Different authors have evaluated the accuracy of this methodology [16, 17, 20–23]. Despite certain limitations, results suggest that it is a promising approach. Therefore, a similar methodology was followed in the present study.

LEM has shown up as a reliable data source for proper calibration of the LII signal. It is common to find in the literature that both the laser sheet and the LEM laser beam are coupled and co-planar in order to ensure a proper alignment. However, in this work LEM laser was tilted an angle of 1 degree with respect to the laser sheet. Considering the assumption that the flame is axisymmetric, as both laser beams cross the spray axis, the measurements were still comparable. Nevertheless, it could introduce some uncertainties that will be discussed later on. In order to compare both LII and LEM signals, the first one has to be integrated along the optical path. Thus, S_{LII} is defined as:

$$S_{LII} = \int_0^L I_{LII} dx \tag{5.9}$$

where I_{LII} is the LII intensity at each pixel of the image. If equations 5.3 and 5.8 are combined, the following expression can be obtained:

$$K_{LEM} = \frac{Ck_{soot}}{\lambda} \cdot I_{LII} = \frac{1}{C^*} \cdot I_{LII} \tag{5.10}$$

where C^* is constant. Then, equations 5.9 and 5.10 can be combined to obtain the following expression:

$$S_{LII} = C^* K_{LEM} L \tag{5.11}$$

The calibration constant C^* can be calculated by comparing $K_{LEM}L$ measurements with the corresponding I_{LII} integrated along the optical path (the width of the flame). In order to compare the LII results with both LEM and 2C, the optical thickness measured with LII ($K_{LII}L$) for $\lambda = 514.5$ nm has been defined according to equation 5.12:

$$K_{LII}L = \frac{1}{C^*} \int_0^L I_{LII} dx \tag{5.12}$$

In figure 5.16, the comparison between S_{LII} and $K_{LEM}L$ for DEC is shown. In this figure, the result of 360 different measurement points are plotted which include all the test conditions and the LEM measurement positions considered for this study. $K_{LEM}L$ values correspond to the average during the last 50 μs just before the LII laser is fired, to minimize scattering caused by the measuring technique (see figure 5.12).

It can be speculated that the data set fulfil the hypothesis of linear relation between $K_{LEM}L$ and S_{LII}. However, it is possible to see that the cloud presents large scattering. De Francqueville et al. [16] suggested that one of the main uncertainty sources was the signal trapping effect. Cenker et al. [17] observed a similar scattering but, in this case, signal trapping was discarded

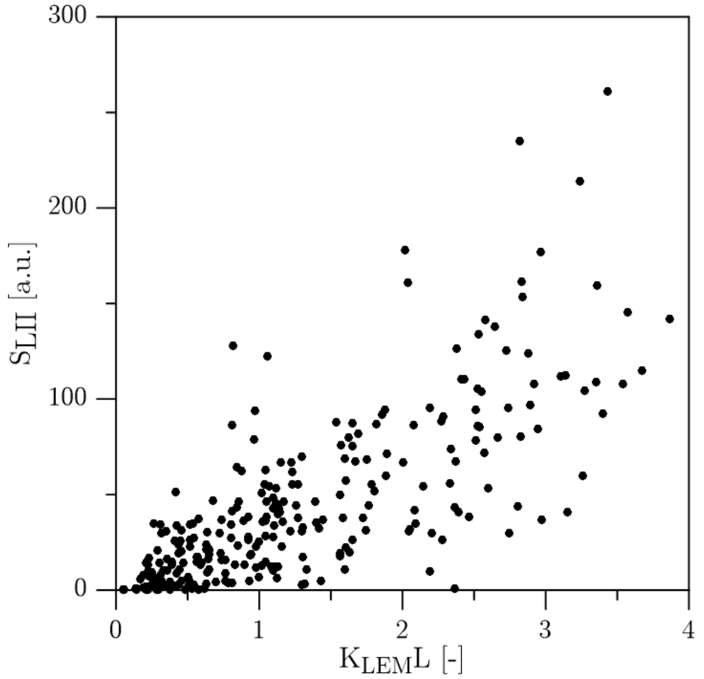

Figure 5.16. *Correlation between $K_{LEM}L$ and S_{LII} for DEC. Single-shot values.*

and it was attributed to a combination of different uncertainty sources from both techniques. Even if both techniques were optimized to minimize the uncertainty sources, the way that they were coupled should be analysed in terms of synchronization and alignment.

In figure 5.17 (A), the single-shot LII signal for different injections of DEC is shown. It is possible to see that there is scattering between different repetitions and, what is more, the flame is not perfectly axisymmetric. The author considers that this behaviour is inherent to the operating conditions of the test rig, caused by the interaction between the spray and the air flow inside the combustion chamber, as described in chapter 3. However, if the average flame (B) is observed, the assumption of axisymmetry seems to be valid. Therefore, the hypothesis followed to couple $K_{LEM}L$ and S_{LII} measurements seems to be more valid if average values are compared.

If the optical setup and the laser fluence is constant, it is possible to obtain a calibration constant (i.e. $1/C^*$) for the whole data set and the value obtained should be independent of the fuel and the in-cylinder conditions. In figure 5.18, average $K_{LEM}L$ and S_{LII} are compared for the four fuels. The average LII signal corresponds to the mean of 75 different images for the nominal points

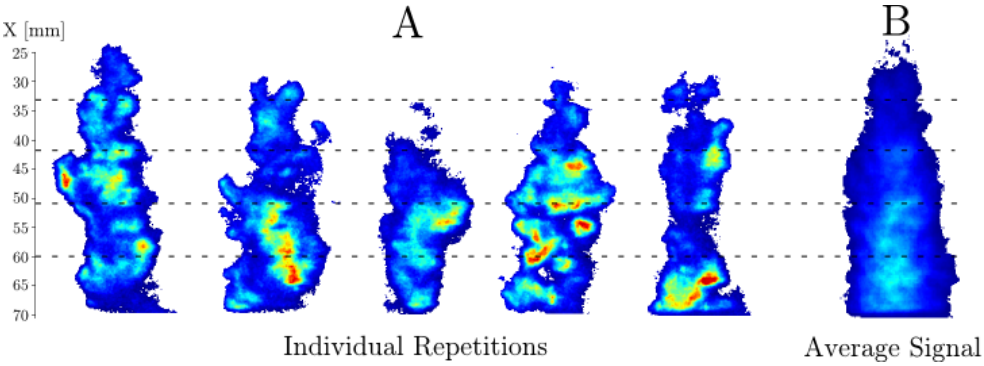

Figure 5.17. *Comparison between individual repetitions and the average I_{LII} signal for DEC, at $\rho_c = 20.73\ kg/m^3$ at TDC and $p_{inj} = 100\ MPa$. The dashed lines represent the positions where laser extinction was measured.*

($p_c = 5.3\ MPa$ at TDC and $p_{inj} = 100\ MPa$) and 30 for the rest of the cases of the tests matrix. It can be seen that linear relation is more visible and even a simple linear regression presents a $R^2 = 0.942$. The calibration constant obtained from the whole data set is 40.27. The hypothesis of axisymmetry presents its limitations as the number of repetitions has to be high enough. This is reflected in the scattering which is still observable in the figure.

5.5.5 Results

LEM, 2C and LII were utilized to study the effect of fuel properties over soot formation. However, a direct comparison between the different techniques also makes it possible to determine the reliability and limitations of each of them, which may be backed up by the measurements of ignition delay and LOL. In the present analysis, $K_{2C}L$ is converted according to equation 5.7, which will be denoted as $K^*_{2C}L$.

One of the main characteristics of the 2C methodology applied in this study is the use of two high-speed cameras. This made it possible to measure spatially resolved $K_{2C}L$ with time resolution, which is an advantage in comparison with the most of the applications of LEM and LII that can be found in the literature. A couple of examples are presented in figure 5.19, where maps of $K^*_{2C}L$ are shown at different instants after SoE. Images correspond to DEC, $p_{inj} = 100\ MPa$ and $\rho_c = 23.25\ kg/m^3$ and $\rho_c = 20.73\ kg/m^3$ at TDC, respectively.

The time evolution of the soot optical thickness obtained by means of 2C and LEM can be easily compared, considering $K^*_{2C}L$ values at the different

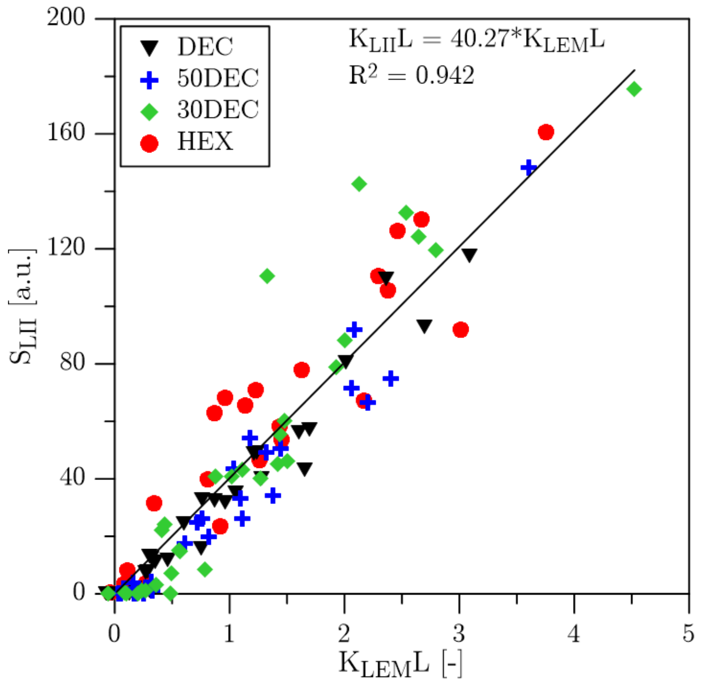

Figure 5.18. *Correlation between $K_{LEM}L$ and S_{LII} for the four fuels. Average values.*

measuring positions. Some examples of this comparison are shown in figure 5.20. Data correspond to DEC, at 33 and 51 mm from nozzle. The first thing that one can notice is that agreement of results with both techniques is sometimes quite poor. At 33 mm, where soot $K_{LEM}L$ is lower, 2C provide similar values for all the cases presented in the figure. However, $K_{LEM}L$ rises when moving to 51 mm while $K^*_{2C}L$ barely changes. The same behaviour is observed for the four operating conditions, but differences between both techniques are higher as $K_{LEM}L$ increases. In the same line, LEM makes it possible to measure spatial variations that are not detected by 2C measurements.

In figure 5.21, the time evolution of soot ($K_{LEM}L$) for the four fuels is compared. Data were measured at 51 mm from nozzle, and correspond to $\rho_c = 23.25\ kg/m^3$ (right) and $\rho_c = 20.73\ kg/m^3$ (left) at TDC, and $p_{inj} = 100\ MPa$ and $p_{inj} = 50\ MPa$ respectively. These operating conditions have been chosen as they represent high and low sooting conditions respectively. In this figure, differences between fuels arise. It is clear that, for both operating conditions, the optical thickness of the flame increases with the

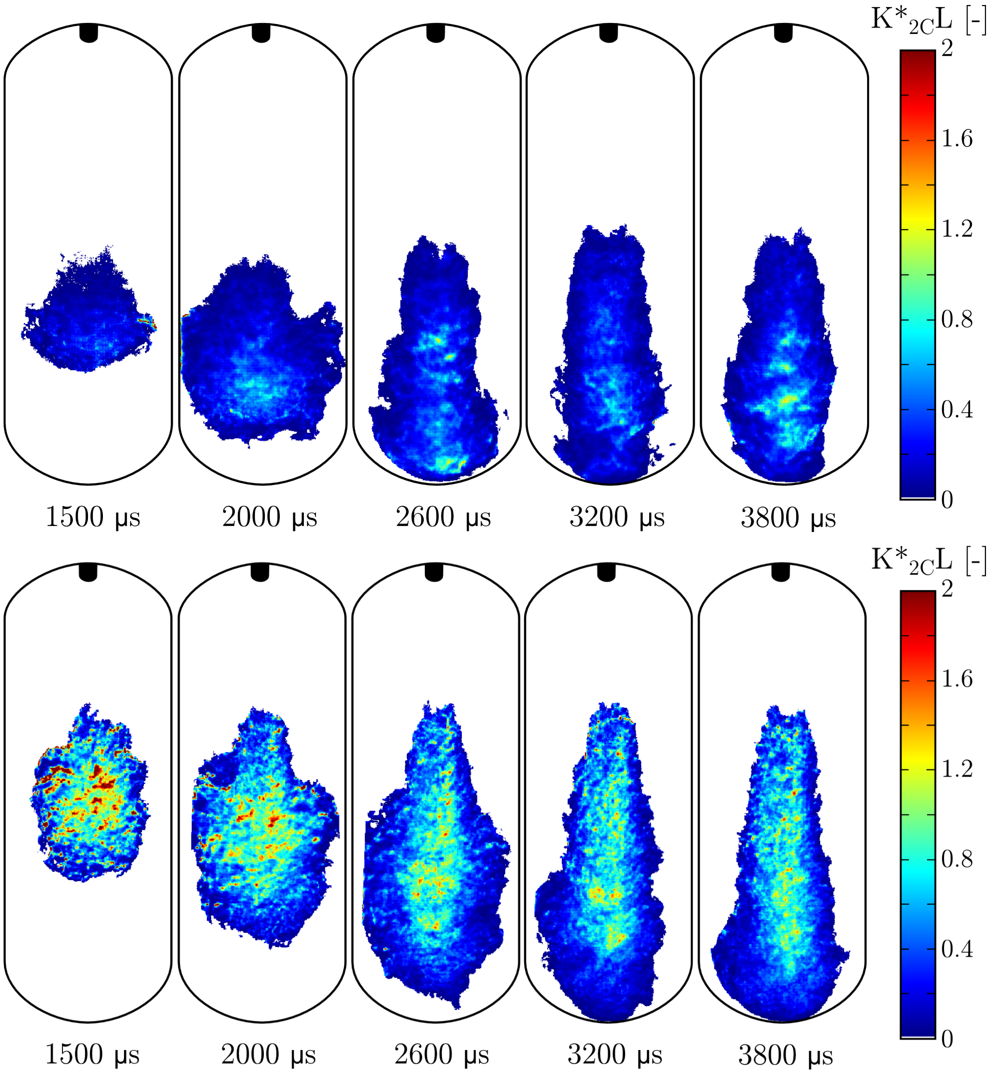

Figure 5.19. *Spatial distribution of $K^*_{2C}L$ at different instants after SoE. Data correspond to DEC, p_{inj} = 100 MPa and ρ_c = 23.25 kg/m^3 (up) and $\rho_c = 20.73$ kg/m^3 (down) at TDC.*

content in n-Hexadecane. In fact, both DEC and HEX represents the upper and lower limits while the two blends are located between them. Another fact that can be observed is that the time evolution of $K_{LEM}L$ is similar for the four fuels. Besides, values located near the maximum peak of the curves are not reliable, specially above $K_{LEM}L = 4$, due to limitations of the measuring range of LEM that has been previously discussed. Thus, this part of the

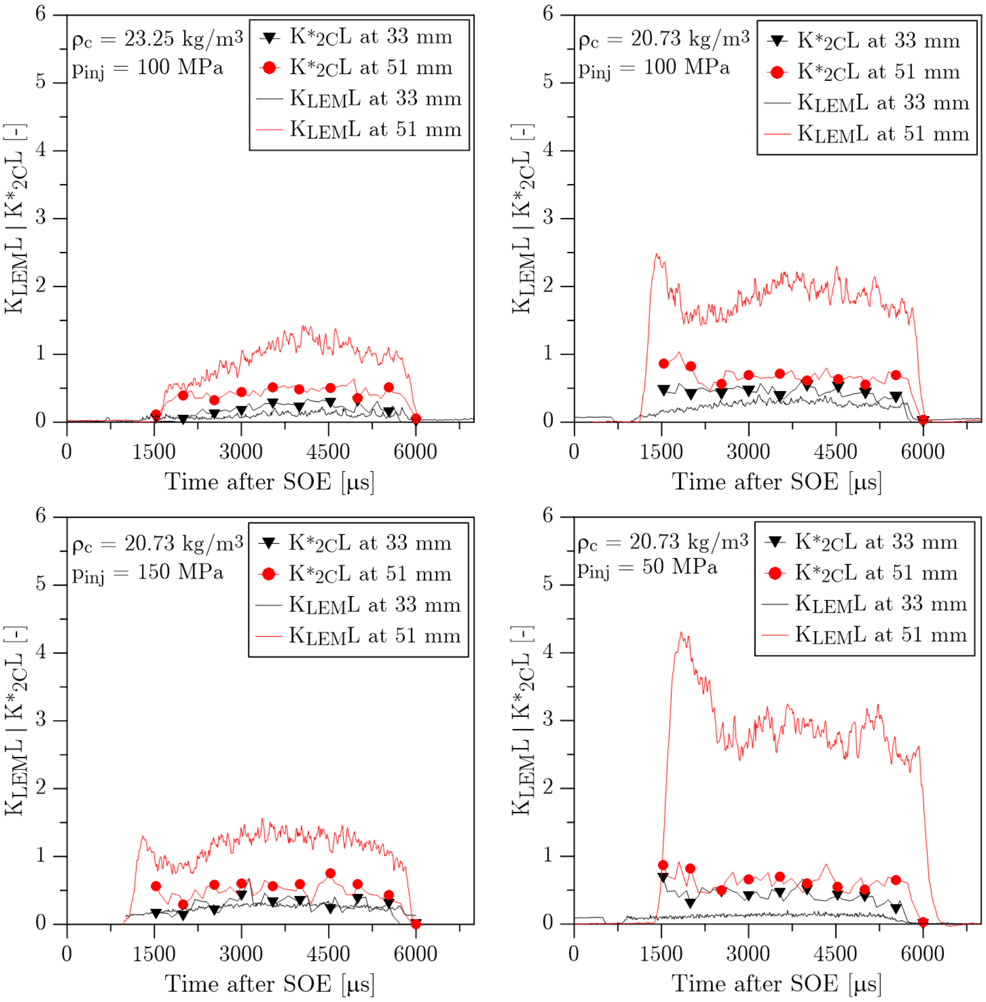

Figure 5.20. *Time evolution of $K^*_{2C}L$ and $K_{LEM}L$, at 33 and 51 mm from nozzle. Data correspond to DEC.*

combustion process should be avoided from the analysis. Considering all of this, it has been decided to focus the analysis of the spatial distribution of soot at one instant, in particular when the LII signal was measured.

From figure 5.22 to figure 5.24 KL soot measurements on the flame axis are presented for the four fuels, at different operating conditions. $K_{LEM}L$ values correspond to the average of the last 50 μs just before the LII laser was fired. $K^*_{2C}L$ values correspond to the 2C results obtained at 3 ms aSoE, coinciding with the LII measurement.

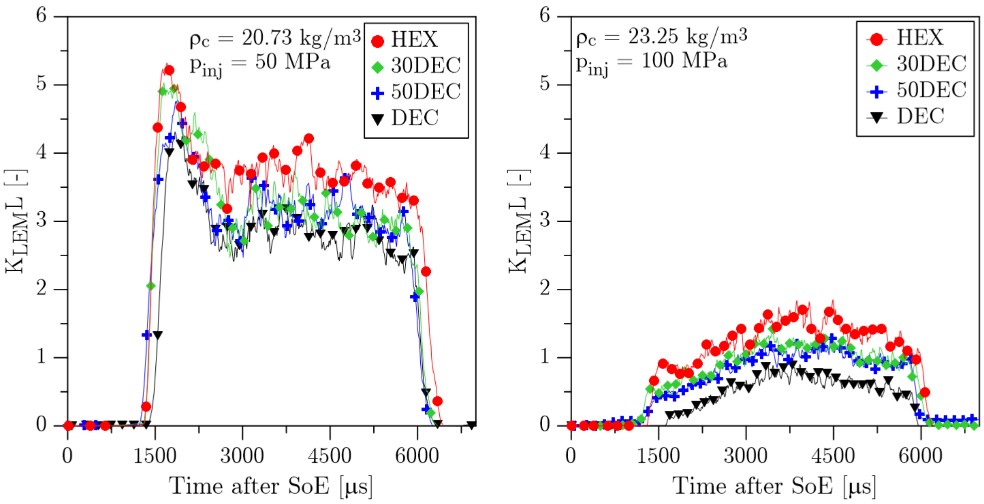

Figure 5.21. *Time evolution of* $K_{LEM}L$ *at 51 mm from nozzle. Data correspond to* $\rho_c = 23.25\ kg/m^3$ *(right) and* $\rho_c = 20.73\ kg/m^3$ *(left) at TDC, and* $p_{inj} = 100\ MPa$ *and* $p_{inj} = 50\ MPa$ *respectively.*

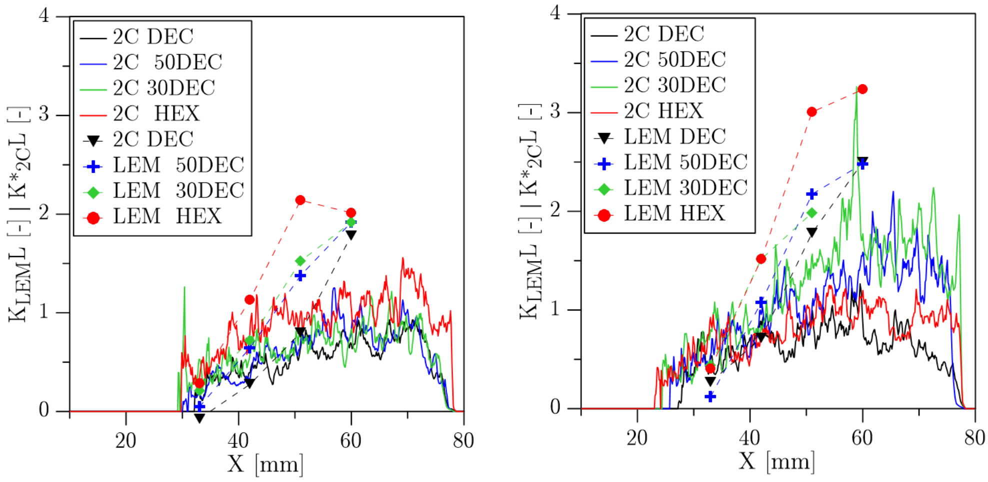

Figure 5.22. $K_{LEM}L$ *and* $K^*_{2C}L$ *on the flame axis for the four fuels, 780 K(left) and 880 K (right) in-cylinder temperature at TDC,* $p_c = 5.3\ MPa$ *at TDC and* $p_{inj} = 100\ MPa$*.*

In general, it is possible to see differences on the optical thickness measured for each fuel, which correlates with the increase in n-Hexadecane content. The higher reactivity of this molecule provides shorter LOL, which affects the soot formation. For 780 K cases, differences among fuels are coherent with the

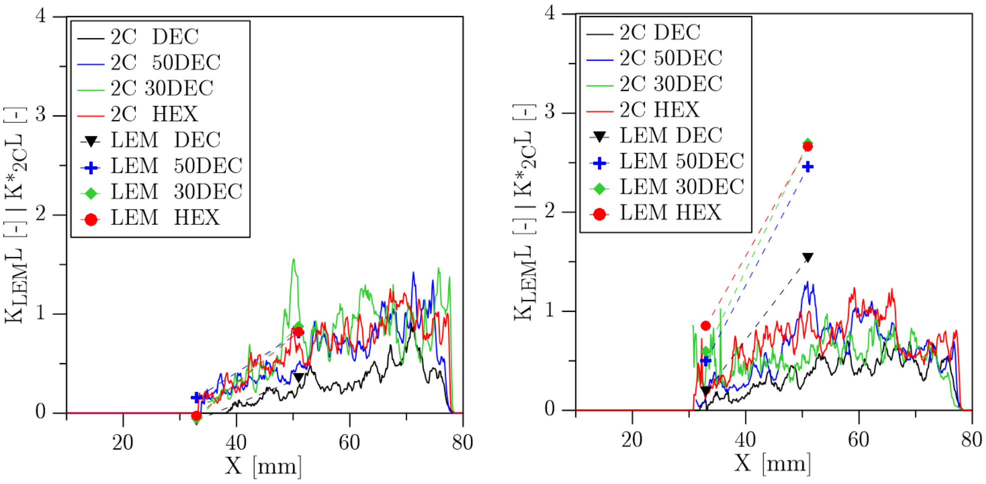

Figure 5.23. *$K_{LEM}L$ and $K^*_{2C}L$ on the flame axis for the four fuels, 4.3 MPa (left) and 7.3 MPa (right) in-cylinder pressure at TDC, $T_c = 780\ K$ at TDC and $p_{inj} = 100\ MPa$.*

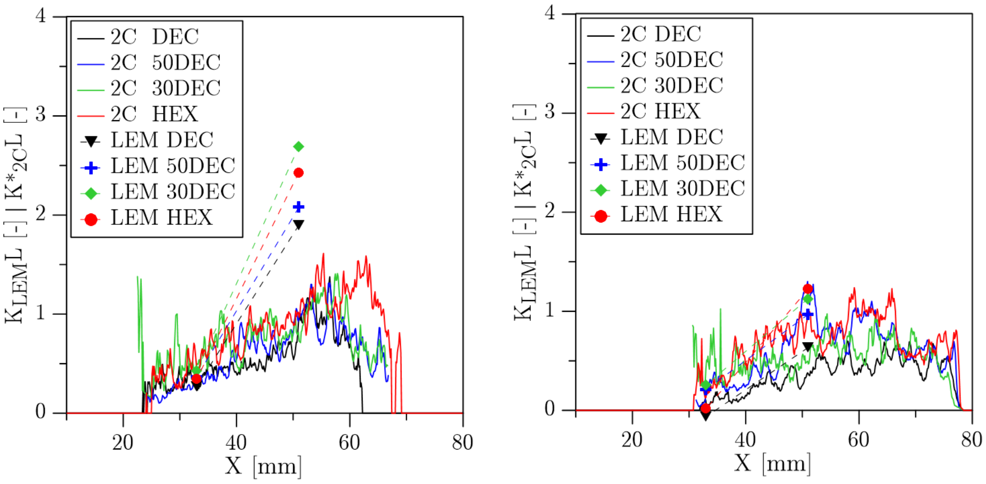

Figure 5.24. *$K_{LEM}L$ and $K^*_{2C}L$ on the flame axis for the four fuels, 50 MPa (left) and 150 MPa (right) injection pressure, $p_c = 5.3\ MPa$ and $T_c = 780\ K$ at TDC.*

values of LOL reported, in agreement with the conclusions presented in [4, 5]. At $p_{inj} = 50\ MPa$ (figure 5.24 -left-), a change in trend between 30DEC and HEX in terms of $K_{LEM}L$ is reported. However, it corresponds with the differences in LOL observable in figure 5.8 (left). The air-fuel ratio at LOL changes as it moves further from nozzle, affecting the soot formation for all the fuels.

When T_c and p_{inj} are increased or p_c is decreased, LOL collapses for all the fuels but differences in terms of optical thickness are still visible. The approach followed by Picket et al. [3, 4] has been utilized to estimate the air-fuel ratio at the LOL (appendix 5.A). A summary of all the calculations is presented in table 5.1. As it can be seen, for the fuels and operating conditions considered in the current study, differences in air-fuel ratio at LOL between DEC and HEX vary from 4% to 20% even for the same LOL. Besides, it can be found in literature [24] that when the size of the molecule increases (for n-alkanes) the Threshold Sooting Index[2] (TSI) also increases, which means that the fuel is more prone to form soot. Therefore, differences in both stoichiometry and chemical kinetics suggest that HEX should form more soot than DEC, which is coherent with the trends represented by $K_{LEM}L$.

ρ_c **[kg/m^3]**	17.03	19.17	20.73	23.25	29.06	32.1
DEC	6.639	4.015	5.781	3.990	5.181	3.421
50DEC	6.830	4.664	6.312	4.654	5.331	3.879
30DEC	6.739	4.859	6.235	4.821	5.346	3.908
HEX	6.892	5.134	6.448	4.820	5.483	4.150

Table 5.1. *Air-fuel ratio at lift-off length for the four fuels. Data correspond to* $P_{inj} = 100\ MPa$.

The effect of the operating conditions on soot formation is similar for the four fuels. An increase of in-cylinder temperature and pressure cause an increase in soot formation. The air-fuel ratio at LOL decreases as it moves closer to the nozzle, which is reflected on the later soot formation. Besides, there are also some kinetic effects that cannot be discarded [4]. When the injection pressure is increased, the LOL moves further from the nozzle and consequently soot formation is reduced, in agreemen with the measurements presented. Moreover, some authors [4] relate this reduction in soot with a decrease of the residence time of fuel at the reaction zones when injection pressure is increased. All these trends are clearly visible with $K_{LEM}L$ but

---

[2] The Threshold Sooting Index was developed by Calcote and Manus [25] to rank the sooting tendency of pure hydrocarbon fuels

not with $K^*_{2C}L$. In general, 2C results present less sensitivity to the operating conditions or fuel properties than results obtained with LEM.

Results obtained with LII are presented from figure 5.25 to 5.27. Data correspond to average LII obtained after using the calibration from the average LII/LEM signals. For each LEM position, 15 LII images were recorded. Therefore, the average signal shown in the following figures corresponds to the mean of 75 different images for the nominal points ($p_c = 5.3\ MPa$ and $p_{inj} = 100\ MPa$) and 30 for the rest of the tests matrix. The equivalent optical thickness ($K_{LII}L$) of the flame along its axis is obtained by means of equation 5.12.

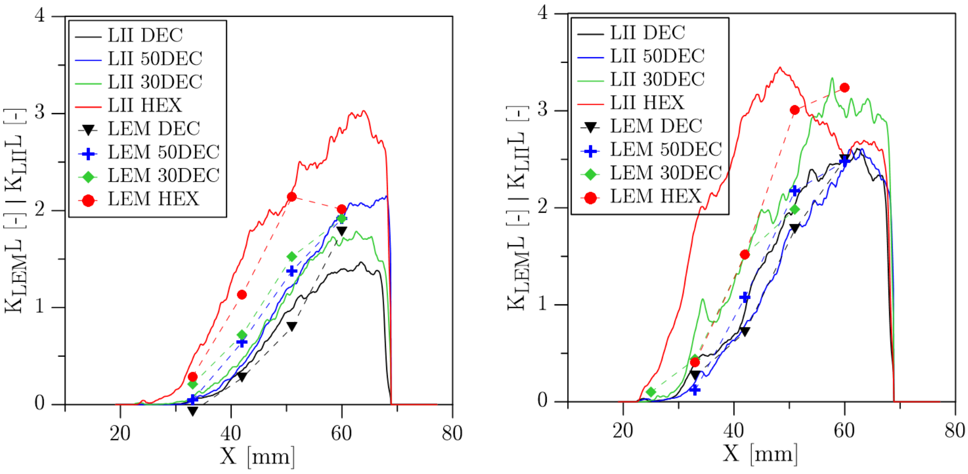

Figure 5.25. *$K_{LEM}L$ and $K_{LII}L$ on the flame axis for the four fuels, 780 K(left) and 880 K (right) in-cylinder temperature at TDC, $p_c = 5.3\ MPa$ at TDC and $p_{inj} = 100\ MPa$.*

In all the figures it can be seen that LII has characterized the effect of both fuel properties and test conditions over soot formation. However, it is important to remark the larger sensitivity of $K_{LII}L$ in comparison with $K^*_{2C}L$. Overall, there is a high agreement between the spatial soot distribution of both LII and LEM, compared to 2C. This proves that, for the conditions investigated, the use of a single calibration proportionality between both techniques is accurate enough to produce meaningful results, even for different fuels.

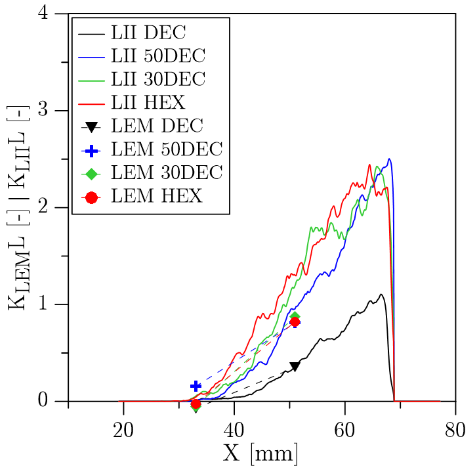

Figure 5.26. $K_{LEM}L$ *and* $K_{LII}L$ *on the flame axis for the four fuels, 4.3 MPa (left) and 7.3 MPa (right) in-cylinder pressure at TDC,* $T_c = 780\ K$ *at TDC and* $p_{inj} = 100\ MPa$.

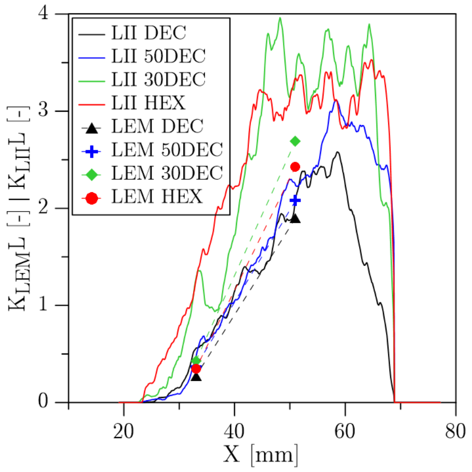

Figure 5.27. $K_{LEM}L$ *and* $K_{LII}L$ *on the flame axis for the four fuels, 50 MPa (left) and 150 MPa (right) injection pressure,* $p_c = 5.3\ MPa$ *and* $T_c = 780\ K$ *at TDC.*

5.5.6 Discussion on the soot diagnostics

When comparing LEM and 2C, it has been possible to see that $K_{LEM}L$ is more sensitive to variations of the soot levels for different operating conditions or fuel properties. Even within the flame, the increase of $K^*_{2C}L$ along the axis is small in comparison with $K_{LEM}L$ trends. The comparison between both techniques has been summarized in figure 5.28. In general, it can be stated that values provided by 2C are lower than the ones obtained by LEM. Furthermore, these differences are shown to increase when the optical thickness of the flame increases (larger $K_{LEM}L$).

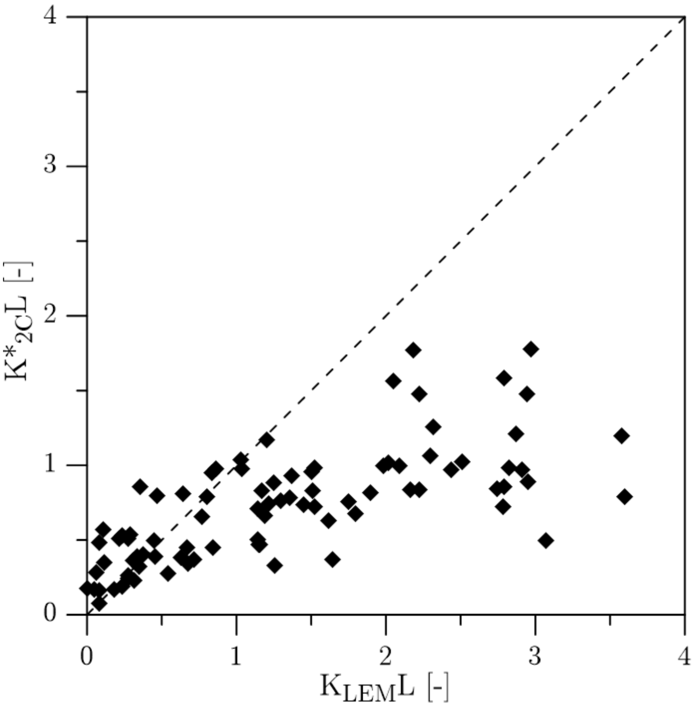

Figure 5.28. *Comparison between experimental $K_{LEM}L$ and $K^*_{2C}L$.*

A theoretical approach has been followed to better understand the behaviour of the 2C technique. Simple radiation propagation concepts have been used, following a similar methodology as Payri et al. [8]. These authors described the behaviour of the 2-Colour Pyrometry technique under different in-cylinder conditions and compared experimental measurements with theoretical predictions, based on the equations shown in the previous sections.

A radial flame profile, perpendicular to its axis, can be discretized as an axisymmetric distribution of layers, with constant k_{soot} and temperature (figure 5.29). Each of these layers both emits ($I_{soot,i}$) and absorbs (α_i) radiation from the previous layers. Thus, the intensity measured by one detector on one side of the flame is the result of an accumulation of emission and absorption processes along the optical path, through all the layers inside the flame. $I_{soot,i}$ is calculated by equation 5.4 while α_i is obtained from equation 5.6. Finally, it is possible to calculate the corresponding optical thickness of the profile ($K_{LEM}L$) as the accumulation of the $K_{LEM}L_i$ from the different "i" layers inside the flame as it is defined by equation 5.13.

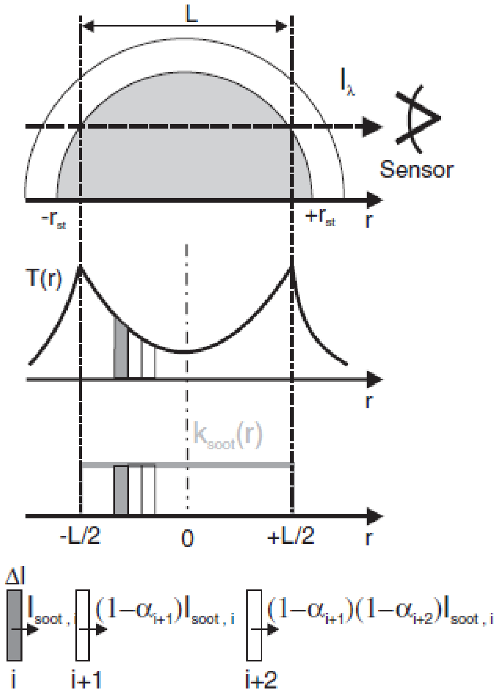

Figure 5.29. *Theoretical interpretation of flame radiation as composition of radiation emitted and absorbed by different layers, with their own soot concentration and temperature. Source: Payri et al. [8].*

$$K_{LEM}L = \sum_{i=1}^{2R} 2.519 k_{soot,i} L_i \tag{5.13}$$

where R represents the maximum radius of the profile and L is the width of each layer. Several flame temperature and k_{soot} radial distributions were evaluated, based on previously published experimental results [8], which are shown in figure 5.30. It must be noted that this approach assumes instantaneous oxidation of soot at the diffusion flame front. Therefore, radial distribution of both temperature and k_{soot} are only considered until that particular location. The shape of k_{soot} profile was kept constant for all the calculations while the $Mink_{soot}$ and $Maxk_{soot}$ values were modified to vary the total amount of soot. The temperature profile shape was kept also constant, but the minimum value was modified in order to evaluate its influence on the final measured $K_{2C}L$. Peak temperature was fixed at 2800 K, close to the values obtained at the edge of the flame for $T_c = 900\ K$ cases.

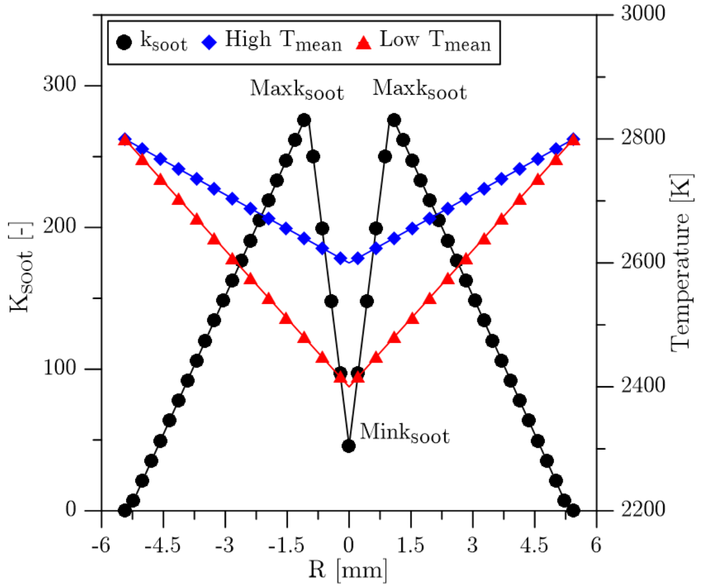

Figure 5.30. *Theoretical profiles for k_{soot} and flame temperature distribution.*

A final radiated intensity was calculated for 650 and 550 nm and equation 5.4 was applied to obtain the corresponding $K_{2C}L$. At the same time, the optical thickness of the profile was also calculated ($K_{LEM}L$). For different k_{soot} and temperature distributions (figure 5.30), the corresponding $K^*_{2C}L$ and $K_{LEM}L$ have been compared. Three data sets are presented in figure 5.31. For each of them, the temperature profile and the value of $Mink_{soot}$ were kept constant, while $Maxk_{soot}$ was modified to simulate the variation in the total soot mass within the flame. Values of $Maxk_{soot}$ were varied between 45 ($Y_{soot} = 13\ ppm$) and 370 ($Y_{soot} = 50\ ppm$).

Theoretical calculations show a trend which is consistent with the experimental results presented in figure 5.28. For the high T_{mean} case, no differences can be observed in $K^*_{2C}L$ when k_{soot} distribution is modified while keeping the total optical thickness of the distribution constant. This suggests that the total amount of soot is more important than its distribution along the flame width. However, if both temperature profiles are compared

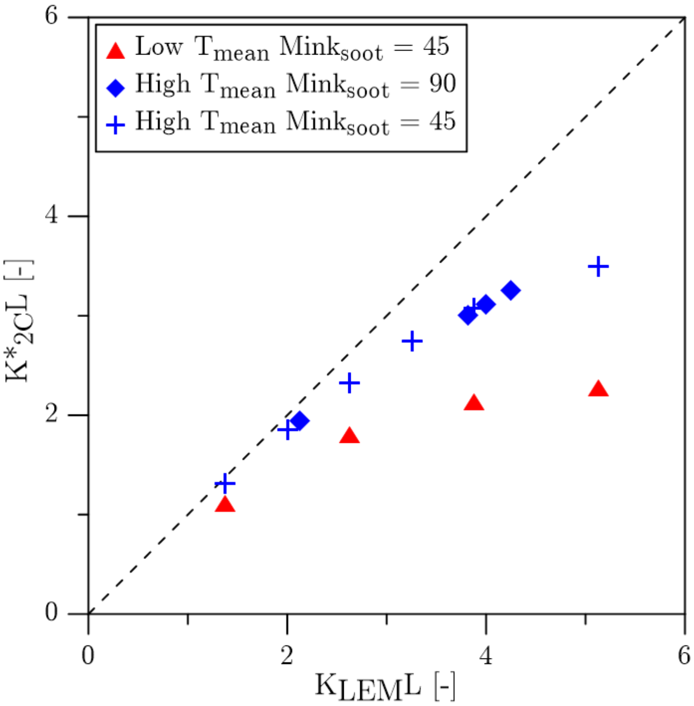

Figure 5.31. *Comparison between theoretical $K_{LEM}L$ and $K^*_{2C}L$ for different k_{soot} and temperature distributions.*

without modifying the soot distribution, an increase in $K^*_{2C}L$ with T_{mean} is observed. This suggest that, in the low T_{mean} case, the influence of the outer (hotter) layers over the final measured radiation is more important, leading to larger differences between $K^*_{2C}L$ and $K_{LEM}L$. This is consistent with some results presented by Payri et al. [8] for heterogeneous distributions of soot and temperature along the flame. Musculus et al. [26] defended a similar conclusion, based on CFD calculations and the integrated radiation from the whole combustion chamber. Svensson [27] also reported differences in optical thickness, with maximum values between 4.49 and 2.66 for $K_{LEM}L$, and between 1.3 and 1.02 for $K^*_{2C}L$. Moreover, Skeen et al. [28] presented variations of the ratio between LEM and 2C from 1.5 at the highest temperature to 5 at the lowest temperature. Nevertheless, their analysis is based on experimental results where soot and temperature varied simultaneously.

According to the previous discussion, $K^*_{2C}L$ measurements are clearly biased by the soot content inside the flame. Moreover, the temperature distribution has shown up as a weighting factor. When soot concentration is low, the influence of absorption from the outer soot layers is less important and its effect over the detected radiation is reduced. Thus, the differences between experimental $K_{LEM}L$ and $K^*_{2C}L$ remain below 20% when $K_{LEM}L$ is lower than 1. However, when soot concentration (and thus the optical thickness) increases, the absorption effect becomes relevant. Logically, $K_{LEM}L$ increases its value, but $K^*_{2C}L$ does not, as a fraction of the intensity emitted by the different soot layers does not reach the detectors. The ratio between both KL values ranges from 20% for $K_{LEM}L \approx 1$ to almost 80% for $K_{LEM}L \approx 4$. Additionally, larger differences in temperature between the internal and external layers will increase the biasing effect. Therefore, care must be taken when using results obtained from 2-Color Pyrometry under highly sooting conditions. The technique is based on the emission of light by hot soot, but radiation attenuation by the soot absorption itself should be also taken into account.

In contrast, Laser-Induced Incandescence has shown similar sensitivity as LEM to detect changes in soot formation when thermodynamic conditions or fuel properties are varied. The combination of both clearly improves the poor spatial resolution of LEM and represents an advantage in comparison with line-of-sight measurements. These ones would require complex deconvolution algorithms [29] to reconstruct information at the symmetry plane of the flame.

It is known that LII can be strongly affected by phenomena like signal trapping or laser light attenuation [19], which would lead to a lack of LII signal at certain areas of the flame. This effect would be observable when $K_{LEM}L$ and S_{LII} were compared, as a deviation from linearity. In this regard, another benefit of the experimental-based calibration procedure is that it offers the possibility to detect any of this effects. De Francqueville et al. [16] use this information to identify a set of experimental conditions where signal trapping is taking place. They identify that under certain conditions, low LII signal is detected when high $K_{KEM}L$ is measured. In the present work, none of these effects are clearly observable (see figure 5.18). Nevertheless, for the case corresponding to HEX at high in-cylinder temperature (figure 5.25 -right-), it is possible to see some discrepancies between $K_{LII}L$ and $K_{LEM}L$. In the region of maximum soot concentration (above 55 mm from nozzle) the $K_{LII}L$ value starts decreasing, while $K_{LEM}L$ continues increasing.

In figure 5.32, the soot volume fraction distribution of DEC (left) and HEX (right) at $\rho_c = 20.73\ kg/m^3$ at TDC and $p_{inj} = 100\ MPa$ is shown. When both distributions are compared, it is possible to see that a maximum region of soot volume fraction is reached before 55 mm for HEX, which cannot be identified in the case of DEC. Moreover, downstream this region, soot distribution seems to be biased to the left side of the flame. With the optical set up described previously, the laser sheet was entering from the left side of the flames depicted in the figure. Thus, it could be interpreted as either beam attenuation or signal trapping by soot particles, as it has been previously reported that both phenomena have a similar effect [16, 20]. In the current work, $K_{LEM}L$ was measured up to 60 mm from nozzle for the reference points and up to 50 mm for the rest of test conditions. In this sense, considering the distributions observed by the three techniques, the regions of maximum soot optical thickness were unfortunately not measured with LEM. Therefore, despite signal trapping could be taking place under certain conditions, it was not possible to be detected when S_{LII} and $K_{LEM}L$ were compared (figure 5.18).

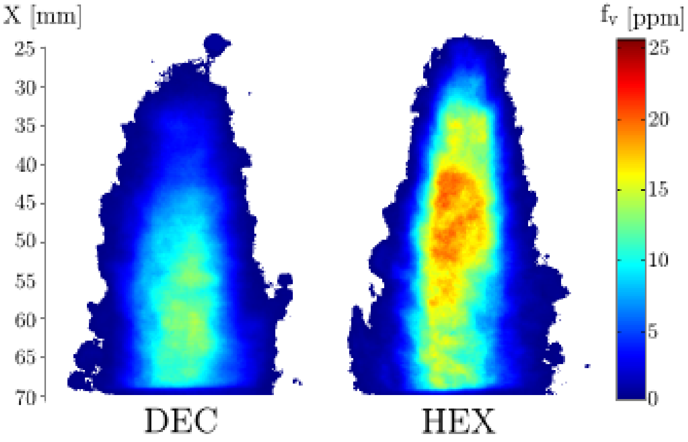

Figure 5.32. *Soot volume fraction distribution for DEC and HEX at* $\rho_c = 20.73\ kg/m^3$ *at TDC and* $p_{inj} = 100\ MPa$.

Equation 5.10 is a good approximation so that LII signal can be calibrated with LEM measurements when no signal trapping or laser attenuation are observed. However, when one of these effects is strong enough to bias the LII signal, it cannot be considered as proportional to soot volume fraction anymore. Besides, other factors like the temperature dependence of the LII signal could invalidate this hypothesis [19]. LEM measurements could provide a reliable information to detect the deviations from linearity of the LII signal. In this sense, the results shown in this work suggest that more than one LEM measuring position within the flame is recommended. A proper selection of the measuring region is mandatory, as it will improve the accuracy of the calibration procedure and will make it possible to easily detect uncertainty sources as signal trapping or laser attenuation.

Considering all the foregoing, only LEM and LII data can be considered in this study as accurate enough to describe the differences between fuels in terms of soot formation. As it has been described previously, the larger the molecule the more soot is formed. In this regard, a summary of the results obtained for all the operating conditions and fuels is presented in figure 5.33. $K_{LEM}L$ for DEC is compared with the other three fuels. The n-Hexadecane content seems to dominate reactivity of the blends. Even for 50DEC, ID and LOL are more similar to those of HEX than to those of DEC. However, this is not visible in terms of soot. Under certain operating conditions, the LOL trends observed could explain the differences in terms of soot. However, when LOL collapses, (e.g. for high temperature conditions), certain differences in soot content are still visible. An increase of the Threshold Sooting Index with the molecule length causes that, even under similar air-entrainment conditions, the fuels form different amounts of soot. In fact, results show that differences between fuels seem to be related with the average size of the molecule. Similar trends have been reported by both LII and LEM.

5.6 Summary and Conclusions

The current chapter presents the second main part of the study carried out in this thesis. The four fuels of study have been characterized in terms of soot formation. For this purpose, the three most extended optical techniques were used: Laser Extinction Method, 2-Color Pyrometry and Laser-Induced Incandescence. The three optical accesses available allowed applying the three techniques simultaneously, so that results were directly comparable.

All measurements were analysed in order to determine the reliability and usefulness of each technique. The main conclusions in this regard are:

- In comparison with $K_{LEM}L$, $K^*_{2C}L$ presents in general lower values and its sensitivity to thermodynamic conditions and fuel properties is reduced. Moreover, it has been observed that $K^*_{2C}L$ seems to saturate when flame optical thickness increases. A further theoretical analysis suggested that the measurements are strongly influenced by soot and temperature distribution within the flame. When soot concentration is small ($K_{LEM}L \leqslant 1$), 2C is still a reliable technique.
- Laser-Induced Incandescence makes it possible to measure the soot distribution at any plane within the flame, which is an advantage

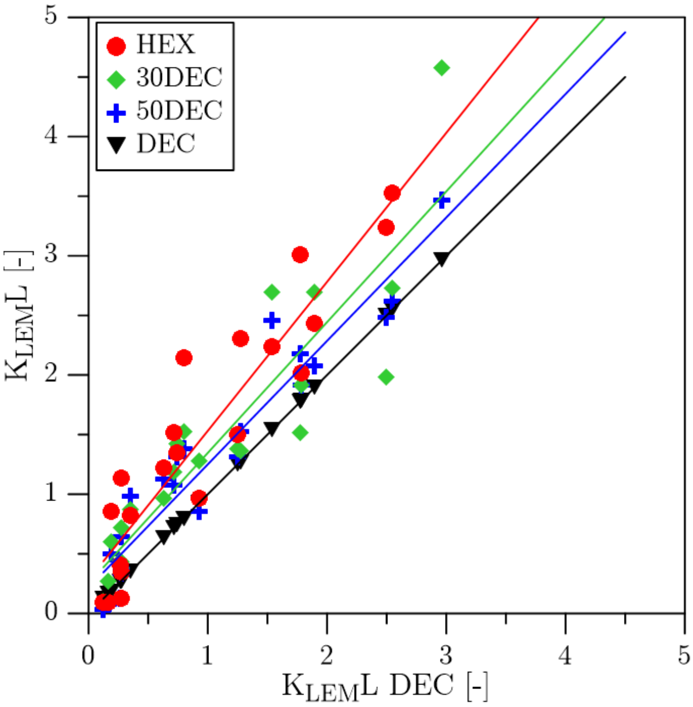

Figure 5.33. *Comparison between $K_{LEM}L$ of DEC and the other three fuels for all operating conditions presented in figure 3.3.*

compared to line-of-sight diagnostics such as LEM and 2C. A calibration procedure based on the combination of LII signal and LEM measurements has been evaluated. The methodology has shown enough sensitivity to characterize the influence of the different experimental parameters. However, the beam attenuation and signal trapping effects could have strong influence on the measurements. A proper selection of the LEM measuring points could allow detecting this problem so that using more than one LEM measuring point along the flame axis is strongly advisable. It is important to remark that if high signal trapping and/or beam attenuation effects were observed, the calibration procedure would not be possible as equation 5.10 would not be valid anymore.

LEM and LII have shown to be accurate enough to characterize the differences in soot formation for the four fuels considered in this study. It has been observed that the larger the molecule the more soot is formed. This is consistent with the ID and LOL characterization shown previously.

A reduction observed in these two parameters implies less oxygen entrainment before reaction is achieved, which leads to higher soot formation. However, under certain conditions, despite no differences have been obtained in this regard, different soot levels between fuels were still detectable. The size of the molecule has been previously related with the sooting tendency, which is coherent with the trends presented in this work.

5.A Air-fuel ratio at lift-off length

The amount of air entrained into a fuel jet at various axial locations relative to the amount of fuel injected, expressed in terms of the cross sectional average equivalence ration, $\overline{\phi}$, can be estimated using the following relationship [3, 4]:

$$\overline{\phi} = \frac{2 \cdot (A/F)_{st}}{\sqrt{1 + 16 \left(\frac{x}{x^+}\right)^2} - 1} \tag{5.14}$$

where $(A/F)_{st}$ is the stoichiometric air-fuel ratio by mass for a given fuel, x is axial distance from injector and x^+ is a characteristic length scale for the fuel jet, which is defined as:

$$x^+ = \sqrt{\frac{\rho_f}{\rho_c}} \cdot \frac{\sqrt{C_a} d}{a \cdot \tan(\alpha/2)} \beta \tag{5.15}$$

where d is the injector orifice tip diameter, C_a is the orifice area contraction coefficient, ρ_c is the ambient gas density, a is a constant with a value of 0.75, $\alpha/2$ is the jet spreading half-angle. All these parameters were measured and their values have been included in previous chapters. The term β was introduced by Pickett et al. [3] to account for a reduction in air entrainment in the reacting region of the fuel jet downstream the lift-off length, caused by heat release effects. For axial locations up to the lift-off length $\beta = 1$ is used since no heat release occurs upstream this positions. Therefore, $\overline{\phi}$ at LOL is calculated for $x = LOL$.

Bibliography

[1] Higgins B., Siebers D. and Aradi A. "Diesel-Spray Ignition and Premixed-Burn Behavior". *SAE Technical Paper*, 2000.

[2] Nerva J-G. *An assessment of fuel physical and chemical properties in the combustion of a Diesel spray*. Doctoral Thesis, Universitat Politècnica de València, Departamento de Máquinas y Motores Térmicos, 2013.

[3] Pickett L.M. and Siebers D.L. "Fuel Effects on Soot Processes of Fuel Jets at DI Diesel Conditions". *SAE Technical Papers*, 10 2003.

[4] Pickett L.M. and Siebers D.L. "Soot in diesel fuel jets: effects of ambient temperature, ambient density, and injection pressure". *Combustion and Flame*, Vol. 138, pp. 114 – 135, 2004.

[5] Payri F., Pastor J.V., Nerva J.-G. and García-Oliver J.M. "Lift-Off Length and KL Extinction Measurements of Biodiesel and Fischer-Tropsch Fuels under Quasi-Steady Diesel Engine Conditions". *SAE International Journal of Engines*, Vol. 4 n^o 2, pp. 2278–2297, 2011.

[6] Pickett Lyle M., Siebers Dennis L. and Idicheria Cherian A. "Relationship Between Ignition Processes and the Lift-Off Length of Diesel Fuel Jets". *SAE Technical Paper*, 2005.

[7] Musculus M.P. and Pickettm L.M. "Diagnostic considerations for optical laser-extinction measurements of soot in high-pressure transient combustion environments". *Combustion and Flame*, Vol. 141 n^o 4, pp. 371 – 391, 2005.

[8] Payri F., Pastor J.V., García-Oliver J.M. and Pastor J.M. "Contribution to the application of two-colour imaging to diesel combustion". *Measurement Science and Technology*, Vol. 18 n^o 8, pp. 2579–2598, 2007.

[9] Zhao H. and Ladommatos N. "Optical diagnostics for soot and temperature measurement in diesel engines". *Progress in Energy and Combustion Science*, Vol. 24 n^o 3, pp. 221–255, 1998.

[10] Hottel H.C. and Broughton F.P. "Determination of true temperature and total radiation from luminous gas flames: Use of special two-color optical pyrometer". *Industrial and Engineering Chemistry*, Vol. 4 n^o 2, pp. 166–175, 1932.

[11] Svensson K.I., MacKrory A.J., Richards M.J. and Tree D.R. "Calibration of an RGB, CCD camera and interpretation of its two-color images for KL and temperature". *SAE Technical Papers*, 2005.

[12] Zhang J., Jing W., Roberts W.L. and Fang T. "Soot temperature and KL factor for biodiesel and diesel spray combustion in a constant volume combustion chamber". *Applied Energy*, Vol. 107, pp. 52–65, 2013.

[13] Jing W., Roberts W. and Fang T. "Comparison of soot formation for diesel and jet-a in a constant volume combustion chamber using two-color pyrometry". *SAE Technical Papers*, 2014.

[14] Yan J. and Borman G.L. "Analysis and in-cylinder measurement of particulate radiant emissions and temperature in a direct injection diesel engine". *SAE Technical Papers*, 1988.

[15] Bobba M. K. and Musculus M.P. "Laser diagnostics of soot precursors in a heavy-duty diesel engine at low-temperature combustion conditions". *Combustion and Flame*, Vol. 159, pp. 832 – 842, 2011.

[16] de Francqueville L., Bruneaux G. and Thirouard B. “Soot Volume Fraction Measurements in a Gasoline Direct Injection Engine by Combined Laser Induced Incandescence and Laser Extinction Method”. *SAE Int. J. Engines 3*, Vol. 1, pp. 163–182, 2010.

[17] Cenker E., Bruneaux G., Pickett L. and Schulz C. “Study of soot formation and oxidation in the engine combustion network (ECN), spray A: Effects of ambient temperature and oxygen concentration”. *SAE International Journal of Engines*, Vol. 6 n^o 1, pp. 352–365, 2013.

[18] Svensson K. I., Richards M. J., J. Mackrory A. and Tree D. R. “Fuel Composition and Molecular Structure Effects on Soot Formation in Direct-Injection Flames Under Diesel Engine Conditions”. *SAE Technical Papers*, 2005.

[19] Schulz C., Kock B.F., Hofmann M., Michelsen H., Will S., Bougie B., Suntz R. and Smallwood G. “Laser-induced incandescence: Recent trends and current questions”. *Applied Physics B: Lasers and Optics*, Vol. 83 n^o 3, pp. 333–354, 2006.

[20] Pastor J.V., García J.M., Pastor J.M. and Buitrago J.E. “Analysis of calibration techniques for laser-induced incandescence measurements in flames”. *Measurement Science and Technology*, Vol. 17 n^o 12, pp. 3279–3288, 2006.

[21] Kook S. and Pickett L.M. “Soot volume fraction and morphology of conventional and surrogate jet fuel sprays at 1000-K and 6.7-MPa ambient conditions”. *Proceedings of the Combustion Institute*, Vol. 33 n^o 2, pp. 2911 – 2918, 2011.

[22] Henriksen T.L., Nathan G.J., Alwahabi Z.T., Qamar N., Ring T.A. and Eddings E.G. “Planar measurements of soot volume fraction and OH in a JP-8 pool fire”. *Combustion and Flame*, Vol. 156 n^o 7, pp. 1480–1492, 2009.

[23] Kook S. and Pickett L.M. “Effect of fuel volatility and ignition quality on combustion and soot formation at fixed premixing conditions”. *SAE Technical Papers*, 2009.

[24] Mensch A., Santoro R. J., Litzinger T. A. and Lee S. Y. “Sooting characteristics of surrogates for jet fuels”. *Combustion and Flame*, Vol. 157 n^o 6, pp. 1097 – 1105, 2010.

[25] Calcote H.F. and Manos D.M. “Effect of molecular structure on incipient soot formation”. *Combustion and Flame*, Vol. 49, pp. 289 – 304, 1983.

[26] Musculus M.P., Singh S. and Reitz R.D. “Gradient effects on two-color soot optical pyrometry in a heavy-duty DI diesel engine”. *Combustion and Flame*, Vol. 153 n^o 1-2, pp. 216–227, 2008.

[27] Svensson K. I. *Effects of fuel molecular structure and composition on soot formation in direct-injection spray Flames.* Doctoral Thesis, Brigham Young University, Department of Mechanical Engineering, 2005.

[28] Skeen Scott, Manin Julien, Pickett Lyle, Dalen Kristine and Ivarsson Anders. “Quantitative Spatially Resolved Measurements of Total Radiation in High-Pressure Spray Flames”. *SAE Technical Paper*, 2014.

[29] Dasch C.J. “One-dimensional tomography: a comparison of Abel, onio-peeling, and filtered backprojection methods”. *Applied Optics*, Vol. 31, pp. 1146–1152, 1992.

Chapter 6

Conclusions and future work

Contents

6.1 Conclusions

In chapter 1, it was stated that the main objective of this work was *the development and improvement of experimental methodologies for the study of the different stages of the injection-combustion process of fuel sprays, with sufficient detail and accuracy to assist development and validation of current and future multi-component evaporation and combustion models.* For this purpose, it was decided to focus the study on the optical diagnostic techniques due to the great potential that they have shown during last years. Complex experimental procedures were designed and evaluated, in search of the maximum accuracy possible.

The literature survey, presented in chapter 2, allowed to identify the most critical stages and parameters of the diesel combustion process. The first one was the evaporation and air-fuel mixture formation, which has been undoubtedly related in the literature with later pollutant formation. It has to be noted that the study of the atomization stage was omitted, as the main experimental tools utilized (for example, the test rig) were not suitable for this purpose. The second one was the autoignition and mixture combustion, which lasts until injection finishes. At this stage, pollutant formation takes place. According to this description, the work was divided in two main blocks:

- *Spray characterization under inert conditions*: evaporation and mixture formation were characterized. Geometric parameters as penetration or spray cone angle were measured, as well as the fuel mass fraction distribution. This part includes one of the main contributions of this thesis, as an experimental procedure was developed to measure the local fuel distribution for fuels with low absorption properties.
- *Combustion characterization under reactive conditions*: autoignition and soot formation were described for the four fuels. Three different optical techniques for measurement of soot were used and compared, to determine the most reliable for the purposes of the current work. This constitutes the second main contribution of this thesis. It was possible to identify advantages and drawbacks of each technique, while providing several recommendations for future works.

The measurement of fuel concentration under inert conditions was carried out by means of UV-VIS Light Absorption and Scattering technique and it was the first time that this tool was proposed to be used with low absorption fuels, as the ones considered in this work. A calibration procedure was designed to obtain in-situ measurements of the absorption coefficient of each fuel, using the same optical set-up as the one proposed for spray measurements. For the conditions and fuels used in the calibration procedure, the following conclusions were obtained:

- Fuel-air mixture inside the chamber was found to be homogeneous and the absorption coefficient calculation was found to be independent of fuel concentration, according to Lambert-Beer's Law. Besides, results showed that the methodology is sensitive to fuel properties, and it was corroborated experimentally.
- Since calibration is made immediately before or after the measurements, it allows to ensure that any degradation of the fuel properties with time will not affect the accuracy of results. This could be specially critical if fuel optical properties such as turbidity can change during long measurement campaigns, as was observed to occur quite often in laboratory test with continuous fuel recirculation, or in future works with other fuels (e.g. biofuels which are know to be oxidized with time).

- Since calibration was carried out in the engine, dependence of the absorption coefficient with pressure and temperature was captured, for a wide range of pressure and temperature values. These data are not available in literature, so that the calibration procedure, though simple, becomes one of the most relevant contributions of this thesis. For this specific application, measured ε values suggested a negligible sensitivity of this parameter to thermodynamic conditions. These results were also validated experimentally, thanks to the consistence observed between fuel distributions measured at different engine operating conditions.
- It was possible to characterize ε for low absorption fuels like DEC and 50DEC. However, it was observed that results presented uncertainties, which could even achieve the 50% of the average value.

The values of ε were utilized to obtain the fuel vapour distribution of three fuels with different optical properties. Moreover, it was combined with a deconvolution algorithm which minimized the effect of measuring noise. The main conclusions can be summarized as follows:

- It was possible to measure vapour fuel distribution near liquid length which is a clear advantage in comparison with other techniques as PRS or PLIF. However, accuracy and quality of results decreased with the absorption coefficient. The limits of the methodology were found for one of the fuels of study. However, it was observed that a slightly increase of the absorption properties could drastically reduce noise and improve accuracy of results.
- Measurements were validated with different data sources. A good agreement was observed between the on-axis fuel distribution obtained with UV-VIS LAS and theoretical calculations. However, the radial profiles were, in general, wider for the experimental data. For this reason, different error sources were evaluated and discussed to determine their effect on measurements. This analysis showed up that the cycle-to-cycle variability of the engine was hindering the spray measurements.

Soot formation was characterized by means of the three most extended optical techniques: 2-Colour Pyrometry, Laser Extinction Method and Laser-Induced Incandescence. The three optical accesses available allowed applying the three techniques simultaneously, so that results were directly comparable. All measurements were analysed in order to determine the reliability and usefulness of each technique. The main conclusions in this regard are:

- After a proper normalization, the KL values obtained with 2-Colour Pyrometry were, in general, lower than those measured with Laser Extinction Method. The sensitivity of the former to thermodynamic conditions and fuel properties was lower too. A further theoretical analysis suggested that measurements are strongly influenced by soot and temperature distribution within the flame. However, when soot concentration was low ($K_{LEM}L \leqslant 1$), 2C was still reliable.

- Laser-Induced Incandescence made it possible to measure the soot distribution at any plane within the flame, which is an advantage compared with line-of-sight diagnostics such as LEM and 2C. A calibration procedure, based on the combination of LII signal and LEM measurements, was followed and showed enough sensitivity to characterize the influence of the different experimental parameters. Besides, it was concluded that a proper selection of the LEM measuring points could allow detecting different uncertainty sources as signal trapping or laser attenuation within the flame.

- LEM and LII were found to be accurate enough to characterize the differences in soot formation for the four fuels and all the operating conditions considered in this study.

All the experimental work allowed to build a complete database for the four fuels. A wide variety of parameters were measured, from maximum liquid length or spray vapour penetration to flame optical thickness. It was possible to determine differences and similarities between fuels at each stage of the mixing-combustion process, while identifying the most relevant physical and chemical properties. The main conclusions that could be extracted from the database are:

- *Mixing process*: The main differences in terms of fuel distribution were located upstream the maximum liquid length, which were caused by the different volatility of the fuels. The maximum liquid length for the pure fuels and blends was related with the distillation curve. Downstream of this point, almost no differences were observed between them, neither for the macroscopic parameters nor for the fuel local distribution. This is consistent with the hydraulic characterization of the injection system, as it was determined that the spray momentum flux for all the fuels was similar, despite the differences in viscosity and density. All measurements were supported by simple theoretical calculations.

- *Combustion process*: The different reactivity of the fuels clearly controlled the autoignition process. The more reactive the fuel, the shorter the ignition delay and the lift-off length. The main consequence is that the amount of oxygen entrained before high temperature reactions were reached decreases with the lift-off length. This clearly affected soot formation, as it was demonstrated previously. Besides, in the case of the blends, it seems that the most reactive fraction controls the process. Finally, it was shown that the slightly different stoichiometry of each fuel was large enough to cause measurable differences in soot formation.

In summary, two pure fuels and two binary blends were characterized in detail. A wide set of experimental tools were applied for this purpose, which were optimized in order to provide the most reliable database. A new methodology for the application of UV-VIS LAS was developed and validated to work with low absorption fuels, as the ones considered in this work. Besides, different soot measuring techniques were compared to determine reliability of each of them for this specific application, and to provide guidelines for future works in this field.

6.2 Future Work

In this thesis some methods have been successfully used for the first time at CMT-Motores Térmicos, and focus has been set on the evaluation of suitability and accuracy, rather than on optimization. Consequently, some methodological aspect can be improved to either simplify the arrangement and speed up data acquisition, or to improve reliability or some other practical aspects. Besides, results obtained in this thesis and their analysis has opened new fields of research or new practical applications which could be addressed in future works. These ideas are outlined in the following paragraphs to conclude this research work:

- The UV-VIS Light Absorption and Scattering methodology could be improved. It has been found in the literature that a diffuse light source has been used for these purposes, instead of a collimated one. The comparison carried out in this thesis confirms the advantages of this type of illumination under diesel engine conditions. Therefore, future works should consider this modification of the original optical set-up. Besides, the optics used should be enlarged, to avoid the need of a translation stage to cover the whole region of interest. The use of a larger collecting lens, in combination with the corresponding camera lenses (attached to each ICCD) would make it possible to visualize the optical access of the engine at once.

- The use of infrared light for Light Absorption and Scattering measurements should be evaluated. Any hydrocarbon molecule absorbs light in the infrared range due to the C-H bonds. Therefore, even simple molecules as the n-alkanes would have acceptable absorption properties. Almost all applications found in literature are based on point measurements due to the reduced size of the detectors and radiation sources available. For this reason, a combination between UV-VIS LAS and IR-VIS LAS is proposed, similar to the one presented in this thesis between LEM and LII.

- It has been shown that 2-Colour Pyrometry measurements can be strongly affected by the optical thickness of the flame itself. However, Planck's and Kirshchoff's laws could be combined with a common deconvolution algorithms (like the Onion-peeling method), to develop a procedure to reconstruct the real soot and temperature distribution that produce the intensity of radiation measured by both cameras. Therefore, it will be possible to solve the main drawback of the 2-Colour Pyrometry when the optical thickness of the flame increases.

- The Light Absorption and Scattering technique offer the possibility of distinguishing between the different components of a binary fuel blend. Each type of hydrocarbon molecule presents a characteristic absorption pattern, due to the different type of bonds that it contains. Therefore, if wavelengths and detectors are selected properly, these differences can be exploited to identify the contribution of each component to the measured signal. However, a selection of fuels with suitable properties is mandatory, which will restrict the applicability of the technique. Moreover, its combination with the state relationship utilized in this thesis would make it possible to calculate the local composition of the mixture within the spray.

- The UV-VIS LAS techniques is nowadays applicable only to single sprays, as two aligned optical accesses are required for this purpose. A similar limitation arises when doing Schlieren visualization. However, different works can be found in literature [1, 2] where an injector holder with a mirror surface is used, creating what is known as "Multi-pass schlieren mirror systems" [3]. With a proper mirror coating, this device could be used to apply UV-VIS LAS to multi-hole nozzles.

Bibliography

[1] Pastor J.V., Payri R., García-Oliver J.M. and Briceño F.J. "Analysis of transient liquid and vapor phase penetration for diesel sprays under variable injection conditions". *Atomization and Sprays*, Vol. 21 n^o 6, pp. 503–520, 2011.

[2] Pastor J.V., García J.M., Pastor J.M. and Zapata L.D. "Evaporating diesel spray visualization using a double-pass Shadowgraphy/Schlieren imaging". *SAE Technical Papers*, 2007.

[3] Settles G.S. *Schlieren and Shadowgraph Techniques.* Springer-Verlag Berlin Heidelberg New York, 2001.

Bibliography

-.
DieselNet: Diesel emissions online.
Information available at http://www.dieselnet.com. (cited on p. 6)

-.
Engine Combustion Network.
Information available at http://www.sandia.gov/ecn/.
(cited on pp. 10, 22, 31, 34, 119, 150, 171)

-.
How Frame-Straddling works.
Information available at http://www.tsi.com. (cited on p. 75)

-.
Peak Oil News and Message Boards.
Information available at http://www.peakoil.com. (cited on p. 5)

-.
Standard Test Method for Distillation of Petroleum Products at Atmospheric Pressure.
Information available at http://www.astm.org. (cited on p. 83)

-.
Vaxa Software Educational Resources.
information available at http://www.vaxasoftware.com. (cited on p. 178)

-.
Worldwide look at Reserves and production.
Oil & Gas Journal, Vol. 110.12, pp. 28–31, 2012. (cited on p. 4)

-.
European Vehicle Market Statistics.
The International Council on Clean Transportation, 2013. (cited on p. 3)

-.
Internal Energy Outlook 2013.
U.S. Department of Energy, 2013. (cited on pp. 3, 4)

Abramovich G.N.
The theory of turbulent sets.
MIT Press, 1963. (cited on p. 151)

Akagawa H., Miyamoto T., Harada A., Sasaki S., Shimazaki N., Hashizume T. and Tsujimura K.
Approaches to solve problems of the premixed lean diesel combustion.
SAE Technical Papers, 1999. (cited on p. 8)

Akesson E.O. and Daun K.J.
Parameter selection methods for axisymmetric flame tomography through Tikhonov regularizaron.
Applied Optics, Vol. 47 n^o 3, pp. 407–416, 2008. (cited on p. 133)

Aldén M., Bood J., Li Z. and Richter M.
Visualization and understanding of combustion processes using spatially and temporally resolved laser diagnostic techniques.
Proceedings of the Combustion Institute, Vol. 33 n^o 1, pp. 69–97, 2011. (cited on p. 37)

Allocca L., Montanaro A., Cipolla G. and Vassallo A.
Spatial-Temporal Characterization of Alternative Fuel Sprays from a Second-Generation Common-Rail Fuel Injection System for Euro4 Passenger Car Application.
SAE Technical Paper, 2009. (cited on p. 110)

Araneo L., Soare V., Payri R. and Shakal J.
Setting up a PDPA system for measurements in a Diesel spray.
Journal of Physics: Conference Series, Vol. 45 n^o 1, pp. 85–93, 2006.
(cited on pp. 26, 30)

Arrègle J.
Análisis De La Estructura y Dinámica Interna De Chorros Diesel.
Doctoral Thesis, Universitat Politècnica de València, Departamento de Máquinas y Motores Térmicos, 1997. (cited on pp. 23, 29)

Badock C., Wirth R., Fath A. and Leipertz A.
Investigation of cavitation in real size diesel injection nozzles.
International Journal of Heat and Fluid Flow, Vol. 20 n^o 5, pp. 538–544, 1999.
(cited on p. 25)

Bartok W. and Sarofim A.
Fossil Fuel Combustion: A Source Book.
John Wiley & Sons, N. Y., 1991. (cited on p. 46)

Belarte E.
Estudio del procesio de combustión premezclada concontrol por la reactividad del combustible en un motor de encendido por compresión.
Doctoral Thesis, Universitat Politècnica de València, Departamento de Máquinas y Motores Térmicos, 2015. (cited on p. 9)

Benajes J., Molina S., García A. and Monsalve-Serrano J.
Effects of direct injection timing and blending ratio on RCCI combustion with different low reactivity fuels.
Energy Conversion and Management, Vol. 99, pp. 193 – 209, 2015. (cited on p. 9)

Benajes J., Payri R., Bardi M. and Martí-Aldaraví P.
Experimental characterization of diesel ignition and lift-off length using a single-hole ECN injector.
Applied Thermal Engineering, Vol. 58, pp. 554 – 563, 2013. (cited on p. 21)

Bermúdez V., García J.M., Juliá E. and Martínez S.
Engine with optically accessible cylinder head: A research tool for injection and combustion processes.
SAE Technical Papers, 2003. (cited on pp. 66, 68)

Berrocal E., Kristensson E., Hottenbach P., Aldén M. and Grönefeld G.
Quantitative imaging of a non-combusting diesel spray using structured laser illumination planar imaging.
Applied Physics B: Lasers and Optics, Vol. 109 n^o 4, pp. 683–694, 2012.
(cited on pp. 27, 28)

Bessonette P.W., Schleyer C.H., Duffy K.P., Hardy W.L. and Liechty M.P.
Effects of fuel property changes on heavy-duty HCCI combustion.
SAE Technical Papers, 2007. (cited on p. 9)

Billings T. P. and Drallmeier J. A.
A detailed assessment of the infrared extinction technique for hydrocarbon vapor measurements in a controlled two-phase flow.
Atomization and Sprays, Vol. 4 n^o 1, pp. 99–121, 1994. (cited on pp. 34, 124)

Bobba M. K. and Musculus M.P.
Laser diagnostics of soot precursors in a heavy-duty diesel engine at low-temperature combustion conditions.
Combustion and Flame, Vol. 159, pp. 832 – 842, 2011. (cited on pp. 37, 49, 204)

Bohren C.F. and Huffman D.R.
Absorption and scattering of light by small particles.
John Wiley & Sons, New York, 1983. (cited on p. 31)

Bosch W.
The fuel rate indicator: A new measuring instrument for display of the characteristics of individual injection.
SAE Technical Papers, 1966. (cited on p. 84)

Bracho G.
Experimental and theoretical study of the direct diesel injection process at low temperatures.
Doctoral Thesis, Universitat Politècnica de València, Departamento de Máquinas y Motores Térmicos, 2011. (cited on p. 87)

Brands T., Hottenbach P., Koss H.-J., Grünefeld G., Pischinger S. and Adomeit P.
Quantitative fuel-air-mixing measurements in diesel-like sprays emanating from convergent and divergent multi-layer nozzles.
SAE Technical Papers, 2012. (cited on p. 33)

Browne K.R., Partridge I.M. and Greeves G.
Fuel property effects on fuel/air mixing in an experimental diesel engine.
SAE Technical Papers, 1986. (cited on pp. 32, 111)

Bruneaux G.
Combustion structure of free and wall-impinging diesel jets by simultaneous laser-induced fluorescence of formaldehyde, poly-aromatic hydrocarbons, and hydroxides.
International Journal of Engine Research, Vol. 9 n^o 3, pp. 249–265, 2008.
(cited on pp. 37, 43, 44, 48)

Calcote H.F. and Manos D.M.
Effect of molecular structure on incipient soot formation.
Combustion and Flame, Vol. 49, pp. 289 – 304, 1983. (cited on p. 214)

Cenker E., Bruneaux G., Dreier T. and Schulz C.
Determination of small soot particles in the presence of large ones from time-resolved laser-induced incandescence.
Applied Physics B: Lasers and Optics, 2014. (cited on p. 49)

Cenker E., Bruneaux G., Pickett L. and Schulz C.
Study of soot formation and oxidation in the engine combustion network (ECN), spray A: Effects of ambient temperature and oxygen concentration.
SAE International Journal of Engines, Vol. 6 n^o 1, pp. 352–365, 2013.
(cited on pp. 49, 204, 205, 206)

Chartier C.
Spray Process in Optical Diesel Engine - Air-Entrainment and Emissions.
Doctoral Thesis, Lund Univesity, Faculty of Engineering, Department of Energy Sciences, 2012. (cited on p. 7)

Charwath M., Suntz R. and Bockhorn H.
Constraints of two-colour TiRe-LII at elevated pressures.
Applied Physics B: Lasers and Optics, Vol. 104 n^o 2, pp. 427–438, 2011. (cited on p. 49)

Chato M., Fukuda S., Sato K., Fujikawa T., Chen R., Li Z., Tian J. and Nishida K.
Fuel Spray Evaporation and Mixture Formation Processes of Ethanol/Gasoline Blend Injected by Hole-Type Nozzle for DISI Engine.
SAE International Journal of Engines, pp. 1836–1846, 2012. (cited on pp. 35, 124, 161)

Chraplyvy A.R.
Nonintruvisve measurements of vapor concentrations inside sprays.
Applied Optics, Vol. 20 n^o 15, pp. 2620–2624, 1981. (cited on p. 34)

Correas D.
Estudio Teórico-Experimental Del Chorro Libre Diesel Isotermo.
Doctoral Thesis, Universitat Politècnica de València, Departamento de Máquinas y Motores Térmicos, 1998. (cited on p. 23)

Dasch C.J.
One-dimensional tomography: a comparison of Abel, onio-peeling, and filtered backprojection methods.
Applied Optics, Vol. 31, pp. 1146–1152, 1992. (cited on pp. 132, 133, 166, 221)

Daun K.J., Thomson K.A., Liu F. and Smallwood G.J.
Deconvolution of axisymmetric flame properties using Tikhonov regularization.
Applied Optics, Vol. 45, pp. 4638–4646, 2006. (cited on pp. 132, 133)

de Francqueville L., Bruneaux G. and Thirouard B.
Soot Volume Fraction Measurements in a Gasoline Direct Injection Engine by Combined Laser Induced Incandescence and Laser Extinction Method.
SAE Int. J. Engines 3, Vol. 1, pp. 163–182, 2010.
(cited on pp. 49, 204, 205, 206, 221, 222)

Dec J. and Coy E.
OH Radical Imaging in a DI Diesel Engine and the Structure of the Early Diffusion Flame.
SAE Technical Paper, 1996. (cited on pp. 37, 43, 46)

Dec J. and Espey C.
Chemiluminescence Imaging of Autoignition in a DI Diesel Engine.
SAE Technical Paper, 1998. (cited on pp. 37, 38, 39, 41)

Dec J.E.
A Conceptual Model of DI Diesel Combustion Based on Laser-Sheet Imaging.
SAE Technical Papers, 1997. (cited on pp. 18, 44, 45, 50)

Dec J.E. and Canaan R.E.
PLIF imaging of no formation in a di diesel engine 1.
SAE Technical Papers, 1998. (cited on p. 46)

Desantes J. M., Payri R., Salvador F. J. and Gimeno J.
Measurements of Spray Momentum for the Study of Cavitation in Diesel Injection Nozzles.
SAE Technical Paper, 03 2003. (cited on p. 85)

Desantes J. M., Payri R., Salvador F. J. and Soare V.
Study of the Influence of Geometrical and Injection Parameters on Diesel Sprays Characteristics in Isothermal Conditions.
In *SAE Technical Paper.* SAE International, 2005. (cited on p. 120)

Desantes J.M., Pastor J.V., García-Oliver J.M. and Briceño F.J.
An experimental analysis on the evolution of the transient tip penetration in reacting Diesel sprays.
Combustion and Flame, Vol. 161 n^o 8, pp. 2137–2150, 2014. (cited on pp. 24, 36, 37)

Desantes J.M., Pastor J.V., Payri R. and Pastor J.M.
Experimental characterization of internal nozzle flow and diesel spray behavior. Part II: Evaporative conditions.
Atomization and Sprays, Vol. 15 n^o 5, pp. 517–543, 2005. (cited on pp. 25, 113, 120)

Desantes J.M., Payri R., Pastor J.M. and Gimeno J.
Experimental characterization of internal nozzle flow and diesel spray behavior. Part I: Nonevaporative conditions.
Atomization and Sprays, Vol. 15 n^o 5, pp. 489–516, 2005. (cited on p. 25)

Desantes J.M., Payri R., Salvador F.J and De La Morena J.
Influence of cavitation phenomenon on primary break-up and spray behaviour at stationary conditions.
Fuel, Vol. 89, pp. 3033–3041, 2010. (cited on p. 26)

Edwards C., Siebers D. and Hoskin D.
A Study of the Autoignition Process of a Diesel Spray via High Speed Visualization.
SAE Technical Paper, 1992. (cited on pp. 36, 37)

Espey C. and Dec J.E.
The effect of TDC temperature and density on the liquid-phase fuel penetration in a D. I. diesel engine.
SAE Technical Papers, 1995. (cited on pp. 31, 32)

Espey C., Dec J.E., Litzinger T.A. and Santavicca D.A.
Planar laser Rayleigh scattering for quantitative vapor-fuel imaging in a diesel jet.
Combustion and Flame, Vol. 109 n^o 1-2, pp. 65–86, 1997. (cited on p. 33)

Fansler T.D. and Parrish S.E.
Spray measurement technology: A review.
Measurement Science and Technology, Vol. 26 n^o 1, 2015. (cited on pp. 27, 32)

Flynn P.F., Durrett R.P., Hunter G.L., Zur Loye A.O., Akinyemi O.C., Dec J.E. and Westbrook C.K.
Diesel combustion: An integrated view combining laser diagnostics, chemical kinetics, and empirical validation.
SAE Technical Papers, 1999. (cited on pp. 45, 50)

Gao J. and Nishida K.
Laser absorption-scattering technique applied to asymmetric evaporating fuel sprays for simultaneous measurement of vapor/liquid mass distributions.
Applied Physics B: Lasers and Optics, pp. 1–11, 2010. (cited on pp. 126, 161)

Gao J., Nishida K., Moon S. and Matsumoto Y.
Characteristics of Evaporating Diesel Spray: A comparison of laser measurements and empirical/theoretical predictions.
SAE Technical Paper, 2009. (cited on p. 35)

García A.
Estudio de los efectos de la post-inyección sobre el proceso de combustión y la formación de hollín en motores diesel.
Doctoral Thesis, Universitat Politècnica de València, Departamento de Máquinas y Motores Térmicos, 2009. (cited on pp. 7, 18)

García-Oliver J. M.
Aportaciones al estudio del proceso de combustión turbulenta de chorros en motores diesel de inyección directa.
Doctoral Thesis, Universitat Politècnica de València, Departamento de Máquinas y Motores Térmicos, 2004. (cited on pp. 18, 20, 24, 32, 37, 44, 46, 74, 98, 102)

Gaydon A. G.
The Spectroscopy of Flames.
Springer Netherlands, 1974. (cited on p. 37)

Gessenhardt C., Zimmermann F., Schulz C., Reichle R., Pruss C. and Osten W.
Endoscopic imaging LIF diagnostics in IC engines.
Proceedings of the European Combustion Meetings, 2009. (cited on p. 10)

Gimeno J.
Desarrollo y Aplicación De La Medida Del Flujo De Cantidad de Movimiento De Un Chorro Diesel.
Doctoral Thesis, Universidad Politècnica de València, Departamento de Máquinas y Motores Térmicos, 2008. (cited on pp. 24, 25, 84, 85)

Glassman I. and Yetter R. A.
Combustion.
Elsevier Inc., 2008. (cited on p. 43)

González R. C. and Woods R. E.
Digital image processing.
Prentice Hall, 2002. (cited on p. 106)

Gumprecht R.O. and Sliepcevich C.M.
Scattering of light by large spherical particles.
Journal of physical chemistry, Vol. 57 n^o 1, pp. 90–95, 1953. (cited on p. 131)

Hattori H., Narumiya K., Tsue M. and Kadota T.
Analysis of Initial Breakup Mechanism of Diesel Spray Injected into High-Pressure Ambience.
SAE Technical Papers, 2004. (cited on pp. 26, 30)

Haynes B.S. and Wagner H.G.
Soot formation.
Progress in Energy and Combustion Science, Vol. 7 n^o 4, pp. 229 – 273, 1981. (cited on p. 46)

He X., Ma X. and Wang J.-X.
Quantitative soot concentration measurement of flame by laser induced incandescence.
Ranshao Kexue Yu Jishu/Journal of Combustion Science and Technology, Vol. 15 n^o 4, pp. 344–349, 2009. (cited on p. 49)

Hecht E. and Zajac A.
Optics.
Addison Wesley, 2003. (cited on p. 129)

Heller W.
Remarks on refractive index mixture rules.
Journal of Physical Chemistry, Vol. 69 n^o 4, pp. 1123–1129, 1965. (cited on p. 178)

Henriksen T.L., Nathan G.J., Alwahabi Z.T., Qamar N., Ring T.A. and Eddings E.G.
Planar measurements of soot volume fraction and OH in a JP-8 pool fire.
Combustion and Flame, Vol. 156 n^o 7, pp. 1480–1492, 2009. (cited on pp. 49, 205)

Heywood J. B.
Internal Combustion Engine Fundamentals.
McGraw-Hill, Inc., 1988. (cited on pp. 19, 36, 41, 43)

Higgins B., Siebers D. and Aradi A.
Diesel-Spray Ignition and Premixed-Burn Behavior.
SAE Technical Paper, 2000. (cited on pp. 37, 39, 40, 41, 188)

Higgins B.S., Mueller C.J. and Siebers D.L.
Measurements of fuel effects on liquid-phase penetration in di sprays 1.
SAE Technical Papers, 1999. (cited on pp. 32, 111, 112)

Hiroyasu H.
Spray breakup mechanism from the hole-type nozzle and its applications.
Automization and Sprays: Journal of the International Institutions for Liquid Atomization and Spray Systems, Vol. 10 n^o 3-5, pp. 511–527, 2000. (cited on p. 25)

Hodges J.T., Baritaud T.A. and Heinze T.A.
Planar liquid and gas fuel and droplet size visualization in a di diesel engine.
SAE Technical Papers, 1991. (cited on p. 31)

Hottel H.C. and Broughton F.P.
Determination of true temperature and total radiation from luminous gas flames: Use of special two-color optical pyrometer.
Industrial and Engineering Chemistry, Vol. 4 n^o 2, pp. 166–175, 1932. (cited on p. 200)

Idicheria C.A. and Pickett L.M.
Quantitative mixing measurements in a vaporizing diesel spray by rayleigh imaging.
SAE Technical Papers, 2007. (cited on p. 33)

Inagaki K., Fuyuto T., Nishikawa K., Nakakita K. and Sakata I.
Dual-fuel PCI combustion controlled by in-cylinder stratification of ignitability.
SAE Technical Papers, 2006. (cited on p. 9)

Ito T., Hosaka T., Ueda M., Senda J. and Fujimoto H.
Detailed kinetic modeling and laser diagnostics of soot formation process in diesel jet flame.
SAE Technical Papers, 2004. (cited on p. 49)

J.E. Dec.
Soot Distribution in a D.I. Diesel Engine Using 2-D Imaging of Laser-induced Incandescence, Elastic Scattering, and Flame Luminosity.
SAE Technical paper series, 1992. (cited on p. 49)

Jermy M.C. and Greenhalgh D.A.
Planar dropsizing by elastic and fluorescence scattering in sprays too dense for phase Doppler measurement.
Applied Physics B: Lasers and Optics, Vol. 71 n^o 5, pp. 703–710, 2000. (cited on p. 26)

Jerrett M., Finkelstein M.M., Brook J.R., Arain M.A., Kanaroglou P., Stieb D.M., Gilbert N.L., Verma D., Finkelstein N., Chapman K.R. and Sears M.R.
A cohort study of traffic-related air pollution and mortality in Toronto, Ontario, Canada.
Environmental Health Perspectives, Vol. 117 n^o 5, pp. 772–777, 2009. (cited on p. 5)

Jing W., Roberts W. and Fang T.
Comparison of soot formation for diesel and jet-a in a constant volume combustion chamber using two-color pyrometry.
SAE Technical Papers, 2014. (cited on pp. 49, 201)

Jing W., Roberts W.L. and Fang T.
Spray combustion of Jet-A and diesel fuels in a constant volume combustion chamber.
Energy Conversion and Management, Vol. 89, pp. 525–540, 2015.
(cited on pp. 44, 48, 49)

Juliá J.E.
Medida de concentraciones de combustible en chorros diesel mediante técnicas de fluorescencia inducida por láser.
Doctoral Thesis, CMT-Motores Térmicos, Universitat Politècnica de València, 2003.
(cited on pp. 34, 74)

Kamimoto T., Yokota H. and Kobayashi H.
Effect of high pressure injection on soot formation processes in a rapid compression machine to simulate diesel flames.
SAE Technical Papers, 1987. (cited on p. 32)

Kimura S., Aoki O., Ogawa H., Muranaka S. and Enomoto Y.
New combustion concept for ultra-clean and high-efficiency small di diesel engines.
SAE Technical Papers, 1999. (cited on p. 8)

Kock B.F., Tribalet B., Schulz C. and Roth P.
Two-color time-resolved LII applied to soot particle sizing in the cylinder of a Diesel engine.
Combustion and Flame, Vol. 147 n^o 1-2, pp. 79–92, 2006. (cited on p. 49)

Kokhanovsky A.A. and Zege E.P.
Optical properties of aerosol particles: A review of approximate analytical solutions.
Journal of Aerosol Science, Vol. 28 n^o 1, pp. 1–21, 1997. (cited on p. 129)

Kook S. and Pickett L.M.
Effect of fuel volatility and ignition quality on combustion and soot formation at fixed premixing conditions.
SAE Technical Papers, 2009. (cited on pp. 49, 205)

Kook S. and Pickett L.M.
Soot volume fraction and morphology of conventional and surrogate jet fuel sprays at 1000-K and 6.7-MPa ambient conditions.
Proceedings of the Combustion Institute, Vol. 33 n^o 2, pp. 2911 – 2918, 2011.
(cited on pp. 49, 205)

Kook S. and Pickett L.M.
Liquid length and vapor penetration of conventional, Fischer-Tropsch, coal-derived, and surrogate fuel sprays at high-temperature and high-pressure ambient conditions.
Fuel, Vol. 93, pp. 539 – 548, 2012. (cited on pp. 31, 88, 120)

Kosaka H., Aizawa T. and Kamimoto T.
Two-dimensional imaging of ignition and soot formation processes in a diesel flame.
International Journal of Engine Research, Vol. 6 n^o 1, pp. 21–42, 2005.
(cited on pp. 37, 44, 47, 48)

Kristensson E., Berrocal E. and Aldén M.
Two-pulse structured illumination imaging.
Optics Letters, Vol. 39 n^o 9, pp. 2584–2587, 2014. (cited on p. 27)

Le Gal P., Farrugia N. and Greenhalgh D.A.
Laser Sheet Dropsizing of dense sprays.
Optics and Laser Technology, Vol. 31 n^o 1, pp. 75–83, 1999. (cited on p. 26)

Lee Jinwoo and Bae Choongsik.
Application of JP-8 in a heavy duty diesel engine.
Fuel, Vol. 90 n^o 5, pp. 1762 – 1770, 2011. (cited on p. 31)

Lee K., Han Y., Lee W., Chung J. and Lee C.
Quantitative measurements of soot particles in a laminar diffusion flame using a LII/LIS technique.
Measurement Science and Technology, Vol. 16 n^o 2, pp. 519–528, 2005. (cited on p. 49)

Lequien G., Berrocal E., Gallo Y., Thermudo e Mello A., Andersson O. and Johansson B.
Effect of jet-jet interactions on the liquid fuel penetration in an optical heavy-duty di diesel engine.
SAE Technical Papers, 2013. (cited on p. 31)

Li H. and Collicott S.H.
Visualization of cavitation in high-pressure diesel fuel injector orifices.
Atomization and Sprays, Vol. 16 n^o 8, pp. 875–886, 2006. (cited on p. 25)

Linne M.
Imaging in the optically dense regions of a spray: A review of developing techniques.
Progress in Energy and Combustion Science, Vol. 39 n^o 5, pp. 403 – 440, 2013.
(cited on pp. 27, 30)

Linne M., Paciaroni M., Berrocal E. and Sedarsky D.
Ballistic imaging of liquid breakup processes in dense sprays.
Proceedings of the Combustion Institute, Vol. 32 n^o 2, pp. 2147 – 2161, 2009.
(cited on pp. 26, 30)

Linne M., Paciaroni M., Hall T. and Parker T.
Ballistic imaging of the near field in a diesel spray.
Experiments in Fluids, Vol. 40 n^o 6, pp. 836–846, 2006. (cited on p. 26)

Liu F., Thomson K.A. and Smallwood G.J.
Soot temperature and volume fraction retrieval from spectrally resolved flame emission measurement in laminar axisymmetric coflow diffusion flames: Effect of self-absorption.
Combustion and Flame, Vol. 160 n^o 9, pp. 1693–1705, 2013. (cited on p. 50)

López J. J., García-Oliver J.M., García A. and Domenech V.
Gasoline effects on spray characteristics, mixing and auto-ignition processes in a {CI} engine under Partially Premixed Combustion conditions.
Applied Thermal Engineering, Vol. 70 n^o 1, pp. 996 – 1006, 2014. (cited on p. 88)

López J.J.
Estudio teórico-experimental del chorro libre Diesel no evaporativo y de su interacción con el movimiento del aire.
Doctoral Thesis, Universitat Politècnica de València, Departamento de Máquinas y Motores Térmicos, 2003. (cited on pp. 23, 43)

Lyn W.T.
Study of burning rate and nature of combustion in diesel engines.
Symposium (International) on Combustion, Vol. 9 n^o 1, pp. 1069–1082, 1963.
(cited on p. 43)

Ma X., Xu H., Jiang C. and Shuai S.
Ultra-high speed imaging and OH-LIF study of DMF and MF combustion in a DISI optical engine.
Applied Energy, Vol. 122, pp. 247–260, 2014. (cited on p. 37)

Macian V., Payri R., Margot X. and Salvador F.J.
A CFD analysis of the influence of diesel nozzle geometry on the inception of cavitation.
Atomization and Sprays, Vol. 13 n^o 5-6, pp. 579–604, 2003. (cited on p. 25)

Manin J.
Analysis of Mixing Processes in Liquid and Vaporized Diesel Sprays Through LIF and Rayleigh Scattering Measurements.
Doctoral Thesis, Universitat Politècnica de València, Departamento de Máquinas y Motores Térmicos, 2011. (cited on p. 178)

Manin J., Bardi M., Pickett L.M., Dahms R.N. and Oefelein J.C.
Microscopic investigation of the atomization and mixing processes of diesel sprays injected into high pressure and temperature environments.
Fuel, Vol. 134, pp. 531 – 543, 2014. (cited on pp. 26, 32)

Manin J., Pickett L.M. and Skeen S.A.
Two-Color Diffused Back-Illumination Imaging as a Diagnostic for Time-Resolved Soot Measurements in Reacting Sprays.
SAE International Journal of Engines, Vol. 6 n^o 4, 2013. (cited on pp. 50, 161)

Matsuoka H., Yamashita H., Hayashi T. and Kitano K.
Effects of Fuel Properties on Diesel Spray Behavior under High Temperature and High Pressure Conditions.
SAE Technical Paper, 2009. (cited on p. 34)

Mensch A., Santoro R. J., Litzinger T. A. and Lee S. Y.
Sooting characteristics of surrogates for jet fuels.
Combustion and Flame, Vol. 157 n^o 6, pp. 1097 – 1105, 2010. (cited on p. 214)

Merola S. S., Vaglieco B. M. and Corcione, F. E.and Mancaruso E.
In-Cylinder Combustion Analysis by Flame Emission Spectroscopy of Transparent CR Diesel Engine.
SAE Technical Paper, 2003. (cited on p. 37)

Merola S.S., Vaglieco B.M. and Mancaruso E.
Analysis of combustion process in a transparent common rail diesel engine by 2D digital imaging and flame emission spectroscopy.
American Society of Mechanical Engineers, Internal Combustion Engine Division (Publication) ICE, Vol. 40, pp. 649–660, 2003. (cited on p. 37)

Merola S.S., Vaglieco B.M. and Mancaruso E.
Multiwavelength ultraviolet absorption spectroscopy of NO and OH radical concentration applied to a high-swirl diesel-like system.
Experimental Thermal and Fluid Science, Vol. 28 n^o 4, pp. 355–367, 2004.
(cited on p. 37)

Miller R.G. and Sorrell S.R.
The future of oil supply.
Philosophical Transactions of the Royal Society A: Mathematical, Physical and Engineering Sciences, Vol. 372, 2014. (cited on p. 5)

Müller S., Dutzler G.K., Priesching P., Pastor J.V. and Micó C.
Multi-component modeling of diesel fuel for injection and combustion simulation.
SAE Technical Papers, 2013. (cited on p. 10)

Molina S., García A., Pastor J.M., Belarte E. and Balloul I.
Operating range extension of RCCI combustion concept from low to full load in a heavy-duty engine.
Applied Energy, Vol. 143 n^o 0, pp. 211 – 227, 2015. (cited on p. 9)

Molina S.A.
Estudio de la influencia de los parámetros de inyección y la recirculación de gases de escape sobre el proceso de combustión, las prestaciones y las emisiones de un motor diesel de 1.8 litros de cilindrada.
Doctoral Thesis, Universitat Politècnica de València, Departamento de Máquinas y Motores Térmicos, 2003. (cited on pp. 7, 20, 41)

Mollenhauer K. and Tschoeke H.
HandBook of Diesel Engines.
Springer Heidelberg Dordrecht London New York, 2010. (cited on pp. 5, 7, 8)

Moon S., Gao J. and Nishida K.
Entrainment, Evaporation and Mixing Characteristics of Diesel Sprays around End-of-Injection.
SAE Technical Paper, 2009. (cited on pp. 124, 132)

Musculus M.P., Dec J.E. and Tree D.R.
Effects of fuel parameters and diffusion flame lift-off on soot formation in a heavy-duty di diesel engine.
SAE Technical Papers, 2002. (cited on p. 50)

Musculus M.P., Miles P.C. and Pickett L.M.
Conceptual models for partially premixed low-temperature diesel combustion.
Progress in Energy and Combustion Science, Vol. 39 n^o 2-3, pp. 246–283, 2013.
(cited on pp. 50, 51)

Musculus M.P. and Pickettm L.M.
Diagnostic considerations for optical laser-extinction measurements of soot in high-pressure transient combustion environments.
Combustion and Flame, Vol. 141 n^o 4, pp. 371 – 391, 2005.
(cited on pp. 50, 196, 197, 204)

Musculus M.P., Singh S. and Reitz R.D.
Gradient effects on two-color soot optical pyrometry in a heavy-duty DI diesel engine.
Combustion and Flame, Vol. 153 n^o 1-2, pp. 216–227, 2008. (cited on pp. 49, 220)

Musculus M.P.B.
Effects of the in-cylinder environment on diffusion flame lift-off in a di diesel engine.
SAE Technical Papers, 2003. (cited on pp. 37, 38, 43, 44)

Musculus M.P.B.
Multiple simultaneous optical diagnostic imaging of early-injection low-temperature combustion in a heavy-duty diesel engine.
SAE Technical Papers, 2006. (cited on pp. 31, 49)

Myong K.-J., Suzuki H., Senda J. and Fujimoto H.
Spray inner structure of evaporating multi-component fuel.
Fuel, Vol. 87 n^o 2, pp. 202–210, 2008. (cited on p. 33)

Naber, J.D.Siebers D.L.
Effects of Gas Density and Vaporization on Penetration and Dispersion of Diesel Sprays.
SAE Technical Paper, 1996. (cited on pp. 110, 119)

Nerva J-G.
An assessment of fuel physical and chemical properties in the combustion of a Diesel spray.
Doctoral Thesis, Universitat Politècnica de València, Departamento de Máquinas y Motores Térmicos, 2013. (cited on pp. 18, 32, 37, 41, 44, 46, 68, 69, 74, 98, 102, 188, 195)

Nishida K., Gao J., Manabe T. and Zhang Y.
Spray and mixture properties of evaporating fuel spray injected by hole-type direct injection diesel injector.
International Journal of Engine Research, Vol. 9, pp. 347–360, 2008.
(cited on pp. 132, 161)

Palomares A.
Análisis de imágenes de chorros Diesel.
Doctoral Thesis, Universitat Politècnica de València, Departamento de Máquinas y Motores Térmicos, 2001. (cited on pp. 32, 107, 154, 173)

Pastor J.V., Arrégle J. and Palomares A.
Diesel spray image segmentation with a likelihood ratio test.
Applied Optics, Vol. 40 n^o 17, pp. 2876–2885, 2001. (cited on pp. 106, 173)

Pastor J.V., García J.M., Pastor J.M. and Buitrago J.E.
Analysis of calibration techniques for laser-induced incandescence measurements in flames.
Measurement Science and Technology, Vol. 17 n^o 12, pp. 3279–3288, 2006.
(cited on pp. 49, 205, 222)

Pastor J.V., García J.M., Pastor J.M. and Zapata L.D.
Evaporating diesel spray visualization using a double-pass Shadowgraphy/Schlieren imaging.
SAE Technical Papers, 2007. (cited on p. 234)

Pastor J.V., García-Oliver J.M., Bermúdez V. and Micó C.
Spray characterization for pure fuel and binary blends under non-reacting conditions.
SAE Technical Papers, 2014. (cited on pp. 31, 32, 142)

Pastor J.V., García-Oliver J.M., García A., Micó C. and Durrett R.
A spectroscopy study of gasoline partially premixed compression ignition spark assisted combustion.
Applied Energy, Vol. 104, pp. 568–575, 2013. (cited on p. 37)

Pastor J.V., García-Oliver J.M., Nerva J.-G. and Giménez B.
Fuel effect on the liquid-phase penetration of an evaporating spray under transient diesel-like conditions.
Fuel, Vol. 90 n^o 11, pp. 3369–3381, 2011. (cited on pp. 31, 74, 108, 110, 111, 112)

Pastor J.V., Garcia-Oliver J.M., Pastor J.M. and Vera-Tudela W.
One-Dimensional diesel spray modeling of multicomponent fuels.
Atomization and Sprays, Vol. 25 n^o 6, pp. 485–517, 2015.
(cited on pp. 88, 89, 90, 92, 93, 142)

Pastor J.V., López J. J., García J.M. and Pastor J.M.
A 1D model for the description of mixing-controlled inert diesel sprays.
Fuel, Vol. 87 n^o 13-14, pp. 2871–2885, 2008. (cited on pp. 88, 89, 112, 113, 120)

Pastor J.V., Payri R., García-Oliver J.M. and Briceño F.J.
Analysis of transient liquid and vapor phase penetration for diesel sprays under variable injection conditions.
Atomization and Sprays, Vol. 21 n^o 6, pp. 503–520, 2011.
(cited on pp. 31, 32, 33, 99, 234)

Pastor J.V., Payri R., Garcia-Oliver J.M. and Briceño F.J.
Schlieren Methodology for the Analysis of Transient Diesel Flame Evolution.
SAE International Journal of Engines, Vol. 6 n^o 3, pp. 1661–1676, 2013.
(cited on pp. 24, 36)

Pastor J.V., Payri R., Gimeno J. and Nerva J.G.
Experimental study on RME blends: Liquid-phase fuel penetration, chemiluminescence, and soot luminosity in diesel-like conditions.
Energy and Fuels, Vol. 23 n^o 12, pp. 5899–5915, 2009. (cited on p. 74)

Payri F., Bermúdez V., Payri R. and Salvador F.J.
The influence of cavitation on the internal flow and the spray characteristics in diesel injection nozzles.
Fuel, Vol. 83 n^o 4-5, pp. 419–431, 2004. (cited on pp. 23, 25)

Payri F. and Desantes J. M.
Motores de Combustión Interna Alternativos.
Reverté, 2011. (cited on pp. 19, 20, 21, 24)

Payri F., Pastor J.V., García-Oliver J.M. and Pastor J.M.
Contribution to the application of two-colour imaging to diesel combustion.
Measurement Science and Technology, Vol. 18 n^o 8, pp. 2579–2598, 2007.
(cited on pp. 49, 50, 74, 199, 200, 201, 217, 218, 220)

Payri F., Pastor J.V., Nerva J.-G. and García-Oliver J.M.
Lift-Off Length and KL Extinction Measurements of Biodiesel and Fischer-Tropsch Fuels under Quasi-Steady Diesel Engine Conditions.
SAE International Journal of Engines, Vol. 4 n^o 2, pp. 2278–2297, 2011.
(cited on pp. 68, 74, 191, 197, 204, 213)

Payri F., Payri R., Bardi M. and Carreres M.
Engine combustion network: Influence of the gas properties on the spray penetration and spreading angle.
Experimental Thermal and Fluid Science, Vol. 53, pp. 236–243, 2014.
The concentration of the second component was gradually increased so the absorption coefficient should also increase. (cited on p. 88)

Payri F., Payri R., Salvador F.J. and Martínez-López J.
A contribution to the understanding of cavitation effects in Diesel injector nozzles through a combined experimental and computational investigation.
Computers and Fluids, Vol. 58, pp. 88–101, 2012. (cited on p. 25)

Payri R., García A., Domenech V., Durrett R. and Plazas A.H.
An experimental study of gasoline effects on injection rate, momentum flux and spray characteristics using a common rail diesel injection system.
Fuel, Vol. 97, pp. 390–399, 2012. (cited on pp. 85, 120)

Payri R., García J.M., Salvador F.J. and Gimeno J.
Using spray momentum flux measurements to understand the influence of diesel nozzle geometry on spray characteristics.
Fuel, Vol. 84 n^o 5, pp. 551–561, 2005. (cited on pp. 23, 86)

Payri R., García-Oliver J.M., Bardi M. and Manin J.
Fuel temperature influence on diesel sprays in inert and reacting conditions.
Applied Thermal Engineering, Vol. 35 n^o 1, pp. 185–195, 2012.
cited By 18. (cited on pp. 72, 88)

Payri R., Gimeno J., Viera J.P. and Plazas A.H.
Needle lift profile influence on the vapor phase penetration for a prototype diesel direct acting piezoelectric injector.
Fuel, Vol. 113, pp. 257–265, 2013.

Payri R., Molina S., Salvador F.J. and Gimeno J.
A study of the relation between nozzle geometry, internal flow and sprays characteristics in diesel fuel injection systems.
KSME International Journal, Vol. 18 n^o 7, pp. 1222–1235, 2004. (cited on p. 25)

Payri R., Salvador F.J., Gimeno J. and Bracho G.
A new methodology for correcting the signal cumulative phenomenon on injection rate measurements.
Experimental Techniques, Vol. 32 n^o 1, pp. 46–49, 2008. (cited on p. 84)

Payri R., Salvador F.J., Gimeno J. and Venegas O.
Study of cavitation phenomenon using different fuels in a transparent nozzle by hydraulic characterization and visualization.
Experimental Thermal and Fluid Science, Vol. 44, pp. 235–244, 2013.
(cited on pp. 25, 26)

Pickett L.M., Kook S., Persson H. and Andersson Ö.
Diesel fuel jet lift-off stabilization in the presence of laser-induced plasma ignition.
Proceedings of the Combustion Institute, Vol. 32 II, pp. 2793–2800, 2009. (cited on p. 43)

Pickett L.M., Kook S. and Williams T.C.
Visualization of Diesel Spray Penetration, Cool-Flame, Ignition, High-Temperature Combustion, and Soot Formation Using High-Speed Imaging.
SAE Technical Paper, 2009. (cited on p. 37)

Pickett L.M., Manin J., Genzale C.L., Siebers D.L., Musculus M.P.B. and Idicheria C.A.
Relationship Between Diesel Fuel Spray Vapor Penetration/Dispersion and Local Fuel Mixture Fraction.
SAE International Journal of Engines, Vol. 4 n^o 1, pp. 764–799, 2011.
(cited on pp. 33, 34)

Pickett L.M., Manin J., Payri R., Bardi M. and Gimeno J.
Transient Rate of Injection Effects on Spray Development.
SAE Technical Paper, 2013. (cited on p. 151)

Pickett L.M. and Siebers D.L.
Fuel Effects on Soot Processes of Fuel Jets at DI Diesel Conditions.
SAE Technical Papers, 10 2003. (cited on pp. 46, 49, 191, 204, 214, 226)

Pickett L.M. and Siebers D.L.
Soot in diesel fuel jets: effects of ambient temperature, ambient density, and injection pressure.
Combustion and Flame, Vol. 138, pp. 114 – 135, 2004.
(cited on pp. 46, 50, 191, 213, 214, 226)

Pickett Lyle M., Siebers Dennis L. and Idicheria Cherian A.
Relationship Between Ignition Processes and the Lift-Off Length of Diesel Fuel Jets.
SAE Technical Paper, 2005. (cited on p. 195)

Plee S. and Ahmad T.
Relative Roles of Premixed and Diffusion Burning in Diesel Combustion.
SAE Technical Paper, 1983. (cited on p. 43)

Powell C.F., Yue Y., Poola R. and Wang J.
Time-resolved measurements of supersonic fuel sprays using synchrotron X-rays.
Journal of Synchrotron Radiation, Vol. 7 n^o 6, pp. 356–360, 2000. (cited on p. 27)

Pratt W. K.
Digital image processing.
Wiley-Interscience Publication, 2001. (cited on p. 106)

Quoc H.X., Vignon J.-M. and Brun M.
A new approach of the two-color method for determining local instantaneous soot concentration and temperature in a D.I. Diesel combustion chamber.
SAE Technical Papers, 1991. (cited on p. 49)

Rabenstein F., Egermann J. and Leipertz A.
Quantitative Analysis of Vapor Phase Structures in Transient Liquid Fuel Sprays.
The 4th International Symposium COMODIA 98, 1998. (cited on p. 33)

Reitz R.D. and Bracco F.V.
Mechanism of atomization of a liquid jet.
Physics of Fluids, Vol. 25, pp. 1730–1742, 1982. (cited on p. 28)

Reitz R.D. and Bracco F.V.
Mechanisms of Breakup of Round Liquid Jets. The Encyclopedia of Fluid Mechanics, volume 3, capítulo 10, pp. 233–249.
Gulf Publishing, 1986. (cited on p. 28)

Reitz R.D., Kokjohn S.L., Hanson R.M. and Splitter D.A.
High efficiency, ultra-low emission combustion in a heavy-duty engine via fuel reactivity control.
Global Powertrain Congress 2009, Vol. 54, pp. 349–381, 2009. (cited on p. 8)

Ruiz S.
Estudio Teórico-Experimental De Los Procesos De Atomización y De Mezcla En Los Chorros Diesel D.I.
Doctoral Thesis, Universitat Politècnica de València, Departamento de Máquinas y Motores Térmicos, 2003. (cited on p. 23)

Salvador F.J.
Estudio Teórico Experimental De La Influencia De La Geometría De Toberas De Inyección Diesel Sobre Las Características Del Flujo Interno y Del Chorro.
Doctoral Thesis, Universitat Politècnica de València, Departamento de Máquinas y Motores Térmicos, 2003. (cited on pp. 23, 25)

Schmidt J.B., Schaefer Z.D., Meyer T.R., Roy S., Danczyk S.A. and Gord J.R.
Ultrafast time-gated ballistic-photon imaging and shadowgraphy in optically dense rocket sprays.
Applied Optics, Vol. 48 n^o 4, pp. B137–B144, 2009. (cited on pp. 26, 29)

Schraml S., Dankers S., Bader K., Will S. and Leipertz A.
Soot temperature measurements and implications for time-resolved laser-induced incandescence (TIRE-LII).
Combustion and Flame, Vol. 120 n^o 4, pp. 439–450, 2000. (cited on p. 49)

Schulz C., Kock B.F., Hofmann M., Michelsen H., Will S., Bougie B., Suntz R. and Smallwood G.
Laser-induced incandescence: Recent trends and current questions.
Applied Physics B: Lasers and Optics, Vol. 83 n^o 3, pp. 333–354, 2006.
(cited on pp. 49, 50, 205, 221, 222)

Schulz C. and Sick V.
Tracer-LIF diagnostics: Quantitative measurement of fuel concentration, temperature and fuel/air ratio in practical combustion systems.
Progress in Energy and Combustion Science, Vol. 31 n^o 1, pp. 75–121, 2005.
(cited on p. 34)

Seasholtz M.B., Archibald D.D., Lorber A. and Kowalski B.R.
Quantitative analysis of liquid fuel mixtures with the use of Fourier transform near-IR Raman spectroscopy.
Applied Spectroscopy, Vol. 43 n^o 6, pp. 1067–1072, 1989. (cited on p. 33)

Settles G.S.
Schlieren and Shadowgraph Techniques.
Springer-Verlag Berlin Heidelberg New York, 2001. (cited on pp. 100, 101, 177, 234)

Siebers D. and Higgins B.
Flame lift-off on direct-injection diesel sprays under quiescent conditions.
SAE Technical Papers, 2001. (cited on p. 44)

Siebers D.L.
Liquid-phase fuel penetration in diesel sprays.
SAE Technical Papers, 1998. (cited on pp. 31, 32, 110, 111)

Siebers D.L.
Scaling liquid-phase fuel penetration in diesel sprays based on mixing-limited vaporization.
SAE Technical Papers, 1999. (cited on pp. 32, 112, 113)

Singh S., Musculus M.P.B. and Reitz R.D.
Mixing and flame structures inferred from OH-PLIF for conventional and low-temperature diesel engine combustion.
Combustion and Flame, Vol. 156 n^o 10, pp. 1898–1908, 2009. (cited on p. 37)

Sjöholm J., Wellander R., Bladh H., Richter M., Bengtsson P.-E., Alden M., Aronsson U., Chartier C., Andersson Ö. and Johansson B.
Challenges for In-Cylinder High-Speed Two-Dimensional Laser-Induced Incandescence Measurements of Soot.
SAE International Journal of Engines, Vol. 4 n^o 1, pp. 1607–1622, 2011. (cited on p. 49)

Skeen Scott, Manin Julien, Pickett Lyle, Dalen Kristine and Ivarsson Anders.
Quantitative Spatially Resolved Measurements of Total Radiation in High-Pressure Spray Flames.
SAE Technical Paper, 2014. (cited on p. 220)

Slabaugh C.D., Pratt A.C. and Lucht R.P.
Simultaneous 5 kHz OH-PLIF/PIV for the study of turbulent combustion at engine conditions.
Applied Physics B: Lasers and Optics, 2014. (cited on p. 37)

Smallwood G.J. and Gülder O.L.
Views on the Structure of Transient Diesel Sprays.
Atomization and Sprays, Vol. 10, pp. 355–386, 2000. (cited on p. 29)

Snelling D.R., Thomson K.A., Smallwood G.J., Gülder O.L., Weckman E.J. and Fraser R.A.
Spectrally resolved measurement of flame radiation to determine soot temperature and concentration.
AIAA Journal, Vol. 40 n^o 9, pp. 1789–1795, 2002. (cited on p. 50)

Sou A., Hosokawa S. and Tomiyama A.
Effects of cavitation in a nozzle on liquid jet atomization.
International Journal of Heat and Mass Transfer, Vol. 50 n^o 17-18, pp. 3575–3582, 2007. (cited on p. 25)

Spalding D. B.
Combustion and mass transfer.
1979. (cited on p. 145)

Stieb D.M., Judek S. and Burnett R.T.
Meta-analysis of time-series studies of air pollution and mortality: Effects of gases and particles and the influence of cause of death, age, and season.
Journal of the Air and Waste Management Association, Vol. 52 n^o 4, pp. 470–484, 2002. (cited on p. 5)

Suh H.K. and Lee C.S.
Effect of cavitation in nozzle orifice on the diesel fuel atomization characteristics.
International Journal of Heat and Fluid Flow, Vol. 29 n^o 4, pp. 1001 – 1009, 2008.
(cited on pp. 25, 26)

Suzuki M., Nishida K. and Hiroyasu H.
Simultaneous concentration measurement of vapor and liquid in an evaporating diesel spray.
SAE Technical Paper, 1993. (cited on pp. 35, 123)

Svensson K. I.
Effects of fuel molecular structure and composition on soot formation in direct-injection spray Flames.
Doctoral Thesis, Brigham Young University, Department of Mechanical Engineering, 2005.
(cited on p. 220)

Svensson K. I., Richards M. J., J. Mackrory A. and Tree D. R.
Fuel Composition and Molecular Structure Effects on Soot Formation in Direct-Injection Flames Under Diesel Engine Conditions.
SAE Technical Papers, 2005. (cited on p. 204)

Svensson K.I., MacKrory A.J., Richards M.J. and Tree D.R.
Calibration of an RGB, CCD camera and interpretation of its two-color images for KL and temperature.
SAE Technical Papers, 2005. (cited on pp. 49, 201)

Thomson K.A., Johnson M.R., Snelling D.R. and Smallwood G.J.
Diffuse-light two-dimensional line-of-sight attenuation for soot concentration measurements.
Applied Optics, Vol. 47 n^o 5, pp. 694–703, 2008. (cited on pp. 160, 161, 163, 165)

Thring M.W. and Newby M.P.
Combustion length of enclosed turbulent jet flames.
Symposium (International) on Combustion, Vol. 4 n^o 1, pp. 789 – 796, 1953.
(cited on p. 143)

Tornatore C., Merola S., Valentino G. and Marchitto L.
In-cylinder spectroscopic measurements of combustion process in a SI engine fuelled with butanol-gasoline blend.
SAE Technical Papers, 2013. (cited on p. 37)

Tree D.R. and Svensson K.I.
Soot processes in compression ignition engines.
Progress in Energy and Combustion Science, Vol. 33 n^o 3, pp. 272–309, 2007.
(cited on pp. 46, 47)

Van de Hulst H.C.
Light Scattering by small particles.
John Wiley & Sons, N. Y., 1957. (cited on p. 31)

Vattulainen J., Nummela V., Hernberg R. and Kytölä J.
A system for quantitative imaging diagnostics and its application to pyrometric in-cylinder flame-temperature measurements in large diesel engines.
Measurement Science and Technology, Vol. 11 n^o 2, pp. 103–119, 2000. (cited on p. 49)

Vickery B.C. and Denbigh K.G.
The Polarisabilities of Bonds Part II: Bond Refractions in the Alkanes.
Transaction of the Faraday Society, Vol. 45, pp. 61–81, 1949. (cited on p. 177)

Weall A. and Collings N.
Gasoline fuelled partially premixed compression ignition in a light duty multi cylinder engine: A study of low load and low speed operation.
SAE Technical Papers, 2009. (cited on p. 8)

Williams B., Ewart P., Wangb X., Stone R., Mac H., Walmsley H., Cracknell R., Stevens R., Richardson D., Fu H. and Wallace S.
Quantitative planar laser-induced fluorescence imaging of multi-component fuel/air mixing in a firing gasoline-direct-injection engine: Effects of residual exhaust gas on quantitative PLIF.
Combustion and Flame, Vol. 157, pp. 1866–1878, 2010. (cited on p. 34)

Winklhofer E. and Plimon A.
Monitoring of hydrocarbon fuel-air mixtures by means of a light extinction technique in optiaclly accessed research engines.
Optical Engineering, Vol. 30, pp. 1262–1268, 1991. (cited on p. 34)

Yamakawa M., Takaki D., Li T., Zhang Y.-Y. and Nishida K.
Quantitative Measurement of Liquid and Vapor Phase Concentration Distribution in a D.I. Gasoline Spray by the Laser Absorption Scattering (LAS) Technique.
SAE Technical Paper, 2002. (cited on pp. 124, 126, 132, 137, 139, 165)

Yan J. and Borman G.L.
Analysis and in-cylinder measurement of particulate radiant emissions and temperature in a direct injection diesel engine.
SAE Technical Papers, 1988. (cited on pp. 49, 202)

Yanagihara H., Sato Y. and Minuta J.
A simultaneous reduction in NOx and soot in diesel engines under a new combustion system (Uniform Bulky Combustion System - UNIBUS).
17th International Vienna Motor Symposium, pp. 303–314, 1996. (cited on p. 7)

Yue Y., Powell C.F., Poola R., Wang J. and Schaller J.K.
Quantitative measurements of diesel fuel spray characteristics in the near-nozzle region using X-ray absorption.
Atomization and Sprays, Vol. 11 n^o 4, pp. 471–490, 2001. (cited on p. 27)

Zapata L.D.
Caracterización de los Procesos de Inyecciónn-Combustiónn Diesel Mediante Visualización y Procesado Digital de Imágenes.
Doctoral Thesis, Universitat Politècnica de València, Departamento de Máquinas y Motores Térmicos, 2010. (cited on pp. 18, 32, 173)

Zhang H.
Approximate calculation of extinction coefficient.
Journal of Physics D: Applied Physics, Vol. 23 n^o 12, pp. 1735–1737, 1990.
(cited on p. 129)

Zhang J., Jing W., Roberts W.L. and Fang T.
Soot temperature and KL factor for biodiesel and diesel spray combustion in a constant volume combustion chamber.
Applied Energy, Vol. 107, pp. 52–65, 2013. (cited on pp. 49, 201)

Zhang Y. Y. and Nishida K.
Vapor distribution measurement of higher and lower volatile components in an evaporating fuel spray via laser absorption scattering (LAS) technique.
Combustion Science and Technology, Vol. 179 n^o 5, pp. 863–881, 2007.
(cited on pp. 35, 124)

Zhang Y.-Y., Nishida K. and Yoshizaki T.
Characterization of Droplets and Vapor Concetration Distributions in Split-Injection Diesel Sprays by Processing UV and Visible Images.
JSME International Journal, Series B: Fluids and Thermal Engineering, Vol. 46, pp. 100–108, 2003. (cited on p. 124)

Zhang Y.-Y., Yoshizaki T. and Nishida K.
Imaging of Droplets and Vapor Distributions in a Diesel Fuel Spray by Means of a Laser Absorption–Scattering Technique.
Applied Optics, Vol. 39 n^o 33, pp. 6221–6229, 2000.
(cited on pp. 35, 124, 131, 132, 137, 139, 165)

Zhao H.
Laser Diagnostics and Optical Measurement Techniques in Internal Combustion Engines.
SAE International, Warrendale, 2012. (cited on pp. 33, 75)

Zhao H. and Ladommatos N.
Optical diagnostics for soot and temperature measurement in diesel engines.
Progress in Energy and Combustion Science, Vol. 24 n^o 3, pp. 221–255, 1998.
(cited on pp. 49, 199, 205)

Zhao H. and Ladommatos N.
Engine combustion instrumentation and diagnostics.
Warrendale, PA: Society of Automotive Engineers, 2001. 842, 2001.
(cited on pp. 31, 32)